

Numerical Studies of Aeroacoustic Aspects of Wind Instruments

Andrey Ricardo da Silva



Computational Acoustic Modeling Laboratory
McGill University
Montreal, Quebec, Canada

October 2008

A thesis submitted to McGill University in partial fulfillment of the requirements for
the degree of Doctor of Philosophy.

© 2008 Andrey Ricardo da Silva

Abstract

The characteristics of the dynamic flow in single-reed mouthpiece systems, as well as the influence of low Mach number mean flows on parameters associated with the acoustic radiation from wind instruments and generic waveguides are investigated in this thesis. In the first case, a numerical technique based on the lattice Boltzmann method coupled to a finite difference scheme is developed in order to investigate the fluid-structure interaction within the mouthpiece-reed system due to an unsteady low Mach number viscous flow. Results obtained for a stationary simulation with a static reed agree very well with those predicted by the literature based on the quasi-stationary approximation. However, simulations carried out for a dynamic regime with an oscillating reed show that the phenomenon associated with flow detachment and reattachment diverges considerably from the theoretical assumptions. The influence of low Mach number mean flows on the acoustic transmission properties of wind instruments and generic waveguides is also investigated by means of an axisymmetric lattice Boltzmann scheme. The results obtained from an unflanged pipe model agree very well with those provided by the available theories and experimental data. The effect of different horn types attached to the open end of a pipe is also investigated in detail. When compared to an unflanged pipe, horns act to significantly increase the gain of the reflection coefficient magnitude ($|R| > 1$) in the same critical regions observed in the unflanged pipe. Conversely, horns act to drastically decrease the end correction in the low-frequency limit. The results suggest that the magnitude of the reflection coefficient is independent of the horn geometry at low Strouhal numbers, whereas the end correction is highly dependent. When the simulations are conducted with the same parameters found during clarinet playing (catenoidal horn and very low Mach numbers), it is observed that the effect of the mean flow becomes negligible in terms of the reflection coefficient magnitude but can be significant on the estimation of the end correction and, consequently, on the calculation of the instrument's fundamental frequency.

Sommaire

Les caractéristiques de l'écoulement dynamique dans les systèmes d'embouchure à anche simple, ainsi que l'influence d'écoulements à faible nombre de Mach sur certains des paramètres liés au rayonnement acoustique des instruments à vent et des guides d'ondes en général sont étudiées dans cette thèse. Dans le premier cas, une technique numérique, basée sur une méthode de Boltzmann couplée à une méthode de différence finie, est développée afin d'étudier l'interaction fluide-structure dans le système bec-anche qui provient d'un écoulement visqueux instable de faible nombre de Mach. Les résultats obtenus, en régime stationnaire avec une anche statique, concident avec ceux prédits par la littérature qui se base sur l'approximation quasi stationnaire. Cependant, les simulations effectuées pour un régime dynamique avec une anche vibrante montrent que les phénomènes associés au détachement et au rattachement de l'écoulement divergent considérablement des prédictions théoriques. L'influence d'un écoulement à faible nombre de Mach sur les propriétés acoustiques des instruments à vent et des guides d'ondes en général est également étudiée à l'aide d'une méthode de Boltzmann sur réseau axisymétrique. Les résultats obtenus à partir d'un modèle de tuyau non-bafflé correspondent très bien à ceux fournis par les théories disponibles et les données expérimentales. L'effet de différents types de pavillon attachés à l'extrémité ouverte d'un tuyau est également étudié en détail. La comparaison de ces résultats avec le tuyau non-bafflé montre que les pavillons ont pour effet d'augmenter significativement le module du coefficient de réflexion pour les mêmes régions critiques ($|R| > 1$) observées dans le cas du tuyau. A l'inverse, les pavillons diminuent considérablement la correction de longueur dans la limite basse fréquence. Les résultats suggèrent que l'importance du coefficient de réflexion est indépendante de la géométrie du pavillon pour les faibles nombres de Strouhal, tandis que la correction de longueur en est fortement dépendante. Quand les simulations sont conduites avec des paramètres correspondant aux conditions normales de jeu d'une clarinette (pavillon catenodale et nombre de Mach très bas), on observe que l'effet de l'écoulement moyen devient négligeable en ce qui concerne le module du coefficient de réflexion, mais qu'il peut être important sur l'évaluation de la correction de longueur et, par conséquent, sur le calcul de la fréquence fondamentale de l'instrument.

Acknowledgments

There are indeed several people I would like to thank.

Firstly, I would like to express my sincere gratitude to Professor Gary P. Scavone, for his outstanding guidance throughout this thesis work. During this entire period, his office's door has been always open to provide suggestions, helpful advice, and encouragement. I am also grateful for his enormous flexibility regarding my choice of research, and for always steering me in the right direction.

I also owe my gratitude to the professors of the Music Technology area, in particular, Prof. Philippe Depalle, for co-advising this thesis and for always providing helpful suggestions and Prof. Marcelo Wanderley for attracting me to Montreal and for the constant and friendly support.

I am extremely indebted to many people who provided different sorts of material and feedback during my Ph.D. research. Among them, I wish to thank Prof. Mico Hirschberg from the Technische Universiteit Eindhoven who provided innumerable research materials and suggestions related to problems involving dynamic flow in single-reed mouthpieces and acoustic radiation from wind instruments. In the same way, I would like to thank Marc-Pierre Verge for also providing helpful literature and for his constant interest on my research. I must not forget Dr. Sabry Allam and Dr. Mats Åbom from The Marcus Wallenberg Laboratory for Sound and Vibration Research in Sweden, for sharing important experimental data used in this research and Dr. Maarten van Walstijn from the Queens University Belfast for sharing his finite difference reed model. My gratitude also goes to Peter in 't Panhuis, from the Technische Universiteit Eindhoven, for sharing his numerical solution of Munt's formulation, Prof. Leonardo Fuks, from the Federal University of Rio de Janeiro, for providing helpful material and suggestions

and Prof. Luc Mongeau from McGill University, for his availability to discuss several topics of my thesis. Special thanks to Professor James Buick, for his helpful extensive review of this thesis. Last but not least, my gratitude to Antoine Lefebvre for helping on the construction of the boundary element models used in this work.

The burden of writing this thesis has been greatly lessened by the support and humor of my roommates and colleagues during essential “coffee talks”. In this sense, my sincere thanks to Mark Zadel, Bruno Giordano, Georgios Marentakis, Cory McKay, Antoine Lefebvre, Bertrand Scherer, Nils Peters, Carmine Casciato and Tristan Matthews. Special thanks to Darryl Cameron for his help and promptness in solving all the logistic and network problems in the lab and to Ethel Scliar for the kind help and generosity during the last days of writing.

This research would not have been possible without the financial support of CAPES (Coordenação de Aperfeiçoamento de Pessoal de Nível Superior - Brazil). I am also thankful to CIRMMT (Centre for Interdisciplinary Research in Music Media and Technology) for their essential travel support that permitted attendance at conferences and meetings.

Finally, very warm and loving thanks to my wife Bianca, who joined me in this long enterprise and whose patience and support were paramount ingredients for my research, and to my son Tomás, who recently appeared in our lives.

Contents

1	Introduction	1
1.1	Traditional Woodwind Instrument Models	2
1.2	Thesis Objectives	5
1.3	Thesis Outline	6
2	Theoretical Background	9
2.1	Introduction	9
2.2	Governing Equations of Fluid Motion	10
2.2.1	The Continuum Assumption for a Fluid	10
2.2.2	Conservation of Mass	11
2.2.3	Conservation of Momentum	13
2.2.4	Energy Conservation for Homentropic Flows	13
2.2.5	The Navier-Stokes Equations	16
2.2.6	Reynolds Number	19
2.2.7	Vorticity	21
2.2.8	Initial and Boundary Conditions	23
2.3	Boundary Layers	25
2.3.1	Boundary Layer Equations	27

2.3.2	The von Karman Momentum Integral	28
2.3.3	Flow Gradient Effect	30
2.3.4	Flow Separation	32
2.4	Acoustics	34
2.4.1	Linearized Momentum Equation for a Stagnant, Uniform Fluid . .	34
2.4.2	Velocity Potential	36
2.4.3	Plane Waves	36
2.5	Numerical Techniques	37
2.5.1	Continuum-Based Techniques	38
2.5.2	Particle-Based Techniques	39
2.5.3	Discussion	41
3	Lattice Boltzmann Theory	45
3.1	Introduction	45
3.2	Fundamental Theory	47
3.2.1	Classical Mechanics at the Particle Level	47
3.2.2	The Boltzmann Equation	48
3.2.3	Collision Invariance and the Maxwell Distribution	50
3.2.4	The BGK Approximation	52
3.2.5	The Isothermal Lattice Boltzmann Equation	53
3.3	Lattice Boltzmann Models	55
3.3.1	Cartesian D2Q9 Model	57
3.3.2	Axisymmetric D2Q9 Model	59
3.4	The LBM Algorithm	60
3.5	Initial Conditions	62

3.6	Boundary Conditions	63
3.6.1	Solid Boundaries	63
3.6.2	Open Boundaries	65
3.7	Dimensionless to Physical Quantities	70
3.8	Discussion	71
4	Fluid-Structure Interactions in the Mouthpiece-Reed System	73
4.1	Introduction	73
4.2	The Mouthpiece-Reed Model	77
4.2.1	The Mouthpiece	77
4.2.2	The Reed	78
4.2.3	Initial and Boundary Conditions	80
4.2.4	Analyzed Geometries	81
4.3	The Quasi-Stationary Theory	83
4.4	Static and Dynamic Approaches	84
4.5	Numerical Procedures	85
4.6	Results	86
4.6.1	Static Analysis	86
4.6.2	Fully-Coupled Analysis	90
4.7	Discussion	100
5	Numerical Study of the Acoustic Radiation From Pipes and Horns	103
5.1	Introduction	103
5.2	Acoustic Transmission of an Unflanged Pipe with Zero Mean Flow	109
5.2.1	Analytical Approach	110
5.2.2	Numerical Procedures	111

5.2.3	Results for the Magnitude of the Reflection Coefficient	114
5.2.4	Results for the Dimensionless End Correction	116
5.2.5	Results for the directivity Factor G_ϕ	118
5.2.6	Discussion	121
5.3	Transmission Properties of an Unflanged Pipe Carrying a Subsonic Mean Flow	122
5.3.1	Analytic solutions	124
5.3.2	Numerical Procedures	125
5.3.3	Results for the Magnitude of the Reflection Coefficient	131
5.3.4	Results for the Dimensionless End Correction	135
5.3.5	Discussion	137
5.4	Acoustic Transmission of Horns with Zero Mean Flow	140
5.4.1	Previous Investigations	140
5.4.2	Numerical Procedures	141
5.4.3	Results for the Magnitude of the Reflection Coefficient	144
5.4.4	Results for the Dimensionless End Correction l/a	146
5.4.5	Discussion	147
5.5	Acoustic Transmission of Horns Carrying a Subsonic Mean Flow	149
5.5.1	Previous Investigations	150
5.5.2	Numerical Procedures	151
5.5.3	Results for the Magnitude of the Reflection Coefficient	152
5.5.4	Results for the End Correction Fraction	156
5.5.5	Mean Flow Effect on the Acoustic Transmission of Woodwind In- struments	161
5.6	Conclusions	166

6 Conclusion	171
6.1 Summary	171
6.2 Limitations of the Analyses	175
6.3 Suggestions for Future Work	175
A Non-aligned and moving boundaries for LBM	177
A.1 Non-aligned boundaries	177
A.2 Moving boundaries	180
A.2.1 Finding the Crossing Particles and their Distances	182
B Axisymmetric LBM model	187
C Coupling Lattice Boltzmann Models with Digital Waveguides	189
C.1 Digital Waveguides	189
C.2 Implementing the Junction between the Waveguide and LBM Models . . .	190
C.3 Impulse Response in a Closed-Closed Pipe	192
D List of Publications	195
References	199

List of Figures

1.1	Block diagram of a generic woodwind instrument model.	2
2.1	Schematic depiction of a boundary layer formation over a semi-infinite plate	26
2.2	Schematic depiction of a boundary layer formation over a semi-infinite plate	30
2.3	Schematic of the flow separation phenomenon in a curved surface in terms of stream lines and boundary layer profiles. The dashed line indicates $u = 0$.	33
2.4	Schematic representation of the major techniques for solving a slightly compressible flow problem.	42
3.1	Scheme of a two-dimensional squared lattice model with 9 sites.	56
3.2	Lattice cell representations of the most common lattice Boltzmann models for different dimensions	56
3.3	Cell representation of the $D2Q9$ model.	58
3.4	Flowchart of a generic lattice Boltzmann algorithm.	61
3.5	Illustration of the bounce-back scheme to simulate the no-slip condition: (a) Situation before propagation at $t = n$, and (b) situation after propagation at $t = n + \Delta t$	64

3.6	Illustration of the specular scheme to simulate the free-slip condition: (a) Situation before propagation at $t = n$, and (b) situation after propagation at $t = n + \Delta t$	65
3.7	Periodic boundary condition in the horizontal direction.	66
3.8	Simple buffer zones placed at the inlet and outlet of the system.	67
3.9	Schematics of the asymptotic target flow technique.	70
4.1	Lattice grid representing the two-dimensional model of the mouthpiece-reed system	78
4.2	Geometry of the single reed.	79
4.3	Different reed channel profiles used in the simulation.	82
4.4	Flowchart of the integrated algorithm	87
4.5	Vena contracta factor as a function of the modified Reynolds number	88
4.6	Pressure difference across the reed channel as a function of the volume flow.	89
4.7	Time histories of the reed displacement measured at the tip for different channel geometries	92
4.8	Channel aperture in terms of fraction of one duty cycle.	93
4.9	Normalized energy flow in terms of fraction of one duty cycle.	94
4.10	Volume flow in terms of fraction of one duty cycle.	95
4.11	Snapshots of the velocity field for different instants within the same duty cycle.	96
4.12	Vena contracta factor obtained for geometry 1 as a function of the modified Reynolds number	98
4.13	Vena contracta factor obtained for geometry 2 as a function of the modified Reynolds number	99

4.14	Vena contracta factor obtained for geometry 3 as a function of the modified Reynolds number	100
4.15	Numerical values for the vena contracta factor as a function of time for one duty cycle	101
5.1	Scheme of the axisymmetric lattice Boltzmann model of a radiating unflanged pipe.	113
5.2	Snapshots from the LB simulation of radiating cylinder	114
5.3	Magnitude value of the complex reflection coefficient at the end of the cylinder as a function of the Helmholtz number ka	116
5.4	Dimensionless end correction, l/a , as a function of the Helmholtz number ka	117
5.5	Directivity factor G_ϕ as a function of the angle ϕ measured from the axis of the cylinder for different values of ka	119
5.6	Radiation impedance as a function of the Helmholtz number ka for a distance $d = 250$ away from the pipe's mouth and $\phi = 0^\circ$	120
5.7	Phase between acoustic pressure and particle velocity as a function of the Helmholtz number ka for a distance $d = 250$ away from the pipe's mouth and $\phi = 0^\circ$	121
5.8	Schematics of the model proposed by Munt (1990).	125
5.9	Scheme of the axisymmetric LB model for the simulation of the transmission phenomena at the open end in the presence of a mean flow	126

5.10	Transient to a steady-state flow in terms of the ratio between the mean flow velocity \bar{u}_0 and the imposed target velocity u_t as a function of time steps measured inside the pipe at a distance $\Delta = 80$ before the open end for different Mach numbers.	129
5.11	Comparison between theory, simulation and experimental results for the magnitude of the reflection coefficient at the open end $ R $ as a function of the Helmholtz number for different values of the Mach number.	132
5.12	Comparison between theory, experiment and simulation results for the reflection coefficient at the open end $ R $ as a function of the Strouhal number for different Mach number values	134
5.13	Mean flow visualization for $M = 0.15$ and $u'/\bar{u}_0 = 0.1$ at the pipe open end for different time frames within a single oscillation period.	136
5.14	Comparison between theory and simulation results for the end correction ratio l/a as a function of the Helmholtz number for different values of the Mach number.	138
5.15	Comparison between theory, experiments and simulation results for the the end correction ratio l/a as a function of the Strouhal number for different Mach number values.	139
5.16	Scheme of the axisymmetric LB model for the simulation of the transmission phenomena at the open end in the presence of a mean flow	142
5.17	Boundary Elements meshes for the pipe terminated by circular horns with different curvatures.	143

-
- 5.18 Comparison between BEM and LBM results for the magnitude of the reflection coefficient $|R|$ as a function of the Helmholtz number ka for two different circular horn profiles in the absence of a mean flow measured at the end of the straight pipe termination. 145
- 5.19 Comparison between BEM and LBM results for the dimensionless end correction l/a as a function of the Helmholtz number ka for two different circular horn profiles in the absence of a mean flow measured at the end of the straight pipe termination. 147
- 5.20 Comparison between BEM and LBM results for the shifted dimensionless end correction $l - r/a$ as a function of the Helmholtz number ka for two different circular horn profiles in the absence of a mean flow, measured at the end of the straight pipe termination. 148
- 5.21 Numerical results for the magnitude of the reflection coefficient at the end of the straight pipe segment $|R|$ as a function of the Helmholtz number ka for two different circular horn profiles and different Mach numbers. 153
- 5.22 Numerical results for the magnitude of the reflection coefficient $|R|$ at the end of the straight pipe segment as a function of the Strouhal number Sr_0 for different circular horn profiles and different Mach numbers. 154
- 5.23 Numerical results for the energy reflection coefficient $|R_E|$ at the end of the straight pipe segment as a function of the Strouhal number Sr_0 for different circular horn profiles and different Mach numbers. 155
- 5.24 Mean flow visualization at the output of the pipe-horn system at different time frames within a single oscillation period. 157

5.25	Numerical results for the dimensionless end correction l/a at the end of the straight pipe segment as a function of the Helmholtz number ka for two different circular horn profiles and different Mach numbers.	158
5.26	Numerical results for the fraction of the end correction l/a at the end of the straight pipe segment as a function of the Strouhal number Sr_0 for two different circular horn profiles and different Mach numbers.	159
5.27	Numerical results for the fraction of the end correction $l - r/a$ at the end of the straight pipe segment as a function of the Strouhal number Sr_0 for two different circular horn profiles and different Mach numbers.	160
5.28	Numerical results for the magnitude of the reflection coefficient for different mean flow values measured at the junction between a cylinder and a catenoidal horn	163
5.29	Numerical results for the dimensionless end correction for different mean flow values measured at the junction between a cylinder and a catenoidal horn	164
5.30	Flow entrainment patterns for two different pipe terminations.	169
A.1	Particle reflection from a non-aligned solid wall when implemented by the simple bounce-back scheme.	178
A.2	Particle reflection from a non-aligned solid wall when implemented by the interpolated bounce-back scheme.: (a) for $q < 1/2$, (b) for $q \geq 1/2$	179
A.3	Scheme of the polygon created by the one-space step translation of a boundary segment in different directions i , according to the D2Q9 model: (a) $i = 8$, (b) $i = 1$	183

A.4	Search domain created around the enclosing polygon for different propagation directions: (a) $i = 8$, (b) $i = 1$	184
C.1	A one-dimensional digital waveguide model of a cylindrical air column.	190
C.2	Scheme of the junction between a LBM grid and the DWG.	191
C.3	Different representations of a closed-closed pipe model.	193
C.4	Impulse responses of two closed-closed pipe models.	193

List of Tables

3.1	Speed of sound and velocity weights for the main lattice models.	57
4.1	Characteristics of a plastic reed (Avanzini and van Walstijn, 2004).	80
4.2	Aspects of dynamic flow in the different channel profiles.	94
5.1	Experimental and estimated flow parameters in the clarinet for tone <i>D3</i> (146.83 Hz)	162
5.2	Frequency variation due to the effect of the mean flow	165

List of Acronyms

BE	Boltzmann Equation
BEM	Boundary Elements Method
CAA	Computational Aeroacoustics
CFD	Computational Fluid Dynamics
DNS	Direct Numerical Simulation
DWG	Digital Waveguide
FDM	Finite Difference Method
FEM	Finite Element Method
LBM	Lattice Boltzmann Method
NS	Navier-Stokes Equations

Nomenclature

α	Vena Contracta Factor
$\bar{\mathbf{u}}_\infty$	Upstream Flow Velocity
$\bar{\mathbf{u}}_o$	Cross Section Averaged Flow Velocity
\bar{F}_B	Space-Averaged Aerodynamic Force on the Reed
\bar{u}_0	Mean Flow Velocity
Δp	Pressure Difference Across the Reed Channel
Δt	Time Increment
Δ	Distance from the Open End Measured Inside the Cylinder
δ	Boundary Layer Thickness
δ^*	Averaged Boundary Layer Thickness
Δ_c	Critical Boundary Layer Thickness
Δ_x	Lattice Discretization (Lattice Pitch)
δ_{12}	Distance Between Measuring Points 1 and 2
\dot{y}_{tip}	Reed Velocity at the Tip
η	Reed's Viscoelastic Damping Coefficient
γ	Specific Heat of a Gas
$\hat{\mathbf{F}}$	Generic Source Term
μ	Dynamic Viscosity
ω_c	Collision Frequency

ϕ	Velocity Potential
ϕ_r	Azimuthal Radiation Angle
ρ'	Density Disturbance
ρ_r	Reed's Material Density
ρ_t	Target Density
ρ_{in}^T	Target Density at the Inlet of the System
ρ_{out}^T	Target Density at the outlet of the System
τ	Collision Period
τ_0	Wall Shear Stress
τ_w	Wall Thickness
θ	Momentum Thickness
φ	Phase between Acoustic Pressure and Particle Velocity
ξ	Linear Momentum
A	Reed's Cross Section Area
a	Cylinder Inner Radius
a	Cylinder Outer Radius
D	Cylinder's Diameter
d	Distance Measured from the Cylinder's Open End
D_{abs}	Thickness of the ABC Buffer
E	Energy Exchanged between the Flow and the Reed
f_i	Distribution Function in the Direction i
f_i^M	Relaxation Distribution Function in the Direction i
f_i^T	Target Distribution Function in the Direction i
G_{ϕ_r}	Acoustic Directivity Factor

H	Heaviside Step Function
h	Reed Channel Height
h_i''	Second-Order Source Term in the Direction i
h_i'	First-Order Source Term in the Direction i
I	Moment of Area about the Logitudinal Axis
$J(f)$	BGK Approximation of the Collision Integral $Q(f, f)$
J_1	Bessel Function of the First Order and First Type
k	Wave Number
ka	Helmholtz Number
L	Cylinder's Length
L	Length Scale of the System
l	End Correction
N_1	Neumann Function of the First Order and First Type
P	Pressure Source
p	Fluid Pressure
p^+	Pressure Wave Component propagating in the Positive Direction
p^-	Pressure Wave Component propagating in the Negative Direction
P_ϕ^2	Mean Square Sound Pressure at Angle ϕ
P_h^2	Mean Square Sound Pressure from an Omnidirectional Source ϕ
p'	Pressure Disturbance
p_0	Undisturbed Fluid Pressure
p_t	Target Pressure
q	Acoustic Volume Source
$Q(f, f)$	Collision integral

R	Complex Reflection Coefficient
r	Curvature Radius of a Cylindrical Horn
R^*	Universal Constant for Gases
R_E	Energy Reflection Coefficient
Re	Reynolds Number
S	Separation Point
Sr	Acoustic Strouhal Number
Sr_0	Strouhal Number
T	Oscillation Period
t	Time
t_0	Initial Time
T_j	Jet Thickness
U_B	Bernoulli Volume Flow
u_t	Target Velocity
u_v	Velocity of the Vortical Instabilities
w	Reed Width
Y	Young Modulus
Z	Acoustic Impedance
Z_Δ	Acoustic Impedance at Δ
ω	Curl of vector \mathbf{u}
\mathbf{c}_i	Lattice Vector in the Direction i
\mathbf{F}	Distributed Force on the Reed
\mathbf{n}	Normal Unity Vector
\mathbf{U}	Acoustic Volume Velocity

u'	Magnitude of the Particle Velocity
u'	Particle Velocity
u_b	Velocity of a Solid Surface
u_o	Flow Velocity
x	Position Vector
ϵ	Lattice Velocity Weight
ρ_0	Undisturbed Fluid Density
ρ	Fluid Density
c_0	Speed of Sound of a Fluid
c	Lattice Speed of Sound
M	Mach Number

Chapter 1

Introduction

The simulation of musical instruments based on computational models has become a popular approach over the last three decades due to the availability of inexpensive and fast computers and new numerical algorithms. This approach has not only created novel possibilities for the generation of sound using computers (Kausse, 2003; Guillemain et al., 2005), but has also improved significantly our understanding of the mechanisms of sound production in traditional instruments (Chaigne, 1997; Facchinetti et al., 2003). In the specific case of woodwind instruments, the computational approach has been well explored using both frequency-domain and time-domain methods. The next sections of this chapter provide a brief description of the most common numerical techniques in the literature used to represent woodwind instruments. Within this context, the scope and the outline of the thesis are also presented.

1.1 Traditional Woodwind Instrument Models

Initial computer models of woodwind instruments were developed using a frequency-domain approach (Worman, 1971, Thompson, 1979, Schumacher, 1978, Stewart and Strong, 1980). The advantage of this particular procedure is mostly related to its computational straightforwardness but presents several drawbacks when it comes to representing non-linear and/or non-stationary phenomena, which can be better described in the time domain.

Time-domain woodwind models normally rely on a general paradigm first presented by Helmholtz (1877) that describes the instrument's oscillatory behavior in terms of a feedback loop system as depicted in Fig. 1.1. The linear and nonlinear elements are fully coupled, that is, the nonlinear component (mouthpiece-reed system) excites its linear counterpart (the instrument's bore) with an energy input, which in turn affects the operation of the nonlinear component (McIntyre et al., 1983).

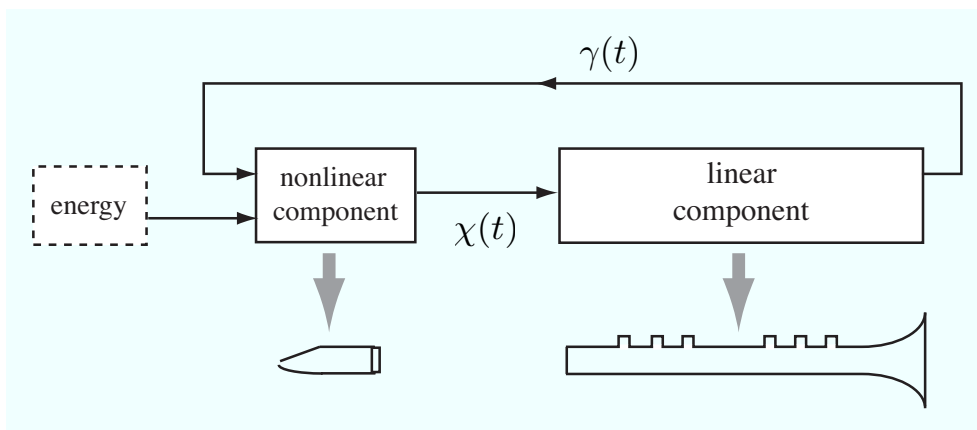


Figure 1.1 Block diagram of a generic woodwind instrument model.

The very first computational time-domain model is attributed to Schumacher (1981). In this case, the bore is simply represented by an impulse response and the oscillation of

the system is achieved by performing a convolution between the bore and the excitation of the mouthpiece-reed system. Hence, it can be argued that this model represents a transition between a frequency- to a time-domain approach inasmuch as its procedure shares the same spirit found in a typical frequency-domain technique.

Several other time-domain techniques have been proposed to represent the linear component of the system. Generally, these techniques are focused on improving the computational efficiency, allowing for a more flexible modular representation of the system elements (keyholes, bells, etc.) and, at the same time, providing an explicit correlation between physical and computational components. A successful example of such a technique is the *digital waveguide* (DWG) proposed by Smith (1986). The main characteristic of the DWG approach is the use of digital delay lines to simulate lossless traveling-wave propagation. The losses, as well as the boundary conditions found at the openings of the bore, are implemented using low-order digital filters. Several different models based on the DWG method have been proposed to represent phenomena associated with more realistic wave propagation, including the ability to represent bores with non-integer delay lengths (Välimäki, 1995), high-amplitude waves (Msallam et al., 1997) and wave propagation in bores with varying cross section (Scavone, 2002). Other methods have been proposed that share very similar characteristics to DWG such as the *multiconvolution algorithm* (Martínez et al., 1988) and more recently, the *digital impedance* technique (Guillemain et al., 2005).

In contrast, the bibliography on numerical techniques for representing the nonlinear component of a woodwind system is much sparser. Normally, the reed is represented as a lumped single-DOF oscillator (Kergomard, 1995b), although distributed representations of the reed have also been proposed (Avanzini and van Walstijn, 2004). Another very common characteristic of these models is the assumption that airflow through the

reed channel is inviscid and incompressible. Thus, the relationship between volume flow, blowing pressure and reed aperture is usually described by the Bernoulli obstruction theory (Backus, 1963, Fletcher, 1979, Saneyoshi et al., 1987, Ollivier, 2002).

The time-domain techniques discussed above have, as a final goal, the synthesis of the instrument's sound rather than serving as a tool for the investigation of the phenomena associated with the generation of sound. For this reason, they rely on significant simplifications that are essential for their real-time implementation. Nevertheless, in spite of all simplifications, most of these models predict fairly well the behavior of woodwinds in terms of onset and steady-state oscillation, but fail at representing the subtleties of the real sound. This is because the production of sound in wind instruments as a whole depends on the contribution of different nonlinear mechanisms involving two very different spatial and temporal scales associated with the acoustic and the flow fields. Some of these mechanisms have already been discussed and include the generation of sound by flow instabilities (Howe, 1975, Ko et al., 1999, Verge, 1995), the influence of low Mach number mean flow on the the radiation properties of cylinders with different open-end conditions (Cargill, 1982a,b, Rienstra, 1983, Munt, 1990) and the affect of aerodynamic forces caused by the viscous flow on the reed's vibratory behavior (Hirschberg et al., 1990, van Zon et al., 1990, Silva et al., 2007). This last phenomenon is also observed in the human phonatory system and plays a crucial role on the sound quality of the human voice (Pelorson et al., 1994, Thomson et al., 2005).

Unfortunately, the representation of such phenomena is only possible when the model is able to resolve the entire range of spatial and temporal scales involved. This requires an extremely expensive computational process and, for this reason, cannot be resolved in real time. On the other hand, the detailed representation can provide very important insights on the mechanisms of sound production and provide results that cannot be

obtained experimentally due to the invasiveness of the available methods.

1.2 Thesis Objectives

There are two primary objectives of this research. The first is to investigate the influence of the unsteady low Mach number viscous flow on the fluid-structure interaction in a single-reed mouthpiece during dynamic regimes, taking into account the influence of the reed channel geometry. The second objective is to assert the effects of low Mach number mean flows on the radiation properties of bores with different geometrical terminations.

Both objectives are accomplished by means of numerical simulations. The numerical approach is justified by the fact that the equations that govern the aforementioned phenomena, namely the Navier-Stokes equations, can only be resolved numerically. Moreover, the experimental approach would not represent an appealing alternative due to its invasive characteristic, specifically concerning the fluid-structure interaction in the mouthpiece-reed system.

In pursuing these objectives three major steps had to be accomplished in a sequential order: a) Development of models that can resolve, in a single time-step, both scales associated with the acoustic and fluid dynamic fields. b) Validation and/or verification of the models with theoretical or experimental results. c) Investigation of the aspects that have not yet been addressed, respecting the limitations of the model that are assessed during the validation/verification process.

The derivation of the numerical procedures used to accomplish the objectives of this thesis have not yet been reported in the literature. This is not a straightforward task due to the two very different scales that must be resolved in order to represent the flow and

the acoustic fields and their mutual interaction. An additional difficulty is found when representing a moving solid boundary (the reed), which has to be coupled with the fluid dynamic and acoustic domains. It must be emphasized that, due to the amount of details and high demand of computational power, the models presented in this thesis diverge from the possibility of a *real-time* implementation. Instead, they aim at improving our understanding of the mechanisms of sound production in woodwind instruments, which can be used, in a second step, to develop *real-time* models.

1.3 Thesis Outline

The presentation of this research work is divided as follows:

Chapter 2 presents the theoretical background related to the acoustic and fluid dynamic phenomena investigated throughout the thesis. Hence, the fundamental equations of fluid motion are presented in Sec. 2.2 along with an overview of the boundary layer theory. Section 2.3 introduces the phenomenon of flow separation. Some simplifications of the theory presented in Sec. 2.2 are presented in Sec. 2.4, which lead to the derivation of the equations of linear acoustics. Section 2.5 discusses the choice of the numerical techniques used to resolve the governing equations presented in the previous sections.

Chapter 3 provides the fundamental concepts of the lattice Boltzmann theory. Section 3.3 discusses the lattice Boltzmann models considered in this thesis. The essential steps of a generic lattice Boltzmann algorithm is described in Sec. 3.4. The solutions found for the implementation of initial and boundary conditions are explained in Sec. 3.5 and 3.6, respectively. Section 3.7 provides the procedure to convert the dimensionless parameters of an LBM analysis into physical quantities. Finally, Section 3.8 discusses

the suitability of LBM on the prediction of the aeroacoustic phenomena investigated in this thesis.

Aspects of the unsteady viscous flow in single-reed mouthpieces and the influence of the reed channel geometry on the reed's oscillatory behavior are investigated in Chapter 4. Section 4.2 provides a detailed description of the hybrid model, its initial and boundary conditions and presents the different geometries considered in this study. Section 4.3 presents the quasi-stationary theory proposed by van Zon et al. (1990) and Sec 4.4 discusses the main differences between the dynamic and the quasi-stationary approaches. The numerical procedure, results, as well as the conclusions are presented in Sec 4.5, 4.6 and 4.7, respectively.

Chapter 5 investigates the acoustic transmission of pipes, taking into account different open-end terminations and different mean flow conditions. Section 5.2 predicts the reflection coefficient R and the directivity factor G_ϕ in an unflanged pipe carrying a null mean flow. The obtained results are compared with those provided by the analytical solution of Levine and Schwinger (1948). Section 5.3 follows a similar rationale. In this case, however, the numeric model takes into account the presence of an outgoing subsonic mean flow and the numerical predictions are compared with the theory provided by Munt (1990) and with the experimental results provided by Allam and Åbom (2006). Section 5.4 predicts the reflection coefficient in pipes terminated by horns with different shapes carrying a zero mean flow. The validity of the results is asserted by comparing them with those obtained through a boundary element model having the same geometric characteristics. The analysis conducted in Sec. 5.5 provides the investigation of the reflection phenomena in horns, taking into account the influence of a subsonic mean flow. The mechanism of energy transfer between the acoustic field and the flow is also discussed. Finally, Sec. 5.6 presents a discussion of the effects of the mean flow tak-

ing into account the physical and dynamic characteristics of a clarinet. Moreover, the general conclusions of the chapter are presented.

Finally, the general conclusions, considerations, as well as the suggestions for future investigations are provided in Chpt. 6.

Chapter 2

Theoretical Background

2.1 Introduction

The goal of this chapter is to provide the theoretical basis of the physical phenomena investigated in the forthcoming chapters of this work. This is accomplished by structuring the proceeding sections as follows: Section 2.2 presents an overview of the fundamental equations of fluid motion based on the continuum theory, which includes the conservation of mass and momentum, as well as a discussion on the conservation of energy in the case of homentropic flows. Moreover, the section discusses fundamental assumptions adopted in this thesis associated with flow compressibility and presents an overview of the governing initial and boundary conditions. A more complete discussion of these topics can be found in Batchelor (1967) and Kundu et al. (2004).

Section 2.3 presents the fundamental aspects of the boundary layer theory, as well as an overview of the effects of pressure gradient and an introduction to flow separation. A very substantial treatment on the boundary layer theory can be found in the following textbooks: Schlichting (1955) and Young (1989).

Some major simplifications of the general equations of fluid motion presented in Sec. 2.2 are provided in Sec. 2.4. These simplifications lead to the derivation of the acoustic wave equations for stagnant and mean flows. A complete description and derivation of the theory presented in this section can be found in Pierce (1981) and Howe (1998).

Finally, Sec. 2.5 discusses the major numerical strategies for solving the governing equations presented previously. Moreover, the choice of the numerical strategy used in the subsequent chapters of this thesis is justified.

2.2 Governing Equations of Fluid Motion

2.2.1 The Continuum Assumption for a Fluid

According to Batchelor (1967, pp. 1), a simple fluid is defined as “a material such that the relative positions of its elements change by an amount which is not small when suitably chosen forces, however small in magnitude, are applied”.

From a microscopic point of view, a fluid is composed of a large number of moving molecules that undergo constant collision against each other. The branch of science responsible for investigating the properties and behavior of fluids from this discrete point of view is known as *statistical mechanics*. However, the majority of problems in engineering are concerned with the macroscopic or ‘averaged’ effects caused by the microscopic motion and collision of molecules. For such cases, it is useful to neglect the discrete molecular structure of matter and replace it by a continuous distribution.

This procedure, known as the *continuum assumption* or *macroscopic approach*, essentially implies that an infinitesimal portion of matter preserves the same macroscopic properties of matter found in a much larger scale. This assumption is only valid for low values of the Knudsen number, $\text{Kn} \ll 1$, $\text{Kn} = \psi/l$, where ψ is the mean free path

between molecules and l is the length scale of the system¹. Fortunately, this condition is met for the majority of fluid dynamic problems, considering that the mean free path ψ is usually very small². The continuum assumption obviously breaks down when the length scale of the system is rather small, as in the case of capillary flows, or when the fluid is extremely rarefied, as happens in high atmospheric altitudes.

The following sections will present the governing equations of fluid motion, whose derivations are entirely based on the continuum assumption. These equations provide exact descriptions of the macroscopic fluid behavior, as long as the low-Knudsen condition is satisfied.

2.2.2 Conservation of Mass

The conservation of mass in a generic volume V implies that the variation of mass at any time t to be equal to the net mass per unit time entering (minus that leaving) the volume V through its surface area S . The rate of increase of mass inside the volume V is expressed by the integral equation

$$\frac{d}{dt} \int_V \rho dV = \int_V \frac{\partial \rho}{\partial t} dV, \quad (2.1)$$

where ρ is the density of the fluid. The rate of mass flow through the volume surface S can be written as

$$\int_S \rho \mathbf{u} \cdot d\mathbf{A}, \quad (2.2)$$

¹The term *length scale* is the following to designate the length or distance of a system, as for instance, by the radius of a pipe through which a mean flow is discharged. The length scale is determined with the precision of one order (or a few orders) of magnitude.

²The mean free path of air at standard conditions is $\sim 5 \times 10^{-5}$ m (Kundu et al., 2004).

where \mathbf{u} is the local velocity of the fluid. According to the mass conservation statement, the rate of mass increase within the volume has to be equal to the rate of inflow through the boundaries. As a result, the integral form of the conservation law from a Eulerian³ perspective becomes

$$\int_V \frac{\partial \rho}{\partial t} dV = - \int_A \rho \mathbf{u} \cdot d\mathbf{A}. \quad (2.3)$$

The divergence theorem is used to transform the right-hand side of Eq. (2.3) into a volume integral, which gives

$$\int_A \rho \mathbf{u} \cdot d\mathbf{A} = \int_V \nabla \cdot (\rho \mathbf{u}) dV. \quad (2.4)$$

In this case, Eq. (2.3) becomes

$$\int_V \left[\frac{\partial \rho}{\partial t} + \nabla \cdot (\rho \mathbf{u}) \right] dV = 0. \quad (2.5)$$

If the integrand in Eq. (2.5) vanishes at any point, the relation holds for any volume. In this case, the differential form of the conservation of mass, also known as *continuity equation*, can be expressed by

$$\frac{1}{\rho} \frac{D\rho}{Dt} + \nabla \cdot \mathbf{u} = 0, \quad (2.6)$$

where D/Dt is the Lagrangian derivative given by

$$\frac{D}{Dt} = \frac{\partial}{\partial t} + u \frac{\partial}{\partial x}. \quad (2.7)$$

³The Eulerian description is based on the flow variables for a fixed volume in space as opposed to the Lagrangian description, which refers to the properties of individual fluid particles moving with the flow (Batchelor, 1967, pp. 71).

2.2.3 Conservation of Momentum

In a viscous fluid with kinematic viscosity ν and in the absence of body forces (gravity, magnetic, etc.), the rate in which a fluid particle changes its momentum is expressed in terms of the pressure p , and the viscous stresses caused by frictional forces between fluid elements with different velocities. In many situations, it is fair to neglect small variations of ν as a function of the temperature T and the compressible form of the momentum conservation, also known as the *equation of motion*, can be written as

$$\frac{D\mathbf{u}}{Dt} = -\left(\frac{1}{\rho}\right)\nabla p + \nu \left[\nabla^2 \mathbf{u} + \frac{1}{3}\nabla(\nabla \times \mathbf{u}) \right]. \quad (2.8)$$

In problems involving a slightly-compressible flow, as those investigated in this work, the convection term $\nabla \times \mathbf{u}$ in Eq. (2.8) can be neglected, provided that the Mach number $M = \bar{u}/c_0 < 0.3$, where \bar{u} and c_0 are the mean flow velocity and the speed of sound, respectively. Moreover, it is assumed that the deviations from the absolute pressure p' are several orders of magnitude lower than p itself (low acoustic amplitude). Thus Eq. 2.8 becomes

$$\frac{D\mathbf{u}}{Dt} = -\frac{1}{\rho}\nabla p + \nu\nabla^2 \mathbf{u}. \quad (2.9)$$

This simplification is known as the *Boussinesq approximation* (Spiegel and Veronis, 1960) and will be discussed in more detail in the next sections of this chapter.

2.2.4 Energy Conservation for Homentropic Flows

The description of the physical phenomena in single-reed instruments, as described in Chapter 1, essentially requires the representation of wave propagation superimposed on a viscous flow at a low Mach number. This is achieved with the solution of the entire

set of the Navier-Stokes equations, which includes the equations for the conservation of mass and momentum (Eqs. 2.6 and 2.9) as well as an energy conservation equation and one equation of state. The equation of state relates the thermodynamic parameters of pressure, density and temperature and the energy conservation equation couples the variations of density and momentum of a fluid with the variations of its temperature.

In many cases, however, the coupling between density, momentum and the temperature is extremely weak and can be neglected. This is particularly true when the amplitude of the acoustic waves represented in terms of variations of the fluid density are several orders of magnitude smaller than the fluid's nominal density and the flow speed is below the threshold of compressibility, defined by $M < 0.3$ (Kundu et al., 2004), which corresponds to the problems studied throughout this work. The justification for the weak coupling comes from the fact that the conduction of heat during the compression and rarefaction process provided by the acoustic oscillation is considered negligible, i.e., the internal energy of the flow is preserved. The rest of this work will focus on flows with this homentropic characteristic.

The advantage of the homentropic assumption is that the differential form of the conservation of energy can be substituted by an exact relation between the temperature, density and pressure, known as *adiabatic approximation* (Skordos, 1995, Batchelor, 1967). The condition of null heat transfer in the homentropic assumption implies that there must exist local heat reservoirs in every point in space, so that the heat generated during compression can be stored and integrally returned to the flow during its rarefaction in a reversible process.

The adiabatic approximation can be derived from the exact Laplacian relation be-

tween pressure, density and temperature, given by

$$\frac{p}{p_0} = \left(\frac{\rho}{\rho_0}\right)^\gamma = \left(\frac{T}{T_0}\right)^{\left(\frac{\gamma}{\gamma-1}\right)}, \quad (2.10)$$

where p , ρ and T are, respectively, the pressure, the density and the absolute temperature value. γ is the specific heat of a gas. The subindex 0 indicates the values before an adiabatic change. The individual changes experienced by each variable can be expressed in terms of the variations p' , ρ' and T' as follows

$$p = p_0 + p' \quad ; \quad \rho = \rho_0 + \rho' \quad ; \quad T = T_0 + T'. \quad (2.11)$$

Expanding the above relations to a first order in small quantities, one obtains

$$\frac{p}{p_0} = 1 + \frac{p'}{p_0} = \left(1 + \frac{\rho'}{\rho_0}\right)^\gamma \simeq 1 + \gamma \frac{\rho'}{\rho_0}. \quad (2.12)$$

In this case,

$$p' = \left(\gamma \frac{p_0}{\rho_0}\right) \rho'. \quad (2.13)$$

In order to continue the derivation of an adiabatic relation between pressure and density, the equation of state for gases is presented:

$$p_0 = RT_0\rho_0, \quad (2.14)$$

where R is the the universal constant for gases, which is equal to $287J \text{ Kg}^{-1}\text{K}^{-1}$ for dry air (Kundu et al., 2004, p. 16). By rearranging Eq. (2.13) into Eq. (2.14), one obtains

$$p' = \gamma RT_0\rho', \quad (2.15)$$

or

$$p' = c_0^2 \rho', \quad (2.16)$$

which defines the adiabatic speed of sound, given by

$$c_0 = \sqrt{\gamma RT_0}. \quad (2.17)$$

From Eqs. (2.11), (2.15) and (2.17), the precise adiabatic relation between pressure and density is expressed as

$$p = c_0^2 \rho + (p_0 - c_0^2 \rho_0). \quad (2.18)$$

The second term on the right-hand side of Eq. (2.18) represents the offset pressure and is normally subtracted from this expression because only the pressure gradient carries relevant information. Thus, Eq. (2.18) is normally simplified to the following relation

$$p = \rho c_0^2. \quad (2.19)$$

The adiabatic relation (Eq. 2.19) holds provided that the variations of pressure and density are small and the flow is below the limit of compressibility defined by low Mach numbers, namely $M < 0.3$.

2.2.5 The Navier-Stokes Equations

A compressible form of the Navier-Stokes equation can now be written by using the continuity equation (Eq. 2.6), the momentum equation (Eq. 2.8) and the adiabatic relation (Eq. 2.19).

As previously explained, the adiabatic relation substitutes the differential equation

for the conservation of energy, which allows the new set of equations to be solved numerically by providing four equations with four unknowns. Moreover, the assumption of a small pressure variation used in the adiabatic relation implies that variation of the temperature of the gas during the compression/relaxation process is rather small. Hence, it becomes logical to assume that the variations of viscosity with the temperature are negligible, so that the kinematic viscosity ν is assumed constant. Having that in mind, the compressible form of the Navier-Stokes equations in vectorial notation is obtained through Eqs. (2.6), (2.8) and (2.19) to become

$$\frac{D\rho}{Dt} + \rho \nabla \cdot \mathbf{u} = 0, \quad (2.20)$$

and

$$\frac{D(\rho u_j)}{Dt} + c_0^2 \frac{\partial \rho}{\partial x_j} - \nu \rho \nabla^2 u_j - \frac{\mu}{3} \frac{\partial(\nabla \cdot \mathbf{u})}{\partial x_j} = 0, \quad (2.21)$$

where the subindex $j = 1, 2, 3$ indicates the spatial directions and $\mu = \rho\nu$ is the dynamic viscosity. In the case of subsonic flows, where $M < 0.3$ and the conditions are almost isothermal, the convective term $\frac{\mu}{3} \frac{\partial(\nabla \cdot \mathbf{u})}{\partial x_j}$ in Eq. (2.21) becomes negligible and the *Boussinesq approximation* can be applied. Thus, expanding Eqs. (2.20) and (2.21) in two dimensions and omitting the convective term leads to a much simplified version of the Navier-Stokes equations, given by

$$\frac{\partial \rho}{\partial t} + \frac{\partial(\rho u_x)}{\partial x} + \frac{\partial(\rho u_y)}{\partial y} = 0, \quad (2.22)$$

$$\left[\frac{\partial u_x}{\partial t} + u_x \frac{\partial u_x}{\partial x} + u_y \frac{\partial u_x}{\partial y} \right] = -\frac{c_0^2}{\rho} \frac{\partial \rho}{\partial x} + \nu \left(\frac{\partial^2 u_x}{\partial x^2} + \frac{\partial^2 u_x}{\partial y^2} \right), \quad (2.23)$$

and

$$\left[\frac{\partial u_y}{\partial t} + u_x \frac{\partial u_y}{\partial x} + u_y \frac{\partial u_y}{\partial y} \right] = -\frac{c_0^2}{\rho} \frac{\partial \rho}{\partial y} + \nu \left(\frac{\partial^2 u_y}{\partial x^2} + \frac{\partial^2 u_y}{\partial y^2} \right). \quad (2.24)$$

The validity of the *Boussinesq approximation* has been thoroughly investigated by Spiegel and Veronis (1960), who confined their analysis to the case where the equation of state may be adequately represented by the perfect gas law. They concluded that the fully compressible form of the momentum equation (Eq. 2.21) in a perfect gas is formally equivalent to its simplified form when the convective term is omitted (Eqs. 2.23 and 2.24), provided that the following assertions are valid: (a) the vertical dimension of the fluid is much less than any scale height, and (b) the density and pressure fluctuations due to fluid motion do not exceed, in order of magnitude, the total static variations of these quantities.

The first assertion only applies when a body force such as gravity is considered. Otherwise, the simplification holds simply if assertion (b) is valid. For the case of gases, this is true if Mach number $M < 0.3$ and $u'/u_0 \equiv \rho'/\rho_0 \ll 1$, where u' is the magnitude of the acoustical particle velocity, u_0 is the flow velocity and $M = \bar{u}_0/c_0$ (Kundu et al., 2004).

Axisymmetric Forms of the Navier-Stokes Equations

For the analysis carried out in the subsequent chapters of this work, it is useful to express Equations (2.22), (2.23) and (2.24) in their axisymmetric forms by using polar cylindrical coordinates. This adaptation is based on the assumption that the flow is symmetric about a pipe's axis and thus the derivatives associated with the azimuthal polar coordinate ϕ , as well as the azimuthal component of velocity v_ϕ vanish, which allows the flow to be simply represented by the axial and radial coordinates, x and r , respectively. Thus

the remaining velocities u_x and v_r , as well as the pressure p must satisfy three equations in the spatial coordinates x and r . Hence, the continuity and momentum equations (Eqs. 2.6 and 2.9) become:

$$\frac{\partial \rho}{\partial t} + \frac{\partial u_x}{\partial x} + \frac{\partial v_r}{\partial r} = -\frac{u_r}{r}, \quad (2.25)$$

$$\frac{Du_x}{Dt} = -\frac{1}{\rho} \frac{\partial p}{\partial x} + \nu \left[\nabla^2 u_x + \frac{1}{r} \frac{\partial u_x}{\partial r} \right] \quad (2.26)$$

and

$$\frac{Du_r}{Dt} = -\frac{1}{\rho} \frac{\partial p}{\partial r} + \nu \left[\nabla^2 u_r + \frac{1}{r} \left(\frac{\partial u_r}{\partial r} - \frac{u_r}{r} \right) \right] \quad (2.27)$$

Equations (2.22), (2.23) and (2.24) as well as their polar cylindrical counterpart (Eqs. 2.25, 2.26 and 2.27) govern the phenomena analyzed in the forthcoming chapters of this work. Analytic solutions to these equations exist only for a few limited cases and thus they must be solved numerically for most practical applications. For this reason, a discussion of the possible numerical techniques that can be used to resolve them is provided in section 2.5. Before that, however, some other important theoretical background must be discussed.

2.2.6 Reynolds Number

The Reynolds number Re is an important non-dimensional parameter used to describe some dynamic characteristics of a flow and it will be extensively used throughout this work. To better explain the applicability of the Reynolds number, it is useful to rewrite the momentum equation (Eq. 2.9) in terms of dimensionless independent parameters. This can be done by considering the averaged flow velocity \bar{u} and the system length

scale L . Thus, the dimensionless parameters become $\mathbf{x}^* = \mathbf{x}/L$ (from which $\nabla^* = \nabla/L$), $\mathbf{u}^* = \mathbf{u}/\bar{u}$, $t^* = t \bar{u}/L$ and $p^* = p \rho/\bar{u}^2$. Hence, by expanding the Lagrangean of Eq. (2.9) and replacing physical by dimensionless parameters, the dimensionless form of the continuity equation becomes

$$\frac{\partial \mathbf{u}^*}{\partial t^*} + (\mathbf{u}^* \cdot \nabla^*) \mathbf{u}^* = -\nabla^* p^* + Re^{-1} \nabla^{*2} \mathbf{u}^*, \quad (2.28)$$

where $Re = \bar{u}L/\nu$ is the Reynolds number. In fact, Re can be seen as a measure of the relative importance of viscous and non-viscous forces acting on a unity volume of the fluid. The non-viscous forces, normally attributed to the motions of a rigid boundary or to the existence of frictional stresses, are represented by the first term on the right-hand side of Eq. (2.28), whereas the viscous forces are represented by the second term. The sum of the two terms results in the inertia term, on the left side of Eq. (2.28). Thus, for $Re \gg 1$ the contribution of viscous effects on the fluid motion becomes negligible. In other words, the inertia term becomes much greater than the viscous term so that, inertia and pressure forces become dominant. On the other hand, when $Re \ll 1$ pressure and viscous forces are dominant in the flow field because the inertia term becomes smaller than the viscous term. All three terms become equally important in the conservation of motion when $Re \sim 1$. An important application of the Reynolds number involves the estimation of the transition between laminar and turbulent flows, which occur at $Re \sim O(10^3)$.

The range of Reynolds numbers considered in this study varies dramatically. This is especially the case in the study of the flow within the reed channel of single-reed mouthpieces (Section 4), where the characteristics of the flow along with the geometric characteristics generates $O(10^1) \leq Re \leq O(10^3)$ within a single period of oscillation of

the reed.

2.2.7 Vorticity

The motion of fluid particles can be described as a superposition of three basic motions, namely the translation, rotation and the distortion of the particle shape due to the existence of external forces (strain). The instantaneous velocity of a fluid at $x_j + dx_j$, relative to the initial point x_j is

$$du_i = \frac{\partial u_i}{\partial x_j} dx_j. \quad (2.29)$$

The term $\partial u_i / \partial x_j$ can be written as a sum of symmetric and non-symmetric parts by

$$\frac{\partial u_i}{\partial x_j} = \frac{1}{2} \left(\frac{\partial u_i}{\partial x_j} + \frac{\partial u_j}{\partial x_i} \right) + \frac{1}{2} \left(\frac{\partial u_i}{\partial x_j} - \frac{\partial u_j}{\partial x_i} \right). \quad (2.30)$$

The symmetric term $e_{ij} = 1/2 (\partial u_i / \partial x_j + \partial u_j / \partial x_i)$ in Eq. (2.30) is called the *rate-of-strain tensor* and corresponds to a stretching of a fluid particle in three perpendicular directions (the principal axes). Conversely, the non-symmetric term $\omega_{ij} = 1/2 (\partial u_i / \partial x_j - \partial u_j / \partial x_i)$, known as *vorticity*, gives a measure of the angular rotation of the fluid particle.

Equation for the Rate of Change of Vorticity

The vorticity part of Eq. (2.30) has three independent terms, since $\omega_{xx} = \omega_{yy} = \omega_{zz} = 0$ and $\omega_{ij} = -\omega_{ji}$. Hence, the nonzero terms can be represented in a vectorial form by

$$\boldsymbol{\omega} \equiv \nabla \times \mathbf{u}, \quad (2.31)$$

where $\nabla \times \mathbf{u}$ is the *curl*⁴ of vector \mathbf{u} . The equation for the rate of change of vorticity can be obtained by taking the curl of the equation of motion (Eq. 2.9), so that

$$\nabla \times \left[\frac{\partial \mathbf{u}}{\partial t} + \mathbf{u} \cdot \nabla \mathbf{u} = -\frac{1}{\rho} \nabla p + \nu \nabla^2 \mathbf{u} \right]. \quad (2.33)$$

Using vectorial identities and noting that the curl of a gradient vanishes, Eq. (2.33) becomes

$$\frac{\partial \boldsymbol{\omega}}{\partial t} + \nabla \times (\boldsymbol{\omega} \times \mathbf{u}) = \nu \nabla^2 \boldsymbol{\omega}. \quad (2.34)$$

The second term of Eq. (2.34) can be written as

$$\nabla \times (\boldsymbol{\omega} \times \mathbf{u}) = (\mathbf{u} \cdot \nabla) \boldsymbol{\omega} - (\boldsymbol{\omega} \cdot \nabla) \mathbf{u}. \quad (2.35)$$

Noting that $\nabla \times \mathbf{u} = 0$ and $\nabla \cdot \boldsymbol{\omega} = 0$, Eq. (2.34) finally becomes

$$\frac{\partial \boldsymbol{\omega}}{\partial t} = (\boldsymbol{\omega} \cdot \nabla) \mathbf{u} + \nu \nabla^2 \boldsymbol{\omega}. \quad (2.36)$$

It is important to notice that the pressure term in the momentum equation does not appear in Eq. (2.35) due to the fact that pressure acts through the center of mass of fluid elements and, for this reason, cannot generate torque. The term $(\boldsymbol{\omega} \cdot \nabla) \mathbf{u}$ represents the rate of change in vorticity due to the stretch of vortex lines. The term $\nu \nabla^2 \boldsymbol{\omega}$ represents the rate of change of $\boldsymbol{\omega}$ due to the diffusion of vorticity. This is analogous to the term $\nu \nabla^2 \mathbf{u}$ in the momentum equation (Eq. 2.9), which represents the acceleration due to the

⁴The curl of a generic vector $\boldsymbol{\xi}$ is expressed by

$$\nabla \times \boldsymbol{\xi} = \left(\frac{\partial \xi_z}{\partial y} - \frac{\partial \xi_y}{\partial z} \right) \hat{\mathbf{x}} + \left(\frac{\partial \xi_x}{\partial z} - \frac{\partial \xi_z}{\partial x} \right) \hat{\mathbf{y}} + \left(\frac{\partial \xi_y}{\partial x} - \frac{\partial \xi_x}{\partial y} \right) \hat{\mathbf{z}}. \quad (2.32)$$

where $\hat{\mathbf{x}}$, $\hat{\mathbf{y}}$ and $\hat{\mathbf{z}}$ are unity vectors at directions x , y and z , respectively.

diffusion of momentum.

2.2.8 Initial and Boundary Conditions

The solution of the time-dependent Navier-Stokes equations presented in Sec. 2.2.5 for a particular flow situation demands the specification of initial and boundary conditions. This essentially means that the flow field at any instant t and position \mathbf{x} can be determined by its initial state and its conditions at the boundaries of the system, which may be a time-dependent or static function. For static boundary conditions, the solution is normally based on a time-independent asymptotic state. Nevertheless, there are situations in which instabilities may occur even for time-independent boundary conditions due to self-excited fluid motions.

Continuity requires that, at any point on a solid boundary, the normal velocity component of the fluid and the boundary be equal. If the solid boundary is static, and if we define \mathbf{n} as the unity vector normal to the surface, then $\mathbf{u} \cdot \mathbf{n} = 0$ on the surface.

One important case in which the solid surface is not stationary happens when it moves in uniform translation normal to the flow with velocity \mathbf{u}_{bT} . In this case, the boundary condition becomes

$$\mathbf{u} \cdot \mathbf{n} = \mathbf{u}_{bT} \cdot \mathbf{n}. \quad (2.37)$$

A significantly more intricate situation happens when the solid body changes its shape as a function of time, such as might be the case of the reed in the single-reed mouthpiece. Supposing that the equation of the solid surface is given by $\chi(\mathbf{x}, t) = 0$, the components of the normal unity vectors on the reed surface are obtained by

$$\mathbf{n} = \frac{\nabla \chi}{|\nabla \chi|}. \quad (2.38)$$

Assuming \mathbf{u}_b to be the velocity of the solid surface at a point \mathbf{x} and time t , the surface equation after a time increment dt can be expressed as

$$\chi(\mathbf{x} + \mathbf{u}_b dt, t + dt) = 0, \quad (2.39)$$

which is equivalent to

$$\mathbf{u}_b \cdot \nabla \chi + \frac{\partial \chi}{\partial t} = 0. \quad (2.40)$$

The normal component of \mathbf{u}_b is $\mathbf{u}_b \cdot \mathbf{n}$. Considering that $\nabla \chi$ is also normal to the surface, one can write

$$\mathbf{u}_b \cdot \mathbf{n} = \frac{-\left(\frac{\partial \chi}{\partial t}\right)}{|\nabla \chi|}. \quad (2.41)$$

Nevertheless, the normal component of the fluid velocity at \mathbf{x} is equal to the normal component of the surface velocity at the same point, so that

$$\mathbf{u} \cdot \mathbf{n} = \mathbf{u}_b \cdot \mathbf{n}. \quad (2.42)$$

Hence, the boundary condition of the fluid velocity at the deforming surface is given by

$$\mathbf{u} \cdot \mathbf{n} = \frac{-\left(\frac{\partial \chi}{\partial t}\right)}{|\nabla \chi|}. \quad (2.43)$$

Applying Eq. (2.38), one can write Eq. (2.43) in terms of the substantial derivative of χ , which becomes

$$\frac{\partial \chi}{\partial t} + \mathbf{u} \cdot \nabla \chi = \frac{D\chi}{Dt} = 0. \quad (2.44)$$

This boundary condition is known as *kinematic* and does not depend on the properties of the fluid. Equation (2.44) states that fluid particles on the solid surface stay on that

surface, because the relative velocity of the fluid particle with respect to the solid can only exist tangentially.

For viscous fluids, however, an additional boundary condition known as *no-slip* is necessary. This condition implies that the tangential component of the fluid velocity at the solid boundary is also zero and is derived from the notion that fluid particles in the vicinity of the surface are in thermodynamic equilibrium with that surface. The consequences of a no-slip condition are discussed in the following section.

2.3 Boundary Layers

The main consequence of the no-slip boundary condition described in Sec. 2.2.8 is that the stagnant fluid particles at the wall act to resist the tangential movement of the fluid particles that are not in contact with the solid boundary. Hence, if we assume a uniform viscous flow with upstream velocity U_∞ entering a thin plate parallel to the flow direction (Fig. 2.1), the downstream region ($x, y > 0$) in which the upstream flow velocity U_∞ is affected by the viscous forces due to the no-slip condition is called the *boundary layer*.

As evidenced by Eq. (2.28), viscous effects become negligible for high Reynolds numbers. However, in the case of viscous flows, there will always be regions where the effects associated with viscosity become dominant. These are the regions within the viscous layer, which exist not only in the vicinity of solid walls, as depicted in Fig. 2.1, but also in the boundary between jets issuing into stagnant fluids, as will be discussed in Chapter 5. In several flow situations, the effect of viscous layers does not represent a significant influence on the general behavior of the flow. In such cases, only the *kinematic* boundary condition as presented in Sec. 2.2.8 is required and the problem can be resolved either by the inviscid version of the momentum equation (also known as

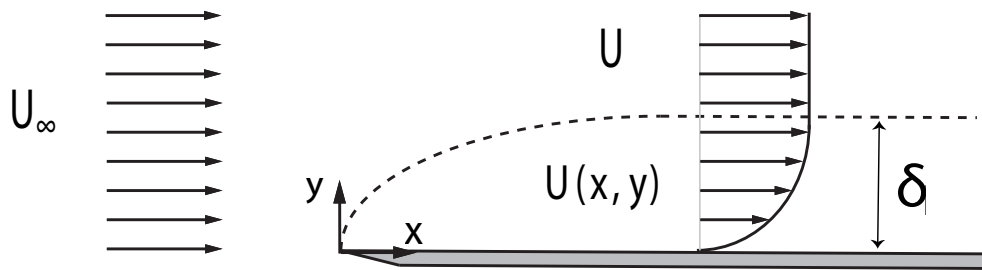


Figure 2.1 Schematic depiction of a boundary layer formation over a semi-infinite plate

Euler equation) or by the potential flow equation (Hofmans, 1998). This simplification becomes impractical, however, in situations where flow separation takes place. In this circumstance, the problem becomes governed by the compressible form of the Navier-Stokes equations (2.22, 2.23 and 2.24).

As it will be shown in Chapter 4, viscous effects are dominant in the interaction between flow and the reed, in which a significant portion of the normal oscillation period (duty cycle) is marked by flow separation. Flow separation plays an important role on the oscillatory behavior of the reed, specifically during the oscillation onset, where hydrodynamic forces caused by the separation/reattachment phenomenon are much stronger than the coupling between the reed and the acoustic field during the steady state.

The next subsections will briefly discuss the influence of viscous effects according to general flow parameters, present the fundamental concepts such as boundary layer equations, boundary layer thickness and the effect of pressure gradients on the flow separation phenomenon.

2.3.1 Boundary Layer Equations

Before deriving the complete two-dimensional boundary layer equations for a plane surface (Fig. 2.1), one should consider the mass and momentum conservation components of the Navier-Stokes equations (Eqs. 2.22 - 2.24). Moreover, it is necessary to assume a significantly high Reynolds number, so that the boundary layer thickness becomes very thin when compared with the length scale in the x direction L .

Therefore, by analyzing Eq. (2.22), we find that $\partial u_x/\partial x \sim U_\infty/L$ and $\partial u_y/\partial y \sim u_y/\delta$, where δ is the boundary layer thickness. Thus, for the spatial derivatives $\partial u_x/\partial x$ and $\partial u_y/\partial y$ in Eq. (2.6) to balance, the magnitude of the vertical component of the fluid velocity u_y must be $u_y \sim U_\infty \delta/L$, which means that the vertical component of the vertical velocity is much smaller than the velocity component along the x axis. Using this value in the momentum equation for the x direction (Eq. 2.23) and assuming balance between viscous and inertial forces in the boundary layer gives $\delta/L \sim \sqrt{\nu/U_\infty L} \sim Re^{-1/2}$. This implies that the boundary layer thickness δ is inversely proportional to the square root of the Reynolds number. In the case of the y -momentum equation (Eq. 2.24), only the term $\partial p/\partial y$ remains, so that the pressure across the boundary layer is assumed constant. Thus, the unsteady boundary layer equations become

$$\frac{\partial u_x}{\partial x} + \frac{\partial u_y}{\partial y} = 0, \quad (2.45)$$

$$\frac{\partial u_x}{\partial t} + u_x \frac{\partial u_x}{\partial x} + u_y \frac{\partial u_x}{\partial y} = -\frac{1}{\rho} \frac{\partial p}{\partial x} + \nu \frac{\partial^2 u_x}{\partial y^2}, \quad (2.46)$$

and

$$0 = -\frac{1}{\rho} \frac{\partial p}{\partial y}. \quad (2.47)$$

As previously discussed, there is no pressure gradient across the direction y normal to the flow, so that the pressure at any point within δ has the same pressure of any point outside in the viscous region in the same x -location. Thus, the pressure p is just a function of the horizontal coordinate x and its gradient can be expressed in terms of Eq. (2.23) by

$$\frac{\partial p(x, t)}{\partial x} = -\rho \frac{\partial U(x, t)}{\partial t} - \rho U(x, t) \frac{\partial U(x, t)}{\partial x}, \quad (2.48)$$

which is the equation of pressure gradient for an unsteady flow and acts to couple the inviscid core of the flow (outside the boundary layer) with the viscous flow within δ . In most flow problems there is no exact solution for the above equation and thus, a numerical approach is required.

2.3.2 The von Karman Momentum Integral

Unfortunately, the exact solutions for the boundary layer equations (Eqs. 2.45 - 2.47) exist only for very simple cases, such as the flow over a flat semi-infinite plate. Nevertheless, an approximate method exists for more complicated flows, which satisfies the boundary layer equations across δ . The method, known as the *Karman momentum integral*, is obtained by integrating the boundary layer equation

$$u_x \frac{\partial u_x}{\partial x} + u_y \frac{\partial u_x}{\partial y} = U \frac{dU}{dx} + \nu \frac{\partial^2 u_x}{\partial y^2}. \quad (2.49)$$

Equation (2.49) is similar to Eq. (2.46), the only difference being the replacement of the pressure gradient by the velocity U , $\partial U / \partial y = 0$ at the edge of the boundary layer, where the inviscid form of Eq. (2.23) applies. Furthermore, the flow is assumed to be steady,

so that $\frac{\partial U(x,t)}{\partial t} = 0$. Adding and subtracting $u_x(dU/dx)$, it is possible to obtain

$$(U - u_x) \frac{dU}{dx} + u_x \frac{\partial(U - u_x)}{\partial x} + u_y \frac{\partial(U - u_x)}{\partial y} = -\nu \frac{\partial^2 u_x}{\partial y^2}. \quad (2.50)$$

With some manipulation and integrating from $y = 0 \rightarrow h$, where $h > \delta$ at any distance above the boundary layer, the integral of Eq. (2.50) becomes

$$U \delta^* \frac{dU}{dx} + \int_0^h \left[u_x \frac{\partial(U - u_x)}{\partial x} + (U - u_x) \frac{\partial u_x}{\partial x} \right] dy = \frac{\tau_0}{\rho}, \quad (2.51)$$

where τ_0 and δ^* are the wall shear stress and the averaged boundary layer thickness, respectively. The integral in Eq. (2.51) equals

$$\int_0^h \frac{\partial}{\partial x} [u_x(U - u_x)] dy = \frac{d}{dx} \int_0^h u_x(U - u_x) dy = \frac{d}{dx} (U^2 \theta), \quad (2.52)$$

where θ is the momentum thickness, defined as

$$\theta = \int_0^\infty \frac{u_x}{U} \left(1 - \frac{u_x}{U} \right) dy. \quad (2.53)$$

Equation (2.51) can now be finally written in its differential form as

$$\frac{d}{dx} (U^2 \theta) + \delta^* U \frac{dU}{dx} = \frac{\tau_0}{\rho}, \quad (2.54)$$

which is called the *Karman Equation*, whose only unknowns are θ , δ^* and τ_0 . Equation (2.54) is valid for both laminar and turbulent regimes and can be used to estimate the boundary layer thickness and other parameters. In the turbulent case, however, τ_0 cannot be derived via analytical means, thus requiring an empirical value.

In a similar way, an unsteady form can be derived from Eq. (2.46) by considering the

temporal derivative $\partial U(x, t)/\partial t$, which gives

$$\frac{U\delta^*}{\delta t} + \frac{d}{dx}(U^2\theta) + \delta^*U\frac{dU}{dx} = \frac{\tau_0}{\rho}. \quad (2.55)$$

2.3.3 Flow Gradient Effect

In the previous section an example was given of a flat plate (Fig. 2.1) whose pressure gradient across the boundary layer was null. However, the assumption $\partial p/\partial y = 0$ does not hold for curved surfaces, such as that depicted in Fig. 2.2. For this type of geometry, the pressure gradient changes drastically, depending on the surface region. Hence, in the case of the geometry shown in Fig. 2.2, the stream velocity $U(x)$ increases in the region upstream of the highest point (flat surface) due to the convergence of the flow streamlines, which causes a pressure drop along the x direction. Conversely, $U(x)$ decelerates in the region downstream of the plateau due to divergence of flow streamlines, which results in an increase of pressure.

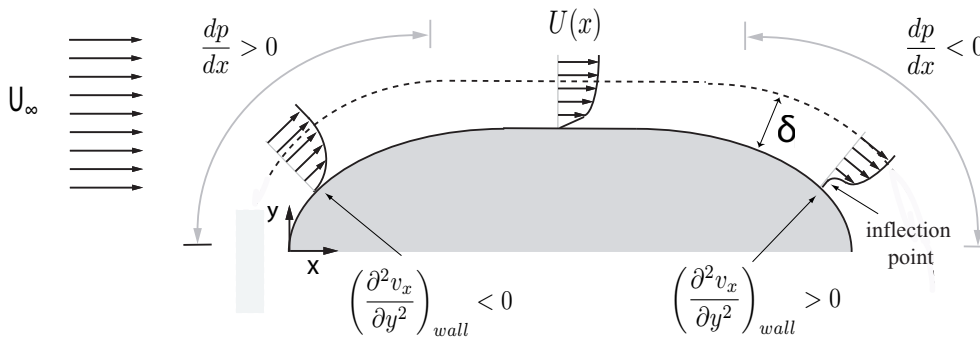


Figure 2.2 Schematic depiction of a boundary layer formation over a semi-infinite plate

As depicted in Fig. 2.2, the pressure gradient acts to distort the shape of the boundary layer and, in some cases, may lead to a complete flow detachment from the surface, which will be discussed in the next subsection. For now, it is useful to evaluate the effect of a pressure gradient on the boundary layer by considering the stationary form of the boundary layer equation (Eq. 2.46), given by

$$u_x \frac{\partial u_x}{\partial x} + u_y \frac{\partial u_x}{\partial y} = -\frac{1}{\rho} \frac{\partial p}{\partial x} + \nu \frac{\partial^2 u_x}{\partial y^2}. \quad (2.56)$$

Due to the no-slip condition, the velocity components are nullified at the wall. Hence, at the wall, Eq. (2.56) becomes

$$\frac{\partial p}{\partial x} = \mu \left(\frac{\partial^2 u_x}{\partial y^2} \right)_{wall}, \quad (2.57)$$

where $\mu = \nu\rho$ is the dynamic viscosity of the fluid. The term $\partial^2 u_x / \partial y^2$ represents the curvature of the velocity profile within the boundary layer. Interestingly, in the acceleration region upstream of the plateau, the term $\partial^2 u_x / \partial y^2$ has the same sign at both the wall and the boundary layer edge. On the other hand, for the decelerating region downstream of the plateau, the curvature of the velocity profile changes sign within the boundary layer. This means that, in a decelerating flow, the boundary layer profile has a point of inflection somewhere between the wall and the boundary layer edge, where $\partial^2 u_x / \partial y^2 = 0$. Thus, the tendency of the boundary layer in the deceleration region is to thicken due to viscous diffusion and advection away from the surface.

As it will be seen next, the rapid increase of the boundary layer thickness during flow deceleration, added to the significant increase of the vertical velocity component u_y , may act to force the flow to detach from the solid surface. This phenomenon is known as flow

separation.

2.3.4 Flow Separation

As previously discussed, the adverse pressure gradient existing in a decelerating flow forces the velocity to slow down in the region next to the wall. In many situations, the adverse pressure gradient may be strong enough to reverse the flow direction, creating a region of backward flow, as shown in Fig. 2.3. The point at which the backward flow equals the forward flow is called *separation point S*.

The Reynolds number of a flow can provide an estimation of the flow pattern downstream of the separation point *S*. For low Reynolds numbers, namely $4 < Re < 40$, the flow separation forms a steady vortex behind the surface whereas, in the case of high Re , the flow becomes unsteady and, sometimes chaotic. The Reynolds number does not predict, however, the location of the separation point *S*, which is mainly determined by the flow geometry. Nevertheless, a turbulent boundary layer is more likely to withstand flow separation than a laminar one (Batchelor, 1967).

Separation may also take place in internal flows whose duct cross section changes gradually, as in the case of a horn attached to a cylinder. For low Reynolds numbers, the vortex originated from the flow separation remains in the vicinity of *S*, whereas, for high values of the Reynolds number, the vortex propagates downstream with a velocity $U/2$ (Peters et al., 1993).

The flow behavior becomes more intricate when one considers an acoustic field superimposed on the flow field, as in the case of a woodwind instrument. Depending on the parameters of the flow and the acoustic field, as well as on the system's geometry, the energy between both fields may be exchanged, causing amplification or damping of

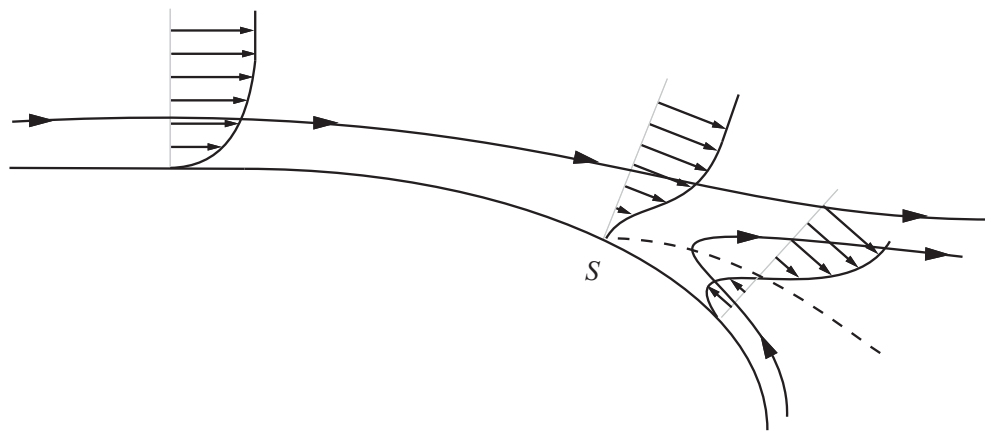


Figure 2.3 Schematic of the flow separation phenomenon in a curved surface in terms of stream lines and boundary layer profiles. The dashed line indicates $u = 0$.

sound. The influence of flow on the acoustic radiation properties of pipes and horns is the topic of Chapter 5 of this thesis.

Moreover, flow separation may be highly influenced by the movement of a solid surface. In the case of woodwind instruments, the movement of the reed influences the flow behavior but, more importantly, the flow behavior plays an important role on the oscillation of the reed. This reciprocal condition is called *fully-coupled fluid-structure interaction* and is investigated in Chapter 4.2.

The boundary layer equations presented in Sec. 2.3.1 can only predict the behavior of the flow for the region upstream of the separation point S . This is because the boundary layer becomes increasingly thick after S , so that the assumptions used to derive Eqs. (2.45, 2.46 and 2.47) become invalid. Hence, the prediction of the flow behavior downstream from the separation point can only be achieved by numerically solving the full Navier-Stokes equations presented in Sec. 2.2.5.

2.4 Acoustics

In most of the problems in acoustics, the variations of the undisturbed pressure of a system are very small, so that a first approximation of the wave equation may be achieved by linearizing the momentum equation (Eq. 2.8). Furthermore, if the scale of propagation is not too large, it is also possible to neglect the sound attenuation by viscous effects.

2.4.1 Linearized Momentum Equation for a Stagnant, Uniform Fluid

By considering the adiabatic approximation discussed in Sec. 2.2.4 and assuming the dissipation due to the fluid viscosity to be negligible⁵, the linearized, inviscid form of the momentum equation (Eq. 2.9) can be derived. Moreover, it is also important to assume that the fluid is stagnant and that the variation of density ρ' and pressure p' from their respective mean values is very small, so that p'/p_0 and $\rho'/\rho_0 \ll 1$. Then, the momentum equation in its linearized and inviscid form becomes:

$$\rho_0 \frac{\partial \mathbf{u}}{\partial t} = -\nabla p'. \quad (2.58)$$

We may also consider now the presence of a force component per unity of volume \mathbf{F} , which can be interpreted as a localized force applied by the solid boundary on the fluid, as for instance, by a vibrating solid. Hence, Eq. (2.58) becomes

$$\rho_0 \frac{\partial \mathbf{u}}{\partial t} + \nabla p' = \mathbf{F}. \quad (2.59)$$

⁵These assumptions tend to be better at lower frequencies due to the fact the viscous dissipation and heat transfer are much weaker when wavelengths are longer (Pierce, 1981)

In the same manner, it is convenient to consider volume sources q in the continuity equation (Eq. 2.6), whose strength $q \equiv q(\mathbf{x}, t)$ is the rate of volume increase per unity volume of the fluid. Thus, q might be interpreted as the influence of the pulsations of a body volume immersed in a fluid. In this case, Eq. (2.6) is written as

$$\frac{1}{\rho} \frac{D\rho}{Dt} + \nabla \cdot \mathbf{u} = q. \quad (2.60)$$

Linearizing Eq. (2.60) one achieves

$$\frac{1}{\rho_0} \frac{\partial \rho'}{\partial t} + \nabla \cdot \mathbf{u} = q. \quad (2.61)$$

It is also possible to eliminate \mathbf{u} between Eqs. (2.59) and (2.61) to find

$$\frac{\partial^2 \rho'}{\partial t^2} - \nabla^2 p' = \rho_0 \frac{\partial q}{\partial t} - \nabla \cdot \mathbf{F}. \quad (2.62)$$

The departure from the mean density ρ' in Eq. (2.62) can be written in terms of p' by using the relation expressed in Eq. (2.16). Moreover, it may be useful to replace both q and \mathbf{F} by a generalized pressure source $P(\mathbf{x}, t)$ and to discard the prime on the acoustic pressure. In this case, Eq. (2.62) becomes

$$\left(\frac{1}{c_0^2} \frac{\partial^2}{\partial t^2} - \nabla^2 \right) p = P(\mathbf{x}, t). \quad (2.63)$$

Equation (2.63) is the nonhomogeneous wave equation, which describes the production of pressure waves by the pressure source $P(\mathbf{x}, t)$.

2.4.2 Velocity Potential

If the fluid is stationary and boundary forces are absent, the small-amplitude acoustic waves can be expressed in terms of velocity potential, so that

$$\mathbf{u} = \nabla\phi, \quad p - p_0 = (\rho - \rho_0)c_0^2 = -\rho_0 \frac{\partial\phi}{\partial t}. \quad (2.64)$$

Thus, by considering Eq. (2.61) one gets

$$\left(\frac{\partial^2}{c_0^2 \partial t^2} - \nabla^2 \right) \phi = -q. \quad (2.65)$$

The variations of p propagate in the form of sound waves. In this case, the velocity component of \mathbf{u} associated with the departure of p from its undisturbed value is called acoustic particle velocity.

2.4.3 Plane Waves

The propagation of a plane wave can be described in a single dimension. Assuming x_1 to be the single propagation direction, the wave equation in terms of velocity potential satisfies

$$\left(\frac{1}{c_0^2} \frac{\partial^2}{\partial t^2} - \frac{\partial^2}{\partial x_1^2} \right) \phi = 0, \quad (2.66)$$

whose general solution is given by

$$\phi = \phi^+ \left(t - \frac{x_1}{c_0} \right) + \phi^- \left(t + \frac{x_1}{c_0} \right), \quad (2.67)$$

where ϕ^+ and ϕ^- are arbitrary functions representing the propagation of disturbances in the fluid at speed c_0 in the positive and negative directions, respectively.

2.5 Numerical Techniques

The phenomena of sound production in single-reed woodwind instruments analyzed in this thesis have been presented in Chapter 1 and can be essentially divided into two major topics. The first investigates the effect of hydrodynamic forces acting on the reed due to the fluid-structure interaction. The second topic asserts the influence of the viscous mean flow on the acoustic transmission properties of this family of instruments. In both cases, the two-dimensional (or axisymmetric) formulation of the problem requires a representation of plane low-amplitude acoustic waves propagating on a low Mach number viscous flow. In this case, a formulation based on the available solutions of Eq. (2.63) does not hold. Moreover, in most situations studied here the flow is expected to become unsteady due to its interaction with moving solid surfaces (in the case of the mouthpiece-reed system) and due to the interaction with the acoustic field (in the case of the acoustic radiation from the openings of a musical instrument bore). Thus, the formulation based on the solutions of Eq. (2.48) or its approximated form given by Eq. (2.54) are also inadequate.

The integrated problems described above are governed by the Navier-Stokes (NS) equation (Eqs. 2.22, 2.23 and 2.24) or their polar cylindrical form (Eqs. 2.25, 2.26 and 2.27). However, available analytical solutions for these equations are restricted to a very limited number of cases (Hui, 1987, Wang, 2003) and, for the scope of the analysis conducted in this thesis, a numerical solution is required. The next sections of this chapter provide a discussion of the available numerical techniques for the solution of the NS equations and their adequacy for addressing the problems described in Chapter 1.

2.5.1 Continuum-Based Techniques

The numerical prediction of sound fields generated by flow instabilities and its interaction with the undisturbed flow is covered by a branch of computational fluid dynamics (CFD) known as computational aeroacoustics (CAA).

Traditionally, CAA belongs to the category of *continuum-based* techniques, that is, the temporal evolution of both the flow and acoustic fields is obtained by linearizing and truncating the governing partial differential equations on the spatial domain. This procedure leads to the spatial discretization of the system into a mesh where each spatial segment (element) represents a linear algebraic equation. The rendering of the temporal behavior of the continuous system from its discrete counterpart is achieved by solving the system of algebraic equations using shape and/or interpolation functions which are provided in discretization schemes such as finite differences (FD) or the finite volumes (FV).

The CAA methods are divided into two main approaches, namely *hybrid* techniques and *direct numerical simulation* techniques (DNS). In essence, the hybrid approach resolves the fluid-acoustic problem by providing two decoupled solutions. The initial solution is achieved by resolving the flow field problem, whose solution is used to create equivalent acoustic sources with distributed strengths by applying the Lighthill-analogy (Lighthill, 1952) or its derivatives (Williams and Hawkings, 1969, Howe, 1975). Finally, the solution of the acoustic field generated by the acoustic sources is obtained by solving the Euler equation (Eq. 2.60) or by acoustic/viscous decompositions (Hardin and Pope, 1994). The decoupled approach used in the hybrid technique is necessary due to the difference in the length scales of the acoustic and the flow fields and, therefore, requires two independent meshes. For this reason, hybrid methods cannot be used to represent

the interaction between both fields. That is, it can only be used for the prediction of the acoustic field generated by an unstable flow but not vice-versa.

On the other hand, the DNS approach resolves both the acoustic and the flow field simultaneously by numerically solving the fully compressible Navier-Stokes equations (Eqs. 2.20 and 2.21) and, for this reason, can adequately represent the fluid-acoustic interaction. This is only possible when the system mesh is able to resolve the entire range of spatial and temporal scales associated with the acoustic and the fluid fields. This includes small dissipative scales associated with the flow instability (Kolmogorov scales) and the scales associated with the characteristic length of the system. Nevertheless, from the computational point of view, the time-domain solutions provided by DNS techniques are extremely demanding due to the large number of required mesh elements and short time steps.

A rich review of the fundamentals and new trends in computational aeroacoustic techniques are provided in publications by Tam (1995) and more recently by Wells and Renaut (1997).

2.5.2 Particle-Based Techniques

As opposed to *continuum-based* techniques, which describe the space-time evolution of the fluid-acoustic fields by solving their governing partial differential equations, *particle-based* techniques render the behavior of the fluid domain at a microscopic level by simulating two essential operations: the propagation and collision of fluid particles.

Normally, these two essential operations are described by the Boltzmann equation (BE) where the “particles” are represented in terms of velocity distribution functions. In other words, a particle represents the probability of encountering a certain number of fluid molecules with velocity \mathbf{u} at the space location \mathbf{x} and time t . The fluid macroscopic

properties such as pressure and velocity are easily recovered from the moments of the velocity distribution functions. A complete description of the Boltzmann equation is provided in Chapter 3.

In fact, the notability of *particle-based* techniques is that a formal link can be established between the Boltzmann equation and the equation that governs the macroscopic behavior of a fluid, that is, the Navier-Stokes equation. This means that, depending on the case, the Navier-Stokes equations can be fully recovered from the Boltzmann equation through an operation known as Chapman-Enskog expansion, after Qian et al. (1992).

In addition to the fact that the Boltzmann equation describes the fluid at a microscopic level whereas the Navier-Stokes equation describes the fluid from a macroscopic viewpoint, three other fundamental differences between the two equations exist. First, the Boltzmann equation can describe a fluid even if the continuum assumption is not met, as in the case of rarefied gases (see Sec. 2.2.1). Second, the molecular point of view provided by the Boltzmann equation offers a direct physical interpretation of the equations of state of a fluid and its viscous stresses. The third difference is associated with the enormous timescale discrepancy between the two equations. In most fluids and common ranges of pressure and temperature, the timescale of the particle collision governed by the Boltzmann equation is $O(-8) \sim O(-9)$ seconds (Hirschfelder et al., 1964, p.15). In the case of the Navier-Stokes equations, the macroscopic parameters such as pressure and velocity are normally described by timescales of order $\sim O(-4)$ seconds. Hence, the normal timescale of the Boltzmann equation is much smaller than the Navier-Stokes timescale. On the other hand, the Boltzmann equation can be solved much more easily.

Some examples of particle-based techniques include the direct simulation Monte-Carlo method (Danforth and Long, 2004), the molecular dynamics method (Frankel and

Smith, 1996, Rapaport, 1995) and the lattice Boltzmann method (Wolf-Gladrow, 2004, Succi, 2001). The difference between these methods essentially consists in the way the Boltzmann equation is solved.

The following section discusses the choice of the numerical technique used throughout this thesis to analyze the phenomena described in Chapter 1.

2.5.3 Discussion

The characteristics of the problems described in Chapter 1 involve the propagation of acoustic waves in a viscous unstable flow. The characteristics of the flow correspond to the limit of low compressibility ($M \ll 1$) and low acoustic amplitude defined as $u/\bar{u} \leq 0.1$, where u is the amplitude of the particle velocity and \bar{u} is the cross-section averaged mean flow velocity. Moreover, the problems are assumed to be isentropic.

Such a set of problems is governed by the compressible Navier-Stokes equation which, in turn, demands an extremely large computational effort to be resolved, as previously discussed. Alternatively, it is possible to profit from the characteristics of the problems investigated here in order to apply a much more simplified approach based on the Boussinesq approximation (Sec. 2.2.5). As previously discussed, the Boussinesq approximation states that the slightly compressible form of the Navier-Stokes equations (Eqs. 2.22, 2.23 and 2.24) can provide second-order accurate solutions of compressible flows as long as the Boussinesq conditions are met, that is, $M < 0.3$ and the flow conditions are almost isothermal.

A very straightforward way for indirectly resolving the slightly-compressible Navier-Stokes equation obtained by applying the *Boussinesq approximation* (Eqs. 2.22, 2.23 and 2.24) can be achieved by the *particle-based* approach. For some particle-based methods, it is shown that the compressible Navier-Stokes equation can be fully recovered from a

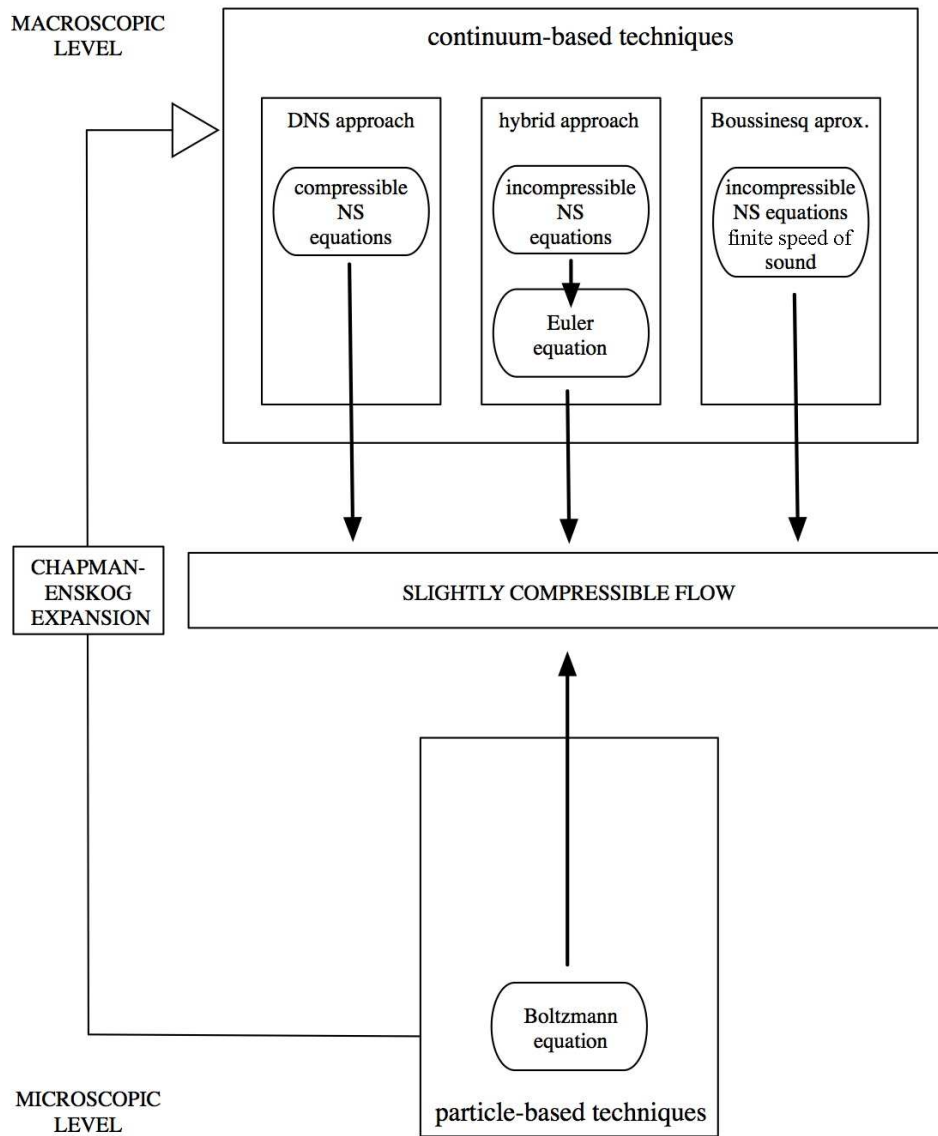


Figure 2.4 Schematic representation of the major techniques for solving a slightly compressible flow problem.

discrete version of the Boltzmann equation.

This essentially means that two identical solutions can be obtained by two distinct approaches for a problem involving a viscous flow at the limit of compressibility. The first approach consists in solving the compressible Navier-Stokes equation with finite speed of sound and the second consists in resolving the Boltzmann equation. However, solving the Boltzmann equation is considerably cheaper from the computational standpoint. Moreover, particle-based techniques provide considerably more stable solutions for complex boundary conditions involving moving walls and anechoic boundaries. Figure 2.4 depicts a graphical representation of the available schemes for solving the family of problems analyzed in this work.

For this reasons, the *particle-based* approach was chosen to represent the problems studied in this thesis. Among all the available *particle-based* techniques, the lattice Boltzmann method was chosen due to its better numerical robustness and its ability to provide accurate second-order solutions for the specific problems addressed in this thesis. The following chapter presents an introductory description of the lattice Boltzmann theory and discusses some of the techniques developed in order to implement the woodwind models investigated in this thesis.

Chapter 3

Lattice Boltzmann Theory

3.1 Introduction

The objective of this chapter is to provide the basic concepts of the lattice Boltzmann method (LBM), as well as to present the detail and solutions found for the lattice Boltzmann models used in the forthcoming chapters of this thesis. As previously discussed, the LBM is used here as a tool to indirectly resolve, with second-order accuracy, the compressible unstable form of the Navier-Stokes equations (Eqs. 2.22, 2.23 and 2.24). The reader can find a more detailed description of LBM in good textbooks by Succi (2001), Wolf-Gladrow (2004) or in the milestone papers by Qian et al. (1992), He and Luo (1997), Qian et al. (1995) and Lallemand and Luo (2000).

Although being extensively used in purely hydrodynamic problems, LBM has only been explored by a limited number of researchers to resolve problems involving acoustic wave phenomena. Skordos (1995) simulated the interaction between fluid flow and acoustic field within organ pipes. Buick et al. (1998) simulated the propagation of linear sound waves using different boundary conditions and later Buick et al. (2000) simulated

the formation of shock waves. Haydock and Yeomans (2001) predicted the acoustic streaming around a cylinder and between two plates of finite length. More recently, Haydock (2005) also predicted the influence of the fluid viscosity on the force applied by an acoustic field on a rigid cylinder. In the specific case of the acoustics of wind instruments, LBM has been also used by Atig (2004) to investigate nonlinear losses at the open end of pipes in the absence of a mean flow. Neal (2002) simulated aspects of flow in brass instrument mouthpieces and Kuehnelt (2003) used a three-dimensional lattice Boltzmann scheme to simulate the sound production in flutes and recorders.

There are essentially two major differences between the previous acoustic-related LBM studies and the ones conducted in this thesis. The first difference is that the present study involves the use of a moving boundary to simulate fully-coupled fluid-structure interaction phenomena. This is used to represent the interaction between the reed and the fluid flow of a clarinet-like instrument. The second difference consists in using an axisymmetric lattice Boltzmann model to evaluate the parameters associated with the acoustic radiation from cylindrical waveguides, such as unflanged pipes and horns. The detailed descriptions of these models are provided in Chapters 5 and 4, respectively. Beforehand, however, it is necessary to provide the fundamental background of LBM.

This chapter proceeds as follows: Section 3.2 provides the fundamental concepts of lattice Boltzmann theory. Section 3.3 discusses the lattice Boltzmann models considered in this thesis. The essential steps of a generic lattice Boltzmann algorithm is described in Section 3.4. Initial and boundary conditions are briefly explained in Sections 3.5 and 3.6, respectively. Section 3.7 provides the procedure to convert the dimensionless parameters from an LBM analysis into physical quantities. Finally, Section 3.8 discusses the suitability of LBM on the prediction of the aeroacoustic phenomena investigated in this thesis.

3.2 Fundamental Theory

3.2.1 Classical Mechanics at the Particle Level

It has been seen in the previous chapter that the temporal evolution of a fluid, described in terms of macroscopic parameters such as pressure and velocity, can be rendered from a microscopic viewpoint by simulating the fundamental behavior of its molecules.

In this sense, one can begin to grasp the usefulness of the Boltzmann equation by imagining a box of volume V filled with a perfect gas containing N molecules at normal conditions. It is important to assume that the size of the molecules is much smaller than the averaged distance d between each other ($d = (V/N)^{\frac{1}{3}}$), so that they can be regarded as point-like structures. Moreover, one must assume that the molecules only interact via two-body collisions¹. Thus, if the classic mechanics approach is used, the state of each molecule i in the box can be described by a generic set of equations, given by

$$\frac{d\mathbf{x}_{k_i}}{dt} = \frac{p_{k_i}}{m} \quad (3.1)$$

$$\frac{dp_{k_i}}{dt} = F_{k_i} \quad i = 1, 2, \dots, N \quad \text{and} \quad k = 1, 2 \text{ and } 3. \quad (3.2)$$

where p_{k_i} and F_{k_i} are, respectively, the linear momentum and the force on a particle i in the direction k .

If only a single molecule is considered inside the box and if the initial and boundary conditions are given, the position and velocity of the particle at a time $t = t_0 + \Delta t$ can be obtained from the solution of a system of six equations resulting from Eqs. (3.1) and (3.2). This apparently simple approach becomes increasingly cumbersome as the

¹As the name suggests, the two-body collision implies that only two particles can collide at the same time t and at \mathbf{x} .

number of molecules is augmented, considering that the number of equations in the resulting system is given by $6N$.

In problems of practical interest, however, the number of molecules is rather too high and the use of the classical mechanics approach becomes unfeasible. To illustrate that, one should consider a problem involving a volume of one cubic centimeter filled with a perfect gas in normal conditions. In this case, the number of molecules in the volume is $\sim 10^{19}$, which implies that the number of necessary equations to describe the state of the particles in the system would be 6×10^{19} . Therefore, this approach becomes entirely unrealistic from the computational point of view, considering that even the fastest available computer is far from solving problems of this magnitude. Moreover, even if such a huge problem could be handled by a computer, it would be jeopardized by the dynamical instability related to the phase-space characteristics of the problem, i.e., any uncertainty in the values of the initial conditions would grow exponentially in time (Succi, 2001).

It should be mentioned that the final objective of any *particle-based* approach is to determine the macroscopic parameters of a fluid such as pressure and velocity. These parameters are the result of the averaged microscopic behavior of a large number of individual molecules. Therefore, instead of estimating the macroscopic parameters by accounting for the dynamical contribution of each individual molecule, it becomes much wiser to circumvent this problem by adopting a statistical approach provided by the Boltzmann equation.

3.2.2 The Boltzmann Equation

The state of a very few number of molecules (position and momentum) at a certain time t could be easily described in terms of the classical mechanical approach. However, due the enormous quantity of molecules found in systems of practical interest, it

becomes more realistic to represent the state of the molecules using a probabilistic approach provided by the *kinetic theory*. In this case, the probability of finding one set of molecules within an infinitesimal volume centered at a position \mathbf{x} with momentum ξ at time t is described by the distribution function $f(\mathbf{x}, \xi, t)$ and the streaming motion of these molecules is described by the kinetic equation, given by

$$[\delta_t + \frac{\xi}{m} \delta_x + \mathbf{F} \delta_\xi] f(\mathbf{x}, \xi, t) = C_{12}. \quad (3.3)$$

The term on the left side represents the motion of molecules along a trajectory defined by a field force \mathbf{F} , where m is the mass of the molecules. The right-side term C_{12} , represents the effects of a two-body collision between molecules. An explicit expression for C_{12} can be easily written in terms of another kinetic equation based, at this time, on a two-body distribution function f_{12} , which represents the probability of finding a molecule around the position \mathbf{x}_1 with momentum ξ_1 and another molecule around \mathbf{x}_2 , with momentum ξ_2 at the same time t . However, an explicit expression for f_{12} can only be written in terms of a three-body collision function C_{123} , which, in turn, can only be expressed in terms of a three-body distribution function f_{123} , and so on. This infinite chain of dependency is known as BBGKY hierarchy, after Bogoliubov, Born, Green, Kirkwood and Yvon (Bogoliubov, 1962).

The Austrian physicist Ludwig Boltzmann derived, in 1872, a way to break the BBGKY hierarchy by making three fundamental assumptions: 1) Only two-body interactions can take place in an instant t ; 2) The velocities between two particles are completely uncorrelated before their collision (*Stolzansatz*). This assumption makes it possible to write $f_{12} = f_1 f_2$; 3) The local collision between two particles is not influenced by the existence of any external force.

By making these assumptions, the collision term, C_{12} , in Eq. 3.3 can be replaced by a collision integral, given by

$$Q(f, f) = C_{12} = \int ([f_{1'2'} - f_{12}][v_1 - v_2]\sigma(\Omega)d(\Omega))dV, \quad (3.4)$$

where f_{12} is the two-body distribution function prior to the molecules' collision and $f_{1'2'}$, the distribution function after. v_1 and v_2 are the velocities of molecules 1 and 2, respectively. σ is the differential cross-section of the volume where the collision takes place and Ω is the angle of incidence of the molecules. Essentially, this collision integral describes the probability of velocity transformation of the two molecules due to their collision. By substituting Eq. (3.3) in Eq. (3.4), one obtains

$$[\delta_t + \frac{\xi}{m}\delta_x + \mathbf{F}\delta_{(\xi)}]f(\mathbf{x}, \xi, t) = \int ([f_{1'2'} - f_{12}][v_1 - v_2]\sigma(\Omega)d(\Omega))dV. \quad (3.5)$$

Equation (3.5) is known as the Boltzmann equation (BE). In essence, Eq. (3.5) implies that the motion of molecules driven by an external force \mathbf{F} and described in terms of distribution function f is equal to the intermolecular interactions following the assumptions discussed above.

3.2.3 Collision Invariance and the Maxwell Distribution

It will be seen that the collision integral (Eq. 3.4) can be significantly simplified if some important properties from the *kinetic theory* are considered.

For the case of gases, one of these properties implies that there should be functions of molecular velocities, known as *collision invariants*, that satisfy the following equation:

$$\psi(\mathbf{u}'_*) + \psi(\mathbf{u}') - \psi(\mathbf{u}_*) - \psi(\mathbf{u}) = 0, \quad (3.6)$$

where \mathbf{u} and \mathbf{u}_* are velocity vectors associated with molecular displacement in R^3 . $\mathbf{u}' = \mathbf{u} - \mathbf{n}(\mathbf{n} \cdot \vartheta)$ and $\mathbf{u}'_* = \mathbf{u}_* - \mathbf{n}(\mathbf{n} \cdot \vartheta)$, where ϑ is the relative velocity defined as $\mathbf{u} - \mathbf{u}_*$ and \mathbf{n} is a unity vector.

In the case of the collision integral $Q(f, f)$ there are five fundamental collision invariants $\psi_k(\mathbf{u})$, where $k = 1, 2, 3, 4, 5$, so that

$$\int Q(f, f) \psi_k(\mathbf{u}) dV = 0. \quad (3.7)$$

These collision invariants are, $\psi_1 = 1$, $\psi_{2,3,4} = \mathbf{u}$ and $\psi_5 = \mathbf{u}^2$. Any other collision invariant can be written as a linear combination of the fundamental collision invariants ψ_k . Moreover, there should exist certain types of distribution functions, $f(v)$ that cancel the collision integral, so that

$$Q(f, f) = 0. \quad (3.8)$$

These distribution functions usually have the following form:

$$f(v) = e^{(a+b\psi_{2,3,4}+c\psi_5)}, \quad (3.9)$$

where a , b and c are constants. One particular set of functions that possesses this characteristic is the set of Maxwell distribution functions f^M . As it will be seen next, these properties will be very useful at deriving a more appealing collision function from the computational point of view. This simplification will represent the embryonic idea behind LBM.

3.2.4 The BGK Approximation

A proof that the collision between two particles can be well represented with a considerable smaller amount of detail than that implicit in the Boltzmann collision integral (Eq. 3.4) was first presented by Bhatnagar, Gross, and Krook (1954).

The approximation involves replacing $Q(f, f)$ by a simplified function $J(f)$, which has to satisfy two constraints: First, $J(f)$ must preserve the same collision invariants, ψ_k as the Boltzmann collision integral $Q(j, j)$, so that $\int \psi_k J(f) d^3x dV = 0$. Secondly, $J(f)$ must approximate a Maxwell distribution, that is, $J(f) \rightarrow f^M$. The solution found by Bhatnagar, Gross, and Krook (1954) consisted in expressing the simplified collision term as

$$J(f) = \omega_c (f^M(\mathbf{x}, \mathbf{u}) - f(\mathbf{x}, \mathbf{u})), \quad (3.10)$$

where the coefficient ω_c is called the collision frequency, which represents the rate of collisions per second between molecules. It is important to notice that the amount of change imposed by the collision term on the distribution function f will depend on how much the distribution f deviates from the Maxwell distribution f^M . Replacing the Boltzmann integral in Eq. (3.5) by Eq. (3.10) leads to the famous BGK approximation of the Boltzmann equation, given by

$$\frac{\delta f}{\delta t} + \mathbf{u} \cdot \nabla f = -\frac{1}{\tau} (f - f^M), \quad (3.11)$$

where $\tau = 1/\omega_c$ is known as the collision period.

3.2.5 The Isothermal Lattice Boltzmann Equation

It is possible to achieve a discrete version of Eq. (3.11) by restricting the streaming velocity to a limited set of directions defined by \mathbf{u}_i and their respective set of distribution functions f_i .

$$\frac{\delta f_i}{\delta t} + \mathbf{u}_i \cdot \nabla f_i = -\frac{1}{\tau}(F_i - F_i^M). \quad (3.12)$$

Equation (3.12) can be written in a dimensionless form by incorporating some characteristic parameters such as the reference speed, U , the reference density, n_r , and the time between particle collisions, t_c , which becomes

$$\frac{\delta F_i}{\delta \hat{t}} + \mathbf{c}_i \cdot \nabla F_i = -\frac{1}{\hat{\tau}\epsilon}(F_i - F_i^M), \quad (3.13)$$

where $\mathbf{c}_i = \vec{v}_i/U$, $\hat{\nabla} = L\nabla$, $\hat{t} = tU/L$, $\hat{\tau} = \tau/t_c$, $F_i = f_i/n_r$ and $\epsilon = t_c U/L$. The discretization of Eq. (3.13) is achieved by substituting the differential terms by generic linear finite difference approximations of the form:

$$\frac{\delta \eta}{\delta j} = \frac{\eta(j + \Delta j) - \eta(j)}{\Delta j}, \quad (3.14)$$

where j and η are generic variables.

Furthermore, replacing the discrete time step Δt by $\Delta \hat{t} = \Delta t/L$ and assuming a Lagrangean behavior so that the lattice velocity $\mathbf{c}_i = \Delta \vec{x}/\Delta \hat{t}$, and $\Delta t = t_c$, one obtains the BGK Lattice Boltzmann equation (LBGK) by

$$f_i(\mathbf{x} + \mathbf{c}_i \Delta t, t + \Delta t) - f_i(\mathbf{x}, t) = -\frac{1}{\tau}(f_i - f_i^M), \quad (3.15)$$

Equation (3.15) is the simplest discrete form of the Boltzmann equation based on a

single collision period τ^2 . The left-hand side of Eq. (3.15) represents the propagation operator and determines the diffusion of the distribution functions f_i . The right-hand term is a simplification of the collision function, which determines the rate at which f_i changes due to intermolecular collisions.

The discrete form of the Maxwell distribution function f_i^M , known as the relaxation function, is obtained by applying the maximum entropy principle under the constraints of mass and momentum conservation (Wolf-Gladrow, 2004, pp.171), which leads to

$$f_i^M = \rho \epsilon_i \left(1 + \frac{\mathbf{u} \cdot \mathbf{c}_i}{c^2} + \frac{(\mathbf{u} \cdot \mathbf{c}_i)^2 - c^2 \mathbf{u}^2}{2c^4} \right), \quad (3.16)$$

where c and ϵ are constants and refer to the lattice speed of sound and the velocity weights, respectively, and depend on the lattice model used (see Table 3.1). Equation (3.16) depends only on the local values of fluid density ρ and velocity \mathbf{u} .

It is interesting to notice that the derivation of LBE from BE represents a link from a microscopic scale (at the molecular level) to a macroscopic scale (at the fluid level). In other words, the distribution function f_i in LBE represents the probability of finding a fluid particle at \mathbf{x} and time t , propagating with velocity \mathbf{c}_i in the direction i . The word “particle” now refers to a group of fluid molecules. Considering that, the macroscopic parameters such as the local fluid density ρ and local fluid velocity \mathbf{u} can be obtained from the moments of the distribution function f_i , such that

$$\begin{aligned} \rho &= \sum f_i \\ \rho \mathbf{u} &= \sum f_i \mathbf{c}_i \end{aligned} \quad (3.17)$$

²More sophisticated models have been proposed in order to take into account multiple relaxation times (MRT) (d’Humières et al., 2002, Li et al., 2006). The advantage of the MRT approach consists in a significant increase of numerical stability for higher Mach numbers. Furthermore, MRT can reduce the high frequency noise intrinsic to LBGK schemes.

Moreover, the isothermal characteristic of Eq. (3.15) allows the pressure p and the kinematic viscosity of the fluid to be written as

$$p = \rho c^2, \quad (3.18)$$

and

$$\nu = c^2 \left(\tau - \frac{1}{2} \right). \quad (3.19)$$

Equation (3.19) provides the physical interpretation of a macroscopic parameter from a microscopic perspective. In fact, for an isothermal situation, the kinematic viscosity of a fluid is directly proportional to the averaged collision period of its molecules, that is, fluids with high viscosities have a higher number of molecular collisions per unit of time than fluids with low viscosity values.

Despite all the reductions and simplifications, the LBGK can still recover the Navier-Stokes equations (Eqs. 2.22, 2.23 and 2.24) in the same way the BE does, provided that flow remains below the limit of compressibility ($M < 0.15$, $M = u/c$). This has been shown by He and Luo (1997) by applying the same Chapman-Enskog expansion used to recover the NSE from the BE.

3.3 Lattice Boltzmann Models

The two essential operations described by the LBGK, namely the propagation and the collision of the distribution functions, can be represented on a one-, two- or three-dimensional lattice, depending on the model. The nodes in the lattice are called cells. Each cell comprises i sites, according to the number of propagating directions i of the model. Each site of a cell hosts a distribution function f_i that propagates to the next cell

at every time step Δt . The cells in the lattice connect to each other by the velocity vectors c_i . Figure 3.1 depicts the structure of a common two-dimensional lattice.

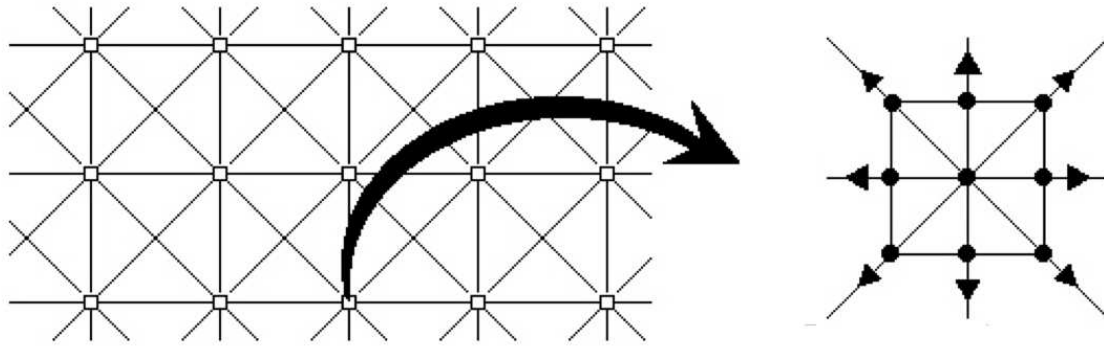


Figure 3.1 Scheme of a two-dimensional squared lattice model with 9 sites.

Figure 3.2 depicts the most common types of lattice geometries, which follows the standard $DdQn$ nomenclature, after Qian et al. (1992). The letter d indicates the number of dimensions of the model while n indicates the number of discrete velocities i . Most of the lattice models have a non-propagating site, normally situated in the center of the cell, which acts to improve the accuracy of the model by removing the unphysical dependency of the speed of sound on the pressure (Qian et al., 1995).

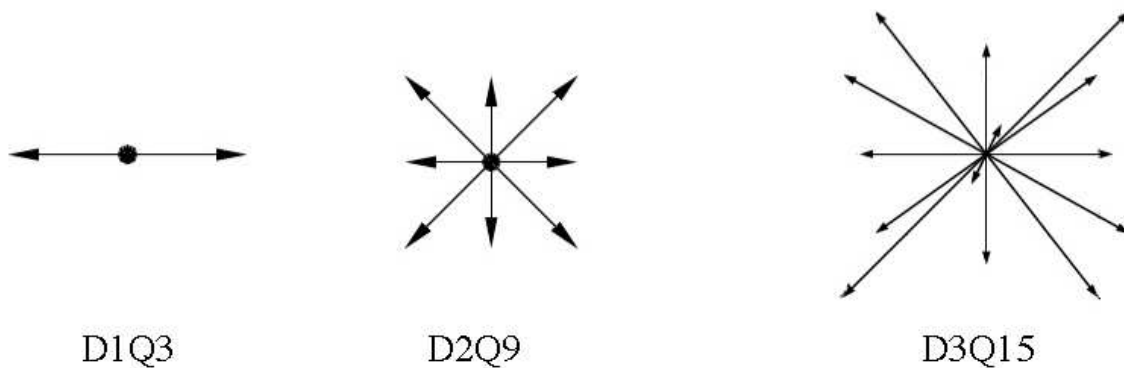


Figure 3.2 Lattice cell representations of the most common lattice Boltzmann models for different dimensions

An important property of a lattice model is the symmetry, which is necessary to guarantee fourth-order tensor isotropy. When there is a lack of symmetry in the lattice, the Navier-Stokes equations cannot be fully recovered because a density-dependent factor originates in the right side of Eqs. (2.23) and (2.24). The velocity weights and the lattice speed of sound associated with each model and used to derive f_i^M according to Eq. (3.16) are presented in Table 3.1.

Table 3.1 Speed of sound and velocity weights for the main lattice models.

model	speed of sound c_0	velocity weights ϵ		
		static	vert. / hor.	diag.
D1Q3	$1/\sqrt{3}$	4/6	1/6	0
D2Q9	$1/\sqrt{3}$	16/36	4/36	1/36
D3Q19	$1/\sqrt{3}$	12/36	2/36	1/36

The values inside each row of the third column of Table 3.1 are displayed in an order so as to indicate the velocity weights associated with the non-propagating direction, vertical or horizontal directions and diagonal directions.

3.3.1 Cartesian D2Q9 Model

There are several lattice structures available for the simulation of two-dimensional fluid dynamic problems. In the analysis conducted in this thesis, the $D2Q9$ lattice model was chosen because it represents a good trade-off between numerical stability and computational efficiency due to the presence of a non-propagating site and reduced number of velocity directions i . Furthermore, when used to resolve the LBGK equation, the $D2Q9$ scheme leads to second-order accurate solutions and can recover the Navier-Stokes equations (Eqs. 2.22, 2.23 and 2.24) through a multi-scale Chapman-Enskog anal-

ysis. The full expansion of Eq. (3.15) into Eqs. (2.22), (2.23) and (2.24) is provided in Wolf-Gladrow (2004, pp. 174).

Figure 3.3 provides a more detailed representation of the $D2Q9$ lattice structure.

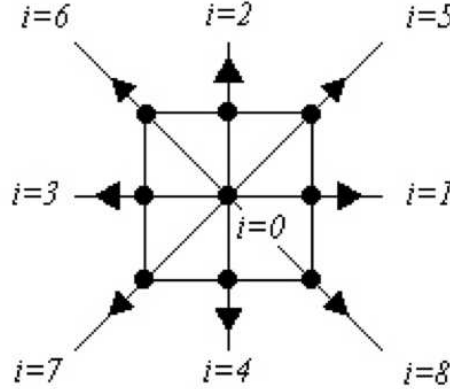


Figure 3.3 Cell representation of the $D2Q9$ model.

More explicit forms of the relaxation function (Eq. 3.16) in the case of the $D2Q9$ model are given for the different propagation directions i as

$$f_i^M = \frac{4}{9}\rho \left[1 - \frac{3\mathbf{u}^2}{2c^2} \right] \quad \text{for } i = 0$$

$$f_i^M = \frac{1}{9}\rho \left[1 + 3\frac{\mathbf{c}_i \cdot \mathbf{u}}{c^2} + \frac{9(\mathbf{c}_i \cdot \mathbf{u})^2}{2c^4} - \frac{3\mathbf{u}^2}{2c^2} \right] \quad \text{for } i = 1, 2, 3, 4$$

$$f_i^M = \frac{1}{36}\rho \left[1 + 3\frac{\mathbf{c}_i \cdot \mathbf{u}}{c^2} + \frac{9(\mathbf{c}_i \cdot \mathbf{u})^2}{2c^4} - \frac{3\mathbf{u}^2}{2c^2} \right] \quad \text{for } i = 5, 6, 7, 8, \quad (3.20)$$

where the velocity vectors \mathbf{c}_i are given by

$$\mathbf{c}_0 = (0, 0), \quad \mathbf{c}_{1,3}, \mathbf{c}_{2,4} = (\pm c, 0), (0, \pm c), \quad \text{and} \quad \mathbf{c}_{5,6,7,8} = (\pm c, \pm c), \quad (3.21)$$

where c is the lattice speed of sound given in Table 3.1.

3.3.2 Axisymmetric D2Q9 Model

The analyses presented in Chapter 5 are conducted by using an axisymmetric LBGK model based on the $D2Q9$ structure. The main advantage of the axisymmetric approach is to provide exact solutions for three-dimensional problems by using reduced two-dimensional representations, which reflects an enormous economy in terms of computational work. Moreover, the dimensional reduction allows for more allocation of computational memory, which can be used to produce a greater spatial refinement. The axisymmetric approach is possible, provided that the analyzed phenomena is symmetric about the system's main axis. This is the case for the phenomena associated with plane wave radiation from cylindrical waveguides, as investigated in Chapter 5.

An axisymmetric form of the LBGK equation is valid when it can recover the polar form of the continuity and Navier-Stokes equations (Eqs. 2.25, 2.26 and 2.27). A first LBGK axisymmetric model has been proposed by Halliday et al. (2001) who demonstrated that Eqs. (2.25), (2.26) and (2.27) could be fully recovered by the Chapman-Enskog expansion if a space- and time-dependent source term is inserted into the standard LBGK equation (Eq. 3.15). In this case, the new form of the LBGK equation becomes

$$F_i(\vec{x} + \mathbf{c}_i \Delta t, t + \Delta t) - F_i(\vec{x}, t) = -\frac{1}{\tau}(F_i - F_i^M) + h_i, \quad (3.22)$$

where the source term h_i is represented by the summation of a first- and a second-order term, h_i' and h_i'' , respectively. These terms are chosen so that the continuity and momentum equations, which arise from the cylindrical polar coordinate system, are recovered. The first-order term h_i' can be easily calculated, whereas the second-order term, as de-

rived by Halliday et al. (2001), is rather awkward to be computed because it comprises many differential terms whose solutions depend on computational techniques that diverge from the simple scalar operations involved in the lattice Boltzmann method. Reis and Phillips (2007) provided a more straightforward expression for the second-order source term and demonstrated that their axisymmetric solution can recover Eqs. (2.25), (2.26) and (2.27) and, at the same time, provides results of second-order accuracy in the same fashion as the traditional form of the LBGK equation in cartesian coordinates. Appendix B presents the expressions for the first- and second-order terms as derived by Reis and Phillips (2007) and proposes a computational solution based on a finite difference scheme in order to obtain the second one.

3.4 The LBM Algorithm

In general, the main operations of a normal LBGK code can be described by the flowchart depicted in Fig. 3.4. The main variation between LBGK algorithms are mainly related to the way the initial and boundary conditions are implemented (operations *a* and *d*, respectively). Sections 3.5 and 3.6 discuss in more detail the major implementation possibilities of these two specific operations.

Operation *a* defines the initial state of the lattice by setting the space-dependent values of pressure p or density ρ and the velocity field \mathbf{u} at time $t = 0$. Based on these values, operation *b* constructs the related distribution functions $f_i(\mathbf{x}, t)$. This is normally done by using the generic expression for the relaxation function f_i^M given by Eq. (3.16). During the first simulation step the newly constructed values of f_i are sent directly to operator *c* in order to perform the propagation of f_i over the lattice in all directions i by forcing $f_i(\mathbf{x}, t) = f_i(\mathbf{x} + \mathbf{c}_i t, t + \Delta t)$. Operator *d* obtains the new values of ρ and \mathbf{u} from

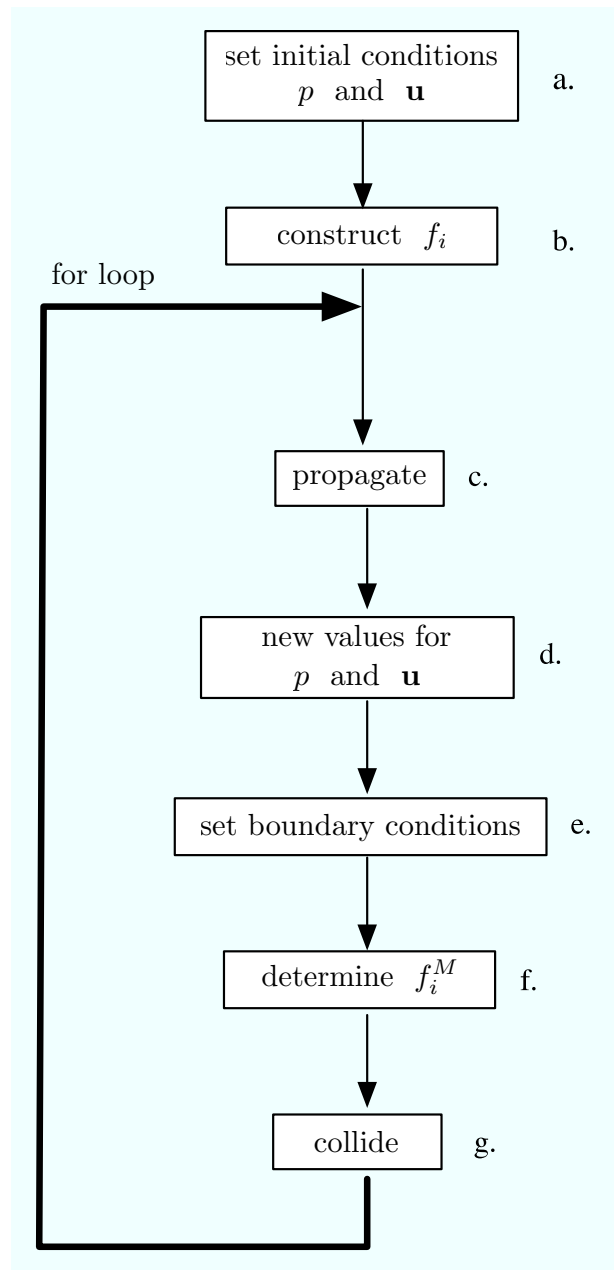


Figure 3.4 Flowchart of a generic lattice Boltzmann algorithm.

f_i using Eq. (3.17). These values are adjusted in operator e according to the current boundary conditions. The new lattice values of ρ and \mathbf{u} proceed to operator f where the new relaxation functions f_i^M are constructed. The two main operations described by the LBGK equation (Eq. 3.15) are decoupled into operators g and c . Operator g performs the collision of the fluid particles represented in terms of f_i by forcing $f_i = f_i + 1/\tau(f_i - f_i^M)$. The iterative process continues by forwarding the new values of f_i to operator c .

3.5 Initial Conditions

The accurate initialization of the fluid flow is an important procedure in unsteady, time-marching simulations. A typical approach is to initialize the system by setting $f_i = f_i^M$ at $t = 0$, as previously mentioned. This implies that the initial flow or sound field is in equilibrium, i.e., its gradients are null or negligibly small. In the case of non-zero velocity and pressure gradients, the non-equilibrium components of f_i have to be reconstructed using an alternative approach. One approach proposed by Skordos (1993) consists in reconstructing f_i based on the spatial and time derivatives of f_i^M . However, a more efficient way to determine the non-equilibrium f_i has been proposed by Chikatamarla et al. (2006) based on Grad's moment closure. This technique reconstructs the unknown distributions at the boundaries without having to perform derivatives and can be applied on the initialization of the flow.

In the simulations conducted in this thesis, the velocity and pressure fields are always homogeneous at the beginning of the simulations, which means that the gradients of pressure p and velocity \mathbf{u} are always zero at $t = 0$. For this reason, the first approach in which $f_i = f_i^M$ is adopted. The initialization of the flow and the acoustic field are achieved by using a boundary condition technique that allows for the prescription of

target values for p and \mathbf{u} . This technique is described in the following section.

3.6 Boundary Conditions

The boundary conditions in LBM are divided into two main schemes depending on whether the boundary is defined by the contact of the fluid with a solid wall (solid boundaries) or with an open region (open boundaries). This section presents an overview of the common boundary condition schemes used in LBM, as well as the solutions found to represent specific boundary conditions required in the simulations presented in Chapters 4 and 5.

3.6.1 Solid Boundaries

No-Slip Condition

In real situations, the tangential component of the flow velocity at a solid wall is null. This is because real solid walls (as in pipes, open surfaces, etc.) have enough rugosity that acts to refrain the tangential advection of solid particles. This condition is known as *no-slip* and can be implemented by using a bounce-back scheme that acts to invert the direction of propagation of the distribution function f_i just before it reaches a solid boundary.

This can be illustrated by considering the distribution function $f_8(\mathbf{x}, t)$ just before it collides against a solid boundary, as depicted in Fig. 3.5(a). At the next time step $t + \Delta t$ the bounce-back scheme implies that $f_6(\mathbf{x}, t + \Delta t) = f_8(\mathbf{x}, t)$, as shown in Fig. 3.5(b).

This procedure creates a null fluid velocity at the walls for both normal and tangential components and provides second-order accuracy to represent viscous boundary

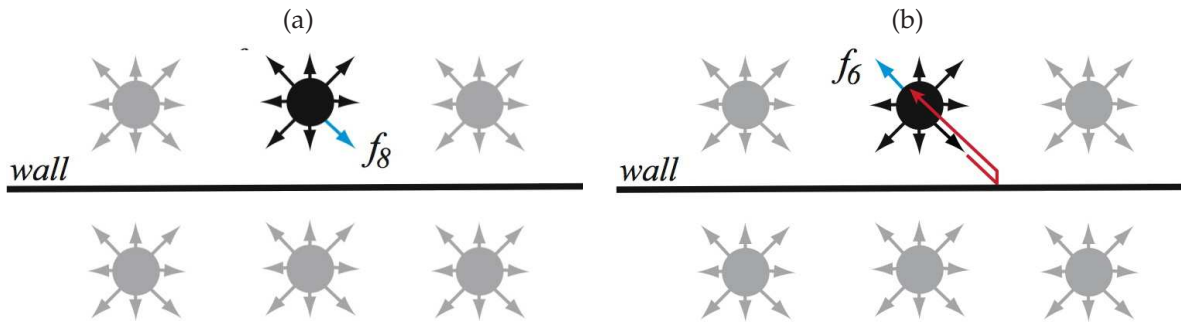


Figure 3.5 Illustration of the bounce-back scheme to simulate the no-slip condition: (a) Situation before propagation at $t = n$, and (b) situation after propagation at $t = n + \Delta t$.

layer phenomena when the boundary is aligned with the lattice. In the simple approach explained above, the fluid always ‘sees’ the boundary in the half-way between two sites. Bouzidi et al. (2001) have proposed a bounce-back technique based on the interpolation of f_i in order to preserve the same order of accuracy for non-aligned boundaries, that is, boundaries that are not aligned in the half-way between sites, such as those found in curvilinear surfaces, etc. Lallemand and Luo (2003) used a similar strategy to derive a bounce-back method for a moving boundary within the lattice domain. This strategy is used in Chapter 4 to describe the movement of the reed. Appendix A provides the details of the non-aligned and moving boundary techniques (Bouzidi et al., 2001, Lallemand and Luo, 2003), and proposes a numerical procedure for their implementation.

Free-Slip Condition

There are situations in which the condition $u_w \neq 0$ is desired, where u_w is the tangential component of the flow velocity at the wall. This may be true when the viscous boundary layer effects need to be neglected or when representing boundaries localized at the axis of symmetry of a system.

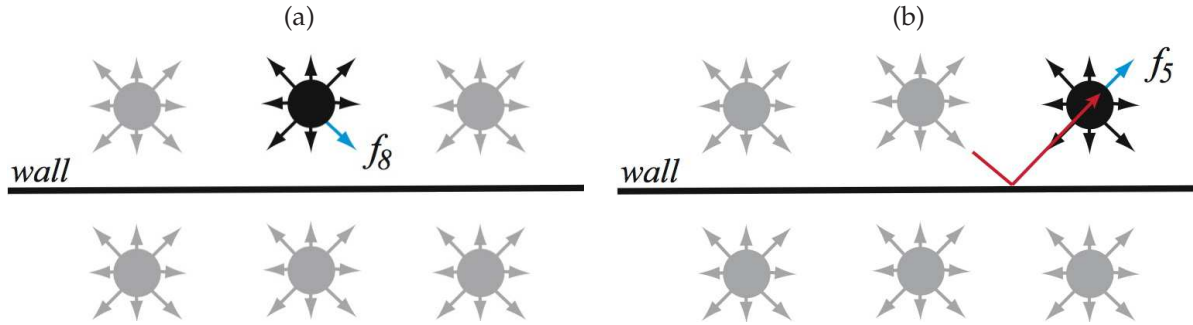


Figure 3.6 Illustration of the specular scheme to simulate the free-slip condition: (a) Situation before propagation at $t = n$, and (b) situation after propagation at $t = n + \Delta t$.

The implementation of a free-slip condition in LBM follows a similar idea to the no-slip case. The difference being that the distribution function f_i propagating diagonally towards a solid boundary is reflected in a specular manner. Again, this is illustrated by considering the distribution function $f_8(\mathbf{x}, t)$ just before it collides against a solid horizontal boundary, as depicted in Fig. 3.6(a). At the next time step $t + \Delta t$ the specular rule implies that $f_5(\mathbf{x} + \mathbf{c}_5\Delta t, t + \Delta t) = f_8(\mathbf{x}, t)$, as shown in Fig. 3.6(b).

3.6.2 Open Boundaries

Open boundary conditions are much more intricate to implement than solid boundaries and, for this reason, represent an important challenge in the LBM research. As previously mentioned, it is quite simple to obtain acoustic variables such as \mathbf{u} and p from the moments of f_i , using Eq. 3.17. However, reconstructing f_i from the values of \mathbf{u} and p is not a trivial task. This implies that the imposition of frequency-dependent acoustic boundaries, such as impedances, requires a more sophisticated approach. We now present some important open-boundary schemes in LBM.

Periodic Boundary

From the programming viewpoint, periodic boundaries represent the easiest type of boundary condition. Although not being physical, this type of boundary condition allows for the representation of acoustic and/or fluid dynamic phenomena that take place in waveguides of infinite length. The periodic boundary is achieved by wrapping the fluid domain around itself as shown in Fig. 3.7. In this case, the distribution function leaving the fluid domain at one of its extremities is re-injected in the opposite side. In the case of the example depicted by Fig. 3.7, this implies that $f_{1,5,8}|_{east} = f_{1,5,8}|_{west}$ and $f_{3,6,7}|_{east} = f_{3,6,7}|_{west}$, according to the *D2Q9* model.

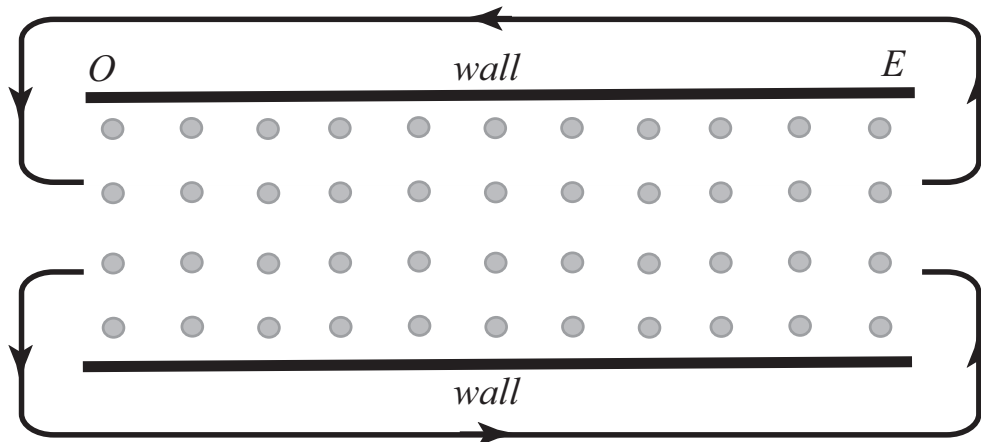


Figure 3.7 Periodic boundary condition in the horizontal direction.

This boundary condition has been used by Buick et al. (1998) to simulate viscous low amplitude acoustic wave propagation in a waveguide of infinite length, and by Buick et al. (2000) to simulate the formation of shock waves.

In purely hydrodynamic problems, the periodic boundary condition has a major drawback associated with the inability to initialize the flow by setting a pressure gradient between the inlet and outlet of the system. Alternatively, the flow can be initialized

by applying a body force term to every distribution function, which works well for the simulation of stable flow phenomena but fails at representing flows characterized by instability (Sterling and Chen, 1996).

Buffer Zones

For problems in which the representation of flow instabilities is required, the initialization of the flow is normally achieved by using sources and drains at the inlet and outlet of the system, respectively, as shown in Fig. 3.8. A very common technique consists in assigning a certain flow profile at the inlet $\mathbf{u}_{in}(y)$, while imposing at the outlet either a pressure P_{out} or a no-flux condition normal to the wall $\partial_n \mathbf{u} = 0$ (Succi, 2001, pp. 90). The inlet condition is achieved by constantly refilling the inlet buffer with $f_{in} = f^M(\rho_{in}, \mathbf{u}_{in})$, where ρ_{in} and \mathbf{u}_{in} are the desired inlet conditions for density and flow velocity, respectively (see Fig. 3.8).

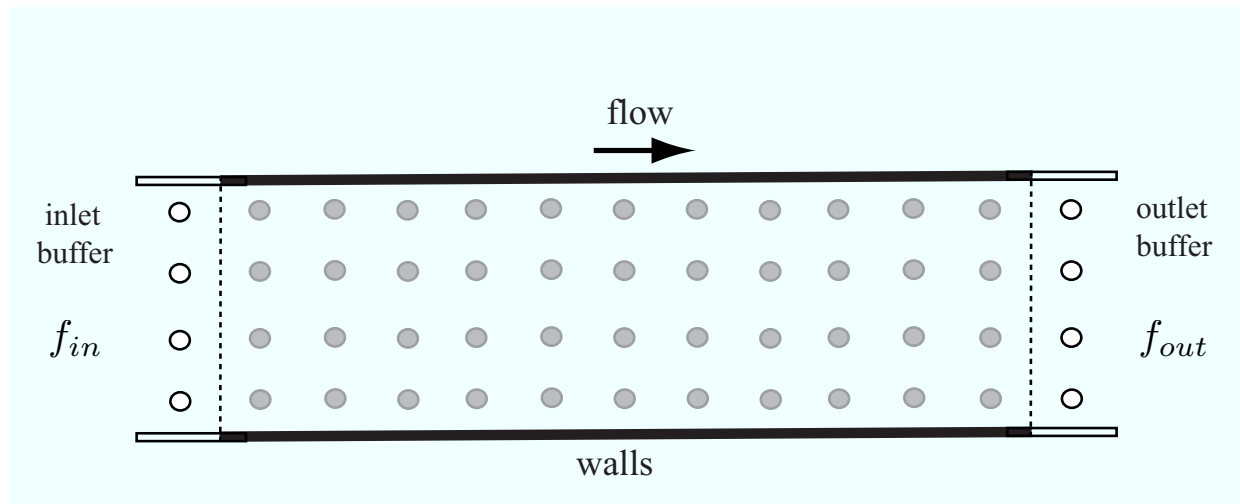


Figure 3.8 Simple buffer zones placed at the inlet and outlet of the system.

The same procedure is used to set the outlet condition, that is, $f_{out} = f^M(\rho_{out}, \mathbf{u}_{out})$. Unfortunately, this approach does not avoid trains of backward propagating distur-

bances in the form of sound waves to be generated at the outlet buffer. These spurious waves invade the fluid domain and may completely corrupt the simulation. Furthermore, this approach is unable to absorb outgoing acoustic waves generated within the fluid domain. In fact, this is a very critical drawback when it comes to representing problems involving an acoustic field because, in many acoustic simulations, an anechoic boundary is paramount to avoid artificial reflections that can drive the solutions towards an incorrect time-stationary state. An alternative for this problem is discussed next.

Absorbing Boundary Condition

The correct representation of anechoic boundaries is an important challenge, not only in LBM but in computational acoustics as a whole. In the LBM literature, several techniques have been proposed in order to provide acoustically absorbing boundaries, as well as boundaries that do not generate acoustic energy during the passage of the fluid flow.

First attempts to provide anechoic boundaries for LBM were effective at absorbing outgoing acoustic waves but failed at avoiding the sound generation at the boundary due to flow conduction (Dorodnitsyn, 2000, Huang et al., 2000). A milestone step towards the development of a more effective boundary condition has been taken by Kam et al. (2006). In their paper, they analyzed the extension to LBM of several absorbing boundary techniques used in *continuum-based* DNS. The energy reflection at the boundary was evaluated in terms of pressure, entropy and vortex pulses. Among the different techniques studied, they found that the absorbing boundary condition method (ABC) was, by far, the most effective and provided results of second-order accuracy.

The concept of the ABC technique is very similar to the perfectly matched layer

method (PML) commonly used in DNS (Hu, 2001). It consists in using a buffer between the fluid region and the open boundary to create an asymptotic transition towards a target flow defined in terms of target distribution functions f_i^T . This is done by adding an extra term to Eq. 3.15, which becomes

$$f_i(\vec{x} + \mathbf{c}_i \Delta t, t + \Delta t) - f_i(\vec{x}, t) = -\frac{1}{\tau}(f_i - f_i^M) - \sigma(f_i^M - f_i^T), \quad (3.23)$$

where $\sigma = \sigma_m(\delta/D)^2$ is the absorption coefficient, σ_T is a constant, normally = 0.3, δ is the distance measured from the beginning of the buffer zone and D is the width of the buffer. The f_i^M is a constant and can be obtained in the same manner as f_i^M by using Eq. (3.16). In this case, the local velocity \mathbf{u} and density ρ are replaced by the target values $\mathbf{u}_T = 0$ and $\rho_T = \rho_0$, where ρ_0 is the undisturbed density of the fluid.

Asymptotic Target Flow

It is possible to prescribe inlet and outlet flows using an approach similar to the ABC technique previously discussed. In this case, however, instead of choosing target values corresponding to an anechoic boundary ($\rho_T = \rho_0$ and $\mathbf{u}_T = 0$), one can initialize the flow by setting $\rho_T \neq \rho_0$ and $\mathbf{u}_T \neq 0$. Figure 3.9 provides a schematic illustration of the asymptotic target flow technique.

This procedure provides two important advantages when contrasted with the use of simple buffer zones: First, the acoustic absorbing characteristic of the ABC method is kept even when $\rho_T \neq \rho_0$ and $\mathbf{u}_T \neq 0$. Second, the generation of acoustic waves due to the flow convection at the boundary is null. This technique is extensively used in the simulations presented in Chapter 4 and 5 and represents an important tool for the simulations conducted in this thesis.

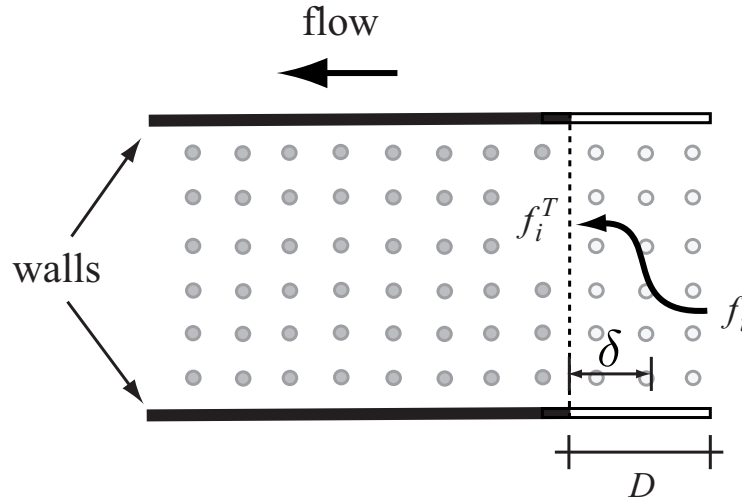


Figure 3.9 Schematics of the asymptotic target flow technique.

3.7 Dimensionless to Physical Quantities

Very often, the parameters associated with a lattice Boltzmann model such as velocity, space, time and viscosity are given in terms of dimensionless parameters such as \mathbf{u} , \mathbf{x} , t and ν . This is due to the fact that the simulation analyses are more conveniently described in terms of dimensionless numbers than with the actual values of the physical properties. However, the physical quantities can be easily obtained from the dimensionless parameters by using the characteristic velocity $\zeta = c_0^*/c_0$ and the lattice discretization (pitch) Δx , where c_0^* is the physical speed of sound. Hence, the physical velocity \mathbf{u}^* , space \mathbf{x}^* , time t^* and viscosity ν^* are obtained from their dimensionless counterparts by applying the following relations:

$$\mathbf{u}^* = \zeta \mathbf{u}$$

$$\mathbf{x}^* = \Delta x \mathbf{x}$$

$$t^* = (\Delta x / \zeta) t \quad \text{and}$$

$$\nu^* = \zeta \Delta x \nu. \quad (3.24)$$

As an example, one can consider a pipe segment of 0.10 m length filled with air at normal conditions ($c_0^* = 340$ m/s, $\rho_0^* = 1.2$ kg m⁻³ and $\nu^* = 1.4 \times 10^{-5}$ m²/s). If we arbitrarily represent this pipe with 1000 lattice cells along its length using the D2Q9 scheme, the lattice pitch becomes $\Delta x = 0.0001$ m, which gives a dimensionless lattice viscosity $\nu = 0.0023$ and a time step $\Delta t = 1.7 \times 10^{-7}$ s.

3.8 Discussion

The previous sections of this chapter provided the fundamental background of the lattice Boltzmann theory and presented the main characteristics associated with the LBGK D2Q9 model used in this work. It has been also argued in Sec. 3.2 that the LBGK equation (Eq. 3.15) can recover the compressible unstable form of the Navier-Stokes equations (Eqs. 2.22, 2.23 and 2.24) by a multiscale expansion, provided that the Mach number remains ≤ 0.15 and that the acoustic amplitude $u'/\mathbf{u}_0 \ll 1$, where u' is the amplitude of the acoustic particle velocity and \mathbf{u}_0 is the velocity of the mean flow.

These conditions are met for most of the playing range of an instrument such as the clarinet. A good estimation of the magnitude of the Mach number found in different parts of a clarinet is achieved by using the experimental data provided by (Fuks, 1998) who measured the volume flow for different playing conditions based on the dynamic level, note and reed type. In his experiments, the maximum value of the volume flow was found to equal 338 ml/s, which corresponds to the note *F5* being played at a *fortissimo* level with a hard reed.

Thus, assuming the speed of sound c_0 to be ~ 340 m/s and the averaged reed channel cross section area to be 1×10^{-5} m² results in $M \sim 9 \times 10^{-2}$. Likewise, an overestimated

Mach number $\sim 6.5 \times 10^{-3}$ is found at the end of the clarinet's bore by assuming that there is no leakage of flow through the keyholes and that its cross sectional area is $\sim 1.5 \times 10^{-4} \text{ m}^2$.

Moreover, although the sound pressure within a clarinet mouthpiece can, in rare circumstances, reach values up to 166 dB (Backus, 1961), the normal range is reported to be approximately 120 – 130 dB (Backus, 1963, Kobata and Idogawa, 1993). Using these values as a reference, an over-estimated acoustic particle velocity \mathbf{u}' is obtained by $\mathbf{u}' = p/Z_0$, where p is the sound pressure level in pascals and $Z_0 = \rho_0 c_0$ is the characteristic impedance of a tube. In this case, the obtained range for the ratio between the particle velocity and the mean flow is $0.02 \sim 0.07$. These characteristics support the applications of the *D2Q9* LBGK model in the analysis of the phenomena described in Chapter 1.

Chapter 4

Fluid-Structure Interactions in the Mouthpiece-Reed System

4.1 Introduction

The study of the acoustical properties of single-reed instruments has followed a paradigm first proposed by Helmholtz (1877), which divides these systems into linear and nonlinear components representing the instrument's bore and mouthpiece-reed, respectively.

Previous research on the resonator component has provided an extensive list of experimental and theoretical studies since the pioneering work of Bouasse (1929). Much light has been shed on the behavior of this system and, consequently, many satisfactory models have been proposed.

Conversely, the amount of available literature on the mouthpiece-reed component is considerably smaller and the majority of models rely on the quasi-stationary approximation to describe the flow behavior. That is, the flow in a mouthpiece with an oscillating reed is assumed to be equal, at any instant, to the flow in a mouthpiece with a static

reed having the same configuration (Chen, 1987). Moreover, the flow is considered to be frictionless and incompressible. Consequently, the dependence of the volume flow U on the pressure difference across the reed Δp and on the reed opening h is normally described by the Bernoulli obstruction theory based on the stationary Bernoulli equation, given by

$$U_B = hw \sqrt{\frac{2|\Delta p|}{\rho}} \operatorname{sgn}(\Delta p), \quad (4.1)$$

where w is the channel's width and ρ is the density of the fluid.

This approach was first presented by Backus (1963), whose semi-empirical model was limited to low blowing pressure regimes. Years later, Worman (1971) presented a more complex model addressing phenomena such as threshold of pressure and Bernoulli forces acting on the reed. Wilson and Beavers (1974) coupled the previous model to an idealized cylindrical resonator. More recent models involving the same approach were developed by Fletcher and Rossing (1998), Fletcher (1979), Saneyoshi et al. (1987), Kergomard (1995a) and Ollivier (2002).

The quasi-stationary approximation has also been used to derive a steady viscous flow representation by Hirschberg et al. (1990). Their semi-empirical model was based on the results obtained from the simulation of flow in a two-dimensional (Borda) tube based on the theory of potential flow. They noticed that, for Reynolds numbers $Re > 10$, two patterns of flow may occur simultaneously, depending on the ratio l/h , where l is the length of the channel and h is its height. For short channels ($l/h < 1$) the flow is fully detached along the channel, whereas for long channels ($l/h > 3$) the flow is reattached at a roughly fixed point, l_r , measured from the channel's entrance. They also observed that, in the case of short channels, the vena contracta factor $\alpha = T_j/h$ was approximately

constant with a value $\simeq 0.6$, where T_j is the thickness of the jet formed at the detached portion of the flow.

van Zon et al. (1990) provided an experimental validation of Hirschberg's model using an idealized prototype of the mouthpiece with a static reed and assuming the flow to be two-dimensional. They also derived a more sophisticated flow model in which the transition between fully separated to attached flow is represented by a boundary layer solution. Other stationary measurements using realistic mouthpieces have found the same flow behavior, such as those conducted by Valkering (1993) and by Dalmont et al. (2003), in the case of clarinet, and by Maurin (1992) in the case of saxophones.

However, previous attempts to characterize flow in dynamic regimes (Gilbert, 1991, van Zon et al., 1990), i.e., flow in a mouthpiece with a moving reed, have suggested that the stationary behavior observed by van Zon *et al.* is unrealistic. This is particularly evident in the case of the steadiness associated with the detachment / reattachment phenomenon, which is strongly affected by subtle modifications on the reed channel geometry as the reed moves. The unsteadiness of the flow modulates the aerodynamic forces acting on the reed and plays an important role in the reed's behavior. In fact, this unsteadiness is responsible for the self-sustained oscillations in systems whose acoustic coupling between the resonator and the exciter is weak or even absent. This is the case in the harmonium (St-Hilaire et al., 1971), in the accordion (Ricot et al., 2005) and in the human phonatory system (Pelorson et al., 1994, Erath and Plesniak, 2006, Thomson et al., 2005, Thomson, 2004, Titze, 1988). Moreover, the unsteadiness of the flow can explain why small modifications in a mouthpiece geometry can correspond to enormous changes on the transient behavior and on the steady-state sound of single-reed instruments (Hirschberg et al., 1994, Benade, 1976).

Unfortunately, the accurate quantification and visualization of a dynamic flow con-

trolled by a moving boundary (in this case, the reed) is a rather complicated task. For this reason, previous attempts to do so are limited to qualitative outcomes (Gilbert, 1991, van Zon et al., 1990). Similar difficulties are found when tackling the problem with unsteady numerical flow simulations using traditional computational fluid dynamic (CFD) techniques based on the *continuum* theory (Shyy, 1995, Liefvendahl and Troeng, 2007).

The first objective of this chapter is to develop a numerical procedure that is able to provide a second-order accurate description of the fluid-structure interaction in a single-reed mouthpiece, taking into account aspects of the dynamic flow and its dependency on the reed channel geometry. The second objective is to verify the validity of the quasi-stationary theory in dynamic regimes. To accomplish that, we implement a two-dimensional dynamic model of a single-reed mouthpiece based on a hybrid numerical approach involving the lattice Boltzmann method (LBM), to represent the fluid and acoustic domains, and on a finite difference scheme to resolve the distributed model of the reed with varying cross section, as proposed by Avanzini and van Walstijn (2004). The main advantage of this approach consists in its simplicity in providing solutions of second-order accuracy to represent the fluid-structure interaction involving a moving boundary (Lallemand and Luo, 2003). This simplicity is contrasted with the complexity and high computational demand associated with traditional CFD techniques. Furthermore, the lattice Boltzmann method can solve the different scales associated with the flow and acoustic fields in a single calculation, thus allowing the direct representation of the acoustic-flow interaction, as discussed in Chapter 3.2.

The influence of the player's lip and the coupling of the proposed system with the instrument's bore and player's vocal tract is not considered in this study. Furthermore, the interaction between flow and the acoustic field, as well as the contribution of eventual aeroacoustic sources, will be left to future work.

This chapter is organized as follows: Section 4.2 provides a detailed description of the hybrid model, its initial and boundary conditions and presents the different geometries considered in this study. Section 4.4 describes the types of analyses conducted based on the type of reed excitation and discusses the quasi-stationary theory proposed by van Zon et al. (1990). The results from all analyses are presented in Sec. 4.6. Finally, Sec. 4.7 discusses the results presented in the previous sections.

4.2 The Mouthpiece-Reed Model

This section describes the implementation of the two-dimensional model of the mouthpiece-reed system. The mouthpiece is represented by the lattice Boltzmann method, which includes solid static boundaries associated with the mouthpiece walls (face, rails and cavity walls) and the fluid domain, described in terms of acoustic and fluid fields. The moving boundary associated with the reed is represented with a distributed model of a clamped-free bar with varying cross-section and resolved with an implicit finite difference scheme, as proposed by Avanzini and van Walstijn (2004).

4.2.1 The Mouthpiece

The mouthpiece model was implemented in a lattice grid using the $D2Q9$ LBGK scheme and containing 1002×502 cells. The physical dimensions of the system are depicted in Fig. 4.1, as well as the dimensions of the grid. The lattice pitch was $\Delta x = 4 \times 10^{-5}$ m and the time step $\Delta t = 6.792 \times 10^{-8}$ s. As a matter of convenience, we have opted to use an undisturbed fluid density $\rho_0^* = \rho_0 = 1.0$ kg/m³. The relaxation time τ was chosen to be 0.505, which implies a lattice viscosity $\nu = 1.68 \times 10^{-3}$ and a physical kinematic viscosity $\nu^* = 3.95 \times 10^{-5}$ m²/s, using $c_0^* = 340$ m/s as the reference speed of sound. A

representation of the mouthpiece model is depicted in Fig. 4.1.

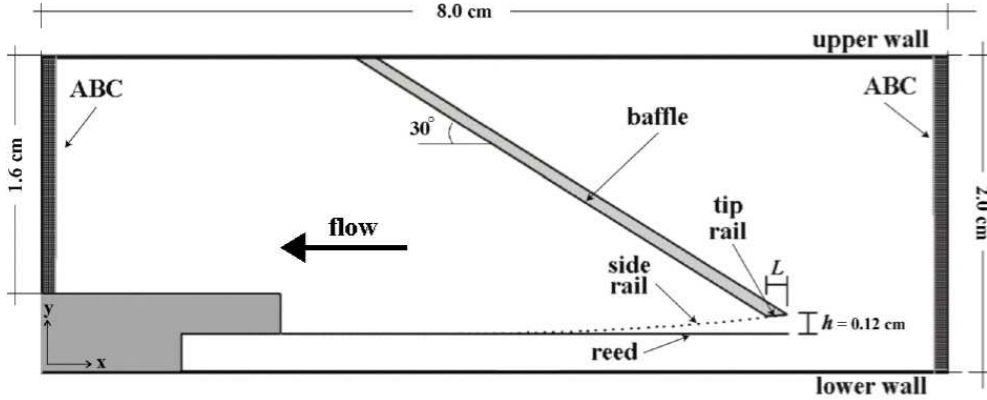


Figure 4.1 Lattice grid representing the two-dimensional model of the mouthpiece-reed system

Although the choice of values for ρ_0 and ν differ considerably from those of air in normal playing conditions, the dynamic similarity with the real system is obtained by forcing $Re \simeq 1200$ for a maximum $M = 0.1$. This setup also allows the two essential criteria of the lattice Boltzmann BGK model to be met: a) the maximum compressibility ($M < 0.15$) before numerical instabilities (Wolf-Gladrow, 2004); and b) a minimum grid resolution (5.6 lattices per wavelength) to avoid spurious dispersion and dissipation effects associated with the numerical bulk viscosity, as described by Wilde (2006).

4.2.2 The Reed

The reed is represented as a clamped-free bar with non-uniform thickness $b(x)$, constant width w , and driven by a force $F(x, t)$. The partial differential equation describing the vertical displacement $y(x, t)$ as a function of $F(x, t)$ is given by

$$\rho_r A(x) \frac{\delta^2 y}{\delta t^2}(x, t) + \frac{\delta^2}{\delta x^2} \left[Y I(x) \left(1 + \eta \frac{\delta}{\delta t} \right) \frac{\delta^2 y}{\delta x^2}(x, t) \right] = F(x, t), \quad (4.2)$$

where $x \in [0, L]$ is the horizontal position, $A(x) = wb(x)$ is the cross-section, ρ_r is the material density, Y is the Youngs modulus, $I(x)$ is the moment of area about the longitudinal axis and η is the viscoelastic damping coefficient. Table 1 shows the values used in the simulation, obtained experimentally by Avanzini and van Walstijn (2004). Equation (4.2) considers only reed motion associated with flexural waves in the vertical direction and thus, torsional and longitudinal modes are neglected.

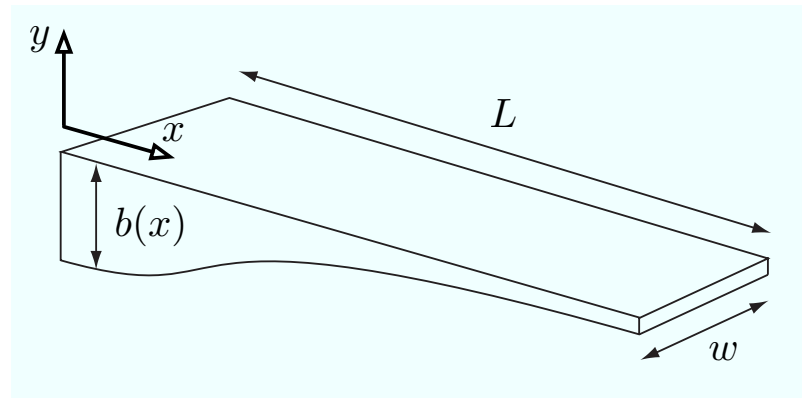


Figure 4.2 Geometry of the single reed.

This is similar to the approach used by Chaigne and Doutaut (1997) to simulate xylophone bars. In our model, however, a term associated with the energy dissipation of the reed due to the work exerted on the surrounding fluid is neglected in Eq. (4.2). However, this is taken into account implicitly by the fully coupled fluid-structure interaction scheme presented in Sec. 4.6.2.

Equation (4.2) is solved by performing a space-temporal discretization based on an implicit finite difference scheme described by Chaigne and Doutaut (1997). This results in a matricial difference equation in which the spatial coordinate is vectorialized

$$\mathbf{y}(n+1) = \mathbf{A}_0 \cdot \mathbf{y}(n) + \mathbf{A}_1 \cdot \mathbf{y}(n-1) + \mathbf{A}_F \cdot \mathbf{F}(n), \quad (4.3)$$

Table 4.1 Characteristics of a plastic reed (Avanzini and van Walstijn, 2004).

Length	$L_{reed} = 34 \times 10^{-3} \text{m}$
Width	$w = 10 \times 10^{-3} \text{m}$
Density	$\rho_{reed} = 500 \text{Kg/m}^3$
Young's modulus	$Y = 5.6 \times 10^9 \text{N/m}^2$
Viscoelastic const.	$\eta = 6.0 \times 10^{-7} \text{s}$
Fluid damping coef.	$\gamma_{air} = 100 \text{s}^{-1}$

where $\mathbf{y}(n+1)$, $\mathbf{y}(n)$ and $\mathbf{y}(n-1)$ represent the displacement vector at successive time instants and \mathbf{A}_0 , \mathbf{A}_1 and \mathbf{A}_F are coefficient matrices. $\mathbf{F}(n)$ is a vector representing the longitudinally distributed force on the reed. The interaction between the reed and the mouthpiece lay is considered to be inelastic. This is achieved by nullifying the kinetic energy of those reed sections that collide with the mouthpiece side rail, which presents an upper boundary to the reed. The inelastic assumption for the reed/lay interaction is justified in (Avanzini and van Walstijn, 2004).

4.2.3 Initial and Boundary Conditions

The algorithm assumes a no-slip condition of flow at the walls by implementing a bounce-back scheme for non-aligned boundaries proposed by Bouzidi et al. (2001). The bounce-back scheme works to invert the direction of propagation of a distribution function f_i just before it reaches a solid boundary. This procedure creates a null fluid velocity at the walls and provides second-order accuracy to represent viscous boundary layer phenomena.

The problem of a moving boundary within the lattice is tackled by using an interpolation scheme proposed by Lallemand and Luo (2003). This technique preserves second-order accuracy in representing the no-slip condition and the transfer of momentum from the boundary to the flow. One constraint of this approach is the velocity limit defined by

$M = u_b/c_o < 0.5$, u_b being the velocity of the boundary. However, such a limitation does not represent a problem in our simulation because it corresponds to values of velocity much higher than those found for reeds at normal playing conditions. Moreover, this boundary velocity limit is much higher than the low compressibility limit associated with the $D2Q9$ LBGK scheme used to construct the model. Both the moving boundary and the no-slip scheme for non-aligned boundaries are described in Appendix A.

The mean flow is initiated by using the absorbing boundary conditions (ABC), as described in Chapter 3. This technique has been adapted to LBM by Kam et al. (2006) and consists in using a buffer between the fluid region and the open boundary to create an asymptotic transition towards a target flow, as described in Chapter 3. The thickness of the ABC buffer was $D = 30$ lattices, which, for the lattice parameters used in the mouthpiece model, provides a rapid flow acceleration from its stagnant condition to the prescribed flow. Furthermore, the same thickness provides a nearly anechoic condition for the outgoing acoustic waves, as described in Chapter 3.

4.2.4 Analyzed Geometries

The effect of the reed channel geometry on the behavior of the flow is investigated for three different mouthpiece geometries as shown in Fig. 4.3. The geometries are described by the ratio l/h , where l and h are the length and the height of the reed channel. For all the simulations involving the geometries depicted in Fig. 4.3 all the lattice parameters, as well as the initial and boundary conditions are kept constant, as described in Sec. 4.2.1 and 4.2.3.

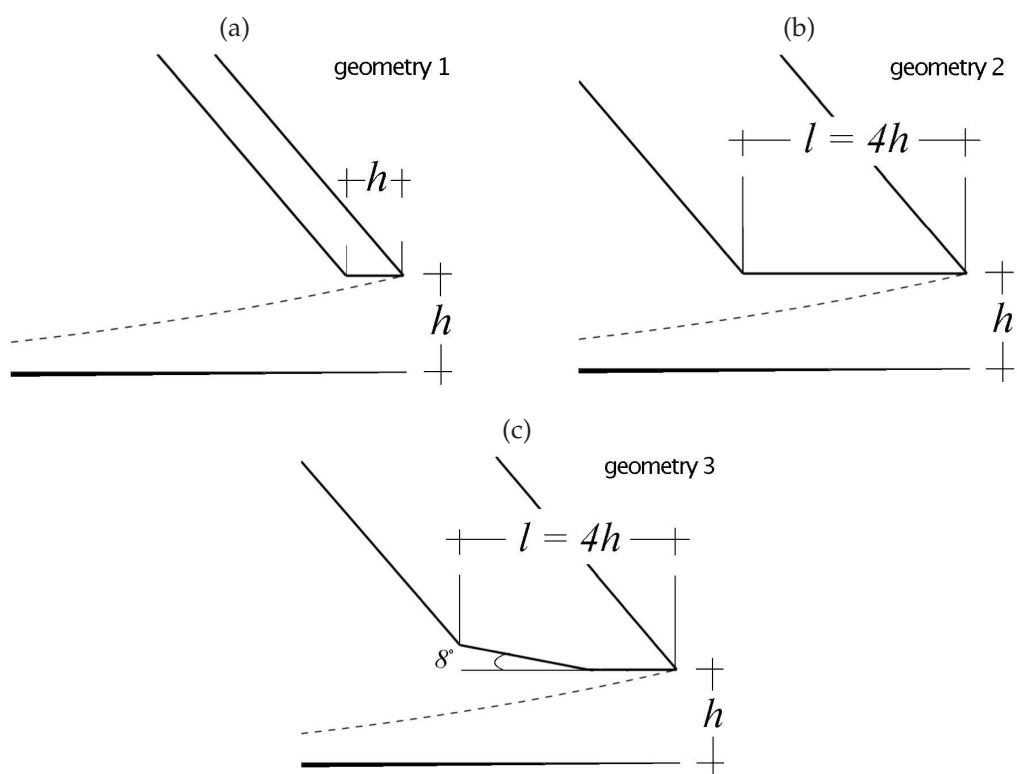


Figure 4.3 Different reed channel profiles used in the simulation: (a) $l/h = 1$, (b) $l/h = 4$, and (c) $l/h = 4$ with a chamfer.

4.3 The Quasi-Stationary Theory

Hirschberg et al. (1990) derived a semi-empirical analytical model for the viscous steady flow in a two-dimensional single-reed mouthpiece channel with constant height. The model was based on the numerical study of a two-dimensional channel (Borda tube) using a potential flow scheme.

They observed two types of flow for Reynolds numbers $Re > 10$ ($Re = U/wv$), depending on the ratio between the channel height h and its length l . In both cases, a jet is formed at the sharp edges of the channel's entrance. For small ratios ($l/h \leq 1$) the jet does not reattach along the channel walls whereas, for high ratios ($l/h \geq 3$) the jet reattaches at a fixed point $l_r \simeq h$ measured from the channel's entrance.

Thus, in the case of short channels, the flow is described by the Bernoulli equation (Eq. (4.1)) scaled with a constant vena contracta factor α , whereas, in the case of long channels, the detached segment is represented by the Bernoulli flow and the reattached part is represented by the Poiseuille flow.

These results were confirmed experimentally for single-reed mouthpieces with constant cross-section by Valkering (1993) and Dalmont et al. (2003), in the case of a clarinet, and by Maurin (1992), for the saxophone.

van Zon et al. (1990) used the results obtained from a stationary measurement involving an idealized two-dimensional prototype of the mouthpiece-reed system to derive a more accurate steady flow model in which the transition between fully separated to Poiseuille flow is described by a boundary layer flow. In this case, the velocity profile $u(x, y)$ within the boundary layer of thickness $\delta(x)$ is assumed to increase linearly with the distance y from the wall.

Similarly to the model proposed by Hirschberg *et al.*, the flow in short channels ($l/h \leq$

1) is given by

$$U = \alpha U_B, \quad (4.4)$$

where, U_B is the Bernoulli flow given by Eq. (4.1) and α , $0.5 \leq \alpha \leq 0.61$, is the constant vena contracta factor whose value depends on the external geometry of the mouthpiece.

For long channels ($l/h \geq 4$) and $\delta(l) > \delta_c$, where δ_c is the critical boundary layer thickness, van Zon *et al.* give the volume flow by

$$U = \frac{\nu w}{c h} (l_c - l_r). \quad (4.5)$$

The term $(l_c - l_r)$ is the length of the transition between fully separated flow to Poiseuille flow, given by

$$\frac{l_c - l_r}{l - l_r} = \frac{12c(1 - \delta^*)^2}{24c - 1} \left[1 - \sqrt{1 - \frac{h^4(24c - 1)\Delta p}{72\rho\nu^2(l - l_r)^2(1 - \delta^*)^2}} \right] \quad (4.6)$$

where δ^* is the generalization of the critical boundary layer thickness δ_c for a channel of arbitrary height h , expressed by

$$\delta^* = \frac{\delta_c}{h} = \frac{4}{9} \left(1 - \sqrt{\frac{5}{32}} \right) = 0.2688, \quad (4.7)$$

and

$$c = \frac{1}{6} \left[4\delta^* + 9 \ln(1 - \delta^*) + \frac{5\delta^*}{1 - \delta^*} \right] = 0.01594. \quad (4.8)$$

4.4 Static and Dynamic Approaches

The numerical investigation of the fluid-structure interaction within the mouthpiece geometries depicted in Fig. 4.3 are carried out by taking into account two different ap-

proaches, namely, static and dynamic. As the name suggests, the static approach implies that the reed remains fixed, meaning that the channel opening remains constant throughout the simulation. These results are then compared with those provided by the available theory for quasi-stationary flows in single-reed mouthpieces proposed by van Zon et al. (1990).

On the other hand, the dynamic approach implies that the reed must be free to oscillate during the simulation and is meant to investigate the characteristics of the oscillation onset, before the coupling between the reed and the acoustic field is fully developed. In this case, the oscillation of the reed is only attributed to the presence of aerodynamic forces caused by flow instability.

In both static and dynamic approaches, the characteristics of the lattice grid are kept constant as described in Sec. 4.2.1.

4.5 Numerical Procedures

Seven different operations are executed at every time step in order to couple the lattice Boltzmann model with the finite difference scheme. The sequence of operations is depicted as a flowchart in Fig. 4.4. Before the simulation begins, the initial conditions associated with the fluid and reed variables are set and the definition of solid boundaries within the lattice are defined. The reed variables such as displacement $y(x, 0)$, velocity $\dot{y}(x, 0)$ and force $F(x, 0)$ are set to zero, as well as the variables associated with the fluid domain, such as the local fluid velocities \mathbf{u} . The initial fluid variables are used to define the initial distribution functions based on Eq. (3.16), so that, in the first time step $f_i = f_i^M$. The flow is started by prescribing a target pressure difference at the ABC layer, defined as $\Delta p^T = (\rho_{in}^T - \rho_{out}^T)c_o^2$, where the indexes *in* and *out* indicate inlet and outlet,

respectively. The values of Δp^T depend on the type of simulation being conducted and are described in the next sections of this study.

With respect to the flowchart in Fig. 4.4, the following operations take place after the initial conditions are set: (a) calculate the relaxation functions $f_i^{M'}$'s using Eq. (3.16); (b) propagate f_i to all directions ignoring the presence of pre-defined solid boundaries and perform their relaxation based on Eq. (3.15); (c) find the lattice positions of f_i that have crossed solid boundaries during the propagation step in (b); (d) replace f_i found by the previous operator with new values based on two different interpolation strategies: f_i at crossed static boundaries are replaced by values calculated using the simple bounce-back scheme, proposed by Bouzidi et al. (2001). Otherwise, f_i are replaced by values calculated using the moving boundary scheme proposed by Lallemand and Luo (2003). In this case, the calculation of the new f_i requires the actual values of $\dot{y}(x, t)$ in order to take into account the transfer of momentum from the reed to the flow; (e) determine new values of \mathbf{u}' and ρ' using Eq. (3.17); (f) evaluate the new distributed force $F(x, t)$ on the reed model based on local lattice pressures across the reed boundary; (g) calculate the reed's new position $y(x, t)$ and velocity $\dot{y}(x, t)$.

4.6 Results

4.6.1 Static Analysis

The stationary simulations were conducted for different cases involving geometries with the same characteristics as that shown in Fig. 4.1 but with different channel profiles as depicted in Fig. 4.3. For each geometry, different steady-state values of U are achieved by prescribing different target pressure values Δp^T from 0 to 9 kPa. The simulations used the same characteristics described in Sec. 4.2.3 in terms of initial and boundary

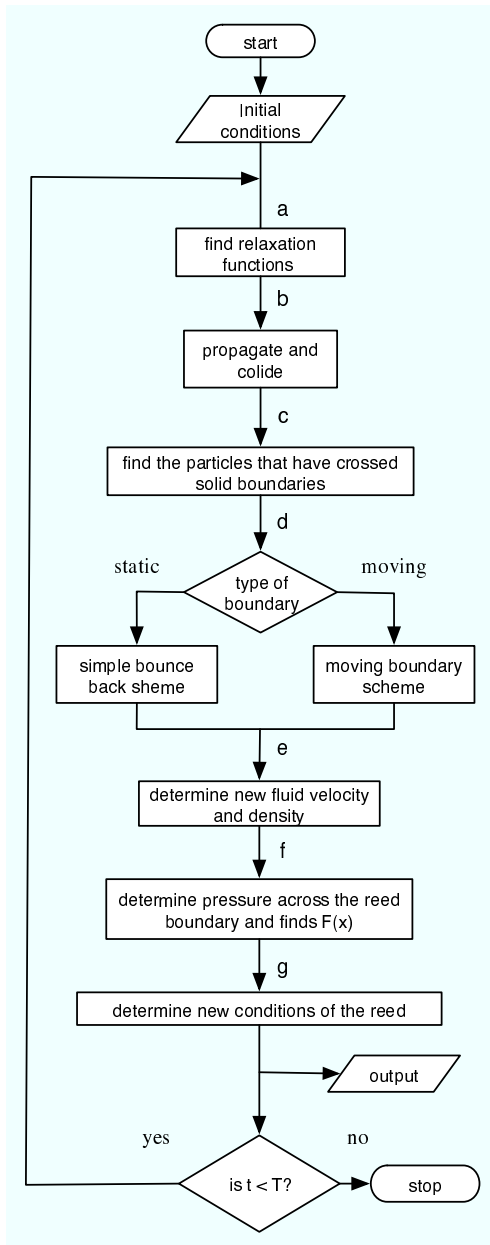


Figure 4.4 Flowchart of the integrated algorithm

conditions, lattice discretization and fluid properties. However, in this case the reed is maintained fixed (or static) throughout the simulations. Figure 4.5 presents the numer-

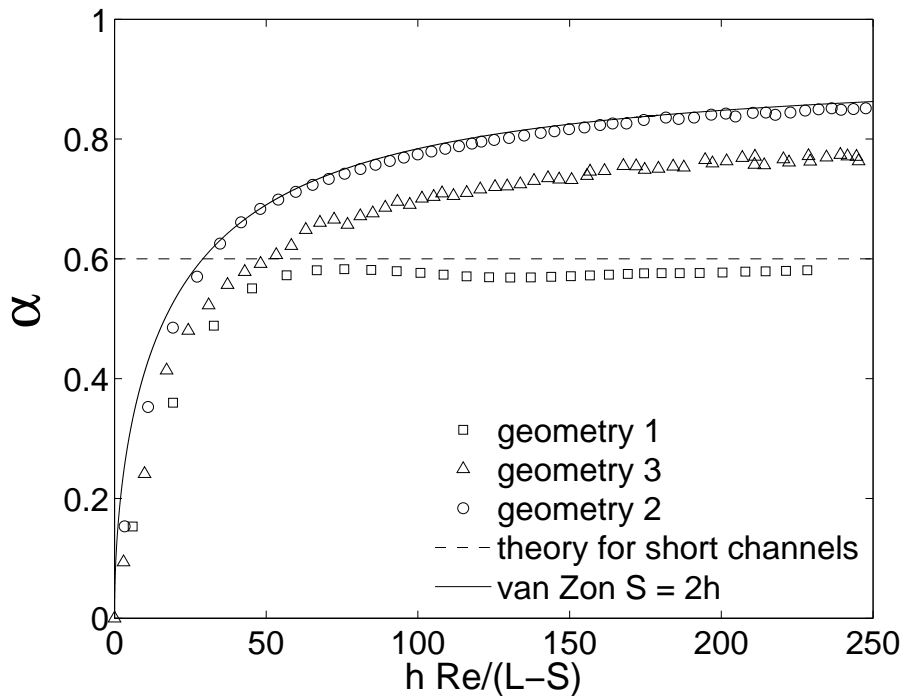


Figure 4.5 Vena contracta factor as a function of the modified Reynolds number

ical results obtained for the three cases in terms of vena contracta factor $\alpha = U/U_B$ as a function of the modified Reynolds number proposed by van Zon et al. (1990). These results are compared with those predicted by the quasi-stationary model presented in the previous section. For short channels, the values of α were chosen to represent two geometry cases, namely, a slit in a infinite wall and a tube with sharp edges (Borda tube). According to potential flow theory, α is determined by the turning angle of the upstream flow into the channel, which depends on the characteristics of the external geometry. For the slit in an infinite wall one finds $\alpha = 0.61$, whereas for the Borda tube $\alpha = 0.5$. Therefore, in the case of a short single-reed mouthpiece channel ($l/h \leq 1$), one

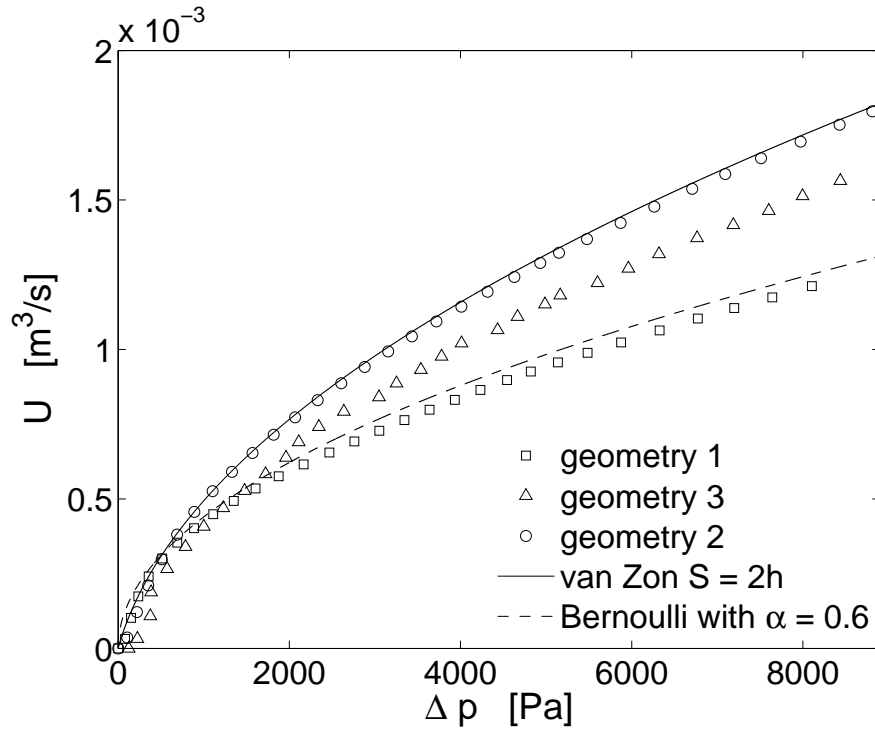


Figure 4.6 Pressure difference across the reed channel as a function of the volume flow.

should expect an intermediate value between the two extreme cases, i.e., $0.5 \leq \alpha \leq 0.61$. Figure 4.6 plots the same simulation results in terms of volume flow U as a function of the pressure difference Δp and compares it with the theory provided for short and long channels as presented in Sec. 4.3.

In general, Figs. 4.5 and 4.6 show that the results obtained for geometries 1, 2 and 3 agree very well with the theory presented in Sec. 4.3. However, Fig. 4.5 shows that the result for geometry 1 is in considerable disagreement for $h Re/(l - s) < 60$ when compared with the limits provided by the theory for short channels and fully detached flow ($0.5 \leq \alpha \leq 0.61$). This type of disagreement is commonly reported in the literature and is attributed to the influence of viscous effects at low Reynolds numbers, as described by Durrieu et al. (2001) and Blevins (1984). Curiously, the results obtained for geometry 2

are very similar to those found for geometry 3 and agree very well with those predicted by the theory for long channels (Eq. 4.5), despite the fact that geometry 3 has a rather diverging channel profile due to the presence of the chamfer.

The flow profiles were found to be roughly constant for all geometries. In the first geometry the flow remained fully separated for $Re > 30$, whereas in geometries 2 and 3 the flow was separated at the beginning of the channel and reattached at $l_r \simeq 2h$ for $Re > 60$.

4.6.2 Fully-Coupled Analysis

The goal of this section is to investigate the main aspects of the fluid-structure interaction in dynamic regimes by using the same geometries investigated in the previous section (Fig. 4.3). We also intend to substantiate the validity of quasi-stationary theory by evaluating the main assumptions associated with the steadiness of the flow reattachment point and steadiness of the vena contracta factor when the oscillation of the reed is taken into account.

For all three cases, we use the same initial and boundary conditions described in Sec. 4.2. The flow is initiated by prescribing $\Delta p^T = 5$ kPa. This value corresponds to a middle point between the threshold of oscillation and the maximum pressure found for a clarinet mouthpiece (Dalmont et al., 2003). It must be stressed that the ABC scheme used at the inlet and outlet of the system (Fig. 4.1) provides a complete anechoic behavior, which avoids any sort of acoustic coupling between the reed and the upstream and downstream chambers.

Therefore, the only possible way that a dynamic regime with an oscillating reed can exist is via an aerodynamic force F_B due to flow detachment with an ensuing reattachment (Hirschberg et al., 1994). The aerodynamic force can explain the movement of

the reed during the transient state of the flow but is insufficient, however, to explain a self-sustained oscillatory regime. This can only happen when the net energy exchanged between the flow and the reed during one duty cycle is positive: $E = \int_0^T \overline{F}_B \cdot \dot{y}_{tip} > 0$, where \overline{F}_B is the space averaged aerodynamic force on the reed and \dot{y}_{tip} is the velocity of the reed measured at its tip. In other words, the amount of energy absorbed by the reed from the flow during one duty cycle has to be greater than the energy given to the flow by the reed. As explained by Hirschberg et al. (1994), in the absence of acoustic coupling, a positive net energy after one duty cycle is possible due to several reasons: a) the difference in the reed channel geometry between opening and closing phase; b) the inertia of the flow in the channel (St-Hilaire et al., 1971); and c) variability of the separation / reattachment point behavior (Erath and Plesniak, 2006).

Figure 4.7 depicts the time histories associated with displacement of the reeds measured at their tips for all geometries. The self-sustained oscillation regime is achieved for all geometries in Fig. 4.3. Long-channel geometries depicted in Fig. 4.2(b) and 4.2(c) present very similar behavior with high oscillation amplitudes, which forces the tip of the reed to close the channel completely. For the geometry with the short channel (Fig. 4.2(a)) the oscillation of the reed is roughly sinusoidal and the average value of the tip displacement $y_{tip} \simeq 8.0 \times 10^{-4}$ m. Long-channel geometries present similar oscillation periods that are $\simeq 6.5\%$ shorter than those found for the short-channel geometry. This vibratory behavior at a frequency close to the reed's first natural frequency f_o was expected, given the absence of acoustic coupling between the reed and the downstream and upstream cavities. Further analysis was carried out by investigating the dynamic characteristics of one single oscillation period. The selected duty cycles are related to the sixth oscillation period of each case and are indicated between dashed lines in Fig. 4.7. Figure 4.9 shows the normalized energy flows $\dot{E} = \overline{F}_B \cdot \dot{y}_{tip}$ as a function of time in terms

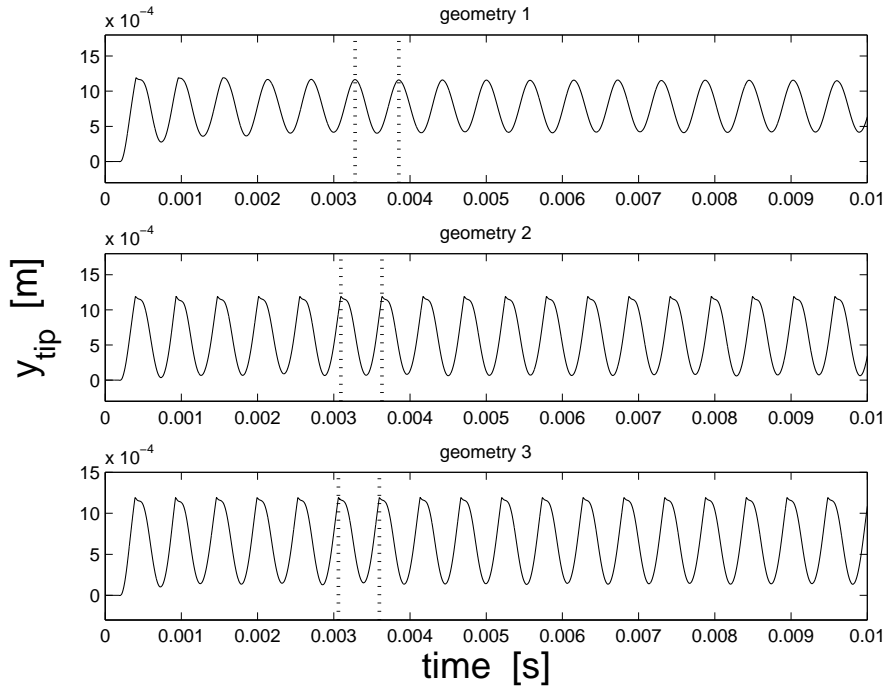


Figure 4.7 Time histories of the reed displacement measured at the tip for different channel geometries

of fraction of one duty cycle. The negative areas indicate transfer of energy to the flow due to the work of the reed. They take place during the phases associated with the opening of the reed, as shown in Fig. 4.8. Conversely, the positive areas in Fig. 4.9 take place when the reed is closing and represent the energy absorption by the reed due to flow work. In the regions of negative energy flow, \dot{y}_{tip} and \overline{F}_B are out of phase but become in phase as the reed starts to close again. In all cases, the shift from negative to positive energy flow also coincides with the maximum volume flow U , shown in Fig. 4.10. These results present the same behavior found in the experiments conducted by Thomson (2004) for an idealized model of the human larynx. The high amplitudes of oscillation found in the case of long-channel geometries are explained by the higher ratios between absorbed E^+ and lost energy E^- during one cycle, as shown in Table 4.2.

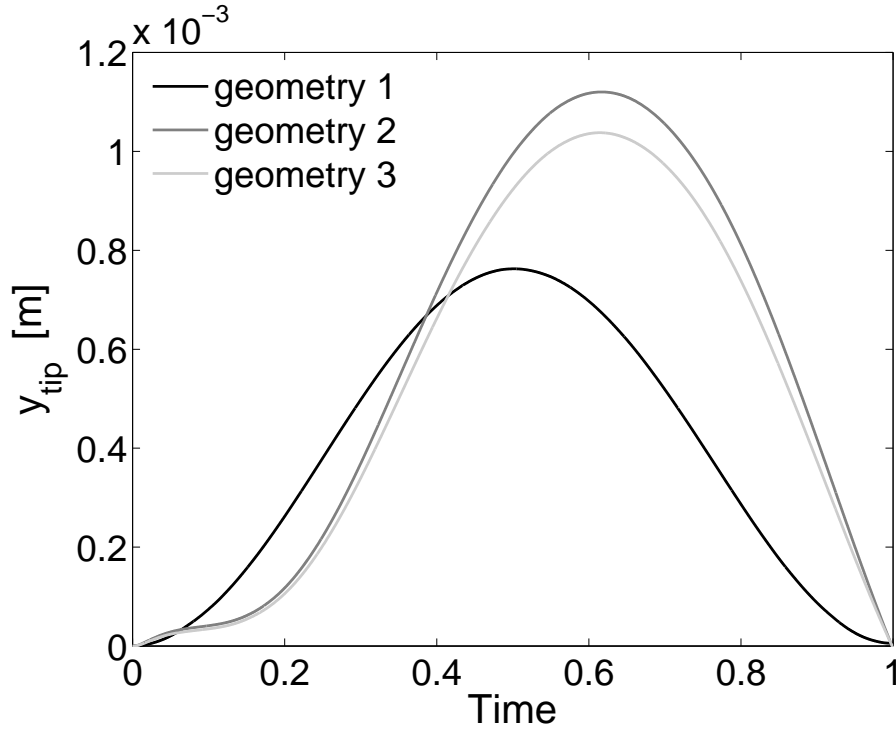


Figure 4.8 Channel aperture in terms of fraction of one duty cycle.

The excess of energy given to the reed is dissipated internally by the viscous damping predicted by the third term on the right of Eq. (4.2) and by the inelastic collision of the reed against the mouthpiece lay. Furthermore, Fig. 4.9 shows that the reeds in the long-channel geometries start to receive energy from the flow at 0.6 T of the duty cycle, which represents a delay of 0.13 T compared to the short channel geometry. This is due to a higher flow inertia caused by larger fluid volume within long channels and due to the effect of flow driven by the moving reed, as will be discussed later in this study. Table 4.2 presents some aspects related to the oscillation frequencies achieved by each geometry, as well as aspects related to the energy exchange between the flow and the reed.

Fig. 4.11 provides a better understanding of the results presented in Figs. 4.8, 4.9 and 4.10 by depicting snapshots of the normalized velocity field $u_{norm} = (u_x^2 + u_y^2)^{1/2} / \max(u_x)$

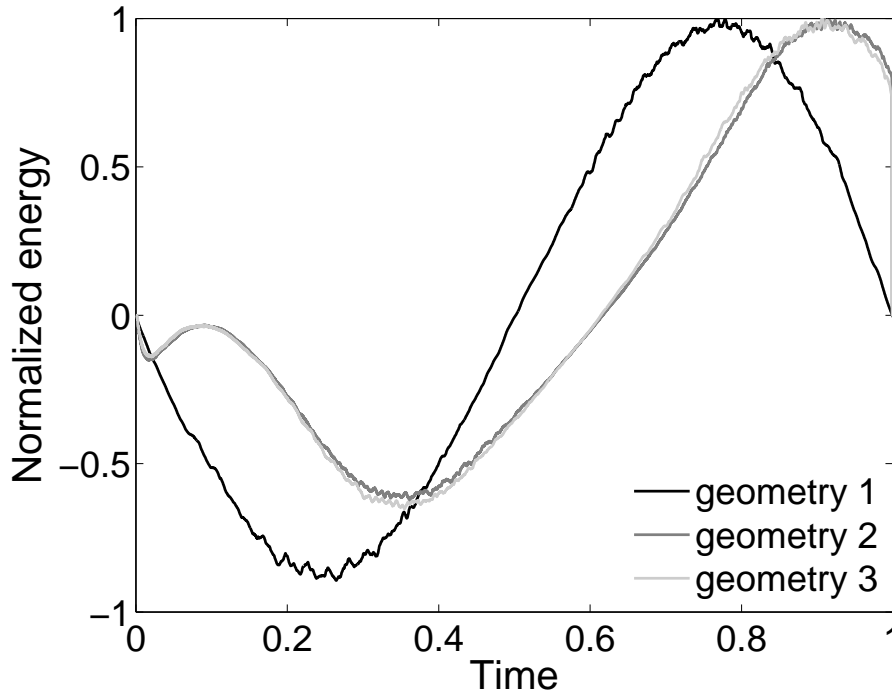


Figure 4.9 Normalized energy flow in terms of fraction of one duty cycle.

in the mouthpiece models, taken at four different instants within the same duty cycle.

In all cases, a jet is formed at the channel's entrance as the reed starts to open. At this point, the jet rapidly adheres to the rail tip but remains detached elsewhere. This situation continues until the gradient of pressures between the jet and the reed is enough to force the jet to attach to the reed's surface. The gradient is originated by the entrainment

Table 4.2 Aspects of dynamic flow in the different channel profiles.

	L/h	$f[\text{Hz}]$	f/f_o	E	$ E^+/E^- $
geometry 1	1	1760.3	1.00	120.28	1.10
geometry 2	4	1877.2	1.07	188.59	1.24
geometry 3	4	1855.7	1.06	179.30	1.22

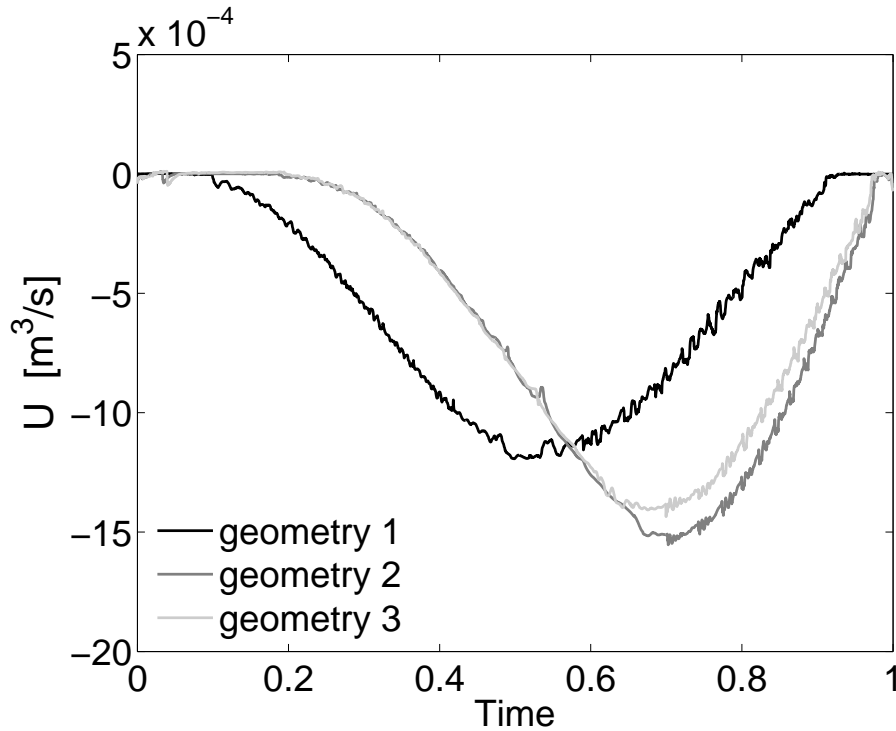


Figure 4.10 Volume flow in terms of fraction of one duty cycle.

of flow between the jet and the reed wall due to viscous momentum transfer and it is proportional to the downstream volume flow. This phenomenon, known as the Coanda effect, plays an important role in the self-sustained oscillations in vocal folds (Pelorson et al., 1994, Erath and Plesniak, 2006, Thomson, 2004, Titze, 1988) and in reed instruments such as the accordion (Ricot et al., 2005) and the harmonium (St-Hilaire et al., 1971).

During the opening stage the volume flow U in the short channel accelerates earlier into the mouthpiece chamber. In fact, for the same channel aperture y_{tip} , the volume flow into the short channel is much higher than that into the long-channel geometries, as shown in Figs. 4.8 and 4.10. The early acceleration provides the necessary pressure gradient for the jet to detach from the rail tip and adhere on the reed at $\simeq 0.5 T$, in

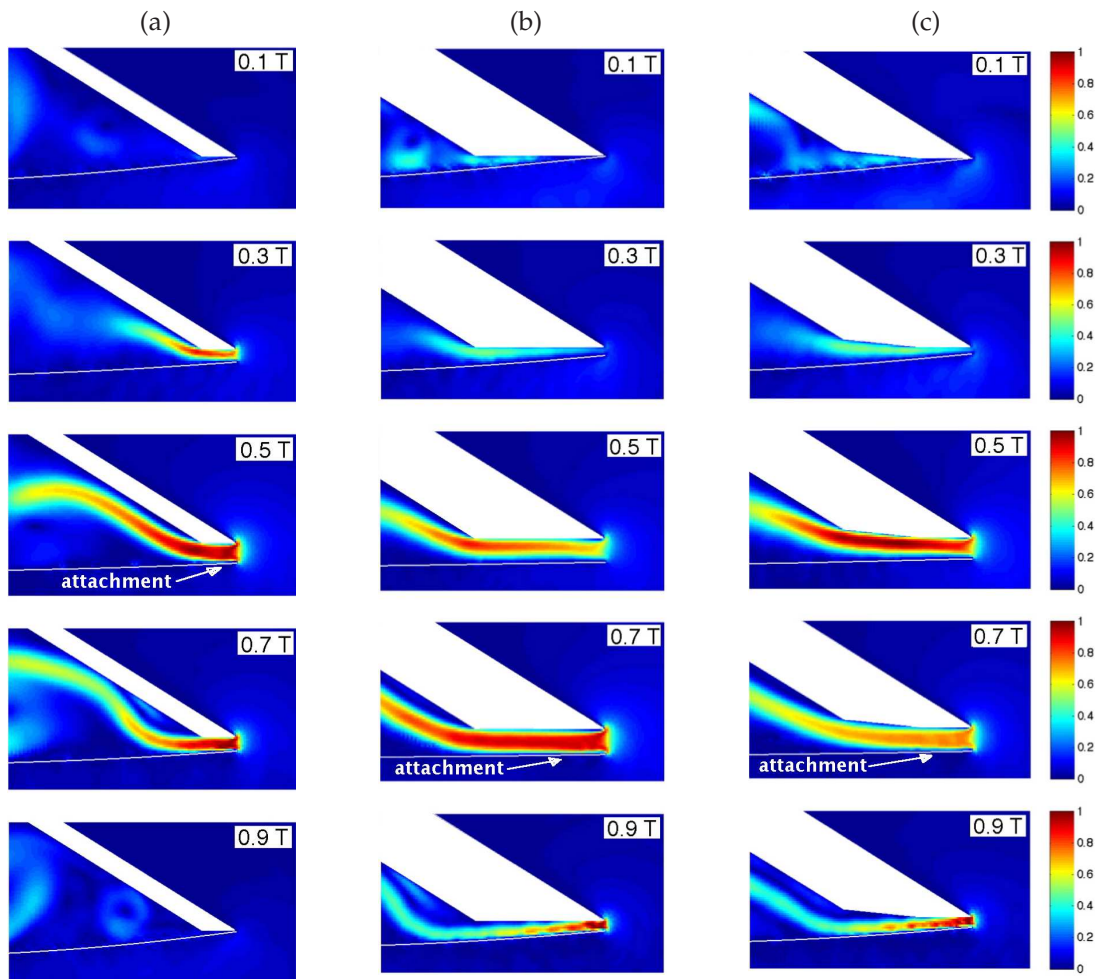


Figure 4.11 Snapshots of the velocity field for different instants within the same duty cycle: (a) $L/h = 1$, (b) $L/h = 4$, and (c) $L/h = 4$ chamfered.

contrast with the long channel geometries in which the same phenomenon happens at $\simeq 0.7 T$, as depicted in Fig. 4.11. The separation / adhesion phenomenon is confirmed by the determination of the skin-friction based on the shear-stress on the reed surface.

As already mentioned, the explanation for the early volume acceleration in the case of the short channel is twofold. The first reason is due to the reduced inertia of the fluid volume within the channel. The second reason is attributed to the effect of the flow driven by the reed U_{wall} . This is because, in the case of a dynamic regime, the

effective volume flow can be expressed by $U = U_{\Delta p} + U_{wall}$, where $U_{\Delta p}$ is the flow driven by the pressure difference Δp across the reed channel. Thus, during the opening stage the reed exerts work on the flow by pulling it out of the mouthpiece chamber in the upstream direction, which means that $U_{\Delta p}$ and U_{wall} are out of phase. In short channels, the influence of U_{wall} on the effective flow U is much smaller than in the case of long channels, which explains the early acceleration.

The effect of U_{wall} also becomes significant during the instants near the complete closure of the channel ($0.9 T \leq t \leq 1$). During this period $U_{\Delta p}$ and U_{wall} are in phase and U_{wall} may become higher than $U_{\Delta p}$, which could explain the considerable unsteadiness of the flow at this fraction of the duty cycle. This phenomenon has been reported by Deverge et al. (2003) in the case of experiments involving prototypes of the human glottis. In their observations, however, the effect of U_{wall} seems to be more evident in channels with constant height. This fact contrasts with our case in which the reed channel becomes divergent near the closure stage.

Furthermore, the aerodynamic force F_B caused by the pressure gradient increases when the jet attaches to the reed and becomes proportional to the attachment length. This explains the higher oscillation amplitudes in geometries (2) and (3). The increase in F_B acts to decelerate the reed until it stops. At this point \dot{y}_{tip} and $\overline{F_B}$ become in phase and the reed starts to receive energy from the flow. The stronger F_B in long channels also explains the positive pitch shift in these geometries, because a stronger F_B forces the reed to close more rapidly.

Discrepancy from the quasi-stationary predictions

The snapshots of flow during one duty cycle depicted in Fig. 4.11 show some fundamental deviations between the quasi-stationary assumptions and the numerical results

regarding the detachment / adhesion phenomenon. In the case of the short channel geometry (Fig. 4.11(a)) the constant fully separated flow assumed in the quasi-stationary theory has not been observed. In fact, for the first half of the duty cycle the flow is detached from the reed but remains attached to the rail tip. For the second half of the duty cycle the flow attaches to both reed and rail tip.

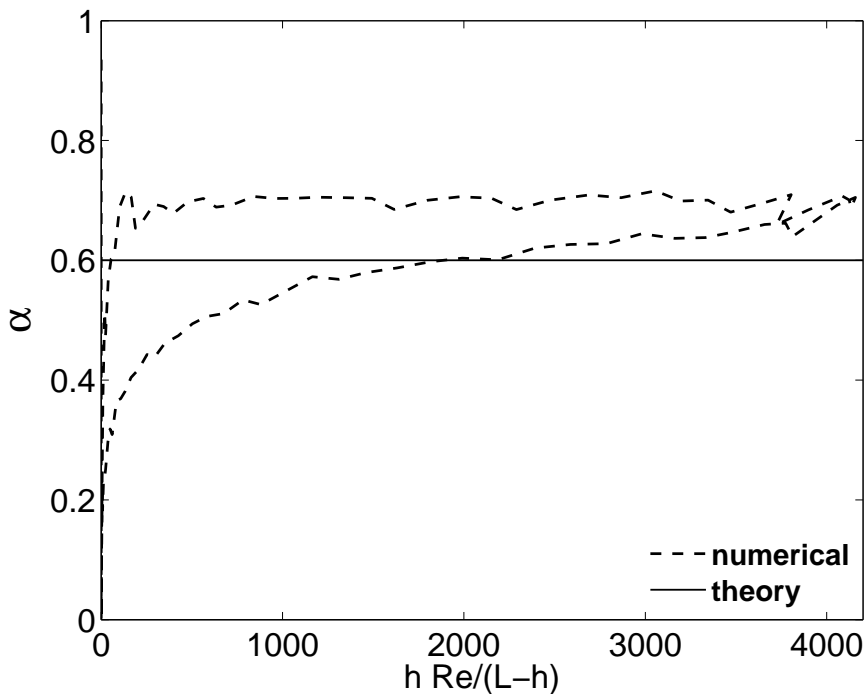


Figure 4.12 Vena contracta factor obtained for geometry 1 as a function of the modified Reynolds number

Geometries 2 and 3 (Fig. 4.11(a) and 4.11(b)) present very similar results between each other. The presence of a chamfer in geometry 3 did not play a significant role on the stability of the attachment phenomenon. In those cases, the flow remains detached from the reed for nearly $\simeq 70\%$ of the duty cycle. At $\simeq 0.7T$ the flow adheres to the reed and gradually detaches from the rail tip until the complete channel closure. This pattern contrasts with the theory, which assumes a constant separation region between

the channel's entrance and $l_r = 2h$ and full attachment of the flow afterwards.

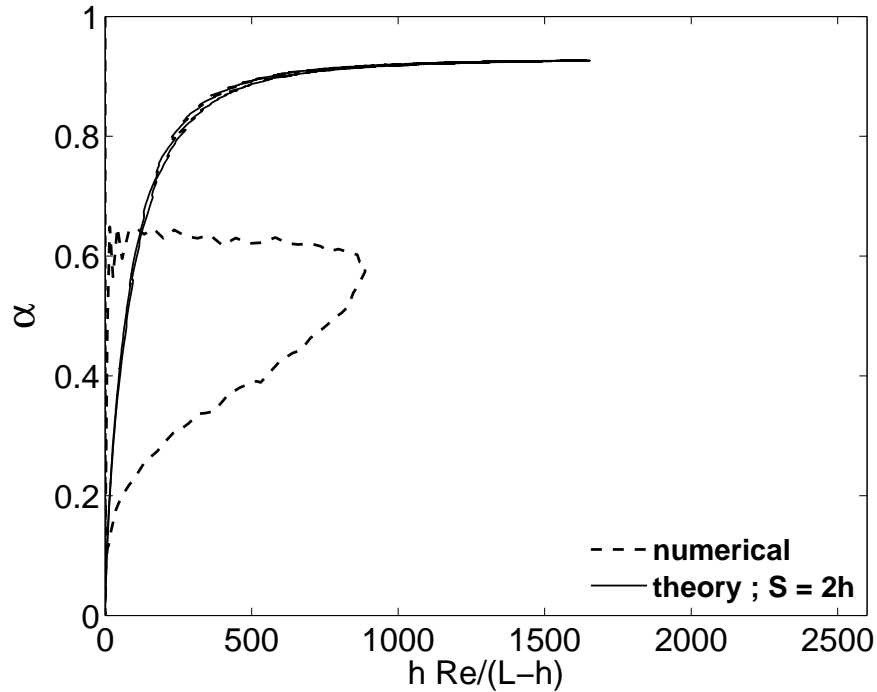


Figure 4.13 Vena contracta factor obtained for geometry 2 as a function of the modified Reynolds number

As expected, the numerical results for the vena contracta factor also diverge considerably from the theoretical predictions. Figures 4.12-4.14 depict the comparison between numerical and theoretical values for α along one duty cycle as a function of the modified Reynolds number proposed by van Zon *et al.*. The hysteresis observed for all cases in Figs. 4.12-4.14 agree qualitatively with those found in a dynamic flow measurement conducted by van Zon *et al.* (1990). The hysteresis observed in the short channel geometry (Fig. 4.12) is much smaller than that observed in the remaining cases (Fig. 4.13 and 4.14). This is probably due to a less significant influence of the flow driven by the reed U_{wall} as previously discussed. Furthermore, the flow adhesion segment is much shorter in the case of geometry 1, which minimizes the contribution shear dissipation on the

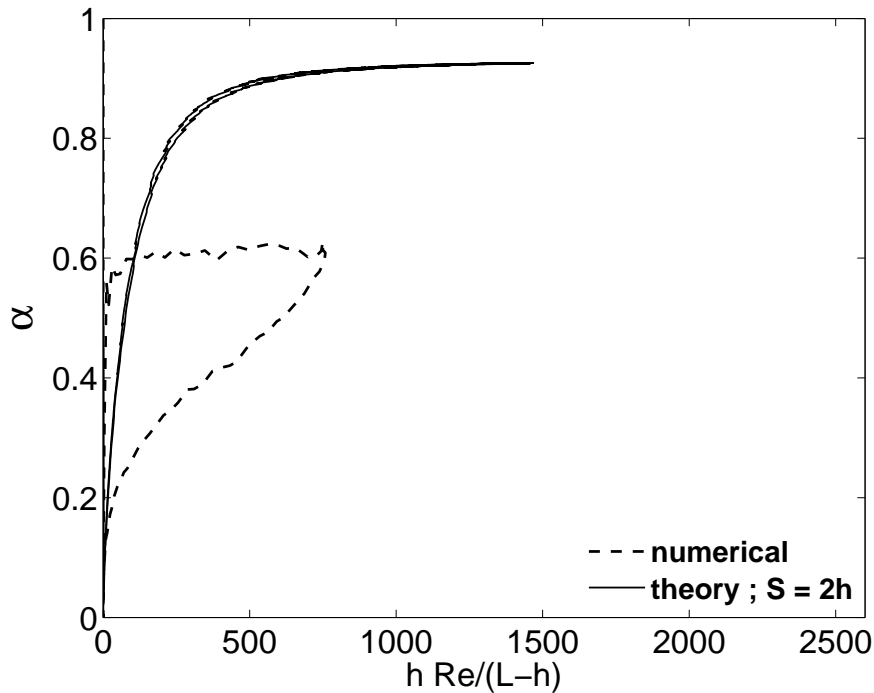


Figure 4.14 Vena contracta factor obtained for geometry 3 as a function of the modified Reynolds number

hysteresis. Figure 4.15 depicts the numerical values of α as a function of time in terms of fraction of a duty cycle. For the short channel, the values of α remain constant for only 35% of the duty cycle, namely $0.50T \leq t \leq 0.85T$. The values of α become very unstable as the reed approaches the closed position. As already discussed, this characteristic is attributed to the effect of U_{wall} which becomes higher than the flow driven by the pressure difference across the reed channel.

4.7 Discussion

This chapter presented a numerical technique based on the lattice Boltzmann and finite difference methods to represent the problem of fully coupled fluid-structure interaction

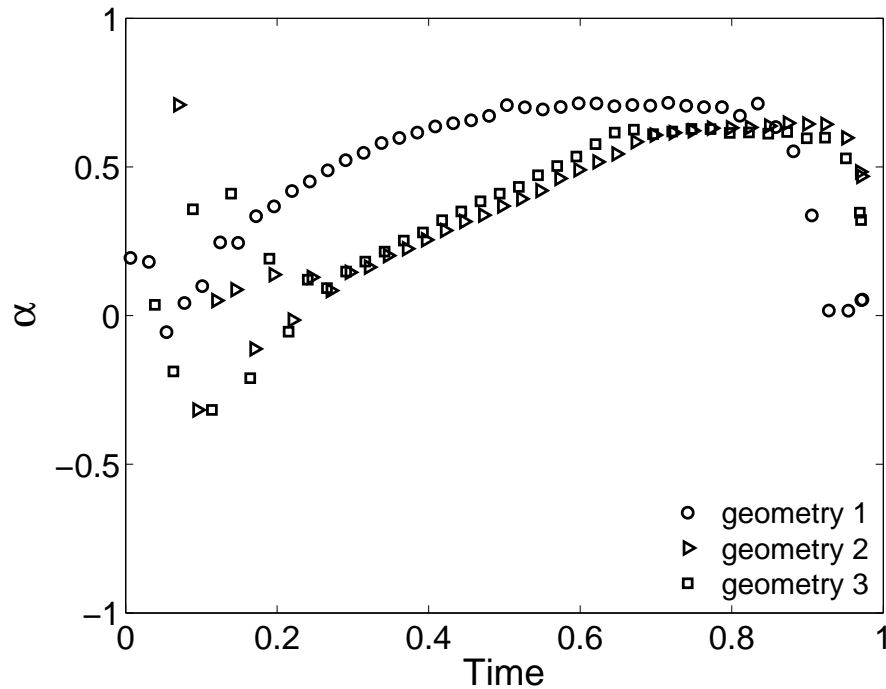


Figure 4.15 Numerical values for the vena contracta factor as a function of time for one duty cycle

in single reed mouthpieces. The model provides second-order accuracy at representing boundary layer phenomena and was used to evaluate the behavior of three different reed channel geometries in two types of regimes, namely, stationary and dynamic. The stationary results agree very well with those predicted by the quasi-stationary theory, in terms of volume flow and vena contracta factor. Furthermore, we observed the same behavior found experimentally by van Zon et al. (1990), associated with the steadiness of the vena contracta factor for different Reynolds numbers, in the case of short channels, and with the steadiness of the detachment / reattachment phenomenon in long channels.

However, the results obtained during the dynamic simulations are very different from those predicted by the quasi-stationary theory. For the short channel geometry α

was found to be constant for only $\simeq 40\%$ of the duty cycle and, for long channels, the values of α were in stark disagreement with the quasi-stationary predictions. Moreover, the patterns observed in stationary measurements such as fully detached flow, in the case of short reed channels, and the twofold pattern, in the case of long channels, were not observed in the dynamic simulations. The main difference in the flow behavior between short and long channels was found to be the time taken by the flow to adhere on the reed wall within one duty cycle. This characteristic was attributed to the effect of inertia associated with different fluid volumes within the reed channel and to the flow driven by the reed. The results also show that different levels of self-sustained oscillations can be achieved in the absence of acoustic feedback due to the complexity of hydrodynamic forces acting on the reed, which supports the hypothesis proposed by Hirschberg et al. (1990, 1994) in the case of single reed mouthpieces.

The two-dimensional nature of our numerical approach restricts the results to a qualitative analysis. Another limitation is associated with the lack of acoustic feedback, which neglects eventual influences of the fluid-acoustic interaction on the flow within the reed channel. Nevertheless, the numerical results presented here correspond to a situation that is much closer to normal playing than that provided by the quasi-stationary approximation and, therefore, contribute to our understanding of the behavior of dynamic flow in single-reed mouthpieces and its dependency on the characteristics of the reed channel geometry.

More investigations are needed to understand the behavior of the flow when the acoustic coupling between mouthpiece-reed system and resonator is taken into account. Another step could be taken in order to investigate the mechanisms of energy transfer between flow and the acoustic field, as well as the characterization of aeroacoustic sources in the mouthpiece and its contribution to the instrument's sound content.

Chapter 5

Numerical Study of the Acoustic Radiation From Pipes and Horns

5.1 Introduction

Much attention has been focused over the last century on the mechanisms of sound reflection at the open ends of waveguides. The characteristics of the reflection experienced by the sound wave as it approaches an open end is crucial in defining major features of the system's acoustic behavior, such as the resonance frequency and its capability of radiating sound. In the case of woodwind instrument models, the accurate representation of these acoustic reflections becomes paramount given that subtle variations of the resonant frequency, namely $\Delta F = O(-1)$, are perceptually important.

The reflection experienced by an acoustic wave at openings in a waveguide can be described in terms of a complex measure known as the reflection coefficient, given by

$$R = \frac{p^-}{p^+} = -|R| e^{i2kl} , \quad (5.1)$$

where $|R|$ is the ratio of the magnitudes of the reflected p^- and incident p^+ pressure waves, taking the open end as a reference plane. The phase term $2kl$ in Eq. (5.1) represents the inertia experienced by the acoustic flow provided by the presence of the surrounding fluid at the open end. In this case, the parameter l , known as the end correction, acts as an extension (or subtraction) of the waveguide length due to the inertia effect. A more intuitive way to interpret the end correction l is to assume that the pressure at the open end is always zero in the low-frequency limit. This condition implies that the reflection coefficient and its phase at the open end become -1 and π , respectively. Thus, the end correction can be understood as a supplementary length added or subtracted to the waveguide necessary to produce the phase $2kl = \pi$.

The behavior of the reflection coefficient will be strongly defined by the geometrical characteristics at the open end. Analytical predictions of R are intricate and usually derived based on several simplifications, from which the most common consists in replacing the sharp edge at the open end by a surrounding infinite flange. This unrealistic boundary condition can be useful in the low frequency limit ($ka \ll 1$) for estimating $|R|$, as discussed by Blechert (1980) and Peters et al. (1993) and for estimating the acoustic field within the hemisphere beyond the open end but becomes rather inaccurate for the prediction of backward radiation and the correct value of the end correction l , as demonstrated experimentally by Tyler and Sofrin (1962). This is due to the fact that the infinite flange approach neglects the influence of diffraction effects that take place at the sharp edge of a realistic open end.

Several analytical predictions for the magnitude $|R|$ of the reflection coefficient, as well as for the end correction l , have been proposed over the years for plane wave propagation using a linear approach, i.e., when the ratio between the magnitude of the particle velocity and the speed of sound $u'/c_0 \ll 1$ and the acoustic Strouhal number

$Sr = \omega a / u' \gg 1$, where a is the pipe radius. Rayleigh (1877) found $l \simeq 0.6a$ for an unflanged cylinder in the low-frequency limit ($ka \ll 1$, where $k = \omega / c_0$ is the wavenumber.). Many years later, King (1936) presented the exact solution for l of a flanged cylinder. At low frequencies he found $l = 0.82a$. Levine and Schwinger (1948) were the first to obtain an exact solution for l of an unflanged cylinder by using the Wiener-Hopf technique. In the low frequency limit, they found $l = 0.6133a$. Furthermore, they also presented exact expressions for R and for the far-field acoustic pressure directivity G_ϕ around the cylinder's open end, both as functions of the characteristic parameter ka , known as the Helmholtz number.

Nevertheless, predicting R and G_ϕ with an analytical approach becomes increasingly difficult as one considers waveguides with complex geometric termination (e. g., horns with different profiles, nozzles, toneholes, chamfered exhausts, diffusers, tailpipes, etc), the presence of a mean flow and nonlinearities at high acoustic amplitudes ($Sr \ll 1$) due to viscous effects and the interaction between the flow and the acoustic field.

The presence of a mean flow $\bar{\mathbf{u}}_o$ may represent a significant change in the behavior of the reflection coefficient components $|R|$ and l , even for low Mach numbers, $M = O(-1)$, where $M = \bar{\mathbf{u}}_o / c_0$. The overbar indicates the average of the mean flow velocity \mathbf{u}_o over the waveguide's cross section. In the case of $|R|$, a mean flow may act to amplify the reflected acoustic wave, so that $|R|$ becomes greater than one for critical regions of ka . Likewise, the presence of a mean flow drastically reduces the end correction l , particularly in the low-frequency limit.

The first solution for the magnitude of the reflection coefficient in the presence of a mean flow at the open end of a thin unflanged pipe was proposed by Munt (1990). The solution is exact for the limits of $0 < ka \leq 1.5$ and $0 < M \leq 0.5$ and provided that the acoustic boundary layer is large compared to the boundary layer of the flow at the open

end.

Approximate solutions for $|R|$ taking into account the influence of a low Mach number mean flow have been presented by Cargill (1982a,b) and Rienstra (1984). Approximate solutions for the dimensionless end correction l/a have also been proposed by Cargill (1982a,b), Rienstra (1984) and Howe (1976), where a is the radius of the pipe. The last study also provided an analysis of the influence of \bar{u}_o at high Strouhal numbers based on the mean flow ($Sr_0 = ka/M$). Generally, their predictions are in agreement that for high Sr_0 , the end correction approximates that found by Levine and Schwinger (1948) for a quiescent fluid, whereas, for $Sr_0 \rightarrow 0$, $l/a = 0.2554a$ (Rienstra, 1984). These predictions agree fairly well with the experimental data provided by Peters et al. (1993) who found $l/a = 0.19a$.

Nonlinearities due to the unsteady separation of the acoustic flow at the open end may play a significant role in the behavior of R even when the mean flow velocity \bar{u}_o is null. In this case, the amplitude of the acoustic particle velocity u' seems to be a preponderant factor on the reflection coefficient behavior and can be expressed in terms of the acoustic Strouhal number Sr . As discussed by Hirschberg et al. (1996), the flow unsteadiness in a quiescent fluid acts mainly to absorb sound by transferring acoustic energy into vortical movement of the flow. For high amplitudes of the particle velocity ($Sr \ll 1$), the produced vortex detaches and propagates away from the open end, whereas, for low acoustic amplitudes ($Sr \gg 1$) the produced vortex due to acoustic flow detachment remains in the vicinity of the open end. Peters et al. (1993) have experimentally observed that, although sound absorption is dominant for most regions of the acoustic Strouhal number, generation of sound can take place when $Sr = O(1)$ for unflanged pipes with finite wall thickness τ_w . In such a case, the displacement of the vortex during one duty cycle is equivalent to the wall thickness τ_w . Peters et al. (1993) point

out that this characteristic may be associated with the phenomenon of pipe tones found in the toneholes of wind instruments. A similar behavior takes place in the open end of horns when a mean flow is present.

The nonlinearities in a quiescent flow have been studied for different types of open end terminations. Cummings and Eversman (1983) and Blechert (1980) have investigated the cases where the opening ends into a nozzle. Similar phenomena have been studied in the case of waveguides terminated in a flat plate with an orifice by Ingard and Labate (1950), Ingard (1967) and by Cummings (1984, 1986). In the case of open ends of unflanged pipes, Disselhorst and Wijngaarden (1980) have provided expressions for the acoustic losses at open ends with different finishing profiles (sharp and rounded edges) at low and high acoustic amplitudes. In their model, the power losses for $Sr \gg 1$ were described in terms of a two-dimensional potential flow using discrete point vortices, whereas the power losses for $Sr \ll 1$ are described in terms of a quasi-steady approach in which a jet formation is assumed to take place during the positive part of the oscillation cycle. During the negative part, a vena contracta is assumed with a turbulent recovery region.

Peters and Hirschberg (1993) have found a similar expression for $Sr \gg 1$, by means of combining a single point vortex with a vortex segment detached from the pipe's edge. Experimental investigations conducted by Peters et al. (1993) have shown that the model derived by Disselhorst and Wijngaarden underestimates the energy absorption by a factor of 2.5 when compared to the model derived by Peters and Hirschberg (1993). This disagreement is attributed to the translation from the two-dimensional flow theory, on which Disselhorst and Wijngaarden's model is based, to a three-dimensional situation. The nonlinearities at the open end of unflanged pipes and the influence of the edge's curvature in a quiescent flow have also been investigated experimentally by Atig et al.

(2004). Interestingly, they confirmed experimentally that the smaller the radius of the rim at the open end, the lower the threshold of particle velocity amplitude in which the contribution of nonlinear losses becomes relevant. In other words, smooth edges reduce nonlinearities at low acoustic Strouhal number, which results in a lower saturation effect (lower acoustic absorption) and, consequently, an instrument with a higher dynamic range. These results confirm the hypothesis discussed by Benade (1976) and explain the necessity of rounding the edges at wind instrument discontinuities.

The goal of the present chapter is twofold. The first objective is to construct an axisymmetric lattice Boltzmann model and to verify its capability of representing the aforementioned phenomena associated with the behavior of $|R|$ and l for different flow and boundary conditions. The second objective is to use the verified model to conduct further investigations of the same phenomena for situations that have not yet been addressed and for which analytical models are not available, such as the reflection coefficient of pipes terminated by horns with different shapes carrying a subsonic mean flow as found in woodwind instruments.

This chapter is organized as follows: Section 5.2 describes the development of a LBM axisymmetric model of an open unflanged pipe for the prediction of the reflection coefficient R and the directivity factor G_ϕ in a quiescent flow situation. The obtained results are compared with those provided by the analytical solution of Levine and Schwinger (1948). Section 5.3 follows a similar rationale. In this case, however, the numeric model takes into account the presence of an outgoing subsonic mean flow and the numerical predictions are compared with the theory provided by Munt (1990) and with the experimental results provided by Allam and Åbom (2006). Section 5.4 predicts the reflection coefficient in pipes terminated by horns with different shapes carrying a zero mean flow. The validity of the results are compared with results obtained for the same geometries

using the boundary element method. The analysis conducted in Sec. 5.5 provides an investigation of the reflection phenomena in the same geometries studied in Sec. 5.4, taking into account the influence of a subsonic mean flow. The mechanism of energy transfer between the acoustic field and the flow is also discussed. For the last model, the validity of the results is substantiated by the good agreement provided by the comparisons presented in Secs. 5.2, 5.3 and 5.4. Finally, Sec. 5.6 presents a discussion of the effects of the mean flow taking into account the physical characteristics and dynamic peculiarities of wind instruments. Moreover, the general conclusions of the chapter are presented.

5.2 Acoustic Transmission of an Unflanged Pipe with Zero Mean Flow

This section addresses the linear phenomena associated with the reflection and radiation of plane sound waves from a cylindrical unflanged pipe immersed in a quiescent fluid and carrying a zero mean flow.

In such a situation, when the internal outgoing wave reaches the open end, part of its energy is radiated to the external space and the remainder is reflected back into the pipe. The incoming wave preserves the same modal characteristics of the outgoing wave, whereas the radiated wave becomes spherical. When the Helmholtz number $ka \rightarrow 0$, $ka = \omega a/c_0$, the velocity potential found within the cylinder at higher frequencies is maintained constant by increasing the cylinder's nominal length by a fraction of its open-end radius. For the specific case of a cylinder conveying a zero mean flow, the maximum reflection $|R| = 1$ is obtained as $ka \rightarrow 0$.

The effect of wall thickness may be significant in certain circumstances. In the low frequency limit ($ka \ll 1$), the correction derived by Ando (1969) implies that the behavior

of $|R|$ is unaffected for cylinders with a certain wall thickness, as long as $a_o/a < 1.1$, where a_o is the outer radius of the pipe. Conversely, the dimensionless end correction l/a is considerably affected as $a_o/a \rightarrow 1.1$ at regions of $ka > 0.5$. For large values of the wall thickness, namely $a_o/a > 2$, both $|R|$ and l/a approach the values found for a cylinder with an infinite flange at the open end. These conclusions have been experimentally verified in (Ando, 1968).

The directivity factor G_ϕ is symmetric about a waveguide's axis if the waveguide is also symmetric about the same line. Thus, in the case of a straight cylinder, G_ϕ is described by a single angle $\phi(x, r)$ measured from the cylinder's axis at a distance d away from its open end.

Our goal now is to determine the end correction l , the amplitude and phase of the reflected wave, represented by the reflection coefficient R , and the directivity factor G_ϕ from a straight cylinder. We then compare the results with those provided by Levine and Schwinger (1948) for inviscid normal mode propagation.

5.2.1 Analytical Approach

The analytical expressions presented below have been obtained by Levine and Schwinger (1948) for a cylinder with negligible wall thickness by the application of the Wiener-Hopf technique and are correct provided that only dominant mode propagation takes place in the pipe. This requires the value of the maximum frequency of analysis to be lower than the cut-off frequency for plane waves. In the case of cylinders, the cut-off frequency for dominant modes can be expressed in terms of the characteristic parameter ka and is determined by the first zero of the derivative of a first-order Bessel function of the first type. In this case $ka = 3.82$.

By choosing the end of the pipe as the reference plane, the complex reflection coeffi-

cient in terms of velocity potential for the dominant mode is given by

$$R = \exp \left[\frac{2ka}{\pi} \int_0^{ka} \frac{\tan^{-1}(-J_1(x)/N_1(x))}{x[(ka)^2 - x^2]^{1/2}} dx - 2ikl. \right] \quad (5.2)$$

Here and in the following J_1 and N_1 are Bessel and Neumann functions of the first order and first type, respectively. The end correction, in units of the pipe radius, is given as

$$\frac{l}{a} = \frac{1}{\pi} \int_0^{ka} \left[\frac{\log[\pi J_1(x)[(J_1(x))^2/N_1(x)]^{1/2}]}{x[(ka)^2 - x^2]^{1/2}} \right] dx + \frac{1}{\pi} \int_0^{\infty} \left[\frac{\log[1/(2I_1(x)K_1(x))]}{x[x^2 + (ka)^2]^{1/2}} \right] dx, \quad (5.3)$$

where I_1 and K_1 are both first order modified Bessel functions of first and second kind, respectively.

The normalized far-field directivity factor obtained by the Wiener-Hopf technique is given by

$$G_\phi = 2 \left(\frac{2ka}{\pi} \right)^{1/2} \frac{J_1(ka \sin \phi)}{\sin \phi (1 + \cos \phi)^{1/2}} \frac{|R|}{1 - |R|^2} \times \dots$$

$$\dots \times \exp \left[ka \cos \phi - \frac{1}{\pi} \int_0^{\infty} \frac{\tan^{-1}(K_1(x)/\pi I_1(x))}{(x^2 + (ka)^2)^{1/2} + ka \cos \phi} \frac{xdx}{(x^2 + (ka)^2)^{1/2}} \right]. \quad (5.4)$$

The integrals in Eqs. (5.2), (5.3) and (5.4) are evaluated numerically using the adaptive Lobatto quadrature method. The infinity upper limits found on the integrals of Eqs. (5.2) and (5.3) are truncated at a value equal to 100, although the integrals converge for upper limits much smaller than this.

5.2.2 Numerical Procedures

The computational model is represented by a closed-open cylinder inserted in a fluid domain surrounded by open boundaries as illustrated in Fig. 5.1. The model uses an

axisymmetric scheme based on a square $D2Q9$ structure as described in Sec. 3.3.2. In this case, the source term h_i of the axisymmetric scheme (see Eq. 3.22) is resolved by using the approach proposed by Lee et al. (2005). The square grid is defined with 1000 lattices along each axis. The walls of the cylinder, as well as its closed end, are represented with dry lattices of thickness $\tau_w = 1$. The cylinder has the length $L = 500$ and radius $a = 10$. Here and in the following, the dimensions are expressed in terms of lattice cells.

As previously mentioned, the Levine and Schwinger (1948) results are based on inviscid wave propagation and an infinitely small wall thickness. Thus, our lattice Boltzmann model must accommodate these restrictions in order for the comparison of results to be valid. In this sense, the first restriction is met by choosing a specular free-slip boundary condition (Succi, 2001) to avoid transfer of momentum by the tangential motion of particles along the walls and thus force the effect of the acoustic boundary layer to be negligible. Furthermore, we choose the viscosity $\nu = 9.5 \times 10^{-4}$ which corresponds to a trade-off between a negligible viscosity and the smallest value supported by the LBGK scheme before being affected by numerical instabilities¹. The second restriction is overcome by adopting the modified version of Eq. 5.3 for cylinders with finite wall thickness, as proposed by Ando (1968). In this case, the value of a is replaced by the value of the outer radius a_o , so that $a_o = a + \tau_w$.

As a matter of convenience, we use an undisturbed fluid density $\rho_0 = 1$. A density perturbation $\rho' = 0.001$ was applied at the closed end of the cylinder in order to excite the system from its rest state (see Fig. 5.1). The perturbation was implemented in the form of a Hanning impulse, so that $\rho = \rho_0 + \rho'[0.5 + 0.5 \cos(\frac{2\pi x}{N} + \pi)]$ and $\mathbf{u}_x = \frac{\rho' c_0}{\rho_0} [0.5 + 0.5 \cos(\frac{2\pi x}{N} + \pi)]$, where $N = 10$ was the width of the impulse. The use of a

¹Numerical instabilities associated with small viscosities in the LBGK scheme result in high frequency noise and are caused by the use of a single relaxation time τ for the entire set of discrete velocities representing the collision function in Eq. (3.15), as described in Lallemand and Luo (2000).

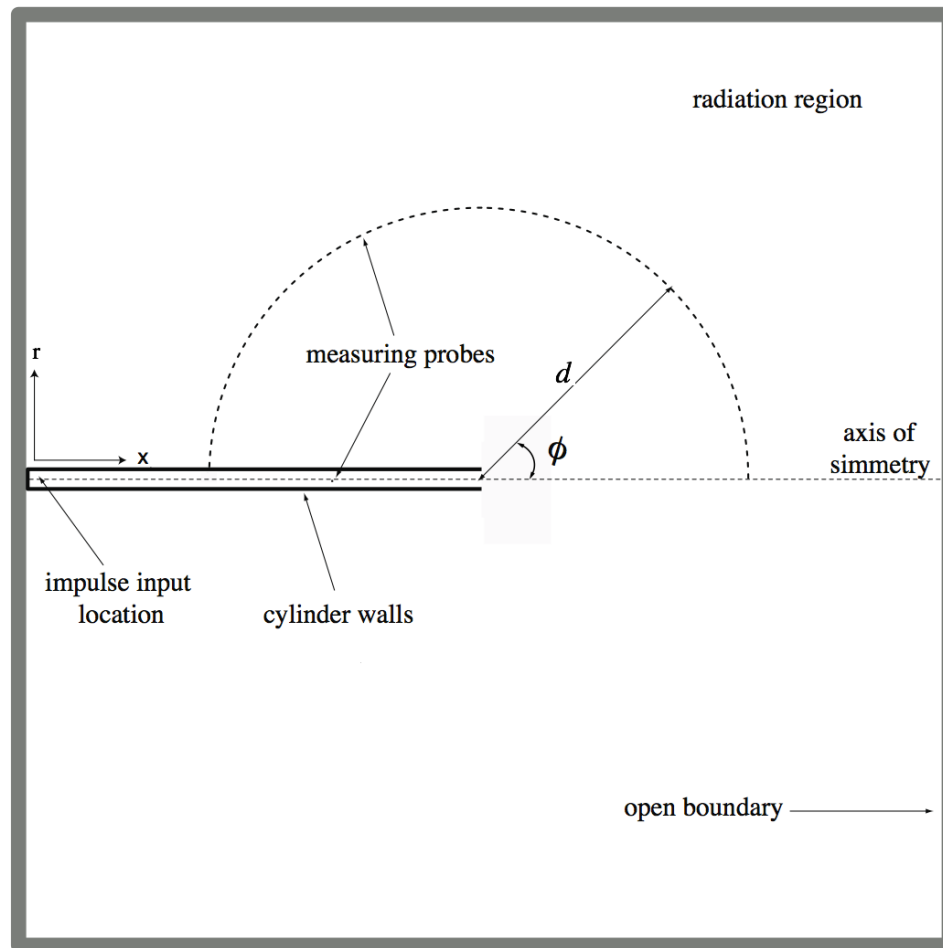


Figure 5.1 Scheme of the axisymmetric lattice Boltzmann model of a radiating unflanged pipe.

smooth impulse is necessary to minimize the production of high frequency noise associated with the LBGK scheme, as previously mentioned. The magnitude of the impulse is chosen to be sufficiently small to guarantee linear wave propagation. The disturbance propagates as a wavefront throughout the cylinder until the open end where it is partially reflected and partially radiated to the outer domain in terms of spherical waves with axisymmetric characteristics. Figure 5.2 depicts different time steps of the lattice Boltzmann simulation.

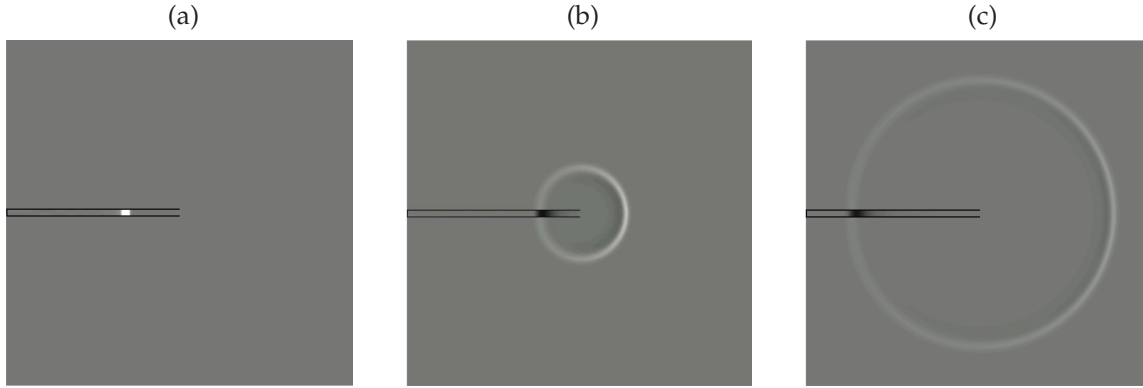


Figure 5.2 Snapshots from the LB simulation of the radiating cylinder. The figures represent the propagation and radiation of the input perturbation in terms of pressure for different time steps: (a) $t = 600$, (b) $t = 1093$, and (c) $t = 1537$.

5.2.3 Results for the Magnitude of the Reflection Coefficient

The complex reflection coefficient for plane waves at any point x inside the cylinder is given by

$$R(x, \omega) = Z_0 \left(\frac{Z(x, \omega)/Z_0 - 1}{Z(x, \omega)/Z_0 + 1} \right), \quad (5.5)$$

where ω is the angular frequency, $Z(x, \omega)$ is the acoustic impedance, defined as the ratio between the acoustic pressure $P(x, \omega)$ and the volume velocity $\mathbf{U}_x(x, \omega)$ and Z_0 is the characteristic impedance of a cylinder. When the acoustic dissipation is negligible and the mean flow is zero, Z_0 is a constant given by $\rho_0 c_0 / A$, where A is the cylinder's cross-section area.

$P(x, \omega)$ and $\mathbf{U}_x(x, \omega)$ are obtained by performing a discrete Fourier transform (DFT) of the time histories associated with the lattice pressure $p(x, t)$ and the lattice velocity $\mathbf{u}_x(\mathbf{x}, t)$ after the system has been excited by the impulse at time $t = 0$. However, p and \mathbf{u}_x cannot be directly measured at the open end of the pipe due to the fact that the

wavefront becomes distorted as it approaches the output and thus, Eq. 5.5 is no longer valid. In order to guarantee a plane wavefront, the values of p and \mathbf{u}_x are measured inside the pipe at $x = -\Delta$ before the pipe opening, where $\Delta = 2a_o$. Dalmont et al. (2001) present an expression for the determination of the complex reflection coefficient $R(\omega)$ at the end of the cylinder based on the acoustic impedance $Z_\Delta(\omega)$ measured inside the cylinder at a distance $-\Delta$ from its open end, given by

$$R(\omega) = \frac{j \tan[\arctan(Z_\Delta(\omega)/jZ_0) - k\Delta] - 1}{j \tan[\arctan(Z_\Delta(\omega)/jZ_0) - k\Delta] + 1}. \quad (5.6)$$

In order to correctly evaluate R , the impedance Z_Δ is determined from the values of p and \mathbf{u}_x representing the time history of one round trip of the input perturbation from the measuring point inside the cylinder to its open end. Figure 5.3 depicts the comparisons between theory and numerical results for the magnitude of the reflection coefficient $|R|$ as a function of the characteristic parameter ka .

The general trend found on the numerical result of the magnitude of the reflection function, R , shows that the fraction of reflected energy at the open end is usually higher than that predicted by the theory (Fig. 5.3). The highest discrepancy between theoretical and numerical results is seen at the region around $ka = 1.5$ where numerical values are higher by $\sim 8\%$.

The discordance between results was expected and is likely to be due to energy leakage caused by the truncation of the time history associated with p and \mathbf{u}_x prior to the application of the discrete Fourier transform to derive Z_Δ in Eq. (5.6). The truncation acts as if the resulting spectra of p and \mathbf{u}_x were obtained by the convolution in frequency of their non-truncated spectra with the spectrum of a rectangular window having the same duration as p and \mathbf{u}_x and magnitude equal to one (Oppenheim and Shafer, 1999). We

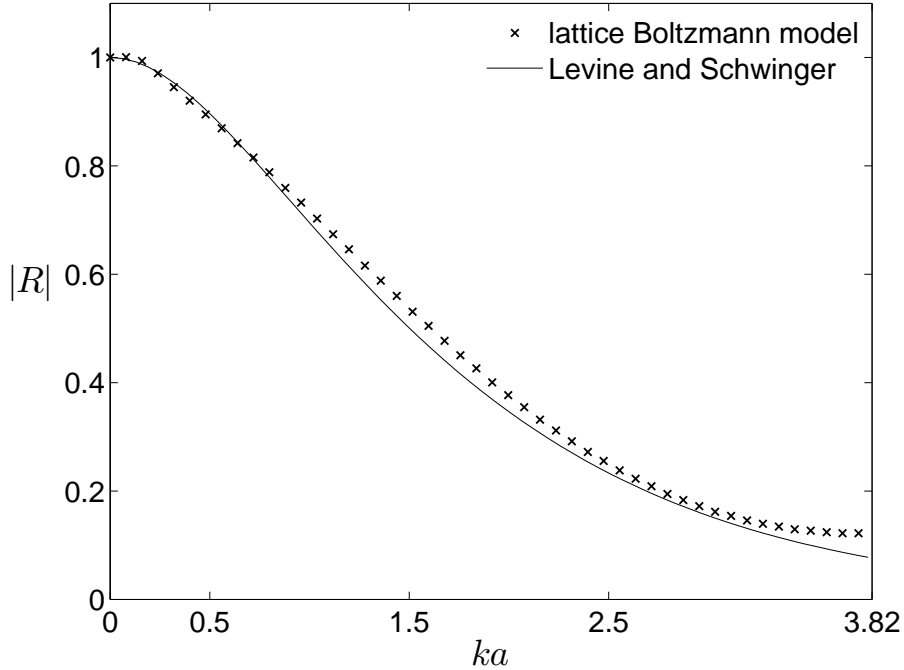


Figure 5.3 Magnitude value of the complex reflection coefficient at the end of the cylinder as a function of the Helmholtz number ka

could minimize the effect of truncation by increasing the size of the time histories of p and \mathbf{u}_x . However, the open boundary used in this model (see Fig. 5.1) was not perfectly anechoic². Therefore, reflections from that region would return back to the measuring points and, consequently, compromise the simulation.

5.2.4 Results for the Dimensionless End Correction

The end correction l is easily obtained from the complex reflection coefficient (Eq. 5.6) by the following relation

$$l = \frac{1}{2jk} \ln \left(\frac{R}{|R|} \right). \quad (5.7)$$

²At this point of the dissertation a solution for perfectly anechoic boundaries had not yet been achieved.

Figure 5.4 depicts the comparison between theory and numerical results for the dimensionless end correction, l/a as functions of the characteristic parameter ka . Cur-

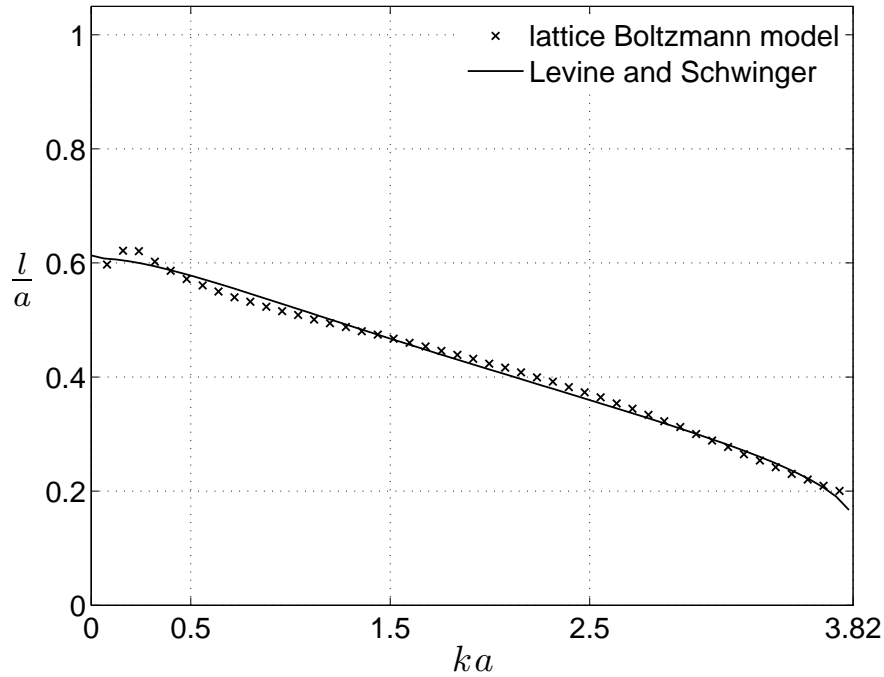


Figure 5.4 Dimensionless end correction, l/a , as a function of the Helmholtz number ka .

ously, the numerical result from the end correction provides a better agreement with the theory than that found for the magnitude of the reflection coefficient. Normally, l/a is much more sensitive to small geometric details than $|R|$, whose behavior is quite robust in terms of small-scale geometric characteristics (Hirschberg, 2007).

The greatest disagreement is found in the low frequency region (small values of ka) where the numerical result is $\sim 4\%$ higher than the analytical prediction. As the case of the magnitude of the reflection coefficient, the disagreement is attributed to the energy leakage caused by the truncation of the time history associated with p and \mathbf{u}_x prior to the application of the discrete Fourier transform, as discussed in the previous section.

5.2.5 Results for the directivity Factor G_ϕ

We now present the results obtained for the radiation directivity G_ϕ , measured from the axis of the pipe. The definition of G_ϕ is given by

$$G_\phi = \frac{P_\phi^2}{P_h^2}, \quad (5.8)$$

where P_ϕ^2 is the mean-square sound pressure at angle ϕ and distance d from a directional acoustic source of a certain acoustic power, whereas P_h^2 is the mean-square sound pressure from an omnidirectional source of equal acoustic power, measured at the same distance.

In our simulation we evaluate P_ϕ by performing a DFT on the values of p_ϕ measured at 85 different angles from the axis of the cylinder between $\phi = 0^\circ$ and $\phi = 170^\circ$. For reasons of computational economy, we restricted our analysis to a fixed distance $d = 250$ from the cylinder's open end. P_h is evaluated from the averaged value of P_ϕ^2 along the angles.

Figure 5.5 presents the results for the directivity factor G_ϕ . A poor agreement between analytical and numerical results can be seen for small values of ka , particularly when $ka < 1$, as depicted in Fig. 5.5(a) and 5.5(b). Conversely, the agreement increases as $ka \rightarrow 3.82$. This trend is explained by the fact that G_ϕ can only be measured in a far-field region whose minimum distance is inversely proportional to the frequency of the acoustic source. The far-field condition is satisfied when the acoustic impedance Z of the diverging spherical wave approximates that of a plane wave, *i.e.*, $Z \rightarrow \rho_0 c_0$ and $\varphi \rightarrow 0$, where φ is the phase between acoustic pressure and particle velocity. Figures 5.6 and 5.7 present the plots of Z and φ as functions of ka , obtained from the LBM model at a distance $d = 250$ and angle $\phi = 0$. From these figures, it is clear that the farfield

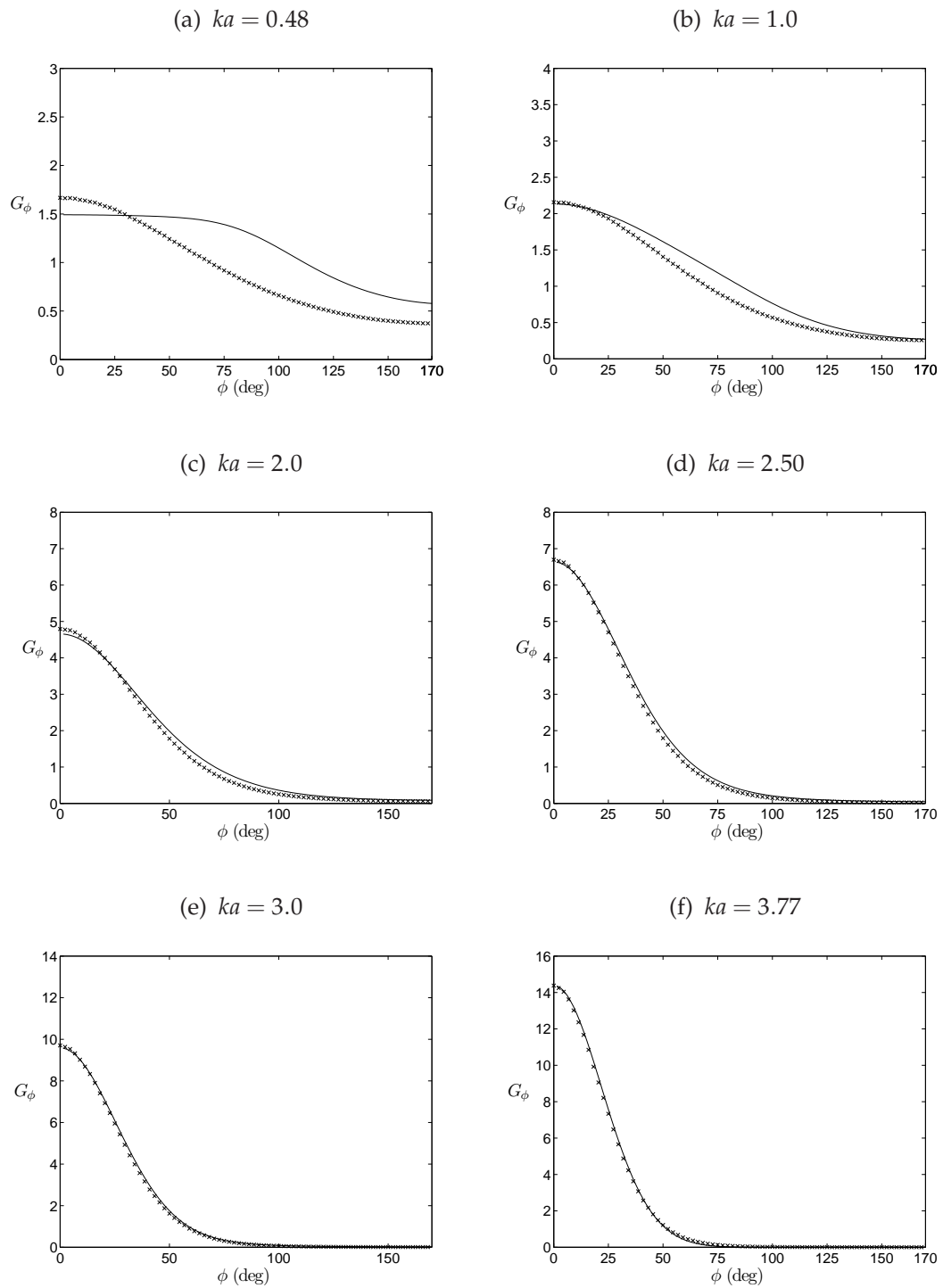


Figure 5.5 Directivity factor G_ϕ as a function of the angle ϕ measured from the axis of the cylinder for different values of ka . The crossed points represent the numerical results and the solid line represents the analytical.

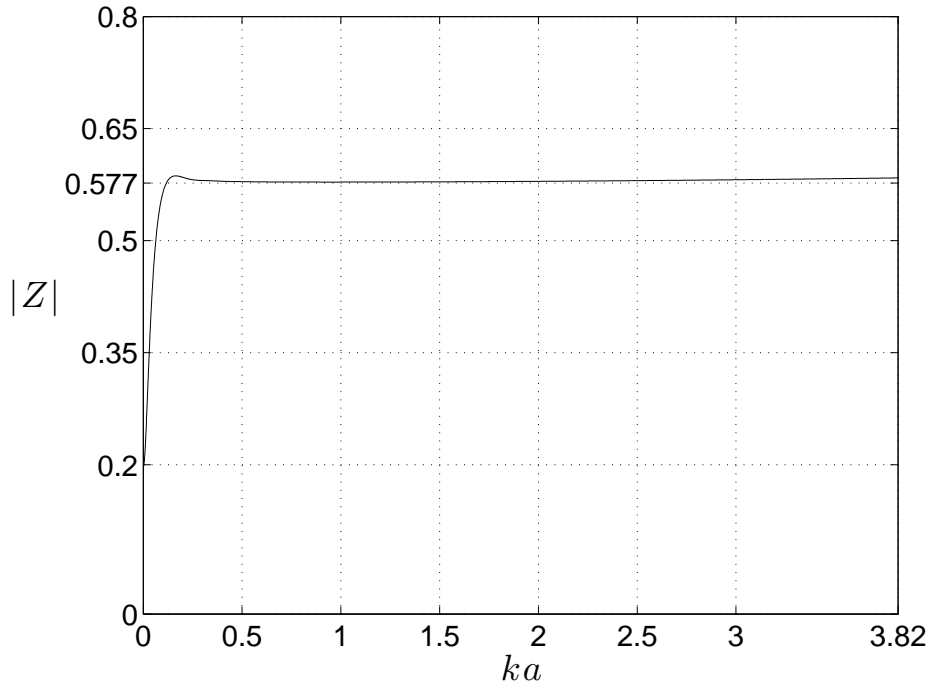


Figure 5.6 Radiation impedance as a function of the Helmholtz number ka for a distance $d = 250$ away from the pipe's mouth and $\phi = 0^\circ$

condition is only met for values of $ka > 1.5$, which explains the discrepancy between theoretical and numerical results for the directivity factor G_ϕ , particularly for values of $ka < 1$, as shown in Fig. 5.5(a) and 5.5(b).

The graphics depicted in Fig. 5.7 show that, although the impedance Z converges rapidly to $\rho_0 c_0$ for small values of ka (Fig. 5.6), the phase between acoustic pressure and particle velocity, φ , only approximates zero for values of $ka > 2$. One should notice that, in the case of the D2Q9 lattice scheme used in this simulation $c_0 = 1/\sqrt{3}$, as previously explained.

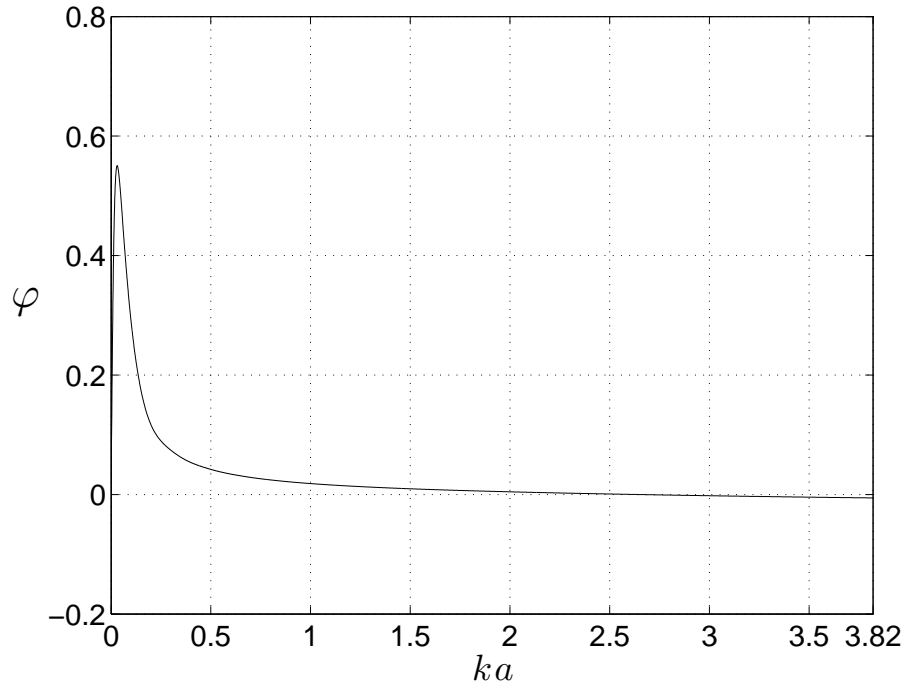


Figure 5.7 Phase between acoustic pressure and particle velocity as a function of the Helmholtz number ka for a distance $d = 250$ away from the pipe's mouth and $\phi = 0^\circ$

5.2.6 Discussion

The results provided in this section demonstrate that the axisymmetric lattice Boltzmann model can be used to accurately represent the parameters associated with the normal mode radiation of an unflanged pipe in the absence of a mean flow. In general, the results for the magnitude of the reflection coefficient $|R|$ agree very well with the theory, particularly in the low frequency limit.

Conversely, a slight discrepancy from the theory is observed in the same region for the results of the dimensionless end correction l/a , which is attributed to the finite wall thickness used during the simulation. The sensitivity of l/a to small geometric modifications agrees with the experimental results provided by Ando (1968) and Peters et al.

(1993). Moreover, the results suggest that a large radiation domain is necessary for the fulfillment of the far-field condition in order to provide an accurate prediction of the directivity factor G_ϕ .

5.3 Transmission Properties of an Unflanged Pipe Carrying a Subsonic Mean Flow

The correct prediction of the reflection and radiation behavior of sound waves as they approach the open end of pipes carrying a mean flow is a long-established problem in acoustics. The variables associated with the open-end reflection are paramount in estimating the proportion of radiated sound and the resonance frequencies of exhaust systems such as those found in aeroengines, tailpipes, nozzles and also woodwind instruments.

Early theoretical approximations of wave reflection at the open end of pipes carrying a mean flow have been derived by Carrier (1956), who formulated the problem by assuming a uniform (plug) flow, and by Many (1973) and Savkar (1975) who derived approximate theories based on the flow mismatch between the jet formed at the outlet and the fluid surrounding the open end.

The first exact solution was presented in terms of integral equations by Munt (1977) for the far-field radiation of an unflanged pipe carrying a uniform subsonic mean flow. This solution was based on the use of the Wiener-Hopf technique and represented the continuation of the theory derived by Levine and Schwinger (1948) for the quiescent flow situation.

Based on this work Howe (1976), Cargill (1982a, 1982b) and Rienstra (1983) derived approximations in the form of explicit solutions. Howe's model predicted the values of

5.3 Transmission Properties of an Unflanged Pipe Carrying a Subsonic Mean Flow 123

$|R|$ and l/a for the limit of low Mach and low Helmholtz numbers. According to this model, when $ka \rightarrow 0$ the values of l/a would converge to a superposition of the end correction values found in the quiescent flow case plus an additional end correction due to the presence of the mean flow. According to this rationale, the mean flow would act to enlarge the value of l/a when compared to a quiescent flow situation. Moreover, Howe predicted that the magnitude of the reflection coefficient continuously increases toward one as $ka \rightarrow 0$.

These predictions diverge significantly from those provided by Cargill (1982a, 1982b) and Rienstra (1983). In the first case (Cargill, 1982a), the model assumes both Kutta/no-Kutta conditions³ at the rim of the open end and predicts that $|R| \rightarrow 1$ as $ka \rightarrow 0$. Later, Cargill (1982b) predicted that $|R|$ may assume values higher than one at $Sr_0 \approx \pi$, which agreed with previous experimental investigations (Mechel et al., 1965, Ronneberger, 1967). The predictions of the length correction l/a found by Howe also diverge significantly from the low ka predictions derived by Rienstra (1983), who found that $l/a \rightarrow 0.2554\sqrt{1 - M^2}$ as $ka \rightarrow 0$. These results have been confirmed by posterior experiments conducted by Davies (1987) and Peters et al. (1993).

The exact solution for the magnitude of the reflection coefficient at the open end of thin-walled pipes in a subsonic mean flow was presented by Munt (1990). The major characteristic of this solution is the assumption of uniform (plug) flow and a full Kutta condition at the edges of the open end to provide values of $ka \leq 1.5$ and $M < 0.3$. This solution agrees with the approximate theory derived by Cargill (1982a, 1982b) and Rien-

³The Kutta condition, also known as the *Kutta-Joukowski* hypothesis, allows for the solution of problems of inviscid flows by imposing an artificial viscous effect at sharp edges, which acts to restrict the pressure and the velocity to finite values and, for this reason, provides singular solutions for the inviscid equations of mass and momentum conservation. In the case of a jet pipe, this assumption implies that outgoing acoustic energy can be transferred into kinetic energy in the jet vortex sheet. A rich discussion of the use of the Kutta condition in aeroacoustic problems is provided by Crighton (1985)

stra (1983) and has been substantiated experimentally by Peters et al. (1993) using the two-microphone method for $ka < 0.3$ and $M < 0.2$. Very recently Allam and Åbom (2006) have provided a full experimental verification for the entire extension of Munt's model, using the full wave decomposition method. For this reason, the theory provided by Munt, as well as the experimental results provided by Allam and Åbom (2006) will serve as benchmarks to verify the axisymmetric LBM model of a radiating unflanged pipe carrying a subsonic mean flow.

5.3.1 Analytic solutions

The model derived by Munt (1990) predicts the acoustic wave reflections at the open end of circular pipes with rigid thin walls issuing a mean flow with cross section averaged velocity $\bar{\mathbf{u}}_o$. Moreover, the model takes into account the presence of an external mainstream flow with velocity u_{out} in the same direction of $\bar{\mathbf{u}}_o$, where the ratio between the outer and the inner flow velocities η is restricted to $\eta \leq 1$. It is assumed that the outgoing mean flow forms a jet at the pipe's outlet, which is separated from the ambient fluid by an infinitely thin vortex sheet. The properties of the fluid inside the jet are described in terms of the density ρ_j , the speed of sound c_j and the fluid velocity $Mc_j = \bar{\mathbf{u}}_o$. Likewise, the properties of the ambient fluid outside the thin shear layer are described by the fluid density $\gamma\rho_j$, the speed of sound c_j/C and the fluid speed $M\eta c_j$, where the non-dimensional parameters γ and C are the ratios between the outer and inner jet parameters for fluid density and speed of sound, respectively.

The solution derived by Munt is expressed in terms of integral equations that have been numerically resolved by Bierkens (2002), who only considered the calculations of the magnitude of the plane wave reflection coefficient, and by in 't Panhuis (2003), who also provided plane wave and higher mode calculations for the phase of the reflection

5.3 Transmission Properties of an Unflanged Pipe Carrying a Subsonic Mean Flow 125

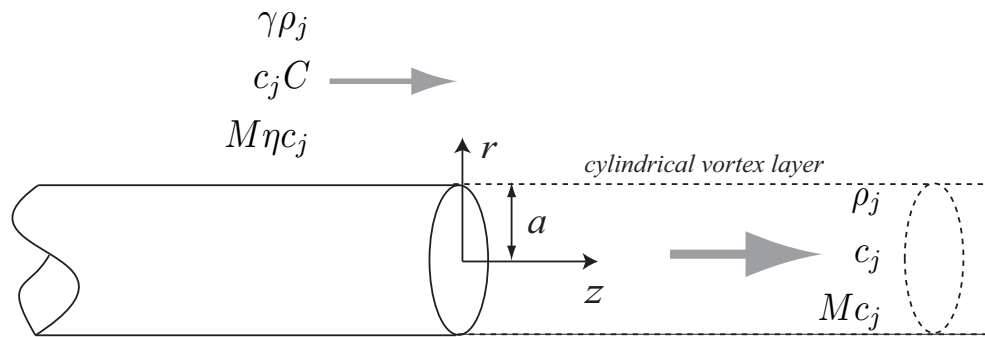


Figure 5.8 Schematics of the model proposed by Munt (1990).

coefficient and the end correction. These numerical calculations of Munt's solution have been recently verified experimentally by Allam and Åbom (2006) using the full wave decomposition method and are correct provided that $M \leq 0.2$ and $0 < ka \leq 1.5$ and that $u' / \bar{u}_o \ll 1$, where u' is the amplitude of the acoustical particle velocity.

5.3.2 Numerical Procedures

The current axisymmetric model to represent the transmission phenomena at the end of a cylinder in the presence of a stationary mean flow differs significantly from the previous model of a radiating pipe in a stagnant fluid (Section 5.2).

The axisymmetric system is represented by a half plane consisting of 250×500 lattice cells, as depicted in Fig. 5.9. The pipe is 250 lattices long and has a radius $a = 20$ lattices. The thickness of the wall corresponds to one lattice, which gives a ratio $a/a_o \sim 0.95$, where a_o is the outer radius of the pipe. Thus, the effect of the wall thickness on the transmission properties can be neglected when a_o is used as the reference radius (Ando, 1969). Although the analytic solution assumes an inviscid flow, the effects of viscosity are taken into account by imposing the *Kutta condition* at the open end. For this reason, a non-slip boundary condition is applied at the walls of the computational model by

using the bounce-back scheme described in Sec. 3.6.1. A lattice kinematic viscosity $\nu = 9.5 \times 10^{-4}$ was chosen in order to provide a trade-off between a negligible viscosity and the smallest value supported by the BGK model before being affected by numerical instabilities (Lallemand and Luo, 2000).

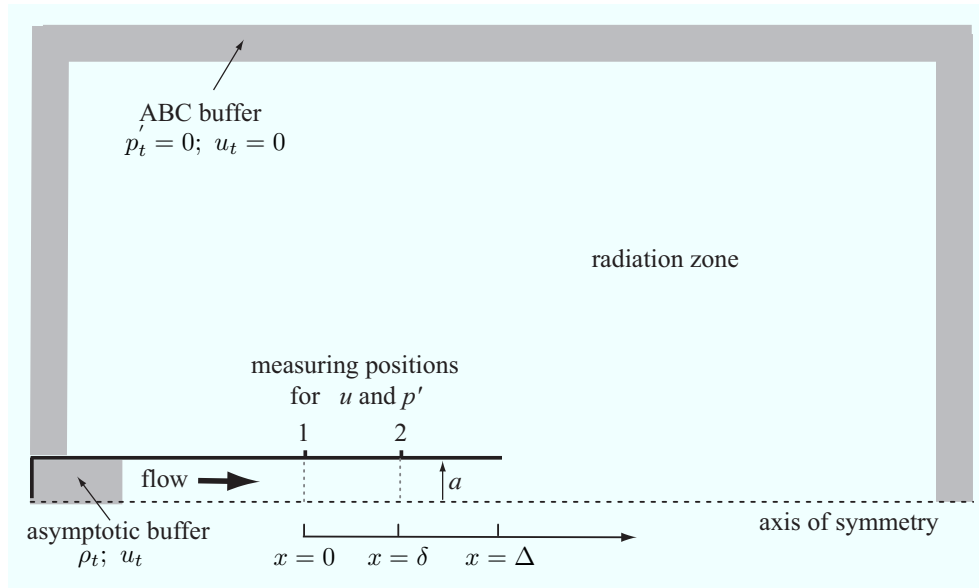


Figure 5.9 Scheme of the axisymmetric LB model for the simulation of the transmission phenomena at the open end in the presence of a mean flow

An anechoic boundary condition is applied on the top, left and right sides of the radiation zone. The anechoic boundary is achieved by using a 15-lattice thick ABC buffer with values for the target pressure p_t and target velocity u_t equal to zero, as proposed by Kam et al. (2006) and described in Sec. 3.6.2. The choice of the buffer thickness was based on a previous test to evaluate the reflection coefficient due to perpendicular and oblique sound wave incidence. The results showed that the order of magnitude of the reflection coefficient measured between the ABC buffer and radiation zone is $R \sim O(-3)$, which is smaller than the order of accuracy of the lattice Boltzmann scheme itself ($O(-2)$). Hence, the reflection coefficient achieved by the 15-lattice buffer is considered satisfactory. The

5.3 Transmission Properties of an Unflanged Pipe Carrying a Subsonic Mean Flow 127

lower boundary of the radiation domain represents the axis of symmetry of the system and, for this reason, the free-slip condition is applied as described in Sec. 3.6.1.

The pipe is excited at its input (closed) end with a sinusoidal acoustic source superimposed on a mean flow. The imposition of both the flow and the acoustic sources is achieved by developing a numerical scheme based on an asymptotic buffer placed at the pipe's closed end. This scheme is very similar to the ABC technique that provides the absorbing boundaries around the radiation zone and has been described in Sec. 3.6.2. The main difference, however, is that the target parameters u_t and ρ_t used as inputs to the asymptotic buffer assume non-zero values. The time-dependent expressions for u_t and ρ_t are given by

$$u_t = \bar{u}_0 + H(n - N_t)u' \sin\left(\frac{3}{2} \frac{n - N_t}{N - N_t} \frac{n\Delta_t c}{a}\right) \quad (5.9)$$

$$\rho_t = \rho_0 + H(n - N_t)\frac{u'\rho_0}{c_0} \sin\left(\frac{3}{2} \frac{n - N_t}{N - N_t} \frac{n\Delta_t c}{a}\right), \quad (5.10)$$

where, n and N are, respectively, the n -th time step and the total number of time steps in the simulation. Δ_t is the time step period of the numerical scheme, u' is the amplitude of the acoustic particle velocity, \bar{u}_0 is the cross-section averaged mean flow velocity, ρ_0 is the undisturbed fluid density and c_0 the speed of sound. H is the Heaviside step function defined as

$$H = \begin{cases} 0 & \text{for } n < 0, \\ 1 & \text{for } n \geq 0, \end{cases} \quad (5.11)$$

where N_t is the number of necessary time steps to accelerate the stagnant flow inside the pipe at $n = 0$ to a steady-state mean flow with velocity \bar{u}_0 . N_t is inversely proportional to the thickness of the asymptotic buffer placed at the closed end of the pipe. For this reason, a thickness equal to 60 lattices was chosen for the buffer in order to reduce the overall computational time by providing a rapid transient towards the steady-state ($N_t \sim 4000$). The choice of a thicker buffer would naturally produce a faster transient but, on the other hand, would not leave enough pipe length between the buffer and the measuring points for the flow to become fully developed (see Fig. (5.9)). Figure 5.10 presents the duration of the flow transient measured at $x = \Delta$ by depicting the ratio between measured and prescribed values of the flow velocity as a function of n for different Mach numbers. The small plateau located around $n = 400$ is attributed to an incoming flow component due to the first wave reflection at the open end.

The Heaviside function is used in Eqs. (5.9) and (5.10) to allow the flow to accelerate from stagnation to a stationary state before the acoustic source, defined by the second terms on the left-hand side of equations 5.9 and 5.10, is superimposed. The frequency of the acoustic source varies linearly with time (linear chirp) and sweeps from 0 Hz at $n = N_t$ to a frequency equivalent to $ka = 1.5$ at $n = N$. This corresponds to the range of Helmholtz numbers ka predicted by the theory (Munt, 1990). Moreover, the ratio $u'/\bar{u}_0 \sim 0.1$ is kept in accordance to the limit of low acoustic amplitude provided by the theory (Munt, 1990).

The complex reflection coefficient at the open end of a pipe is given by

$$R = \left(\frac{p_1^+}{p_1^-} \right) \exp(ik\Delta), \quad (5.12)$$

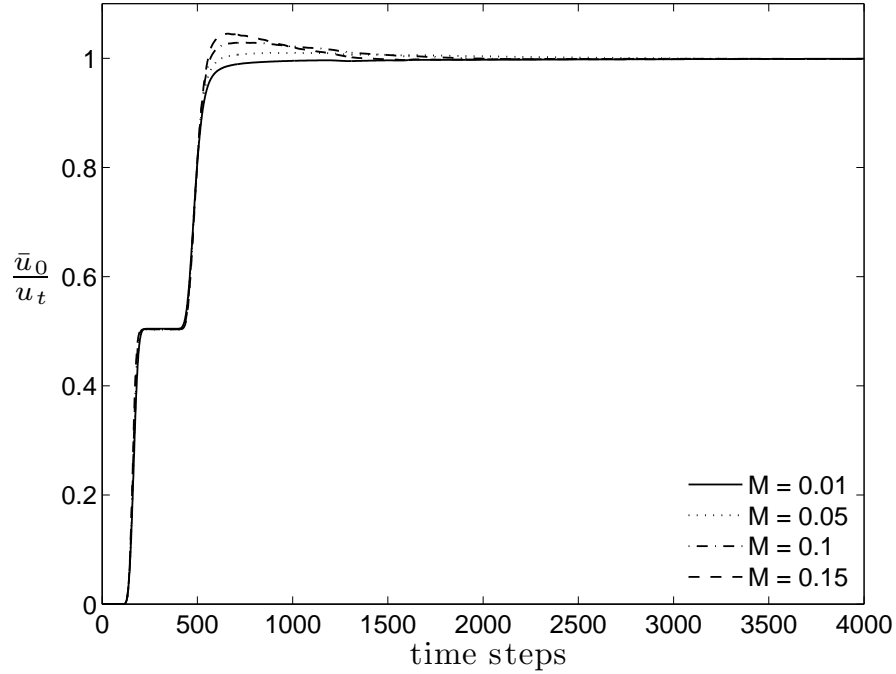


Figure 5.10 Transient to a steady-state flow in terms of the ratio between the mean flow velocity \bar{u}_0 and the imposed target velocity u_t as a function of time steps measured inside the pipe at a distance $\Delta = 80$ before the open end for different Mach numbers.

where p_1^- and p_1^+ are the reflected and incident wave amplitudes measured inside the pipe at a distance $x = \Delta$ from the open end and k is the wavenumber.

For plane waves propagating in a viscous mean flow the wavenumber is complex and described by two components $k = k^+ + k^-$, where k^+ and k^- are the components associated with the incident and reflected waves, respectively. The unknowns p^+ , p^- and k to be used in Eq. (5.12) are obtained from a system of equations describing the acoustic field inside the pipe at two different points. The system is constructed by using time histories of the pressure $p(t)$ and particle velocity $u'(t)$ measured at point 1 and 2

(see Fig. 5.9). The equations describing the sound field at point 1 are then given by

$$p_1(f) = p_1^+ + p_1^-, \quad (5.13)$$

and

$$u_1(f) = \frac{1}{\rho_0 c_0} (p_1^+ - p_1^-), \quad (5.14)$$

where $p_1(f)$ and $u_1(f)$ are the discrete Fourier transform of the pressure and particle velocity time histories $p_1(t)$ and $u_1(t)$, respectively. Here and in the following, the subindices on the left-hand sides of Eqs. (5.13) and (5.14) indicate the measuring point. Likewise, the sound field at point 2 is described by

$$p_2(t) = p_1^+ \exp(-ik^+ \delta_{12}) + p_1^- \exp(ik^- \delta_{12}), \quad (5.15)$$

and

$$u_2(t) = \frac{1}{\rho_0 c_0} (p_1^+ \exp(-ik^+ \delta_{12}) + p_1^- \exp(ik^- \delta_{12})), \quad (5.16)$$

where δ_{12} is the distance between the points 1 and 2. Equations (5.13), (5.14), (5.15) and (5.16) can be rearranged in a system whose solution for the unknowns is given by

$$\begin{Bmatrix} p_1^+ \\ p_1^- \\ A \\ B \end{Bmatrix} = \begin{bmatrix} 1 & 1 & 0 & 0 \\ 0 & 0 & 1 & 1 \\ 1/\rho_0 c_0 & -1/\rho_0 c_0 & 0 & 0 \\ 0 & 1/\rho_0 c_0 & -1/\rho_0 c_0 & 0 \end{bmatrix}^{-1} \begin{Bmatrix} p_1 \\ p_2 \\ u_1 \\ u_2 \end{Bmatrix}, \quad (5.17)$$

where $A = p_1^+ \exp(-ik^+ \delta_{12})$ and $B = p_1^- \exp(ik^- \delta_{12})$. Thus, the incident and reflected

5.3 Transmission Properties of an Unflanged Pipe Carrying a Subsonic Mean Flow 131

wavenumber components are obtained by

$$k^+ = -\frac{1}{i\delta_{12}} \ln\left(\frac{A}{p_1^+}\right) \quad \text{and} \quad k^- = \frac{1}{i\delta_{12}} \ln\left(\frac{B}{p_1^+}\right). \quad (5.18)$$

Finally, the end correction l at the open end is given by

$$l = \Re\left(\frac{1}{i(k^+ + k^-)} \ln\left(\frac{R}{|R|}\right)\right). \quad (5.19)$$

5.3.3 Results for the Magnitude of the Reflection Coefficient

The graphics of Fig. 5.11 depict the results for the magnitude of the reflection functions at the open end $|R|$ plotted as a function of the Helmholtz number ka for different Mach numbers. In general, the numerical results agree very well with the theoretical and experimental data provided by Munt (1990) and Allam and Åbom (2006).

The amplification of sound in regions where $|R| > 1$ is also well predicted by the model. According to the theory provided by Munt (1990), values of the reflection coefficient greater than one are caused by the transfer of kinetic energy from the flow to the acoustic field due to the interaction of the unstable vortex sheet with the lip of the pipe. The instability of the vortex sheet is, in turn, triggered by the sound transmitted through the open end.

Better agreement is found for low Mach numbers. The highest discrepancy from the theory is found for $M = 0.15$ at $ka = 1.5$, at which the deviation is $\sim 6\%$ (Fig. 5.11). As the Mach number decreases to 0.01, the highest deviation is found at $ka = 1.5$ and becomes $< 1\%$.

The deviation of the simulation from the theoretical and experimental results at high Reynolds number is attributed to the limit of compressibility of the LBGK scheme. As

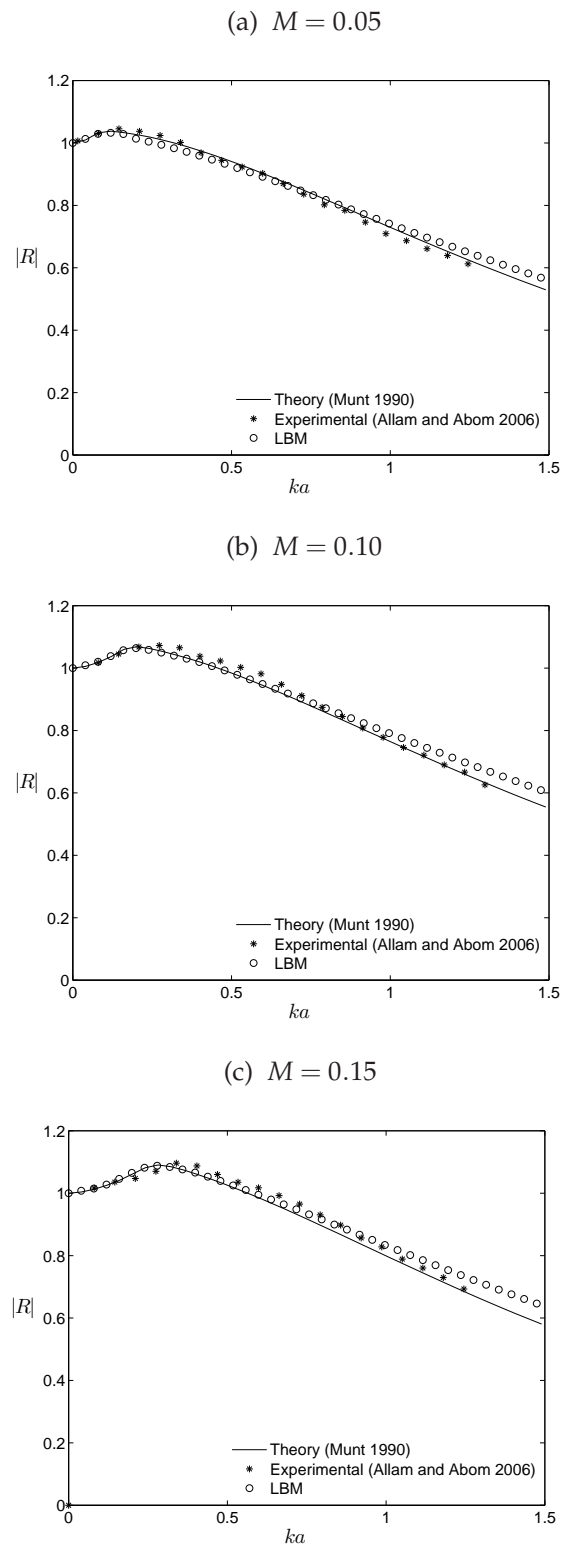


Figure 5.11 Comparison between theory, simulation and experimental results for the magnitude of the reflection coefficient at the open end $|R|$ as a function of the Helmholtz number for different values of the Mach number.

5.3 Transmission Properties of an Unflanged Pipe Carrying a Subsonic Mean Flow133

demonstrated by Halliday et al. (2001) and Reis and Phillips (2007), the Navier-Stokes equations in polar coordinates (Eqs. 2.25, 2.26 and 2.27) can be fully recovered from the axisymmetric lattice Boltzmann scheme used in this study for the low compressibility limit, or more precisely for $M \leq 0.15$. The simulations performed for $M = 0.15$ are thus at the upper limit of this range and the accuracy is likely degraded to some extent. The discrepancy found in the high frequencies may be associated with an insufficient number of lattice cells per wavelength (CPW). Although it is generally accepted that, for high order schemes, 12 CPW should be used (Wilde, 2006), this simulation uses a much finer grid (26 CPW). However, the minimum CPW requirement depends on the specificities of the spatial scheme.

Similar to the experimental results reported by Allam and Åbom (2006), better agreement with the theory is found when the theoretical values of $|R|$ are calculated using the maximum flow speed inside the pipe $u_0|_{r=0}$ instead of using the cross section averaged velocity \bar{u}_0 .

As explained by Allam and Åbom (2006), this is due to the fact that in the uniform flow model assumed by Munt, the convection speed of the vortical instabilities become $Mc_j/2$ when the outer fluid is stagnant. However, for a real jet issuing in a stagnant fluid, whose upstream flow profile is non-uniform, the convection speed becomes $u_0|_{r=0}/2$ (Freymuth, 1965). Thus it is reasoned that one should choose a correct flow speed, so as to preserve the correct vortex speed based on $u_0|_{r=0}$, instead of using the cross-section averaged value of flow velocity.

Figure 5.12 presents the same results of the magnitude of the reflection coefficient $|R|$ as a function of the Strouhal number $Sr_0 = ka/M$. When $|R|$ is plotted as a function of Sr_0 the peaks of all the curves have their maximum at $Sr_0 \sim \pi/2$, which is half of what has been predicted by Cargill (1982b).

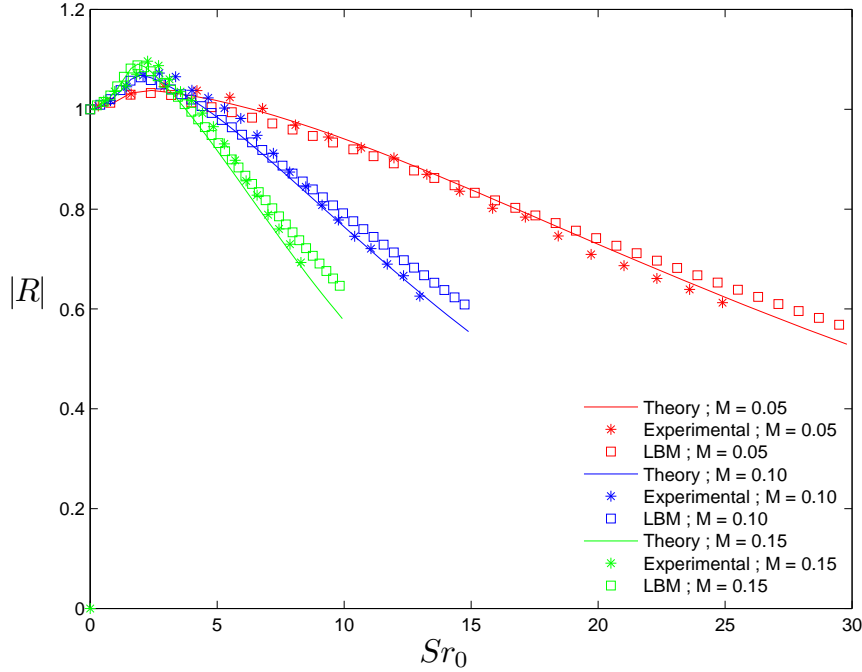


Figure 5.12 Comparison between theory, experiment and simulation results for the reflection coefficient at the open end $|R|$ as a function of the Strouhal number for different Mach number values

An interesting way to explain the physical meaning of the peak region is obtained by manipulating the relation $Sr_0 = ka/M \sim \pi/2$, which leads to

$$T \sim 4a/\bar{u}_0, \quad (5.20)$$

where T is the oscillation period of the acoustic source. Considering that the propagation velocity of the vortical instabilities u_v at the vortex sheet of a jet in a stagnant fluid is given by $u_v \sim \bar{u}_0/2$ (Freythuth, 1965), the above relation becomes

$$T \sim D/u_v, \quad (5.21)$$

where D is the pipe diameter. Equation (5.21) implies that the maximum reflection coefficient magnitude occurs when the oscillation period of the acoustic source is approximately equal to the time necessary for the vortical instabilities to propagate a distance equal to the pipe diameter D .

Figure 5.13 provides a qualitative description of the interaction of the unstable vortex sheet with the lip of the pipe by depicting snapshots of the flow stream lines (in blue) superimposed on the velocity field (in red) at the pipe exit for $M = 0.15$. In this particular case, instead of using the excitation scheme described by Eqs. (5.9) and (5.10), the acoustic source is sinusoidally excited by a single frequency equivalent to $Sr_0 = \pi/2$, which corresponds to the region of the Strouhal number where the maximum transfer of energy from the flow to the acoustic field takes place. The snapshots were taken for different intervals within a single oscillation cycle of the particle velocity u' , measured at the pipe open end. The fraction of the oscillation cycle associated with each snapshot is depicted at the upper right corner of each figure.

5.3.4 Results for the Dimensionless End Correction

Figure 5.14 provides a comparison between numerical, theoretical and experimental results for the dimensionless end correction as a function of the Helmholtz number. In this case, the most significant influence of the mean flow is to strongly reduce the values of the end correction when $ka \rightarrow 0$.

In general, the numerical results agree very well with Munt's theory, specifically at the high frequency limit ($ka > 0.5$) for which the dimensionless end correction values approximate those obtained for the same pipe carrying a zero mean flow (Levine and Schwinger, 1948). In the low frequency region ($ka < 0.5$), where the effect of the mean

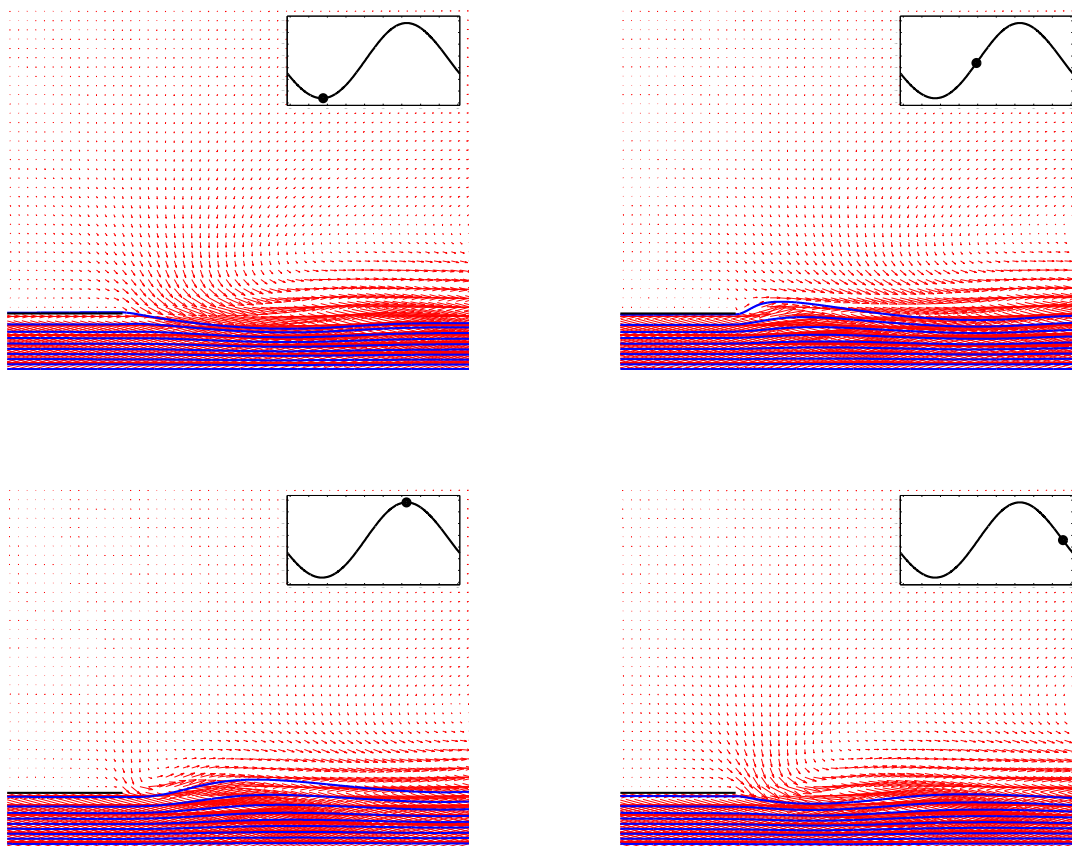


Figure 5.13 Mean flow visualization for $M = 0.15$ and $u/U = 0.1$ at the pipe open end for different time frames within a single oscillation period. The boxes on the top indicate the frame position in terms of the flow velocity cycle measured at the open end. The stream lines are depicted in blue and red arrows indicate the velocity field.

5.3 Transmission Properties of an Unflanged Pipe Carrying a Subsonic Mean Flow 137

flow becomes significant, the numerical results diverge slightly from the theory. Interestingly, a similar discrepancy is found for the experimental results and can be attributed to the effect of the finite wall thickness used in both the experimental and numerical evaluations as opposed to the infinitely thin wall assumed by the theory. In fact, as already reported by Peters et al. (1993) and Atig (2004), the end correction seems to be much more sensitive to small geometric details than the magnitude of the reflection coefficient $|R|$. Moreover, the small discrepancies between numerical and theoretical results seem to increase with the Mach number for the entire range of ka . This is because the simulations approach the low compressibility limit ($M \rightarrow 0.15$) for which the full Navier-Stokes equations can be recovered from the lattice Boltzmann equation, as discussed previously.

Figure 5.15 depicts the same curves of the dimensionless end correction plotted as a function of the Strouhal number Sr_0 . At low Strouhal numbers ($Sr_0 < \pi$) the graphs for different Mach numbers tend to collapse into a single curve and $l/a \rightarrow 0.2554\sqrt{1 - M^2}$ as $ka \rightarrow 0$, which is the low limit value predicted by Rienstra (1984).

5.3.5 Discussion

The objective of this section was to verify the validity of the lattice Boltzmann method at representing the acoustic transmission phenomena at the open end of an unflanged pipe carrying a cold laminar subsonic mean flow that issues in a stagnant ambient fluid having the same thermodynamic properties. The acoustic transmission phenomena is described in terms of the magnitude of the reflection function at the open end $|R|$ and the dimensionless end correction l/a .

The model was verified by comparing the numerical results with both the theory provided by Munt (1990) and with the experimental investigations conducted by Allam and Åbom (2006) for the entire range of the Helmholtz number $0 < ka \leq 1.5$ and three

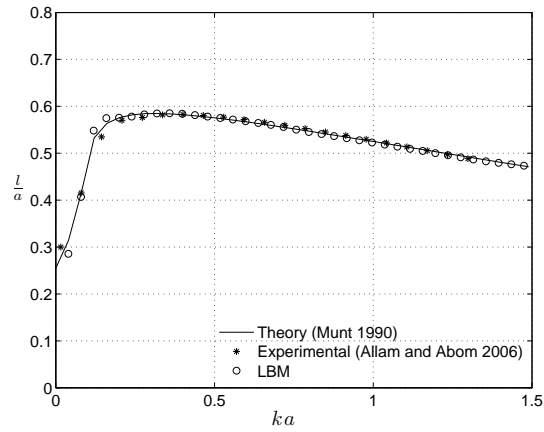
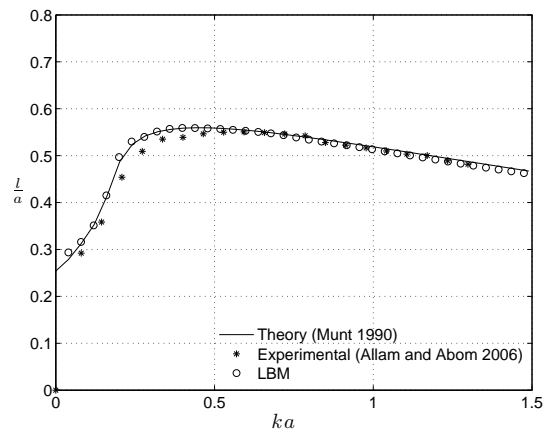
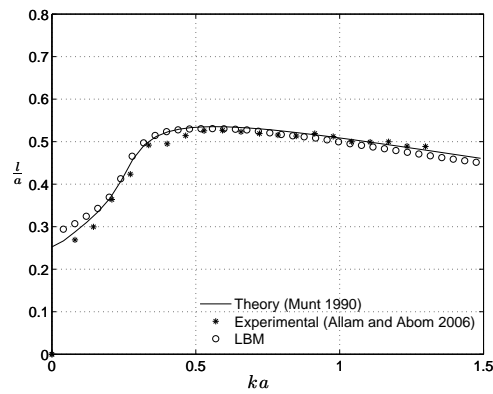
(a) $M = 0.05$ (b) $M = 0.10$ (c) $M = 0.15$ 

Figure 5.14 Comparison between theory and simulation results for the end correction ratio l/a as a function of the Helmholtz number for different values of the Mach number.

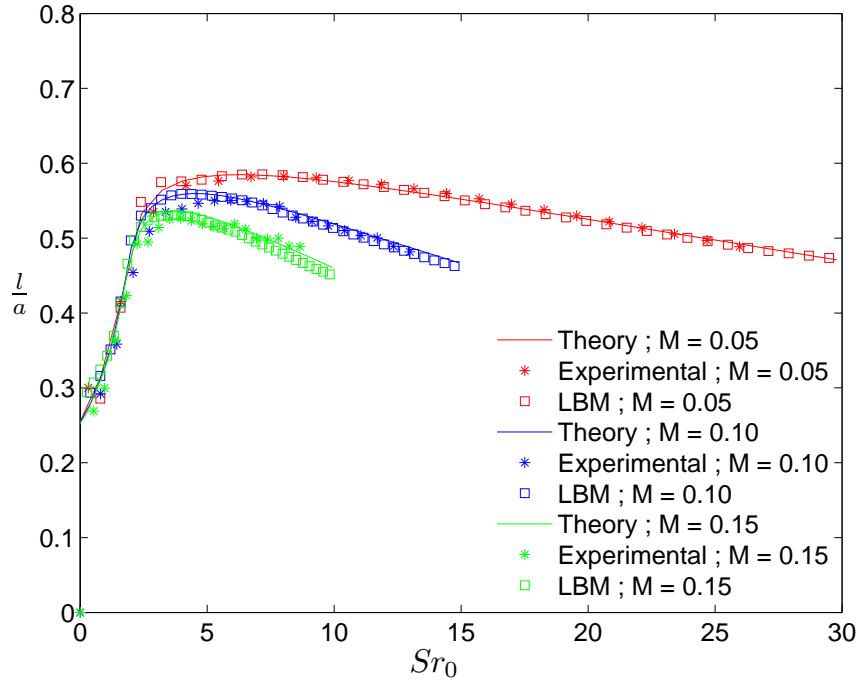


Figure 5.15 Comparison between theory, experiments and simulation results for the the end correction ratio l/a as a function of the Strouhal number for different Mach number values.

different flow velocities based on the Mach number, namely $M = 0.05, 0.10$ and 0.15 .

The verification has shown that the axisymmetric lattice Boltzmann scheme described in Sec. 5.3.2 is sufficiently accurate to represent the aforementioned phenomena. In general, the discrepancy between the numerical and theoretical results increases as $M \rightarrow 0.15$, which corresponds to the limit of low compressibility at which the polar cylindrical form of the Navier-Stokes equations (Eqs. 2.25, 2.26 and 2.27) can be recovered from the lattice Boltzmann equation as shown in Chapter 3. Another discrepancy from the theoretical predictions is found for the dimensionless end correction l/a at the low frequency limit ($ka \rightarrow 0$). This deviation is attributed to the effect of the wall with finite thickness ($\tau_w = 1$ lattice) and is consistent with the experimental results from Allam and

Åbom (2006), whose experimental setup also involved a pipe with finite thickness, as opposed to an infinitely thin wall assumed by Munt's theory. The next sections of this chapter will use a similar numerical procedure in order to investigate the behavior of the same acoustic transmission phenomena when a circular horn is connected to the end of the pipe.

5.4 Acoustic Transmission of Horns with Zero Mean Flow

The objective of this section is to verify the usability of the axisymmetric lattice Boltzmann model described in the previous sections at predicting the magnitude of the reflection coefficient $|R|$ and the dimensionless end correction l/a of pipes terminated by unflanged circular horns in the absence of a mean flow. Given that there are no analytic solutions for the aforementioned parameters in the case of horns, the verification will be based on the comparison of the LBM results with those obtained from a boundary element model with the same geometric characteristics.

5.4.1 Previous Investigations

The exact solutions for the reflection coefficient $|R|$ and end correction l/a in the absence of a mean flow are limited to simple cases such as pipes terminated by an infinite flange (King, 1936) or thin unflanged pipes (Levine and Schwinger, 1948).

In general, problems involving the radiation from circular waveguides terminated by flaring horns are tackled by assuming that the boundary condition at the very end of the flare is equal to that of an unflanged pipe. This approximation is fairly reasonable for the magnitude of the reflection coefficient $|R|$ in the limit of low Helmholtz number ka , but becomes rather inaccurate at higher frequencies and inappropriate for the estimation of

the dimensionless end correction l/a .

When the mean flow is neglected, an alternative way to obtain accurate predictions of acoustic transmission parameters such as $|R|$ and l/a for geometries whose analytical solutions are not available is to use long established numerical techniques such as the finite element method (FEM), boundary element method (BEM), finite difference method (FDM), to name but a few. In the case of pipes terminated by flaring ends, the numerical approach has been adopted by Dalmont et al. (2001) who used FDM to predict the behavior of the end correction at the low frequency limit of catenoidal horns with different shapes. Selamet et al. (2001) provided a more extended analysis of the end correction and magnitude of the reflection function of cylindrical horns with different flaring radii. Their analysis included values for a wide range of the Helmholtz number, namely $0 < ka \leq 3.0$ and the results agree with previous experimental investigations provided by Peters et al. (1993).

5.4.2 Numerical Procedures

The numerical analysis conducted in this section takes into account two different cylindrical horns having different curvature radii, namely $r = 2a$ and $r = 4a$, where a is the radius of the pipe. Here and in the following, the results for the magnitude of the reflection coefficient and for the end correction are measured at the termination of the pipe straight section in accordance with the previous numerical and experimental analysis conducted by Selamet et al. (2001) and Peters et al. (1993), respectively. For this reason, the magnitude of the reflection coefficient $|R|$ omits the subscript *end* used in previous sections of this chapter.

The axisymmetric lattice Boltzmann model used in the present analysis has the same lattice parameters as the one described in Sec. 5.3.2, except for the implementation of a

horn at the open end and the absence of the mean flow terms u_0 and ρ_0 in Eqs. (5.9) and (5.10), respectively. Figure 5.16 depicts the two horns with different flaring curvature used in the present analysis.

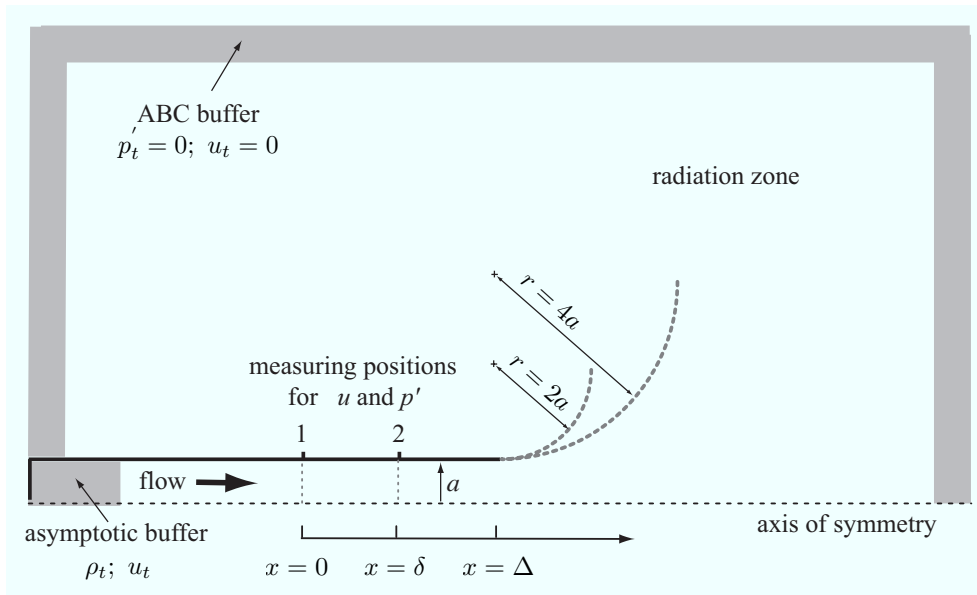


Figure 5.16 Scheme of the axisymmetric LB model for the simulation of the transmission phenomena at the open end in the presence of a mean flow

The boundary elements analysis was conducted using the software package Sysnoise. The analysis provides a solution of sound field in terms of pressure and particle velocity at a distance equal to $4a$ upstream from the end of the pipe's straight section. These values can be used to compute the acoustic impedance Z_{Δ} , which is used to determine $|R|$ and l/a at the pipe-horn junction by using Eqs. (5.6) and (5.7).

The internal sound field at $x = \Delta$ using BEM is found by resolving the Kirchoff-Helmholtz equation, which is described in terms of the strength of the sound sources applied at the pipe's closed end and by the values of the sound pressure and sound velocity on the closed surface of the system. This approach implies that the boundary element model is simply represented by the boundary surface of the system instead of

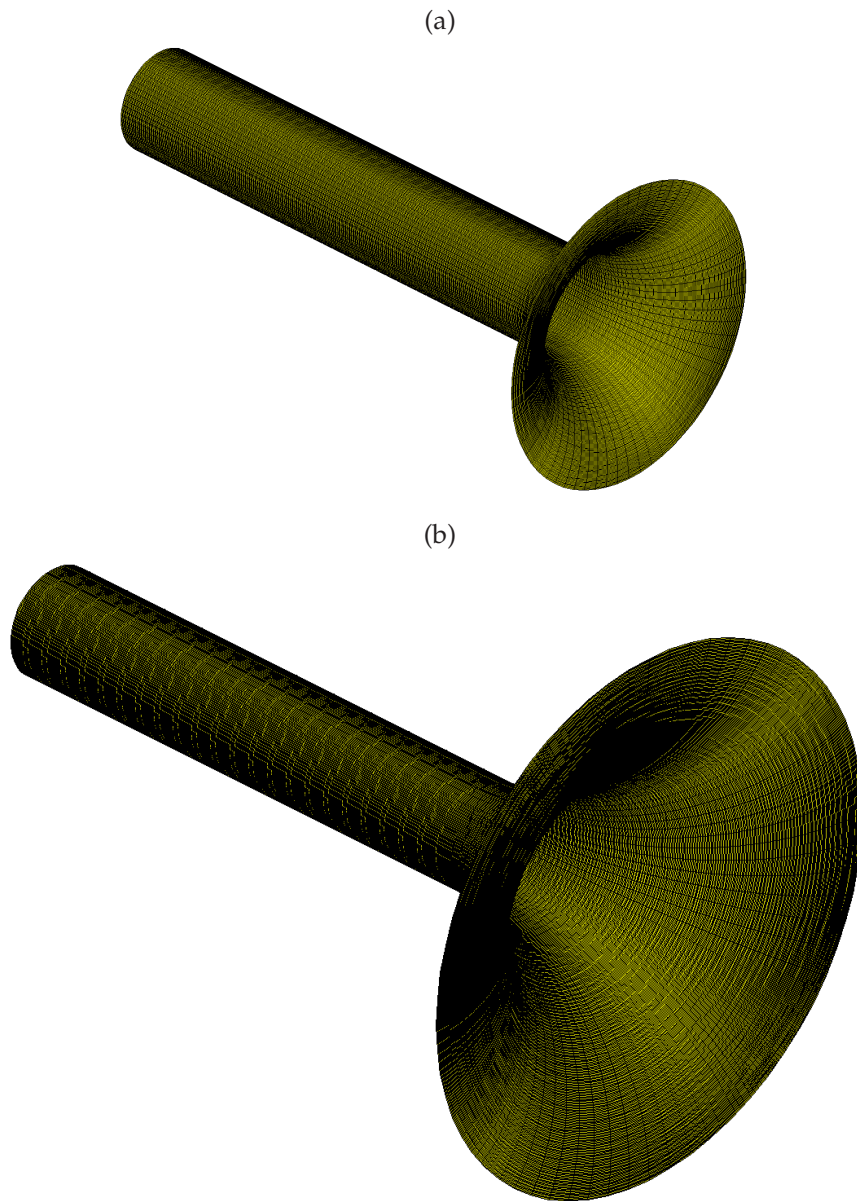


Figure 5.17 Boundary elements meshes for the pipe terminated by circular horns with different curvatures: (a) $r = 2a$; and, (b) $r = 4a$.

requiring the entire representation of the fluid domain. The solution of the Kirchoff-Helmholz equation is numerically achieved by discretizing the boundary surface into a number of elements which comprise the system mesh.

The parameters used to build the BEM models are very similar to those used by Selamet et al. (2001). The mesh uses a discretization of forty elements per wavelength and the frequency-domain results of the acoustic field were calculated for a frequency step of 20 Hz and for a frequency range equivalent to $0 < ka \leq 1.5$. Figure 5.17 depicts the meshes of the two models considered in the analysis.

5.4.3 Results for the Magnitude of the Reflection Coefficient

The following analysis addresses the effect of a horn on the magnitude of the reflection coefficient $|R|$ relative to the end of the straight section of the pipe, consistent with Peters et al. (1993) and Selamet et al. (2001). Figure 5.18 depicts the comparison between the lattice Boltzmann model and the boundary elements model for horns with two different curvature radii r attached to the open end of an unflanged pipe.

The results obtained with BEM agree with results provided by Selamet et al. (2001) using the same method. An excellent agreement is found between BEM and LBM results. In general, the effect of the horn curvature radius on $|R|$ does not play an important role for the low frequency limit ($ka < 0.2$) and both results approximate those found for an unflanged pipe. Nevertheless, the difference between the behavior of the reflection coefficient for the two curvature radii becomes significant at high frequencies. As expected, the smaller the curvature radius, the higher the amount of reflected wave, particularly at high frequencies. Moreover, in the absence of a mean flow, the reflection coefficient is never greater than 1.

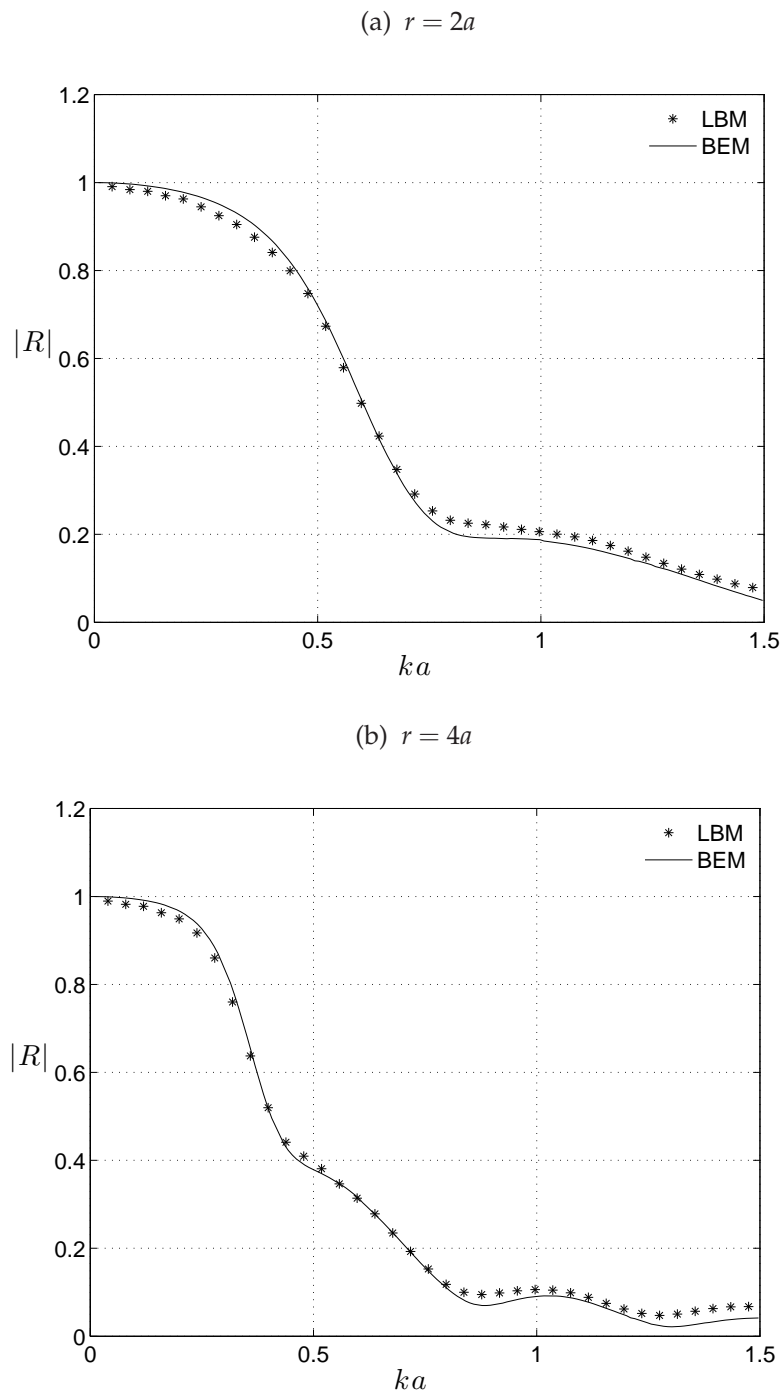


Figure 5.18 Comparison between BEM and LBM results for the magnitude of the reflection coefficient $|R|$ as a function of the Helmholtz number ka for two different circular horn profiles in the absence of a mean flow measured at the end of the straight pipe termination.

5.4.4 Results for the Dimensionless End Correction l/a

As in the previous section, the results obtained with BEM for the end correction l/a are identical to the results provided in (Selamet et al., 2001). Figure 5.19 depicts the results for l/a as a function of the Helmholtz number ka obtained with BEM and LBM for the same horn curvatures.

Again, very good agreement between both numerical techniques was found. For the low frequency limit $ka \rightarrow 0$ and $r = 2a$ the LBM and BEM methods give $l/a = 1.78$ and $l/a = 1.72$, respectively. In the same way, for $r = 4a$, the LBM and BEM methods give $l/a = 2.38$ and $l/a = 2.33$, respectively. These last values agree with $l/a \simeq 2.3$ found experimentally for the same geometry and nullified mean flow by Peters et al. (1993).

The end correction l/a is very sensitive to the horn curvature at low frequencies, but becomes negligible for high frequencies, where values of l/a converge for the two different horns analyzed, as shown in Fig. 5.19. This behavior is essentially opposed to the behavior of $|R|$ for the same geometries.

As mentioned in the introduction of this chapter, the end correction is caused by the inertial effects of the fluid load surrounding the open end. The values of l/a depicted in Fig. 5.19 correspond to the dimensionless end correction found at the end of the pipe segment, which means that the values comprise not only the inertial effects but also the effect due to the length extension provided by the horn segment. Hence, a more straightforward way to evaluate the effect of the horn curvature on the dimensionless end correction caused only by the inertial effects is to subtract the end correction l from the horn radius r , as depicted in Fig. 5.20. This procedure essentially shifts the point of reference of the end correction to the open end of the horn.

An interesting feature in Fig. 5.20 is the fact that horns tend to diminish the iner-

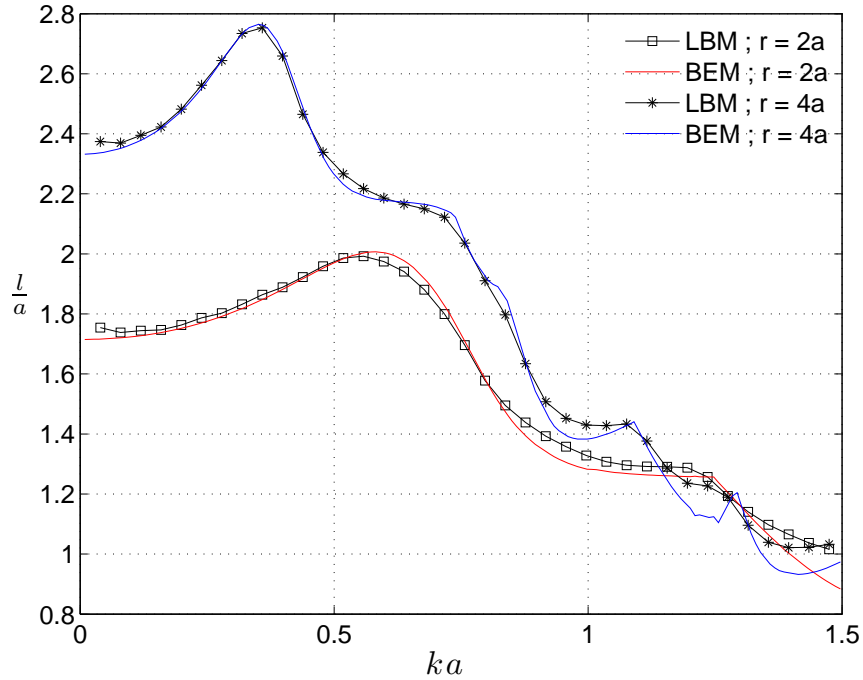


Figure 5.19 Comparison between BEM and LBM results for the dimensionless end correction l/a as a function of the Helmholtz number ka for two different circular horn profiles in the absence of a mean flow measured at the end of the straight pipe termination.

tial effect provided by the fluid loading to the point that the length correction becomes negative. In other words, the wave components do not propagate very far into the horn before they are reflected back into the pipe. In general, the bigger the curvature radius r is, the bigger the negative end correction becomes.

5.4.5 Discussion

The goal of this section was to verify the axisymmetric lattice Boltzmann model for the prediction of the reflection coefficient $|R|$ and the dimensionless end correction l/a of cylindrical pipes terminated by circular horns with different radii of curvature in the absence of a mean flow.

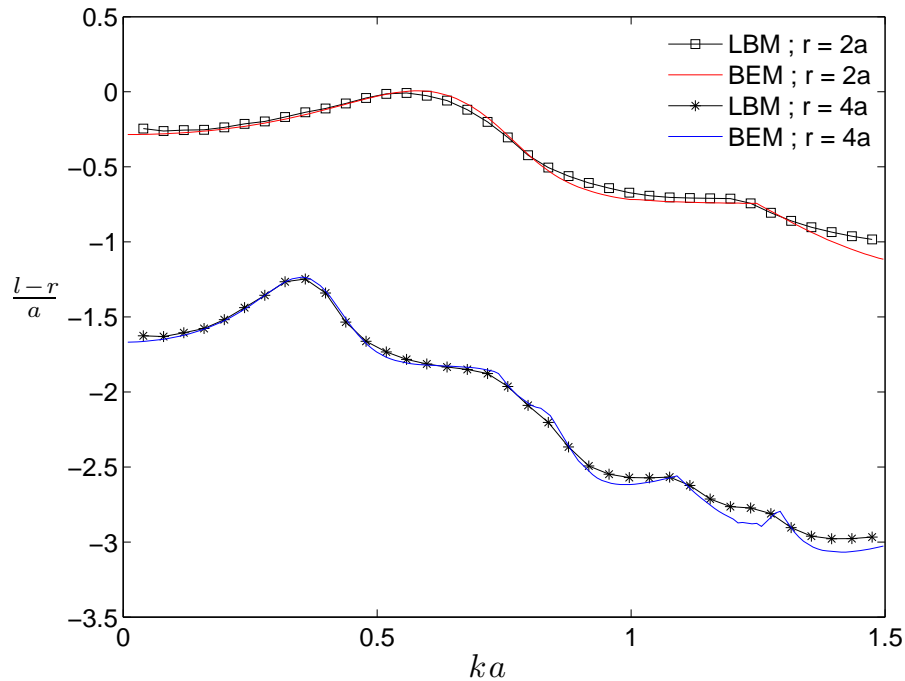


Figure 5.20 Comparison between BEM and LBM results for the shifted dimensionless end correction $l - r/a$ as a function of the Helmholtz number ka for two different circular horn profiles in the absence of a mean flow, measured at the end of the straight pipe termination.

This was achieved by comparing the results provided by the LBM model with the results obtained by a boundary element analysis resolved with the software package Sysnoise, which themselves are identical to the results provided by Selamet et al. (2001). Moreover, the value of l/a for the low frequency limit obtained with the LBM model was compared with the experimental results presented by Peters et al. (1993) for the horn with $r = 4a$.

The excellent agreement found between the LBM predictions and both the experimental, analytical and BEM results presented in the previous sections of this chapter strongly support validity of the method for the representation of transmission phenomena in waveguides with different terminations and flow conditions.

In the following section, the same LBM model will be used to investigate the behavior of the dimensionless end correction l/a and the reflection coefficient $|R|$ in horns carrying a subsonic mean flow, for which analytical models are nonexistent.

5.5 Acoustic Transmission of Horns Carrying a Subsonic Mean Flow

In the foregoing sections of this chapter the main objective was to ascertain the validity and the extension of applicability of LBM on the prediction of the acoustic transmission phenomena in waveguides, taking into account different geometric configurations and flow parameters. This objective was achieved by comparing the LBM results with those provided by available theoretical models and by previous experimental investigations.

The objective of the present section, however, is to investigate the same phenomena in pipes terminated by circular horns with different curvatures carrying a subsonic mean flow. For this reason, the lattice parameters used here are identical to those described previously, the main difference being the implementation of a flow source in the same way as that described in Sec. 5.3.2.

As previously discussed, when the mean flow is not present the acoustic field induces an unsteady vorticity at the open end, which mainly acts as a sound absorber. In the presence of a mean flow, the acoustic and flow fields become coupled and the unsteady vorticity is convected downstream where it acts as a source of sound, thereby converting vortical kinetic energy into acoustic energy. This nonlinear behavior is highly influenced by the geometric characteristics of the pipe termination.

Unfortunately, the available literature for pipes terminated by horns carrying a subsonic mean flow, as in the case of wind instruments, is rather sparse. Hence, a full verification of the entire extension of the results provided here is not possible. On the other

hand, the validity of the results is highly supported by the good agreement achieved in the previous analysis of this chapter, for which analytical and experimental benchmarks were available.

In the present analysis three different flow velocities are taken into account, corresponding to the Mach numbers $M = 0.05, 0.10$ and 0.15 . The acoustic reflection experienced by the wave at the junction between the straight pipe and the horn is thus investigated in terms of energy and pressure reflection coefficients $|R_E|$ and $|R|$, as well as in terms of the dimensionless end corrections l/a and $l - r/a$ for a range of the Helmholtz number $0 < ka \leq 1.5$ and its respective Strouhal number defined as $Sr_0 = ka/M$. The ratio between the acoustic amplitude and the cross section averaged mean flow u'/\bar{u}_0 is kept constant for all the cases and equal to 0.1 , which is an averaged value found in wind instruments during normal playing. Moreover, a qualitative description of the interaction between the acoustic field and the vortex sheet is provided in terms of flow visualizations at the open end of the pipe-horn system.

5.5.1 Previous Investigations

The behavior of the acoustic reflection coefficient due to a cross section expansion in a pipe carrying a low Mach number mean flow has been extensively investigated in the past. These geometric configurations are commonly encountered in piping systems in the form of flow diffusers, as well as in pipe terminations in the forms of horns and nozzles. In the case of diffusers, the acoustic transmission phenomena has been investigated by Kwong and Dowling (1994) who observed that diffusers of certain geometric characteristics may induce severe self-sustained oscillations in piping systems due to the transfer of vortical energy into acoustic energy. Lier et al. (2001) provided a more detailed description of the aeroacoustic behavior of diffusers by evaluating the effect

of geometrical configurations on the enthalpy reflection coefficient. Some years later, Dupère and Dowling (2001) conducted an analytical and experimental study correlating the sound absorption in diffusers with their geometric characteristics.

In the specific case of pipes terminated by horns carrying a subsonic mean flow, a primary experimental study has been provided by Hirschberg et al. (1989) who observed that horns placed at the termination of pipes that are connected to side branches can considerably increase the transfer of kinetic energy from the flow to the acoustic field at the open end, as opposed to a simple unflanged termination. Years later, Peters et al. (1993) conducted an experimental investigation of the transmission properties of pipes terminated by a circular horn with curvature radius $r = 4a$. Their investigations were carried out for the energy reflection coefficient R_E , expressed by Mechel et al. (1965) in terms of the magnitude of the pressure reflection coefficient $|R|$ and defined as the ratio of the intensities of the reflected and incident acoustic energy at the end of the pipe's straight section, given by

$$|R_E| = |R|^2 \left(\frac{1 - M}{1 + M} \right)^2, \quad (5.22)$$

where M is the Mach number. They also investigated the behavior of the end correction for very low Strouhal numbers ($0 < Sr_0 < 2.5$). Their investigations showed that $|R_E|$ can become greater than unity for a critical region $Sr_0 \sim \pi a/r$. Moreover, they found that the end correction l/a becomes negative as $Sr_0 \rightarrow 0$.

5.5.2 Numerical Procedures

The lattice Boltzmann model, as well as the numerical procedures used to obtain the values of the energy reflection coefficient $|R_E|$ and the dimensionless end correction l/a by a pipe carrying a low Mach number mean flow, is similar to that used in Sec. 5.3,

with the addition of the circular horns of different curvature as discussed in Sec. 5.4 and depicted in Fig. 5.16. Likewise, the predictions of $|R|$ and l/a are defined relative to the end of the straight section of the pipe, consistent with Peters et al. (1993) and Selamet et al. (2001).

5.5.3 Results for the Magnitude of the Reflection Coefficient

Figure 5.21 depicts the effect of the mean flow on the behavior of the magnitude of the reflection coefficient $|R|$ as a function of the Helmholtz number ka for the two different horn profiles shown in Fig. 5.16.

From a qualitative standpoint, the effect of the mean flow on $|R|$ is found to be similar to that encountered for the unflanged pipe discussed in Sec. 5.3.2. That is to say, the influence of the mean flow is only significant for low Helmholtz numbers, namely $0 < ka < 0.5$. In this region, $|R|$ assumes values greater than one and $|R| \rightarrow 1$ as $ka \rightarrow 0$. For higher values of ka , $|R|$ is close to the solution obtained in the absence of a mean flow.

From a quantitative point of view, however, the behavior of $|R|$ diverges considerably from the unflanged pipe case (see Fig. 5.11). For a given Mach number, the amplitude of the peak of $|R|$ becomes $\sim 20\%$ higher when a circular horn is attached to the pipe's open end. Interestingly, horns with different curvature radius present the same peak magnitude for the same Mach number. This characteristic becomes more evident when $|R|$ is plotted against the Strouhal number $Sr_0 = ka/M$, as depicted in Fig. 5.22.

In this case, the curves of $|R|$ for different horns and the same Mach number collapse into each other for $Sr_0 < 5$, which implies that, for such a region, the effect of the horn curvature is negligible and the behavior of $|R|$ is predominantly dictated by the Mach number. Furthermore, Fig. 5.22 shows that the maxima of $|R|$ always appear at $Sr_0 = \pi/2$, regardless of Mach number or horn curvature. This is essentially the same Strouhal

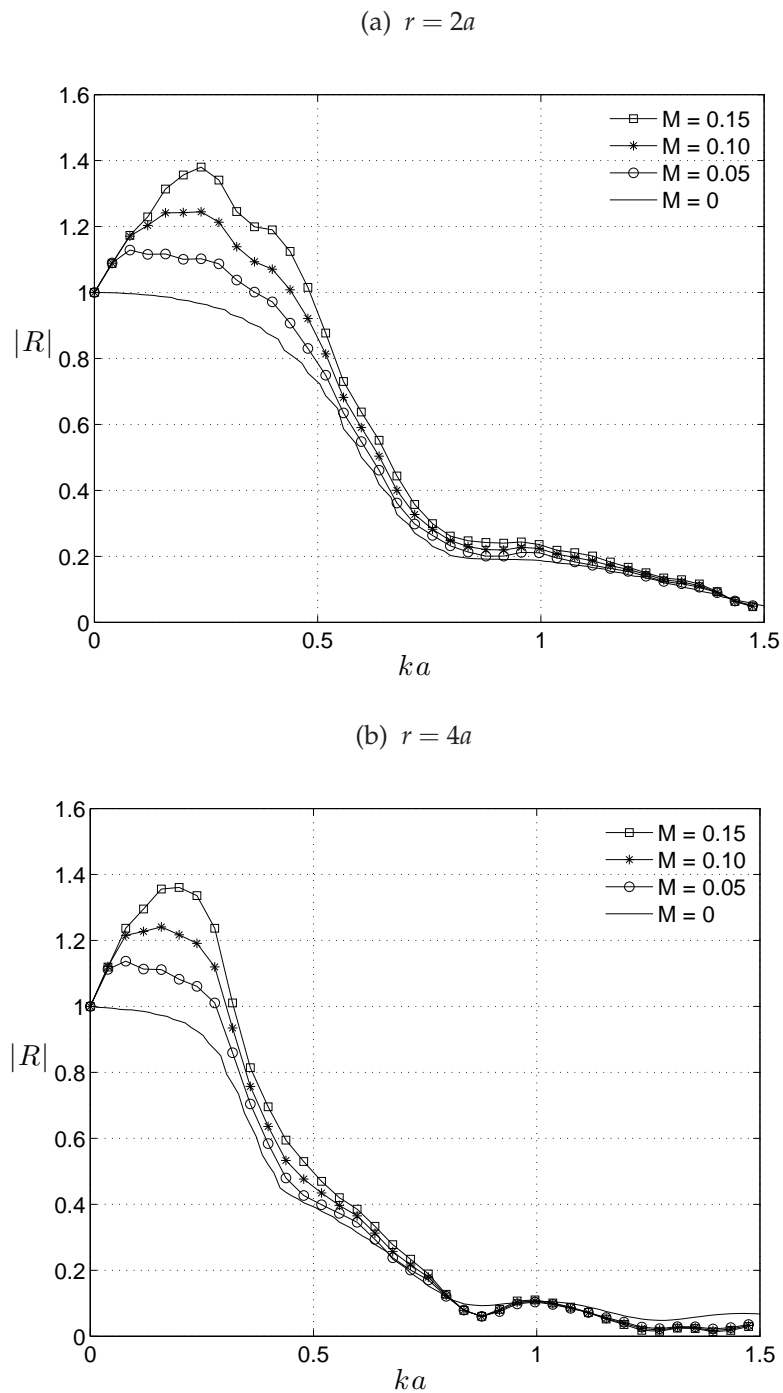


Figure 5.21 Numerical results for the magnitude of the reflection coefficient at the end of the straight pipe segment $|R|$ as a function of the Helmholtz number ka for two different circular horn profiles and different Mach numbers.

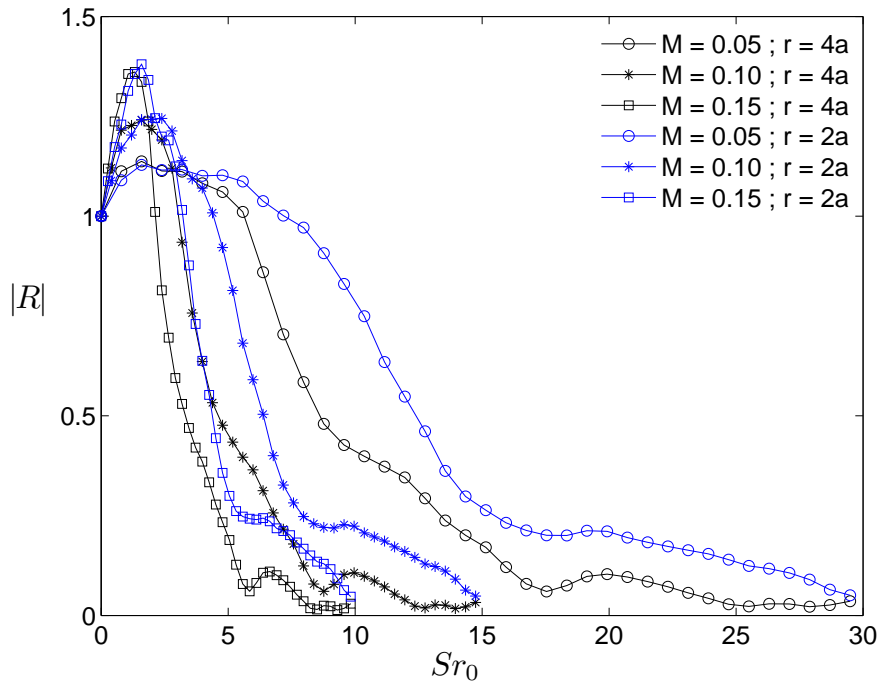


Figure 5.22 Numerical results for the magnitude of the reflection coefficient $|R|$ at the end of the straight pipe segment as a function of the Strouhal number Sr_0 for different circular horn profiles and different Mach numbers.

number at which the maxima of $|R|$ takes place in the unflanged pipe situation (see Fig. 5.12) but diverges from the experimental data provided by Peters et al. (1993), who found that the maximum magnitude of $|R|$ appears at $Sr_0 = \pi a/r$ for a circular horn with $r = 4a$.

The reflection phenomena at the pipe-horn junction can also be plotted in terms of the energy reflection coefficient, defined as $R_E = |R|^2 \left(\frac{1-M}{1+M}\right)^2$ as depicted in Fig. 5.23, which represents the ratio between outgoing and reflected energy.

For the critical region $Sr_0 \sim \pi/2$ the values of $|R_E|$ become greater than unity. This behavior agrees with the experimental data of Peters et al. (1993) for a horn with $r = 4a$. In their results, however, the peak of the energy reflection function was found at

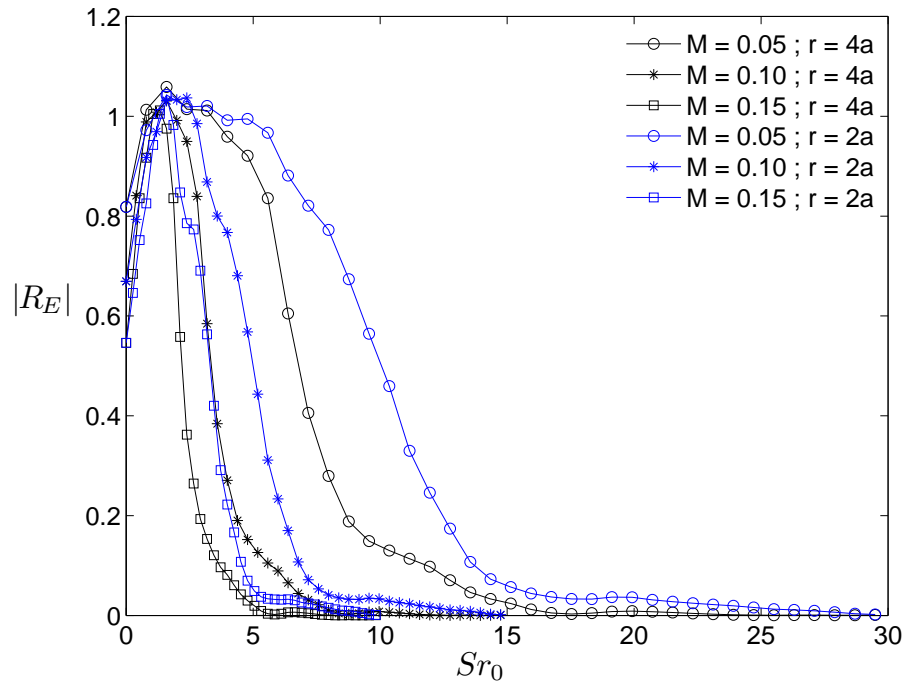


Figure 5.23 Numerical results for the energy reflection coefficient $|R_E|$ at the end of the straight pipe segment as a function of the Strouhal number Sr_0 for different circular horn profiles and different Mach numbers.

$Sr_0 \sim \pi/4$. In the critical Strouhal region, the amount of incoming acoustic energy is greater than the amount of radiated energy. This paradox is explained by the transfer of kinetic energy from the unsteady vortex sheet to the acoustic field inside the pipe and it is similar to the phenomenon in unflanged pipes issued a mean flow. Nevertheless, in the case of pipes terminated by flaring horns, the mechanism of energy transfer from the flow to the acoustic field seems to be much more effective.

Peters et al. (1993) explain that the maximum energy transfer happens when the traveling time of the vortical instabilities across the horn matches the acoustic oscillation period. According to this rationale, the location of the critical region, expressed in terms of the Strouhal number, would also be a function of the horn curvature r . As previously

discussed, however, the results suggest that the region of maximum transfer is independent of the horn geometry ($Sr_0 = \pi/2$). Hence, the explanation given in Sec. 5.3.2 for the region of maximum energy transfer in the case of unflanged pipes can be generalized to pipes terminated by circular horns. That is, the maximum reflection coefficient happens when the oscillation period of the acoustic source is approximately equal to the time necessary for the vortical instabilities to propagate a distance equal to the pipe diameter D as expressed in Eq. (5.21).

Figure 5.24 provides a qualitative description of the interaction of the unstable vortex sheet with the lip of the pipe by depicting snapshots of the flow stream lines (in blue) superimposed on the velocity field (in red) at the pipe exit for $M = 0.15$. In this particular case, instead of using the excitation scheme described by Eqs. (5.9) and (5.10), the acoustic source is sinusoidally excited by a single frequency equivalent to $Sr_0 = \pi/2$, which corresponds to the region of the Strouhal number where the maximum transfer of energy from the flow to the acoustic field takes place. The snapshots were taken for different intervals within a single oscillation cycle of the particle velocity u' , measured at the pipe open end. The fraction of the oscillation cycle associated with each snapshot is depicted at the upper right corner of each figure.

5.5.4 Results for the End Correction Fraction

The dimensionless end correction l/a as a function of ka is presented in Fig. 5.25 for different Mach numbers and for the two different horn geometries.

The general behavior agrees with that found for a pipe with an unflanged termination. That is, the effect of a mean flow appears to be only relevant in the low frequencies, namely before the end correction maxima found at $ka \sim \pi/2\kappa$ for both geometries, where $\kappa = r/a$. In this region, the end correction drops dramatically. The magnitude of the end

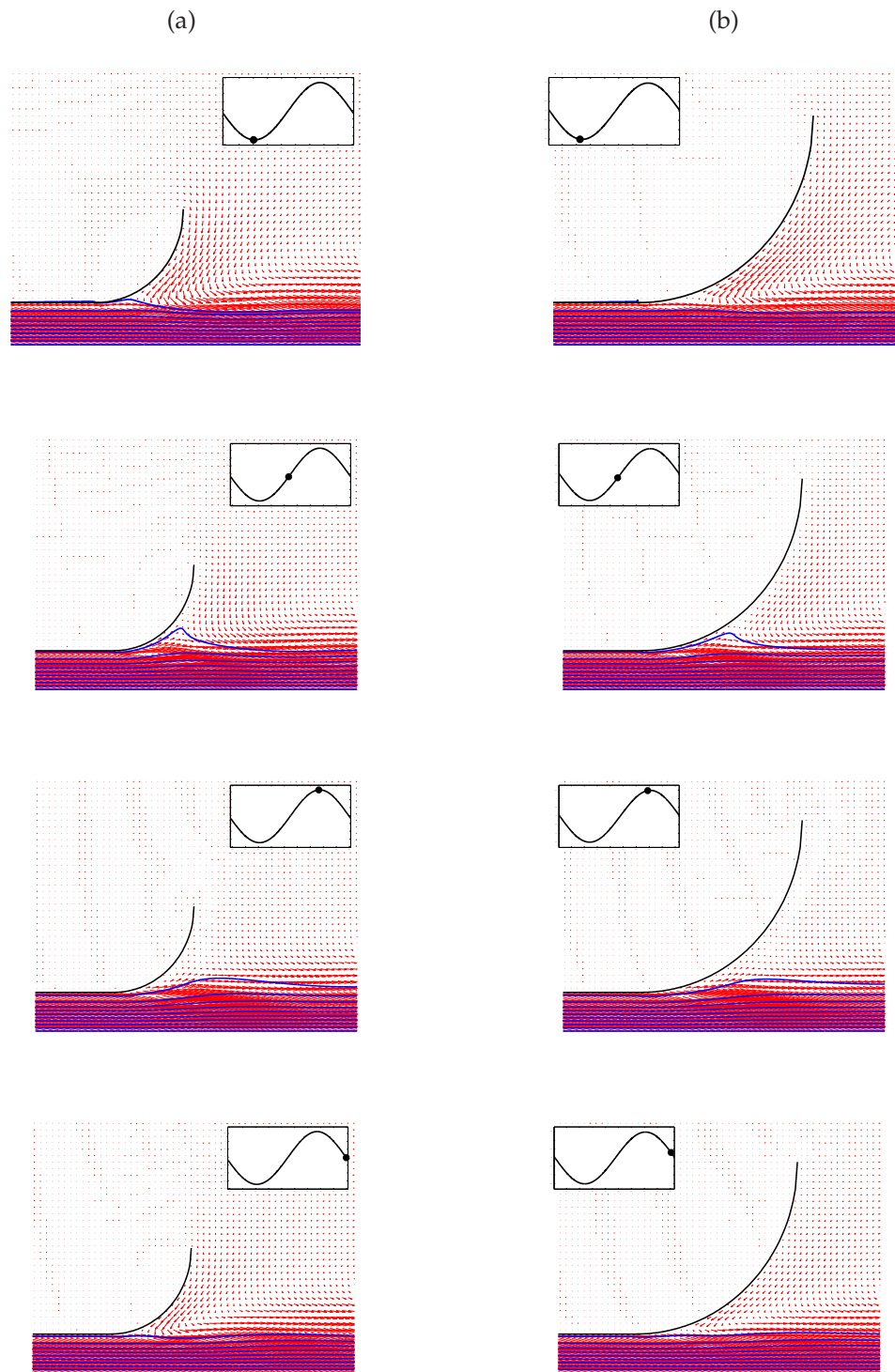


Figure 5.24 Mean flow visualization at the output of the pipe-horn system at different time frames within a single oscillation period. The boxes on the top indicate the frame position in terms of the flow velocity cycle measured at the pipe-horn junction. The stream lines are depicted in blue and red arrows indicate the velocity field: (a) $M = 0.15$ and $r = 2a$; (b) $M = 0.15$ and $r = 4a$;

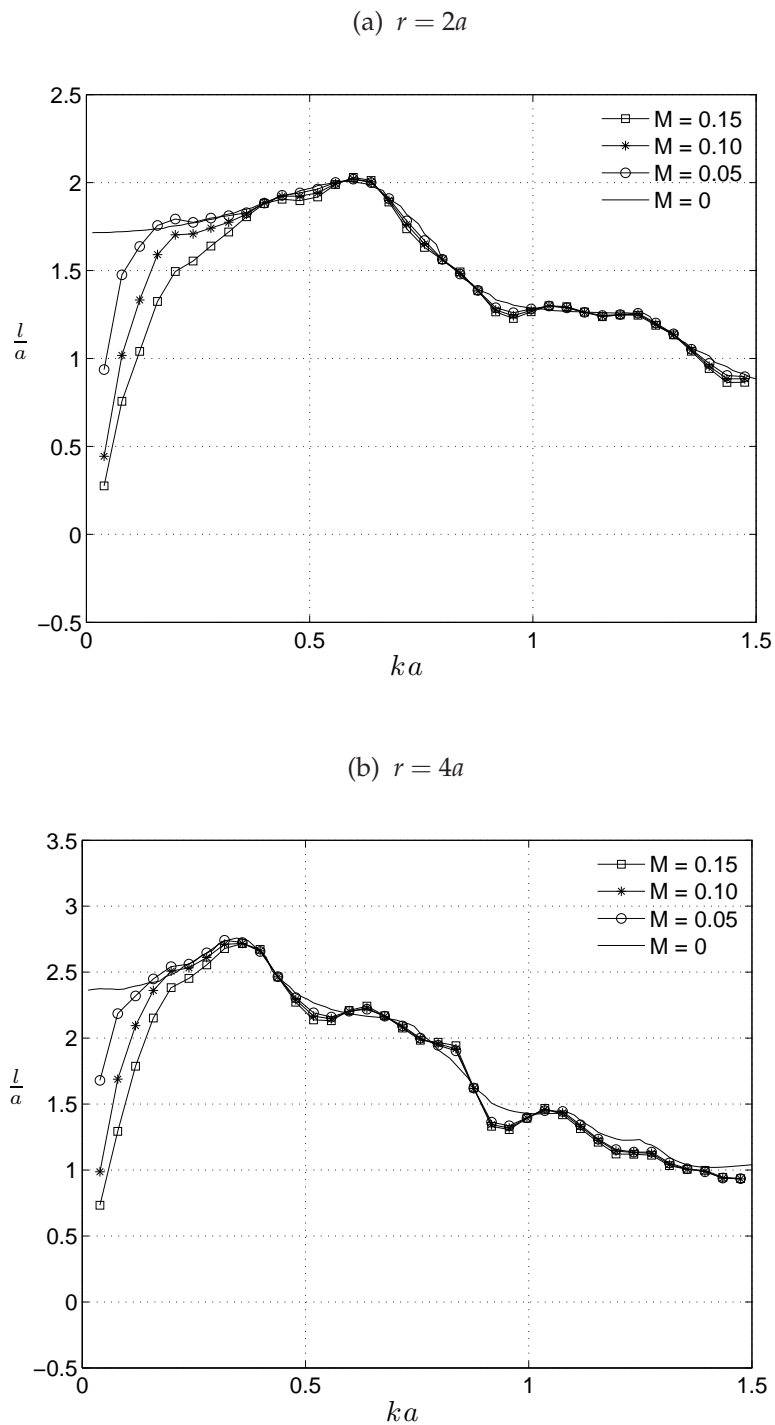


Figure 5.25 Numerical results for the fraction of the end correction l/a at the end of the straight pipe segment as a function of the Helmholtz number ka for two different circular horn profiles and different Mach numbers.

correction maxima are independent of the flow speed. This behavior is opposite that for the reflection coefficient $|R|$, where the amplitude of the peaks depends only on the flow velocity. The effect of flow becomes negligible for higher frequency values, namely $ka > 0.5\pi/\kappa$ for which l/a approximates the solution obtained in the absence of a mean flow for the same geometries.

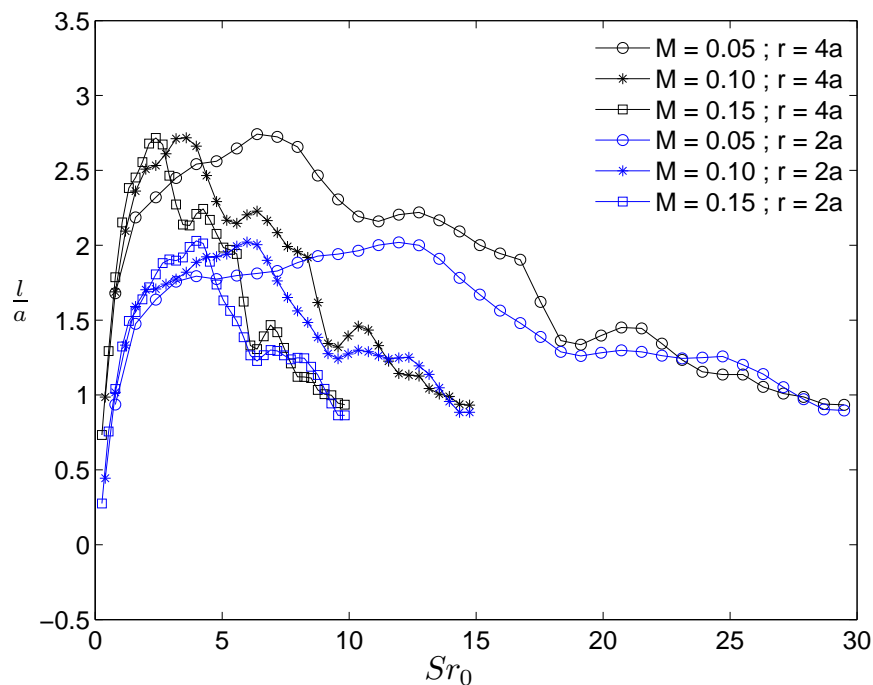


Figure 5.26 Numerical results for the fraction of the end correction l/a at the end of the straight pipe segment as a function of the Strouhal number Sr_0 for two different circular horn profiles and different Mach numbers.

The results for l/a are also presented as a function of the Strouhal number Sr_0 in Fig. 5.26. For very low Strouhal number values ($Sr_0 < \pi/2$) the graphs obtained for the same geometry and different Mach numbers collapse into a single curve. As $Sr_0 \rightarrow 0$, l/a tends to converge to very low values, namely $\rightarrow 0$, for the termination with curvature $r = 2a$, and $\rightarrow 0.2$ for the termination whose curvature is $r = 4a$. For the last case, Peters et al.

(1993) found experimentally a negative value $l/a \sim -0.25$ and a maximum value ~ 2.3 .

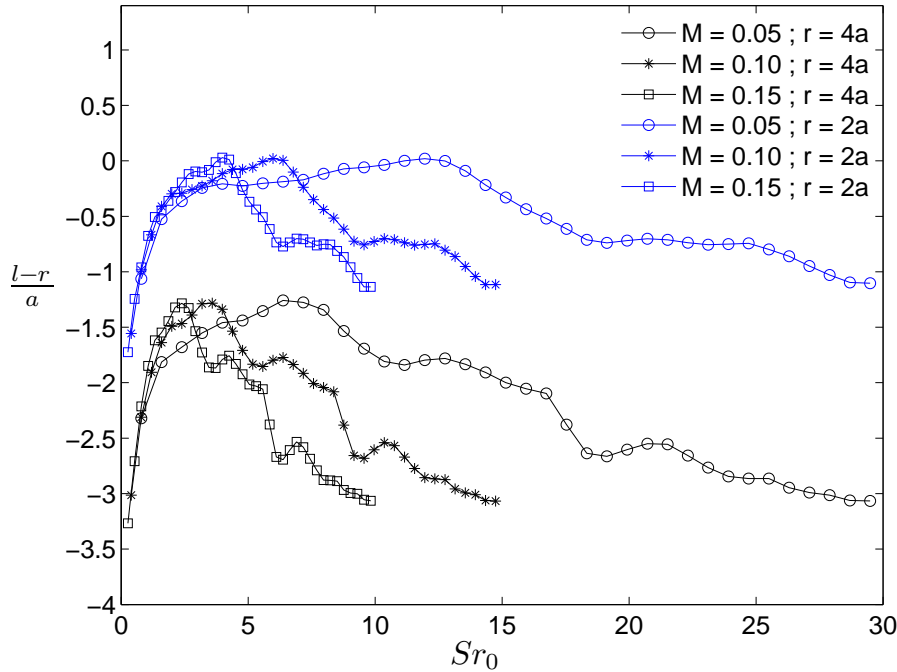


Figure 5.27 Numerical results for the fraction of the end correction $l - r/a$ at the end of the straight pipe segment as a function of the Strouhal number Sr_0 for two different circular horn profiles and different Mach numbers.

Figure 5.27 depicts the effect of flow on the end correction only due to the inertia provided by the fluid loading at the open end. In this case, the end correction becomes negative for most Strouhal values. The results show that the curvature radius of the horn is inversely proportional to the end correction. As discussed before, the end correction can be interpreted as the distance, measured from open end, at which the acoustic wave finds the same boundary conditions associated to an open end at the low frequency limit, that is the pressure $p' = 0$ and inverted phase π . In the case of the unflanged pipe, the wave has to propagate an extra length downstream the pipe's open end before it gets reflected back. In a pipe terminated by a horn with a big curvature radius, the negative

end correction implies that the wave is reflected with inverted phase much before the horn's open end.

5.5.5 Mean Flow Effect on the Acoustic Transmission of Woodwind Instruments

The previous section has shown the influence of a subsonic mean flow on the behavior of $|R|$ and l/a at the junction between an open-ended pipe and a horn, for horns with different curvature radii. Nothing has been said, however, about the consequences of the mean flow on the acoustic behavior of wind instruments. This section presents a more detailed investigation in this regard by considering the typical range of mean flow found in wind instruments during normal playing.

For the investigations to be performed, the values of the volume flow at the open end need to be known. Unfortunately, precise values of the volume flow at the open end of wind instruments for different registers and dynamic levels is rather sparse in musical acoustics. On the other hand, several works have reported measurements of the volume flow through the reed channel of woodwind instruments (Bouhuys, 1964, 1965, Pawlowski and Zoltowski, 1987). In cases where the flow was measured using the lowest register, that is, when all the toneholes are closed, the volume flow at the open end can be easily estimated by assuming conservation of mass. Some of the results of the volume flow through the mouthpiece of a clarinet for the lowest register for different dynamic levels is provided by Fuks (1998). These results are presented in Table 4.2 with other estimated parameters which will be useful in evaluating the influence of the mean flow

The Strouhal number Sr_0 is given by ka/M , where the radius $a = 7.5 \times 10^{-3}$ m at the throat of the clarinet horn was used as the reference for the calculation of $ka = 2\pi fa/c_0$ and $M = U_{mp}/\pi a^2 c_0$ and $c_0 = 340$ m/s, where U_{mp} is the volume flow measured in the

Table 5.1 Experimental and estimated flow parameters in the clarinet for tone *D3* (146.83 Hz)

Situation	Reed Type	Dynamic Level	Volume Flow [m^3/s]	M $\times 10^{-3}$	Sr_0
A	soft	pp	7.4×10^{-5}	1.2	16.5
B		mf	9.3×10^{-5}	1.5	13.2
C		ff	1.6×10^{-4}	2.7	7.64
D	hard	pp	1.1×10^{-4}	1.8	11.1
E		mf	1.5×10^{-4}	2.5	8.14
F		ff	2.5×10^{-4}	4.2	4.88

mouthpiece. A simulation was conducted using the same lattice parameters and boundary conditions as described in the previous section. In this case, a horn typically found in clarinets was attached to the pipe's open end. The horn profile is given by the catenoidal function $y = a \cosh(x/h)$, where h is a constant, normally $h = 0.015$, and the length of the horn $L_H = 4a$. The simulations were run for three different Mach numbers to cover the range of values presented in Table 5.1, namely, $M = 0, 0.001$ and 0.005 .

The simulation results depicted in Fig. 5.28 show that the behavior of $|R|$ is nearly insensitive to the Mach numbers considered in the simulations. In other words, results obtained for $M = 0.001$ and 0.005 are very close to that obtained for a zero mean flow ($M = 0$). Hence, the assumption of a null mean flow on the estimation of $|R|$ provides a reasonable approximation.

On the other hand, the results for the end correction l/a were found to be significantly different from the zero mean flow situation as depicted in Fig. 5.29. The black dots represent the end corrections associated with each playing condition presented in Table 5.1. They were obtained by performing a linear interpolation between the experimental and the numerical results for $ka \sim 0.02$, which corresponds to the tone *D3*.

The interpolated values of the end correction can be used to estimate the effect of

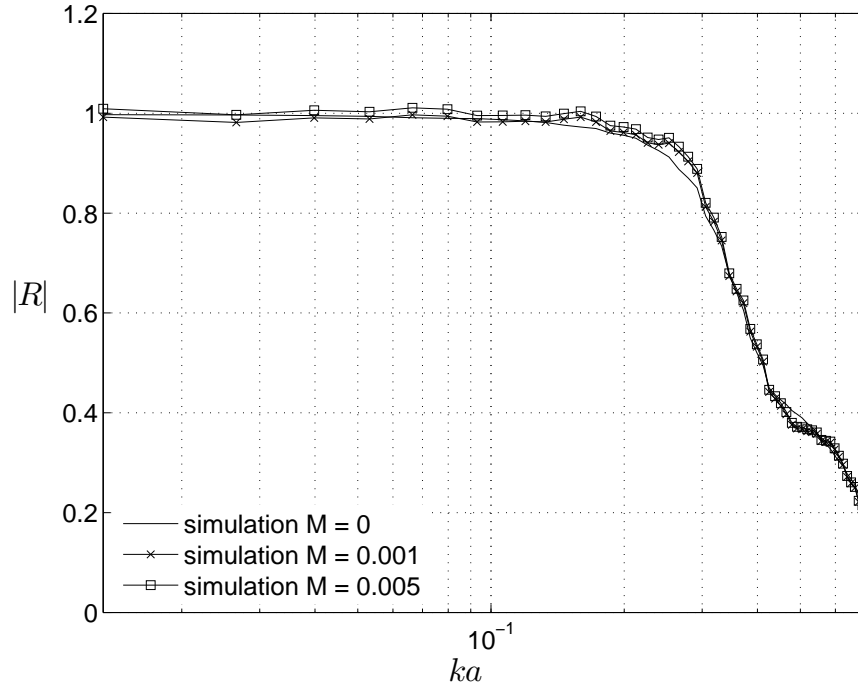


Figure 5.28 Numerical results for the magnitude of the reflection coefficient for different mean flow values measured at the junction between a cylinder and a catenoidal horn

the mean flow on the instrument's fundamental frequency f_0 for the different dynamic ranges presented in Tab. 5.1. This is achieved by assuming that the fundamental frequency of a pipe (nearly) closed at one end and open at the other is given by

$$f_0 = \frac{c_0}{4(L + l)}, \quad (5.23)$$

where L is the nominal length of the pipe and l is the end correction. Equation (5.23) implies that $f_0 \propto M$ because $l \propto 1/M$. Manipulating Eq. (5.23) and recalling that L is a constant leads to an expression for the resulting frequency f_0^* due to a variation of the

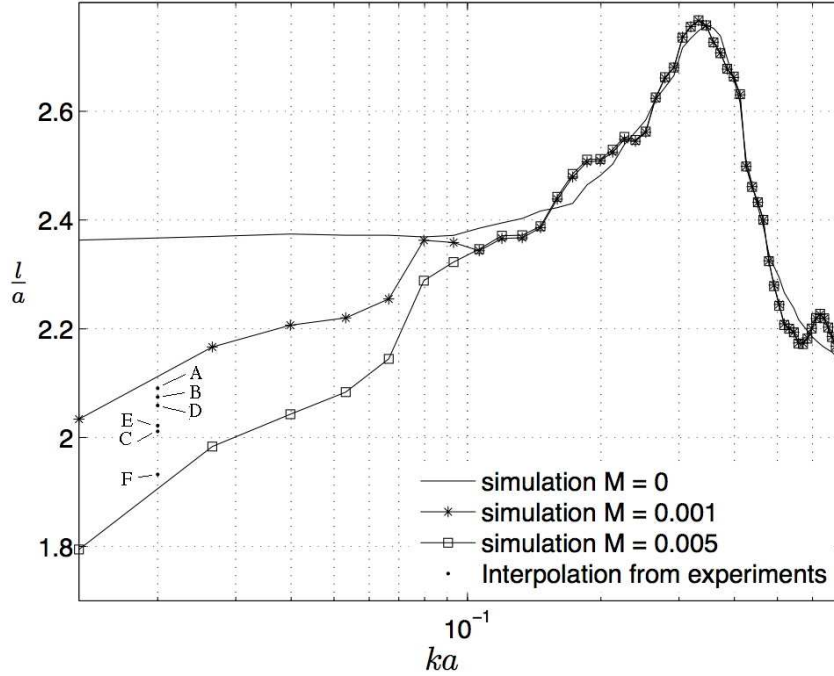


Figure 5.29 Numerical results for the dimensionless end correction for different mean flow values measured at the junction between a cylinder and a catenoidal horn

end correction Δl , given by

$$f_0^* = \frac{f_0 c_0}{4 f_0 \Delta l + c_0}. \quad (5.24)$$

Table 5.2 provides some parameters that illustrate the effect of the mean flow on the frequency. The parameter $e_f = f_0^* - f_0$ represents the error obtained when the frequency is estimated by using an end correction value l corresponding to a zero mean flow solution. In this case f_0 is assumed to be = 146.83 Hz, which corresponds to the tone *D3*, and f_0^* is obtained through Eq. (5.24), where Δl is the difference between the end correction for zero and non-zero mean flow at $ka = 0.02$, as shown in Fig. 5.29. Δf is the percentage of frequency shift from f_0 to f_0^* and Δf_{dyn} is the frequency shift between dynamic ranges.

The most significant frequency variation between zero and non-zero mean flow cal-

Table 5.2 Frequency variation due to the effect of the mean flow

Situation	Reed Type	Dynamic Range	f_0^* [Hz]	Δl $\times 10^{-3}$ [m]	e_f [Hz]	Δf %	Δf_{dyn} %
A	Soft	pp	147.36	-2.1	0.53	0.36	0.00
B		mf	147.39	-2.2	0.56	0.38	0.02
C		ff	147.52	-2.7	0.69	0.46	0.10
D	Hard	pp	147.42	-2.3	0.59	0.40	0.00
E		mf	147.50	-2.6	0.67	0.45	0.05
F		ff	147.67	-3.3	0.84	0.57	0.16

culations was found for the situation F, which corresponds to a hard reed played at *fortissimo* dynamic level. In this case, the frequency variation Δf and the frequency error e_f were, respectively 0.57% and 0.84 Hz. For both hard and soft reeds, the maximum effect of the mean flow on the frequency was found between *pianissimo* (pp) and *fortissimo* (ff) dynamic ranges, which corresponds to a frequency shift f_{dyn} equal to 0.16% and 0.10%, respectively.

Previous studies on the perception of frequency variations suggest that the results presented in Tab. 5.2 are musically relevant. These tests have observed that the limen of frequency discrimination at ~ 150 Hz can be as low as 0.5% for frequency modulation (Fastl and Zwicker, 2007)⁴ and $\sim 0.15\%$ for frequency difference (Nordmark, 1968).

The results in Tab. 5.2 are only valid for the particular case associated with the lower (chalumeau) register in which all the toneholes of the bore are covered. Obviously, in situations other than that the volume flow produced by the player partially escapes from the open toneholes and, consequently, the Mach number, as measured at the horn throat, is drastically decreased. Moreover, the effect of the Mach number on higher frequencies ($ka > 0.1$) seems to be irrelevant on the behavior of the length correction, as shown in

⁴The discrimination of a frequency modulation of $\Delta f = 0.5\%$ was conducted using a modulation frequency of 4 Hz (Fastl and Zwicker, 2007) and was found to be amplitude independent for sound levels above 25 dB.

Fig. 5.29.

These results can, in part, explain the positive correlation between blowing pressure and frequency shift. Naturally, this correlation involves another mechanism associated with the lip pressure, as precisely described by Bak and Domler (1987).

5.6 Conclusions

As previously mentioned, the first objective of this chapter was to provide a relatively simple numerical technique capable at representing the acoustic radiation and transmission phenomena in axisymmetric waveguides carrying a mean flow. The second objective was to use the same technique in order to provide a deeper understanding of the influence of a subsonic mean flow on the transmission phenomena associated with the reflection coefficient and end correction at the open ends of pipes and horns.

The first objective was achieved by constructing different axisymmetric models of radiating waveguides using lattice Boltzmann techniques based on the D2Q9 LBGK scheme. The process of constructing the models had to overcome several difficulties whose solutions were essential to correctly represent the acoustic transmission phenomena in waveguides that carry a mean flow. Among these difficulties, the most challenging one was the development of an excitation scheme involving an acoustic source superimposed on a flow source. Another important difficulty was associated with the construction of adequate boundary conditions in order to avoid spurious acoustic wave generation that could jeopardize the simulation results.

The results from the simulation of an unflanged pipe with zero mean flow agree very well with the available analytical solution provided by Levine and Schwinger (1948). In this case, one drawback of the model proposed here was the inability to properly rep-

resent the directivity factor G_ϕ at low frequencies. The results suggest that this problem can be circumvented by increasing the area of the radiation domain, so that the measurements of the pressure and particle velocity can be calculated in the far field.

More exciting results are obtained when the simulations take into account the presence of a mean flow carried by the waveguides. In this case, the results obtained for the unflanged pipe model (Sec. 5.3) agree very well with the analytical theory proposed by Munt (1990) and with the experimental results provided by Allam and Åbom (2006). This is particularly interesting, considering that the analytical theory (Munt, 1990) was derived based on the assumption that the vortex sheet that separates the issuing jet and the environment fluid is infinitely thin. In real situations, as well as in the simulations presented here, the vortex sheet increases in thickness due to the flow entrainment phenomenon. Even so, the results seem to hold with the theory.

From a qualitative point of view, the results for the horn carrying a subsonic mean flow (Sec. 5.5) indicate a very similar behavior to those found for an unflanged pipe (Sec. 5.3). That is to say, the maximum value of the magnitude of the reflection coefficient takes place at $T \sim D/u_v$, regardless of the geometric characteristics of the open end. When this condition is met, trains of vortices are shed from the open end and propagate downstream on the mixing layer between the jet and the outer stagnant fluid at a speed $u_v = u_0|_{r=0}/2$ (Fig. 5.5.3). Conversely, when $T \neq D/u_v$ the vortex generated by the interaction between the flow and acoustic fields remains in the vicinity of the open end.

From a quantitative perspective, significant differences are found between an unflanged pipe and a pipe terminated by a horn in terms of magnitude of the reflection coefficient $|R|$, as well as in terms of the dimensionless end correction l/a . The most striking difference is related to the different maxima of $|R|$ achieved in each case. For the same flow conditions, pipes terminated by horns normally have their maximum

amplitudes of the reflection coefficient magnitude $\sim 20\%$ higher than unflanged pipes, regardless of the horn curvature.

In both cases, the amplification of the reflection coefficient, i.e. $|R| > 1$, is caused by a transfer of kinetic energy from the flow to the acoustic field. This happens because the instability caused by the acoustic field \mathbf{u}' induces the roll up of the vortex sheet into regions of concentrated vorticity. In turn, the vorticity transforms its vortical kinetic energy into acoustic energy. A powerful basis to analyze this phenomenon is provided by Howe (1984) who describes the transfer of vortical kinetic energy into the acoustic field in low Mach number and isentropic flows by

$$P' = -\rho_0 \int_A \overline{\mathbf{u}' \cdot (\boldsymbol{\omega} \times \mathbf{u})} dx, \quad (5.25)$$

where P' is the instantaneous acoustic power and $\boldsymbol{\omega}$ is the *curl* of \mathbf{u} , as introduced in Sec. 2.2.7. The integral on the right-hand side of Eq. (5.25) represents the vortex 'strength' and is carried over the area A of $\boldsymbol{\omega}$. The overline indicates the time-average over one oscillation cycle. The placement of a horn at the open end acts to augment the vortex strength term in Eq. (5.25) due to two main reasons: First, the instability of the pressure gradient at the horn walls triggered by the acoustic field forces a cyclic adhesion/separation of the jet at the walls, thereby generating additional vorticity (see Fig. 5.24). The second reason may be associated with the entrainment of the surrounding fluid into the jet due to the viscous drag at the vortex sheet. This can be better understood by considering Fig. 5.30.

For an unflanged pipe, the surrounding flow can be more easily drawn into the jet in comparison to the pipe terminated by a horn. As a result of that, more mass is entrained near the open end and the thickness of the jet increases faster, which forces the kinetic

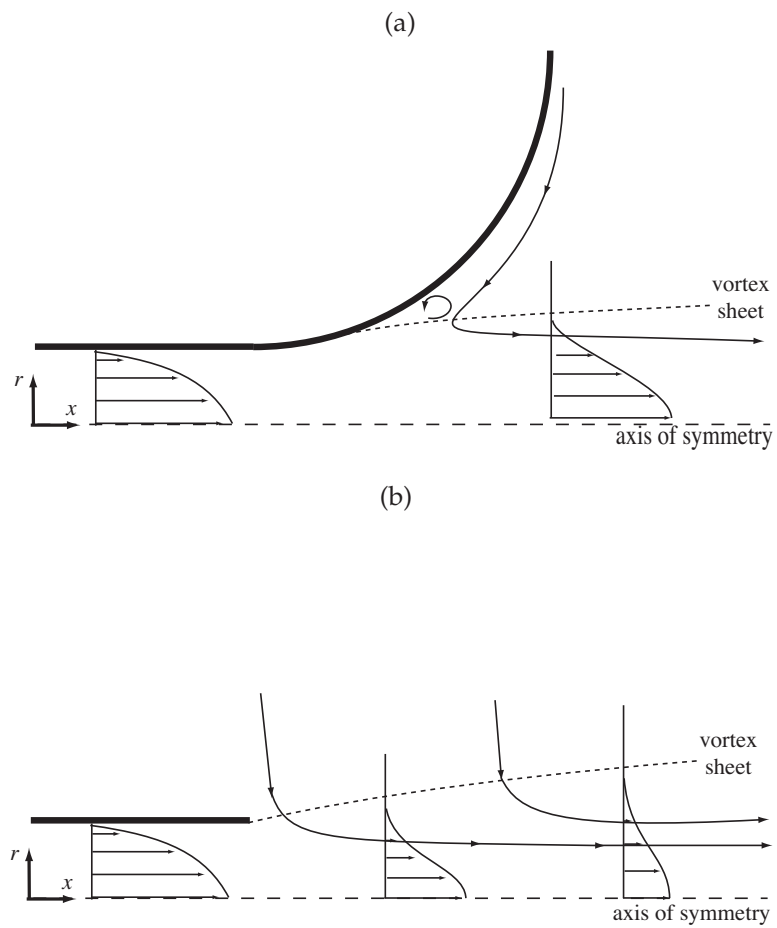


Figure 5.30 Flow entrainment patterns for two different pipe terminations: (a) unflanged pipe ; and, (b) cylindrical horn.

energy of the flow in the jet to be decreased. This is due to the fact that the pressure gradient dp/dx inside the jet is zero. Therefore, there is no net force acting on the jet, which requires the rate of flow of x -momentum through the jet cross section to be conserved in the x direction (Kundu et al., 2004).

Chapter 6

Conclusion

This research investigated aeroacoustic and fluid-structure interactions in single-reed woodwind musical instruments when a viscous unstable and low Mach number mean flow is considered. The investigations were conducted with numerical simulations using a two-dimensional lattice Boltzmann scheme that provides results with second-order accuracy and were focused on two main aspects. 1 - The unstable viscous flow through the reed channel and its influence on the oscillatory behavior of the reed, as well as the influences of different channel geometries; 2 - The effect of the mean flow on the acoustic transmission properties such as the magnitude of the reflection coefficient and the end correction.

6.1 Summary

1 - The Fluid-Structure Interaction in a mouthpiece-reed system

This investigation was conducted by constructing a numerical model of the mouthpiece-reed system to represent the problem of fully coupled fluid-structure interaction in sin-

gle reed mouthpieces. Second-order accurate results were obtained by using a two dimensional lattice Boltzmann scheme, to represent the fluid domain, coupled to a distributed model of the reed, which is resolved with a finite difference scheme. The behavior of the viscous flow through the reed channel was evaluated in three different mouthpiece geometries and two types of regimes, namely stationary and dynamic.

For the stationary regime, that is, when the reed was kept fixed in its rest position, the numerical results agreed very well with those predicted by the available quasi-stationary theory in terms of volume flow and steadiness of the vena contracta factor (van Zon et al., 1990). Conversely, the results diverged significantly from the same theory when a dynamic simulation was conducted, i.e., when the reed was free to oscillate. In this case, the assumption of a constant vena contracta α used by the theory was only observed within $\sim 40\%$ of the oscillation cycle, for short channel geometries and within less than 25% of the oscillation cycle for long channel geometries. Moreover, the patterns observed in stationary measurements such as fully detached flow, in the case of short reed channels, and the twofold pattern, in the case of long channels, were not observed in the dynamic simulations. The main difference in the flow behavior between short and long channels was found to be the time taken by the flow to adhere on the reed wall within one duty cycle. This characteristic was attributed to the effect of inertia associated with different fluid volumes within the reed channel and to the flow driven by the reed. The results also showed that different levels of self-sustained oscillations can be achieved in the absence of acoustic feedback due to the complexity of hydrodynamic forces acting on the reed, which supports the hypothesis proposed by Hirschberg et al. (1990, 1994) in the case of single reed mouthpieces.

2 - Acoustic Transmission from Unflanged Pipes and Horns

This set of analyses investigated the influence of a subsonic mean flow on the transmission phenomena associated with the reflection coefficient and end correction at the open ends of pipes and horns. This was achieved by developing axisymmetric models based on the lattice Boltzmann method. The analyses were carried out for a range of Mach and Helmholtz numbers corresponding to $0 \leq M \leq 0.15$ and $0 \leq ka \leq 1.5$, respectively. Furthermore, the ratio between the amplitude of the acoustic particle velocity and the cross-sectional averaged mean flow velocity was kept constant and equal to 0.1.

The results obtained from an unflanged pipe agreed very well with the theory provided by Levine and Schwinger (1948), for a pipe carrying a zero mean flow, and with experimental and theoretical results for an unflanged pipe carrying a subsonic mean flow, provided by Allam and Åbom (2006) and Munt (1990), respectively. Simulations were carried out by preserving the same numerical parameters used in the unflanged pipe situation in order to evaluate the behavior of the magnitude of the reflection coefficient and the end correction when horns with different profiles are placed at the end of the pipe.

Similarly to the unflanged pipe situation, it was found that the magnitude reflection function $|R|$ becomes greater than one for a critical region of the Strouhal number $Sr = ka/M$ when the pipe carries a subsonic mean flow. Interestingly, the maxima of $|R|$ was found to be fixed at $Sr = \pi/2$ for both unflanged pipes and horns. This value of the Strouhal number is achieved when the frequency of the acoustic field inside the pipe corresponds to a period $T \sim D/u_v$, where D is the pipe diameter and $u_v = u_o/2$ is the speed of propagation of the vortex sheet disturbances. When this condition is met, trains of vortices are shed from the open end, which propagate downstream at the vor-

tex sheet. Conversely, when $T \neq D/u_v$ the vortex generated by the interaction between the flow and acoustic fields remains in the vicinity of the open end. Furthermore, the results suggest that, for low values of the Strouhal number ($St < 2.5$), the geometry of the horn does not play a significant role on the behavior of $|R|$, which is mainly defined by the Mach number. However, it was observed that, within the critical region, horns provide values of $|R|$ which are $\sim 20\%$ higher than those provided by an unflanged pipe. In the case of the end correction l/a , it was observed that the drop due to the presence of a mean flow at low regions of the Strouhal number is much more accentuated when a horn is placed at the open end of the pipe. Conversely from the behavior for $|R|$, however, it was found that the end correction l/a is highly dependent on the horn geometry, especially at $St < 2.5$. In this case, the curvature radius is directly proportional to the end correction drop.

Common values of the mean flow obtained experimentally by Fuks (1998) during clarinet performance were used to predict the behavior of $|R|$ and l/a for different playing conditions (dynamic ranges). It was found that $|R|$ is not affected by the range of the Mach numbers observed during normal clarinet playing. On the other hand, small variations of the end correction are observed when they are calculated using the Mach numbers measured during different dynamic ranges. When only the effect of the mean flow is taken into account, the variations may cause an alteration of the fundamental frequency equal to 0.53%, which corresponds to 0.84 Hz when the lowest register of a clarinet (~ 148 Hz) is used as a reference. This effect may be more accentuated in brass instruments, in which the Mach number is normally higher and the bells have a much more rapid flare, thus partially explaining the effect of pitch shift as a function of the blowing pressure.

6.2 Limitations of the Analyses

In the case of the analyses involving the mouthpiece-reed system, the two-dimensional nature of our numerical approach restricts the results to a qualitative analysis. Another limitation is associated with the lack of acoustic feedback, which neglects eventual influences of the fluid-acoustic interaction within the reed channel. Nevertheless, the numerical results presented here correspond to a situation that is much closer to normal playing than that provided by the quasi-stationary approximation and, therefore, contribute to our understanding of the behavior of dynamic flow in single-reed mouthpieces and its dependency on the characteristics of the reed channel geometry.

The analyses involving the radiation from pipes with different terminations are restricted to internal parameters, that is, the magnitude of the reflection coefficient and the end correction. This is because the determination of far-field directivity factors at low frequencies requires an extremely large radiation domain, which would be very expensive from the computational point of view. Moreover, the external sound generated by the energy transfer from the flow to the acoustic field at the open end cannot be accurately determined from a two-dimensional axisymmetric model, such as the one used. This is because a two-dimensional representation ignores the contribution of the vortex filament curvature existent in a real three-dimensional situation, which is responsible for the dissipation of energy by means of self-induced velocity (Peters et al., 1993). Thus the two-dimensional approach would lead to an overestimation of the produced sound.

6.3 Suggestions for Future Work

In the case of the mouthpiece-reed analyses, more investigations are needed in order to understand the behavior of the dynamic flow at lower values of the Strouhal number,

generally observed in normal playing. Moreover, it would be also interesting to evaluate the influence of the acoustic coupling between mouthpiece-reed system and resonator on the flow behavior. In the first case, a simplified solution can be attained by forcing the reed to oscillate at frequencies that correspond to the bore resonances. One possible way to investigate the second issue can be achieved by using the same LBM model as discussed in Appendix C. More challenging steps could be taken towards the investigation of the mechanisms of energy transfer between flow and the acoustic field, as well as the characterization of aeroacoustic sources in the mouthpiece and its contribution on the instrument's sound content. In both cases, a three-dimensional model is required, which would represent an increase of $\sim 3 \cdot \chi^{3/2}$, where χ is the computational demand of the two-dimensional approach.

Appendix A

Non-aligned and moving boundaries for LBM

This section provides the details of the implementation of the algorithms used to represent the bounce-back scheme for static solid boundaries that are not aligned with the fluid grid, as well as for solid boundaries that move within the fluid grid as a function of time.

A.1 Non-aligned boundaries

Bouzidi et al. (2001) provided a solution to overcome a major limitation of the traditional bounce-back scheme used to represent the non-slip boundary condition in LBM. The limitation is related to the fact that the traditional bounce-back algorithm always "sees" the solid boundary at a distance $\delta_x/2$ away from the closest fluid cell in the grid, regardless of their real distance. This drawback can be explained with the following example: One can imagine a particle at a position x_j propagating towards the wall (di-

rection c_1), at an arbitrary distance $q\delta_x$ away from it, where $q \equiv |x_3 - x_w|/\delta_x$ and $q \neq 1/2$ (Fig. A.1). Intuitively, the particle will depart from its initial position at x_j , travel a distance $q\delta_x$ with velocity c_1 , hit the solid wall, reverse its momentum, then return to its starting point at x_j with velocity c_3 . In this case, the total distance traveled by the particle at the end of one time step δ_t would be $2q\delta_x$.

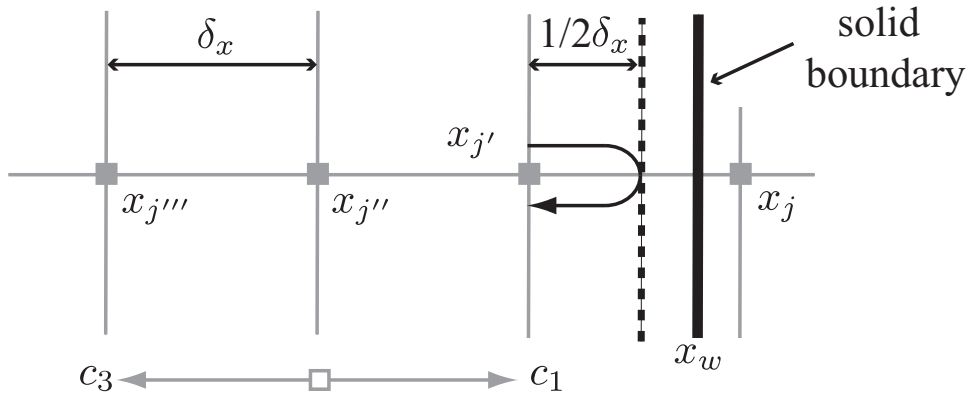


Figure A.1 Particle reflection from a non-aligned solid wall when implemented by the simple bounce-back scheme.

Nevertheless, considering the fact that the propagation velocity $c = |c_1| = |c_3|$ and the time step δ_t are constants in LBM, the real distance propagated by the particle during one time step will always be $\delta_x = c\delta_t$. Thus, when $q \neq 1/2$, the particle would end up in a position x_{na} that does not exist in the lattice grid and, therefore, $f_3(x_j')$ could not be created. The traditional bounce-back scheme simplifies this problem by assuming the boundary to be at $q\delta_x = 1/2$, as represented by the dashed line in Fig. A.1. One consequence of this simplification is the reduced order of accuracy of the boundary representation due to the “staircase” effect (Succi, 2001).

The solution found by Bouzidi *et. al.* for taking into account the real position of the solid boundaries when $q \neq 1/2$ consists in recreating the values of $f_3(x_j')$ based on the values at x_{na} , which in turn, are obtained by quadratic interpolation based on the values

of $x_j, x_{j'}, x_{j''}$ and $x_{j'''}$ before the reflection on the wall.

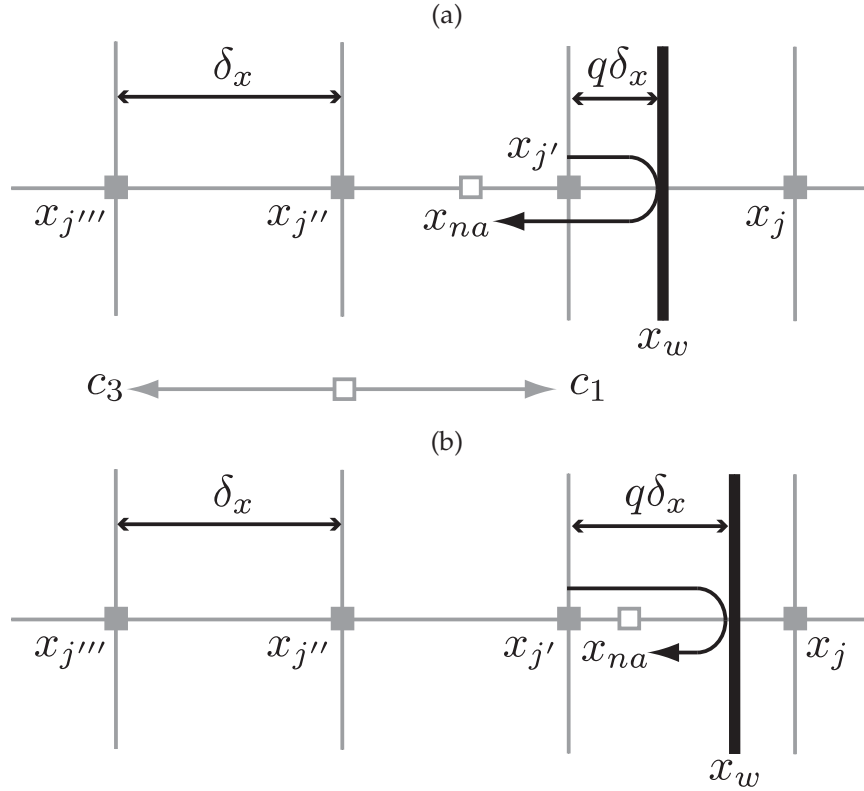


Figure A.2 Particle reflection from a non-aligned solid wall when implemented by the interpolated bounce-back scheme.: (a) for $q < 1/2$, (b) for $q \geq 1/2$.

This is easy to understand by observing that $f_1(x_{na})$ becomes $f_3(x_{j'})$ after one time step, in the same way that $f_1(x_{j'})$ becomes $f_3(x_{na})$. In this case, the interpolation scheme before the reflection will depend on whether $q < 1/2$ or $q \geq 1/2$. For $q < 1/2$, $f_1(x_{na})$ is determined by the values of $f_1(x_j)$, $f_1(x_{j'})$ and $f_1(x_{j''})$ (Fig. A.2(a)). For $q \geq 1/2$, $f_1(x_{na})$ is determined by the values of $f_1(x_j)$, $f_3(x_{j''})$ and $f_3(x_{j'''})$ (Fig. A.2(b)). Bouzidi et al. (2001) give the formulas for generalized propagation directions i by:

$$f_{\hat{i}} = q(1 + 2q)f_i(\mathbf{x}_j + \mathbf{c}_i\delta_t, t) + (1 - 4q^2)f_i(\mathbf{x}_j, t) - q(1 - 2q)f_i(\mathbf{x}_j - \mathbf{c}_i\delta_t, t) \quad (\text{A.1})$$

for $q < 1/2$

and

$$f_{\hat{i}} = \frac{1}{q(2q + 1)}f_i(\mathbf{x}_j + \mathbf{c}_i\delta_t, t) + \frac{2q - 1}{q}f_i(\mathbf{x}_j - \mathbf{c}_i\delta_t, t) - \frac{2q - 1}{2q + 1}f_i(\mathbf{x}_j - 2\mathbf{c}_i\delta_t, t) \quad (\text{A.2})$$

for $q \geq 1/2$.

where the index i defines the propagation direction and $\hat{i} = -i$. The above formulas can be implemented in a BGK lattice Boltzmann algorithm by following the steps:

1. Perform the relaxation step (collision).
2. Perform the propagations step.
3. Substitute the particles that have crossed solid boundaries by using the relations in equations A.1 and A.2

It is important to notice that the interpolation formulas A.1 and A.2 require values of distributions functions that cross the solid boundary after each time step. Determining these values is relatively easy for static boundaries but becomes more intricate for moving boundaries, as will be discussed in the next section.

A.2 Moving boundaries

Lallemand and Luo (2003) extended the non-aligned boundary technique developed by Bouzidi et al. (2001) for cases where the solid boundaries move within the fluid domain

as a function of time and whose maximum boundary velocity $\mathbf{u}_w \leq c/2$. The main difference from the static technique is the addition of a new term to equations A.1 and A.2, which refers to the contribution of momentum transfer from the solid to the fluid. Thus, equations A.1 and A.2 become:

$$\begin{aligned} f_i &= q(1 + 2q)f_i(\mathbf{x}_j + \mathbf{c}_i\delta_t, t) + (1 - 4q^2)f_i(\mathbf{x}_j, t) \\ &- q(1 - 2q)f_i(\mathbf{x}_j - \mathbf{c}_i\delta_t, t) + 3w_i(\mathbf{c}_i \cdot \mathbf{u}_w) \quad \text{for } q < 1/2 \end{aligned} \quad (\text{A.3})$$

and

$$\begin{aligned} f_i &= \frac{1}{q(2q + 1)}f_i(\mathbf{x}_j + \mathbf{c}_i\delta_t, t) + \frac{2q - 1}{q}f_i(\mathbf{x}_j - \mathbf{c}_i\delta_t, t) \\ &- \frac{2q - 1}{2q + 1}f_i(\mathbf{x}_j - 2\mathbf{c}_i\delta_t, t) + \frac{3w_i}{q(2q + 1)}(\mathbf{c}_i \cdot \mathbf{u}_w) \quad \text{for } q \geq 1/2. \end{aligned} \quad (\text{A.4})$$

where the term $w_i(\mathbf{c}_i \cdot \mathbf{u}_w)$ corresponds to the contribution of the momentum impinged by the solid boundary propagating with velocity \mathbf{u}_w . The derivation of this term relies on conservation of mass and momentum at the solid boundary in case there exists a forcing term F_i due to the fluid-solid interaction. In this case, $\sum_i F_i = 0$ and $\sum_i \mathbf{c}_i F_i = \rho_0 \mathbf{u}_w$ due to the conservation of mass and momentum, respectively. For the D2Q9 model used in Chapters 4 and 5, $w = 2/9$ for $i = 1 - 4$ and $w = 2/36$ for $i = 5 - 8$.

The algorithm for the moving boundary can be implemented in a BGK lattice Boltzmann model by taking the following steps.

1. Perform the relaxation step (collision).
2. Perform the propagations step.
3. Find the particles (distribution functions) that have crossed solid boundaries and

their respective distances in terms of the ratio q .

4. Determine the new velocity of the boundary points associated with each particle found in step 3.
5. Substitute the particles that have propagated across solid boundaries using the relations in equations A.3 and A.4.

The execution of the steps listed above is relatively straightforward from the computational point of view, except for step 3. The technique for the determination of the fluid particles that cross a moving generic boundary at every time step may require a heavy computational effort, and it is not provided in the paper of Lallemand and Luo (2003). The next section describes the solution found for evaluating the particles that cross a solid boundary at every time step and their respective distances from the boundary.

A.2.1 Finding the Crossing Particles and their Distances

The moving solid boundary in the implementation presented in Chapter 3 consists of a distributed model of the reed resolved with the finite difference method. Thus, the reed is represented by several straight line segments. The role of the algorithm provided in this section is to perform step 3 of the tasks presented in the previous section, i.e., to find the particles that cross each line segment of the reed at every direction and every time step. The substeps to accomplish step 3 are defined in the following sequence:

- 3.1 Create a polygon by the projection of the line segment in the direction i .
- 3.2 Enclose the polygon with a rectangular window.
- 3.3 Determine those particles within the rectangular window that are enclosed by the polygon.

3.4 Find the distances of the particle from the boundary in the propagation direction i

The first step aims to enclose all the particles that have crossed the boundary at a given propagation direction i , after one time step. This can be done by creating a polygon described by a one-step translation of the line segment in the direction i , as illustrated by Fig. A.3(a) and A.3(b).

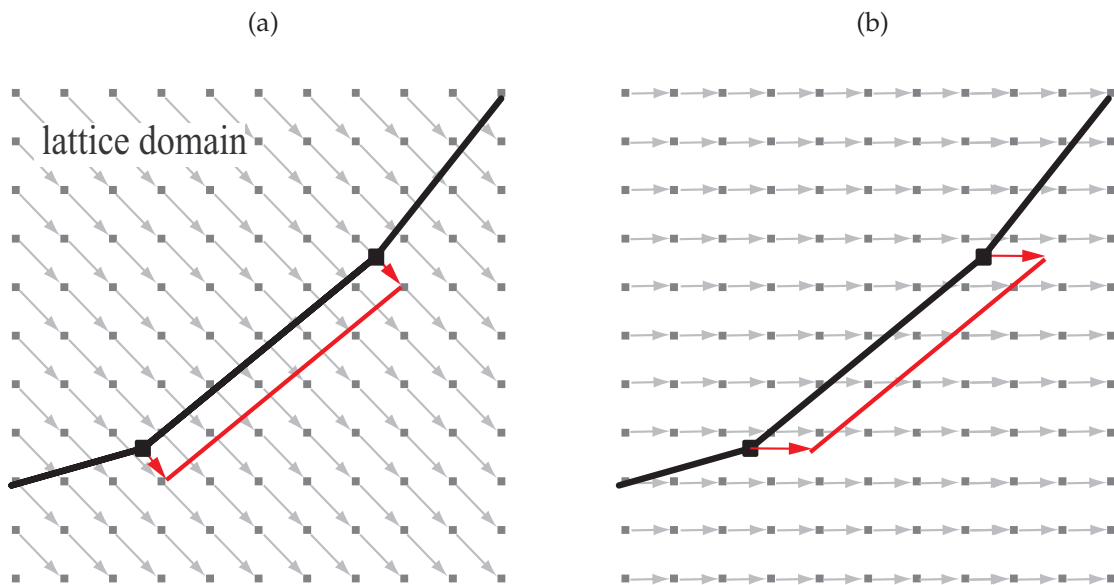


Figure A.3 Scheme of the polygon created by the one-space step translation of a boundary segment in different directions i , according to the D2Q9 model: (a) $i = 8$, (b) $i = 1$.

Step 3.2 consists in enclosing the created polygon with a rectangular window, whose boundaries are aligned with the lattice nodes (Fig. A.4(a) and A.4(b)). The objective of the window is to reduce the search domain when evaluating whether a particle lies within the polygon or not. If the window is neglected, the algorithm has to search for all the lattice points in the entire lattice domain, which represents a wasteful computational effort.

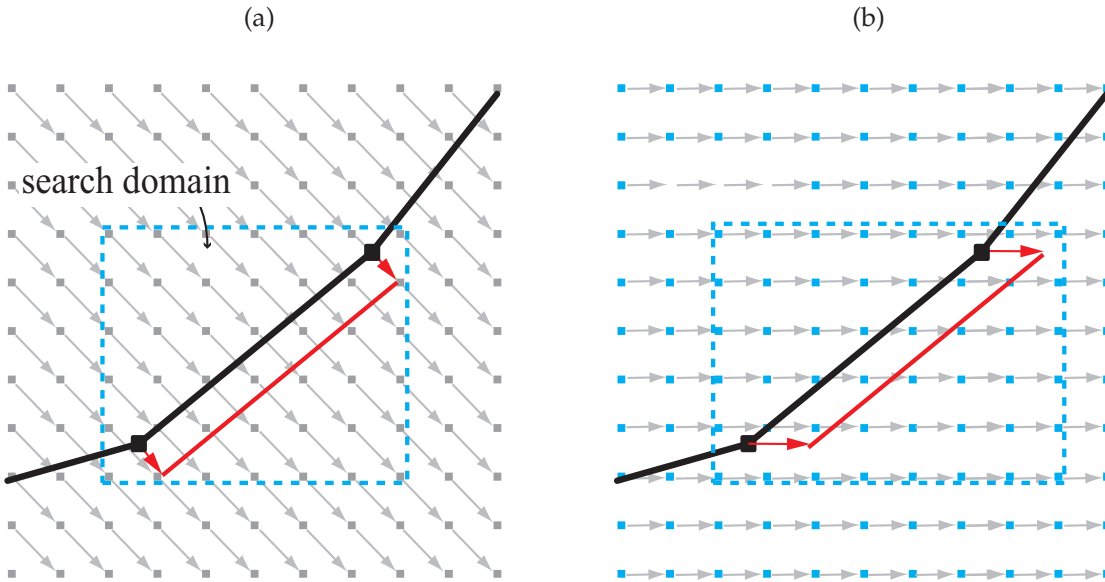


Figure A.4 Search domain created around the enclosing polygon for different propagation directions: (a) $i = 8$, (b) $i = 1$.

Step 3.3 is executed with function *InPolygon* from MATLAB [®]. Given the vectors X and Y that describe the coordinates of all lattice nodes enclosed by the window and the vectors xv and yv that describe the coordinates of the polygon vertices, the function returns the points enclosed in the polygon and their respective coordinates.

To determine the distances of the crossed particles from the line segment in step 3.4, it is necessary first to determine the linear coefficient B and angular coefficient A from the line equation describing each segment. Having these coefficients, as well as the coordinates of each particle obtained in sub-step 3.3, the relative distance q of the particles from the line segment is obtained by the simple trigonometric relations, given by:

$$q = \begin{cases} \frac{1}{\delta_x} \left| \left(x_p - \frac{y_p - B}{A} \right) \right| & \text{for } i = 1, 3 \\ \frac{1}{\delta_x} \left| (y_p - (A x_p + B)) \right| & \text{for } i = 2, 4 \\ \frac{1}{\delta_x \sqrt{2}} \sqrt{\left(x_p - \frac{B - Y_p - X_p}{A - 1} \right)^2 + \left(y_p - \frac{B - A(y_p - x_p)}{1 - A} \right)^2} & \text{for } i = 5, 7 \\ \frac{1}{\delta_x \sqrt{2}} \sqrt{\left(x_p - \frac{B - Y_p - X_p}{A + 1} \right)^2 + \left(y_p - \frac{B + A(y_p + x_p)}{1 + A} \right)^2} & \text{for } i = 6, 8 \end{cases} \quad (\text{A.5})$$

Appendix B

Axisymmetric LBM model

This appendix section describes the axisymmetric LBM model used in Chapter 5, which was first derived by Halliday et al. (2001) and improved by Reis and Phillips (2007). The common objective of these models is to recover the cylindrical polar form of the Navier-Stokes equations (Eqs. 2.25, 2.26 and 2.27) from the LBGK equation. This can be achieved by adding a space- and time- dependent source term h_i in the lattice Boltzmann equation (Eq. 3.15), so that it becomes

$$F_i(\vec{x} + \mathbf{c}_i \Delta t, t + \Delta t) - F_i(\vec{x}, t) = -\frac{1}{\tau}(F_i - F_i^M) + h_i, \quad (\text{B.1})$$

where,

$$h_i = h'_i + h''_i, \quad (\text{B.2})$$

and h'_i and h''_i are first- and second- order terms, respectively. The derivations conducted by both Halliday et al. (2001) and Reis and Phillips (2007) agree on the form of the first-

order term which is easily obtained by the expression

$$h'_i = -\frac{\epsilon_i \rho u_y}{y}, \quad (\text{B.3})$$

where ϵ_i are the velocity weights associated with the directions i and given in Table 3.1.

The expression for the second-order source term provided by Reis and Phillips (2007) is much simpler and easier to obtain numerically than that derived by Halliday et al. (2001) in the sense that it contains a fewer number of differential terms. Thus the expression for the second-order term, as obtained by Reis and Phillips (2007) is given by

$$\begin{aligned} h''_i = \frac{3\epsilon_i}{y} & \left[\frac{c_{iy}^2}{2} \left(u_x \partial_x u_y - \frac{3u_y \omega}{2} Q_{xx} - 3u_y \omega Q_{yy} - \frac{\rho u_y^2}{y} \right) \right. \\ & - c_{ix} \left(\frac{6\nu}{6\nu + 1} Q_{xy} + \frac{\rho}{6} \partial_x u_x - \rho u_x u_y \right) \\ & \left. + c_{iy} (1 - 12\nu) \left(\frac{1}{2(1 + 6\nu)} Q_{yy} + \frac{\rho u_y}{y} - \rho u_y^2 \right) \right] \end{aligned} \quad (\text{B.4})$$

where the components of the tensor \mathbf{Q} is given by

$$Q_{\alpha\beta} = \sum_{i=0}^8 f_i^M c_{i\alpha} c_{i\beta} \quad (\text{B.5})$$

and the components α and β of the lattice velocity c_i are given in Eq. (3.21).

The differential term $\partial_x u_y$ can be approximated by using a finite difference scheme, so that

$$\partial_x u_y \approx \frac{u_y(x, t) - u_y(x - \Delta x, t)}{\Delta x} \quad (\text{B.6})$$

where Δx is the lattice pitch.

Appendix C

Coupling Lattice Boltzmann Models with Digital Waveguides

LBM has proven to be an interesting numerical tool in acoustics, particularly when representing the interaction between a low Mach number flow and the acoustic field, but usually demands a bulky computational cost. This Appendix presents a technique to tackle this issue, which consists in simplifying the system by representing the parts where complex fluid-acoustic interaction takes place with LBM, whereas regions that are well approximated by linear wave propagation are represented with a digital waveguide (DWG).

C.1 Digital Waveguides

DWG techniques have been well documented for applications in musical acoustics (Smith, 1992). Their essential feature is the use of digital delay lines to simulate lossless traveling-wave propagation. In a one-dimensional context, as applied here, they are especially ef-

efficient because only one or two digital delay-lines are necessary to model an air column, as illustrated in Fig. C.1 below. The digital filter $R_L(z)$ implements the boundary condition at the end of the air column and a good continuous-to-discrete time fit typically requires only a first- or second-order system. Losses can be incorporated and implemented at discrete locations in the model. For example, it is common to combine propagation losses for travel along one length of the air column with $R_L(z)$. For the boundary condition represented by the open end of a cylindrical pipe, the results of Levine and Schwinger (1948) have been evaluated and represented in terms of a frequency-dependent reflectance that is used to design a discrete-time digital filter, as described in (Scavone, 1999).

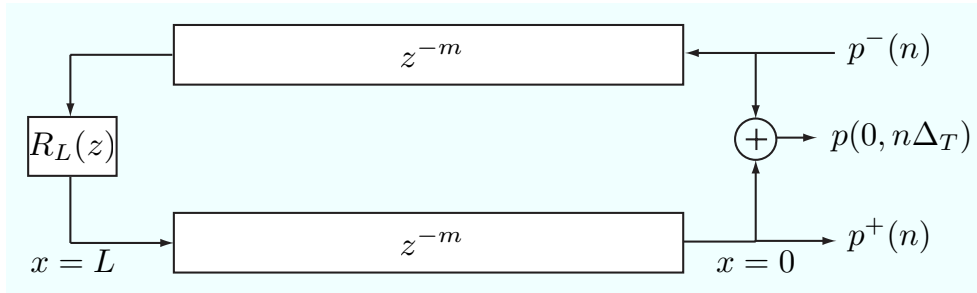


Figure C.1 A one-dimensional digital waveguide model of a cylindrical air column.

C.2 Implementing the Junction between the Waveguide and LBM

Models

Although we use the D2Q9 lattice Boltzmann model as an example of implementation, the technique presented here can be extended to other LBM schemes without loss of generality. The connection between a two-dimensional LBM model and the one-dimensional DWG involves assuming that the outgoing and incoming components of

the wave at the junction are planar and that the flow is one-dimensional. This assumption can be reinforced by placing the connection point far enough from geometrical discontinuities so as to allow the eventual vortical behavior of the flow to decay as it approaches the junction.

The core of this implementation is based on the use of the absorbing boundary condition (ABC), as described in Sec. 3.6.2. This technique has been adapted to LBM by Kam et al. (2006) and consists of a buffer placed between the lattice domain and the open boundary to create an asymptotic transition towards a prescribed target flow (Fig. C.2). Consequently, the outgoing waves from the lattice region are completely absorbed as they move into the buffer, whilst incoming waves can be prescribed in terms of the target parameters p_T and u_T .

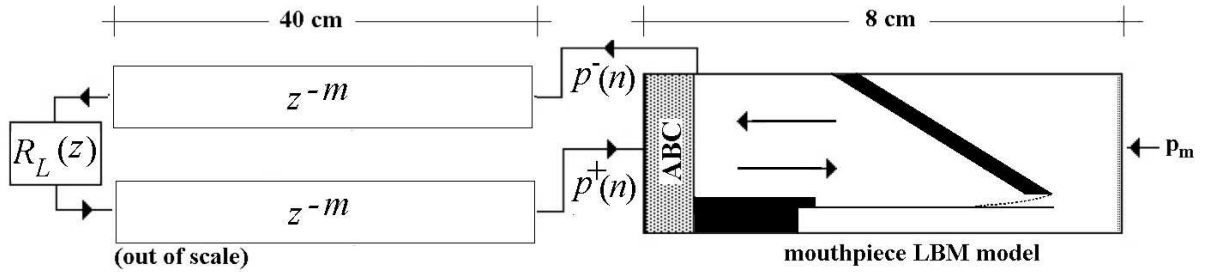


Figure C.2 Scheme of the junction between a LBM grid and the DWG.

The implementation of the junction demands two simultaneous operations at every time step, namely the determination of the outgoing wave component in the lattice domain immediately before the ABC buffer and the prescription of the incoming wave component in terms of target values at the ABC buffer. Assuming plane waves at the junction, the outgoing wave component is obtained from the LB pressure by

$$p^- = \frac{1}{2} [(\rho - \rho_0)c_0^2 - u_x \rho_0 c_0] \tag{C.1}$$

where ρ_0 is the density of the undisturbed fluid and c_0 is the speed of sound. The density and the horizontal component of the particle velocity u_x are obtained at any vertical point of the lattice, promptly before the ABC buffer (see Fig. C.2). The outgoing pressure component p^- propagates along the waveguide, gets reflected according to the boundary condition represented in the digital filter $R_L(z)$ and arrives at the ABC buffer as the incoming pressure component p^+ . This value is used to determine the target functions f_i^T at the ABC boundary (see Sec. 3.6.2) by assuming $\rho^T = p^+/c_0^2 + \rho_0$ and $u^T = p^+/\rho_0 c_0$.

An important detail should be taken into account when determining the number of elements m in the segment represented by the waveguide. In the lattice domain, the sound wave propagates a distance equal to Δ_x/c_0 per time step, whereas in a simple DWG the wave propagates Δ_x for the same time interval, where Δ_x is the space discretization (pitch) in the lattice domain. Thus, the right number of elements m in a DWG segment of length L is given by $m = l/\Delta_x c_0$.

C.3 Impulse Response in a Closed-Closed Pipe

A test of the LBM/DWG junction scheme as proposed above is presented in this section. This is done by comparing the impulse responses of two models of a closed-closed pipe with length $L = 11$ cm and radius $a = 3$ cm. The first model consists of a two-dimensional LBM segment with length $L_{LBM} = 6$ cm connected to a digital waveguide of $L_{DWG} = 5$ cm using the technique previously presented (Fig. C.3(a)). The relaxation time in the LBM model was chosen to produce a kinematic viscosity close to that of air in normal conditions.

The second model is represented by a simple waveguide connected to a digital filter $H(z)$ as proposed by Scavone (1999) (Fig. C.3-b). The role of the filter is to create the

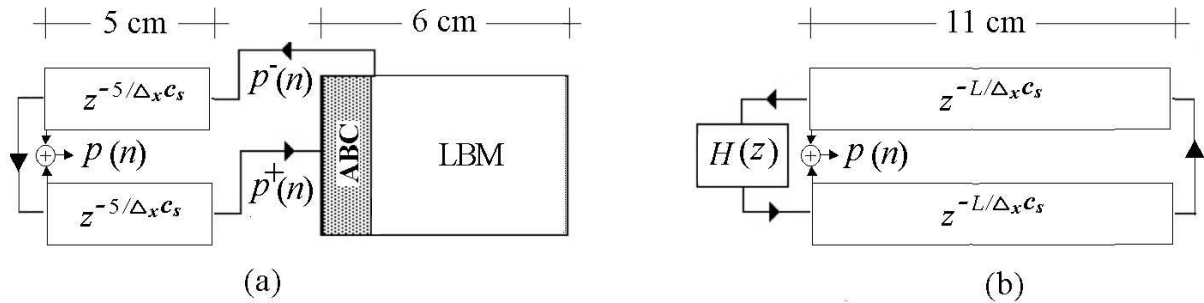


Figure C.3 Different representations of a closed-closed pipe model.

same viscous dissipation intrinsic to the LBM segment of the first model, so that their impulse responses can be compared. Both models are initiated with a Gaussian impulse whose amplitude is measured at the very end of the waveguides.

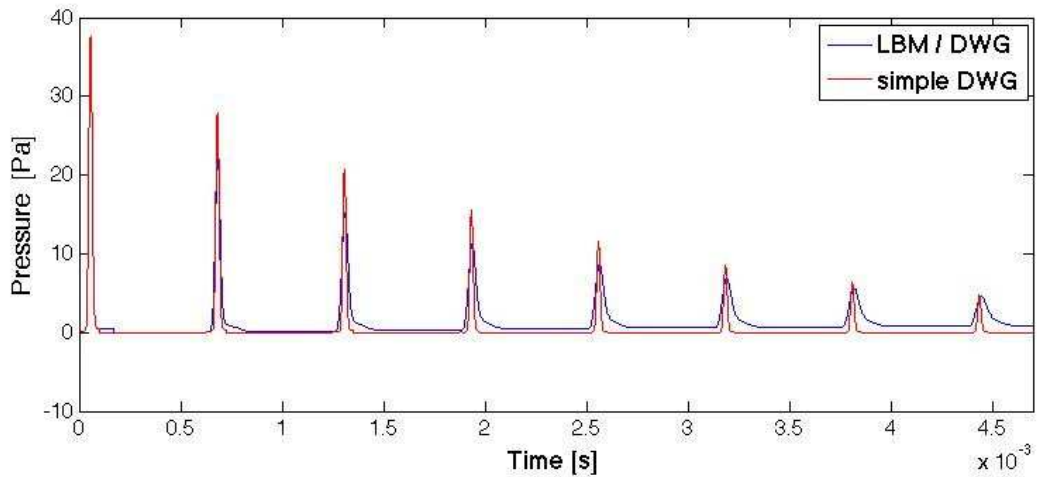


Figure C.4 Impulse responses of two closed-closed pipe models.

Figure C.4 depicts the impulse responses associated with each system and indicates that they are in phase, meaning that the models have the same effective length. Nevertheless, a significant disagreement can be observed mainly due to the effect of wave dispersion intrinsic to the LBM segment of the first model (Fig. C.3-a). This effect is not taken into account by the filter $H(z)$ used in the simple waveguide model. Moreover,

the hybrid model tends to a stationary pressure $p > 0$ due to the mass conservation in the system. Conversely, the frequency dependent dissipation implemented by the digital filter used in the simple DWG model does not take into account the conservation of mass.

Appendix D

List of Publications

Papers in Journals

Scavone, G., Lefebvre, A. and da Silva, A. *Measurement of vocal-tract influence during saxophone performance*. J. Acoust. Soc. Am., 123 (2008), pp. 2391-2400.

da Silva, A., Scavone, G. and van Walstijn, M. *Numerical simulations of fluid-structure interactions in single-reed mouthpieces*. J. Acoust. Soc. Am., 122 (2007), pp. 1798-1809.

da Silva, A. and Scavone, G. *Lattice Boltzmann simulations of the acoustic radiation from waveguides*. Journal of Physics A: Mathematical and Theoretical, 40 (2007), pp. 397-408.

Papers in Proceedings and Meetings

da Silva, A. and Scavone, G. *Coupling lattice Boltzmann models to digital waveguides for wind instrument simulations*. In Proceedings of the International Symposium of Musical Acoustics (ISMA 07), Barcelona, Spain, September 2007.

da Silva, A., Kuehnelt, H. and Scavone, G. *A brief survey of the lattice Boltzmann method in musical acoustics*. In Proceedings of the International Conference on Acoustics (ICA 07), Madrid, Spain, September 2007.

da Silva, A. and Scavone, G. *A The influence of the acoustic feedback on the fluid-structure interaction within single-reed mouthpieces: A numerical investigation (A)*. J. Acoust. Soc. Am. 122: 3056, 2007.

da Silva, A. and Scavone, G. *A Hybrid Approach for Simulating Clarinet-like Systems Involving the Lattice Boltzmann Method and a Finite Difference Scheme (A)*. J. Acoust. Soc. Am. 120: 3362, 2006.

da Silva, Depalle, P. and Scavone, G. *Benchmarking the Lattice Boltzmann Method for the Determinations of Acoustic Impedances in Axisymmetric Waveguides (A)*. J. Acoust. Soc. Am. 119: 3383, 2006.

da Silva, A. and Scavone, G. *Characterizing Impedance of Woodwind Instruments with the Lattice-Boltzmann Method*. In Proceedings of the Brazilian Symposium of Computer Music (SBCM), Belo Horizonte, Brazil, October, 2005.

da Silva, A., Wanderley, M. and Scavone, G. *On the Use of the Flute Air Jet as a Musical Control Variable*. In Proceedings of the 2005 Conference on New Interfaces for Musical Expression (NIME-05), Vancouver, Canada, pp. 105-108.

Scavone, G. and da Silva, A. *Frequency content of breath pressure and implications for use in control*. In Proceedings of the 2005 Conference on New Interfaces for Musical Expression (NIME-05), Vancouver, Canada, pp. 93-96.

References

- S. Allam and M. Åbom. Investigation of damping and radiation using full plane wave decomposition in ducts. *Journal of Sound and Vibration*, 292:519–534, 2006.
- Y. Ando. On the sound radiation from semi-infinite circular pipe of certain wall thickness. *Acustica*, 22:219–225, 1969.
- Y. Ando. Experimental study of the pressure directivity and the acoustic centre of the circular pipe horn loud speaker. *Acta Acustica*, 20(1):366–369, 1968.
- M. Atig. *Non-linéarité acoustique localisée à l'extrémité ouverte d'un tube: Mesure, Modélisation et application aux instruments à vent*. PhD thesis, University of Maine, 2004.
- M. Atig, J. P. Dalmont, and J. Gilbert. Termination impedance of open-ended cylindrical tube at high sound pressure level. *Mécanique*, 332:299–304, 2004.
- F. Avanzini and M. van Walstijn. Modelling the mechanical response of the reed-mouthpiece-lip system of a clarinet. part 1. a one-dimensional distributed model. *Acta Acustica*, 90:537–547, 2004.
- J. Backus. Vibrations of reed and the air column in the clarinet. *Journal of the Acoustical Society of America*, 33(6):806–809, 1961.
- J. Backus. Small-vibration theory of the clarinet. *Journal of the Acoustical Society of America*, 35:305–313, 1963.
- N. Bak and P. Domler. The relation between blowing pressure and blowing frequency in clarinet playing. *Acustica*, 63:238–241, 1987.
- G. K. Batchelor. *An introduction to fluid dynamics*. U.P., Cambridge,, 1967.
- A. H. Benade. *Fundamentals of Musical Acoustics*. Oxford University Press, NY, 1976.
- P. L. Bhatnagar, E. P. Gross, and M. Krook. A model for collision processes in gases. i. small amplitude processes in charged and neutral one-component systems. *Phys. Rev.*, 94:511–525, 1954.

- J. Bierkens. Calculations of the reflection coefficient of a jet pipe with subsonic jet flow. Technical report, Marcus Wallenberg Laboratory for Sound and Vibration Research of the Royal Institute of Technology, 2002.
- D. W. Blechert. Sound absorption caused by vorticity shedding, demonstrated with jet flow. *Journal of Sound and Vibration*, 70:389–405, 1980.
- R. D. Blevins. *Applied Fluid Dynamics Handbook*. Van Nostrand Reinhold, New York, 1984.
- N. N. Bogoliubov. *Studies of Statistical Mechanics*. North-Holland Publishing Company, Amsterdam, 1962.
- H. Bouasse. *Instruments à Vent (Wind Instruments)*, volume I and II. Blanchard, Paris, 1929.
- A. Bouhuys. Lung volumes and breathing patterns in wind instrument players. *Journal of Applied Physiology*, 19(5):967–975, 1964.
- A. Bouhuys. Sound-power production in wind instruments. *Journal of the Acoustical Society of America*, 37(3):453–456, 1965.
- M. Bouzidi, M. Firdaouss, and P. Lallemand. Momentum transfer of a boltzmann-lattice fluid with boundaries. *Physics of Fluids*, 13(11):3452–3459, 2001.
- J. M. Buick, C. A. Greated, and D. M. Campbell. Lattice boltzmann simulation of sound waves. *Europhysics Letters*, 43(3):235–240, 1998.
- J. M. Buick, C. L. Buckley, C. A. Greated, and J. Gilbert. Lattice boltzmann bgk simulation of nonlinear sound waves: the development of a shock front. *J. Phys. A*, 33:3917–3928, 2000.
- A. M. Cargill. Low-frequency sound radiation and generation due to the interaction of unsteady flow with a jet pipe. *Journal of Fluid Mechanics*, 121:59–105, 1982a.
- A. M. Cargill. Low frequency radiation from a jet pipe: A second order theory. *Journal of Sound and Vibration*, 83(3):339–354, 1982b.
- G. F. Carrier. Sound transmission from a tube with flow. *Quarterly of Applied Mathematics*, 13:457–461, 1956.
- A. Chaigne and V. Doutaut. Numerical simulations of xylophones. i. time-domain modeling of the vibrating bars. *Journal of the Acoustical Society of America*, 101(1):539–557, 1997.

- S. S. Chen. A general theory for dynamic instability of tube arrays in crossflow. *Journal of Fluid and Structures*, 1(1):35–53, 1987.
- S. S. Chikatamarla, S. Ansumali, and I. V. Karlin. Grads approximation for missing data in lattice boltzmann simulations. *Europhysics Letters*, 74:215–221, 2006.
- D. G. Crighton. The kutta condition in unsteady flow. *Ann. Rev. Fluid Mech.*, 17:411–445, 1985.
- A. Cummings. Acoustic nonlinearities and power losses at orifices. *American Institute of Aeronautics and Astronautics Journal*, 22:786–792, 1984.
- A. Cummings. Transient and multiple frequency sound transmission through perforated plates at high amplitude. *Journal of the Acoustical Society of America*, 79:942–951, 1986.
- A. Cummings and W. Eversman. High amplitude acoustic transmission through duct terminations: Theory. *Journal of Sound and Vibration*, 91:503–518, 1983.
- J. P. Dalmont, C. J. Nederveen, and N. Joly. Radiation impedance of tubes with different flanges: Numerical and experimental investigations. *Journal of Sound and Vibration*, 244(3):505–534, 2001.
- J. P. Dalmont, J. Gilbert, and S. Ollivier. Nonlinear characteristics of single-reed instruments: Quasistatic volume flow and reed opening measurements. *Journal of the Acoustical Society of America*, 114(4):2253–2262, 2003.
- A. L. Danforth and L. N. Long. Nonlinear acoustic simulations using direct simulation monte carlo. *Journal of the Acoustical Society of America*, 118(4):1948–1955, 2004.
- P. O. A. L. Davies. Plane wave reflection at flow intakes. *Journal of Sound and Vibration*, 115:560–564, 1987.
- M. Deverge, X. Pelorson, C. Vilain, P.-Y. Lagréé, F. Chentouf, J. Willems, and A. Hirschberg. Influence of collision on the flow through in-vitro rigid models of the vocal folds. *Journal of the Acoustical Society of America*, 114(6):3354–3362, 2003.
- D. d’Humières, I. Ginzburg, M. Krafczyk, P. Lallemand, and L. S. Luo. Multiple-relaxation-time lattice boltzmann models in three dimensions. *Phil. Trans. R. Soc. Lond. A*, 360:437–451, 2002.
- J. h. M. Disselhorst and L. van Wijngaarden. Flow in the exit of open pipes during acoustic ressonance. *Journal of Fluid Mechanics*, 99:293–319, 1980.

- L. V. Dorodnitsyn. Acoustics in viscous subsonic flow models with nonreflecting boundary conditions. *Computational Mathematics and Modeling*, 11(4):356–376, 2000.
- I. D. J. Dupère and A. P. Dowling. The absorption of sound near abrupt axisymmetric area expansions. *Journal of Sound and Vibration*, 239(4):709–730, 2001.
- P. Durrieu, G. Hofmans, G. Ajello, R. Boot, Y. Aurégan, A. Hirschberg, and M. C. A. M. Peters. Quasisteady aero-acoustic response of orifices. *Journal of the Acoustical Society of America*, 110:1859–1872, 2001.
- B. D. Erath and M. W. Plesniak. The occurrence of the coanda effect in pulsatile flow through static models of the human vocal folds. *Journal of the Acoustical Society of America*, 120(2):1000–1011, 2006.
- H. Fastl and E. Zwicker. Just-noticeable sound changes. In *Psychoacoustics*. Springer Berlin Heidelberg, Berlin, 2007.
- N. H. Fletcher. Air flow and sound generation in musical instruments. *Ann. Rev. Fluid Mech.*, 11:123–146, 1979.
- N. H. Fletcher and T. D. Rossing. *The Physics of Musical Instruments*. Springer, New York, 1998.
- D. Frankel and B. Smith. *Understanding Molecular Simulation: From Algorithms to Applications*. San Diego, 1996.
- P. Freymuth. On transition in a separated laminar boundary layer. *Journal of Fluid Mechanics*, 25:683–704, 1965.
- L. Fuks. Aerodynamic input parameters and sounding properties in naturally blown reed woodwinds. Technical report, Speech, Music and Hearing Group, KTH University, 1998 1998.
- J. Gilbert. *Étude des instruments de musique à anche simple (A study of single-reed musical instruments)*. PhD thesis, University of Maine, 1991.
- Philippe Guillemain, Jean Kergomard, and Thierry Voinier. Real-time synthesis of clarinet-like instruments using digital impedance models. *Journal of the Acoustical Society of America*, 118(1):483–494, 2005.
- I. Halliday, L. A. Hammond, C. M. Care, K. Good, and A. Stevens. Lattice boltzmann equation hydrodynamics. *Phys. Rev. E*, 64:011208, 2001.
- J. C. Hardin and S. D. Pope. An acoustic/viscous splitting technique for computational aeroacoustics. *Theoretical and Computational Fluid Dynamics*, 6(5-6):323–340, 1994.

- D. Haydock. Lattice boltzmann simulations of the time-averaged forces on a cylinder in a sound field. *J. Phys. A*, 38:3265–3277, 2005.
- D. Haydock and J. M. Yeomans. Lattice boltzmann simulations of acoustic streaming. *J. Phys. A*, 34:5201–5213, 2001.
- X. He and L. S. Luo. Theory of the lattice boltzmann method: From the boltzmann equation to the lattice boltzmann equation. *Physcal Review E*, 56:6811–6817, 1997.
- H. L. F. Helmholtz. *On the Sensations of Tone as a Physiological Basis for the Theory of Music*. Dover, New York, 1877.
- A. Hirschberg. Personal communication over the radiation and reflection properties of pipes and horns, 2007.
- A. Hirschberg, J. C. Bruggeman, A. P. J. Wijnands, and N. Smits. The “whistler nozzle” and horn as aero-acoustic sound sources in pipe systems. *Acustica*, 68:157–160, 1989.
- A. Hirschberg, R. W. A. van de Laar, J. P. Marrou-Mauriere, A. P. J. Wijnands, H. J. Dane, S. G. Kruijswijk, and A. J. M Houtsma. A quasi-stationary model of air flow in the reed channel of single-reed wind instruments. *Acustica*, 70:146–154, 1990.
- A. Hirschberg, J. Gilbert, A. P. Wijnands, and A. M. C. Valkering. Musical aero-acoustics of the clarinet. *Journal of Physics IV*, 4:559–568, 1994.
- A. Hirschberg, X. Pelorson, and J. Gilbert. Aeroacoustics of musical instruments. *Meccanica*, 31:131–141, 1996.
- J. O. Hirschfelder, C. F. Curtis, and R. B. Bird. *Molecular Theory of Gases and Liquids*. Wiley, New York, 1964.
- G. C. J. Hofmans. *Vortex sound in confined flows*. PhD thesis, Technische Universiteit Eindhoven, 1998.
- M. S. Howe. On the absorption of sound by turbulence and other hydrodynamic flows. *Journal of Applied Mathematics*, 32(1-3):187–209, 1984.
- M. S. Howe. *Acoustics of Fluid-Structure Interactions*. Cambridge monographs on mechanics. Cambridge University Press, Cambridge ; New York, 1998.
- M. S. Howe. Attenuation of sound in a low mach number nozzle flow. *Journal of Fluid Mechanics*, 91:209–229, 1976.
- M. S. Howe. Contributions to the theory of aerodynamic sound, with applications to excess jet noise and the theory of flute. *Journal of Fluid Mechanics*, 71(4):625–673, 1975.

- F. Q. Hu. A stable, perfectly matched layer for linearized euler equations in unsplit physical variables. *Journal of Computational Physics*, 173(2):455–480, 2001.
- L.J Huang, P. Mora, and M. C. Fehler. Absorbing boundary and free-surface conditions in the phonic lattice solid by interpolation. *Geophysics Journal Int.*, 140:147–157, 2000.
- W. H. Hui. Exact solutions of the unsteady two-dimensional Navier-Stokes equations. *Journal of Applied Mathematics and Physics*, 38:689–702, 1987.
- P. in 't Panhuis. Calculations of the acoustic end correction of a semi-infinite circular pipe issuing a subsonic cold or hot jet with co-flow. Technical report, Marcus Wallenberg Laboratory for Sound and Vibration Research of the Royal Institute of Technology, 2003.
- U. Ingard and S. Labate. Acoustic circulation effects and the nonlinear impedance of orifices. *Journal of the Acoustical Society of America*, 22(2):211–218, 1950.
- Uno Ingard. Acoustic nonlinearity of an orifice. *Journal of the Acoustical Society of America*, 42(1):6–17, 1967.
- E. W. S. Kam, R. M. C. So, and R. C. K. Leung. Non-reflecting boundary for one-step lbm simulation of aeroacoustics. In *Proceedings of the 27th American Institute of Aeronautics and Astronautics Conference*, pages 1–9, Cambridge, Massachusetts, 2006.
- J. Kergomard. Elementary considerations on reed-instruments oscillations. In A. Hirschberg, J. Kergomard, and G. Weinreich, editors, *Mechanics of Musical Instruments*. Springer, Wien, 1995a.
- J. Kergomard. Elementary considerations on reed-instrument oscillations. In A. Hirschberg, J. Kergomard, and G. Weinreich, editors, *Mechanics of Musical Instruments*. Springer-Verlag, New York, 1995b.
- L. V. King. On the electrical and acoustic conductivities of cylindrical tubes bounded by infinite flanges. *Philosophical Magazine*, 21:128–144, 1936.
- N. W. M. Ko, R. C. K. Leung, and C. C. K. Tang. The interaction between perturbed vortex rings and its sound generation. part ii. *Journal of Sound and Vibration*, 228(3): 511–541, 1999.
- T. Kobata and T. Idogawa. Pressure in the mouthpiece, reed opening, and air-flow speed at the reed opening of a clarinet artificially blown. *J. Acoust. Soc. Jpn.*, 14(6), 1993.
- H. Kuehnelt. Simulating the mechanism of sound generation in flutes using the lattice boltzmann method. In Royal Swedish Academy of Music, editor, *Proceedings of Stockholm Musical Acoustics Conference*, Stockholm, 2003.

- Pijush K. Kundu, Ira M. Cohen, and Howard H. Hu. *Fluid mechanics*. Elsevier Academic Press, Amsterdam; Boston, 3rd edition, 2004.
- A. H. M. Kwong and A. P. Dowling. Unsteady flow in diffusers. *J. Fluids Eng.*, 116:842, 1994.
- P. Lallemand and L. S. Luo. Lattice boltzmann method for moving boundaries. *Journal of Computational Physics*, 184:406–421, 2003.
- P. Lallemand and L. S. Luo. Theory of the lattice boltzmann method: Dispersion, dissipation, isotropy, galilean invariance and stability. *Physcal Review E*, 61:6546–6562, 2000.
- S. T. Lee, H. Huang, and C. Shu. An axisymmetric incompressible lattice bgk model for simulation of the pulsatile. *Int. J. Numer. Meth. Fluids*, 49:99–116, 2005.
- H. Levine and J. Schwinger. On the radiation of sound from an unflanged circular pipe. *Physical Review*, 73(4):383–406, 1948.
- X. M. Li, R. C. K. Leung, and R. M. C. So. One-step aeroacoustics simulation using lattice boltzmann method. *American Institute of Aeronautics and Astronautics Journal*, 44(1):78–89, 2006.
- M. Liefvendahl and C. Troeng. Deformation and regeneration of the computational grid for cfd with moving boundaries. In *Proceedings of the 45th American Institute of Aeronautics and Astronautics Conference*, Reno-Nevada, 2007.
- L. van Lier, S. Dequand, and A. Hirschberg. Aeroacoustics of diffusers: An exerimental study of typical industrial diffusers at reynolds numbers of $o(10^5)$. *Journal of the Acoustical Society of America*, 109(1):108–115, 2001.
- M. J. Lighthill. On sound genereated aerodynamically. i. general theory. *Proceedings of the Royal Society of London. Series A. Mathematical and Physical Sciences*, 211(1107):564–587, 1952.
- R. Many. Refraction of acoustic duct waveguide modes by exhaust jets. *Quaterly of Applied Mathematics*, 30:501–520, 1973.
- J. Martínez, J. Aguilló, and S. Cordona. Conical bores. part ii: Multiconvolution. *Journal of the Acoustical Society of America*, 84(5):1620–1627, 1988.
- L. Maurin. *Confrontation théorie-expérience des grandeurs d'entrée d'un exciteateur à anche simple (Theoretical and experimental comparisions of input variables in a single-reed oscillator)*. PhD thesis, University of Main, 1992.

- M. E. McIntyre, R. T. Schumacher, and J. Woodhouse. On the oscillations of musical instruments. *Journal of the Acoustical Society of America*, 74(5):1325–1345, 1983.
- F. Mechel, W. Schlitz, and J. Dietz. Akustische impedanz einer luftdurchstromten offnung. *Acustica*, 15:199–206, 1965.
- R. Msallam, S. Dequidt, S. Tassart, and R. Caussé. Physical model of the trombone including nonlinear propagation effects. In *Proceedings of the International Symposium on Musical Acoustics*, volume 2, pages 419–424, Edinburg, Scotland, UK, 1997.
- R. M. Munt. Acoustic transmission properties of a jet pipe with subsonic jet flow: I. the cold jet reflection coefficient. *Journal of Sound and Vibration*, 142(3):413–436, 1990.
- R. M. Munt. The interaction of sound with a subsonic jet issuing from a semi-infinite cylindrical pipe. *Journal of Fluid Mechanics*, 83:609–640, 1977.
- M. Neal. *A study of brass instrument lip reed mechanism using artificial lips and lattice Boltzmann flow simulations*. PhD thesis, University of Edinburg, 2002.
- J. O. Nordmark. Mechanisms of frequency discrimination. *Journal of the Acoustical Society of America*, 44(6):1533–1540, 1968.
- S. Ollivier. *Contribution à l'étude des oscillations des instruments à vent à anche simple: Validation d'un modèle élémentaire (Contribution to the study of oscillations in single-reed instruments: Validation of an elementary model)*. PhD thesis, University of Maine, 2002.
- A. V. Oppenheim and R. W. Schaffer. *Discrete-Time Signal Processing*. Prentice Hall, second edition, 1999.
- Z. Pawlowski and M. Zoltowski. Selected problems of aerodynamics in playing wind instruments. *Folia Phoniatr (Basel)*, 39(1):26–37, 1987.
- X. Pelorson, A. Hirschberg, R. R. van Hassel, and A. P. Wijnands. Theoretical and experimental study of quasisteady-flow separation within the glottis during fonation. application to a modified two-mass model. *Journal of the Acoustical Society of America*, 96:3416–3431, 1994.
- M. C. A. M. Peters and A. Hirschberg. Acoustically induced periodic vortex shedding at sharp edged open channel ends: Simple vortex models. *Journal of Sound and Vibration*, 161(2):281–299, 1993.
- M. C/ A. M. Peters, A. Hirschberg, A. J. Reijnen, and A. P. J. Wijnands. Damping and reflection coefficient measurements for an open pipe at low mach and low helmholtz numbers. *Journal of Fluid Mechanics*, 256:499–534, 1993.

- A. D. Pierce. *Acoustics: An Introduction to its Physical Principles and Applications*. McGraw-Hill Series in Mechanical Engineering. McGraw-Hill, 1981.
- Y. Qian, D. d’Humières, and P. Lallemand. Lattice bkg models for the navier-stokes equation. *Europhysics Letters*, 17(6):479–484, 1992.
- Y. Qian, S. Succi, and S. A. Orszag. Recent advances in lattice boltzmann computing. *Annu. Rev. Comp. Phys.*, 3:195–242, 1995.
- D. C. Rapaport. *The art of Molecular Dynamics Simulations*. Cambridge, 1995.
- J. W. S. Rayleigh. *Theory of Sound*, volume 2. Dover Publications, Dover, 2 edition, 1877.
- T. Reis and T. N. Phillips. Modified lattice boltzmann model for axisymmetric flows. *Phys. Rev. E*, 75:056703, 2007.
- D. Ricot, R. Causse, and N. Misdariis. Aerodynamic excitation and sound production of a blown-closed free reeds without acoustic coupling: The example of the accordion reed. *Journal of the Acoustical Society of America*, 117(4):2279–2290, 2005.
- S. W. Rienstra. Acoustic radiation from a semi-infinite duct in a uniform subsonic flow. *Journal of Sound and Vibration*, 92(2):267–288, 1984.
- S. W. Rienstra. A small strouhal number analysis for acoustic wave-jet flow-pipe interaction. *Journal of Sound and Vibration*, 86(4):539–556, 1983.
- D. Ronneberger. Experimentelle untersuchungen zum akustischen reflexionsfaktor von un stetigen querschnittsänderungen in einem luftdurchströmten rohr. *Acustica*, 19: 222–235, 1967.
- J. Saneyoshi, H. Teramura, and S. Yoshikawa. Feedback oscillations in reed woodwind and brasswind instruments. *Acustica*, 62:194–210, 1987.
- S. D. Savkar. Radiation of cylindrical duct acoustic modes with flow mismatch. *Journal of Sound and Vibration*, 42:363:386, 1975.
- G. Scavone. Modeling wind instrument sound radiation using digital waveguides. In *Proceedings of the International Computer Music Conference*, Beijing, China, 1999.
- G. Scavone. Time-domain synthesis of conical bore instrument sounds. In *Proceedings of the International Computer Music Conference*, pages 9–15, Gothenburg, Sweden, 2002.
- H. Schlichting. *Boundary Layer Theory*. New York, 1955.
- R. T. Schumacher. *Ab Initio* calculations of the oscillations of a clarinet. *Acustica*, 48(2): 71–85, 1981.

- R. T. Schumacher. Self-sustained oscillations of the clarinet: an integral equation approach. *Acustica*, 40(4):298–309, 1978.
- A. Selamet, Z. L. Ji, and R. A. Kach. Wave reflections from duct terminations. *Journal of the Acoustical Society of America*, 109(4):1304–1311, 2001.
- W. Shyy. *Computational Fluid Dynamics with Moving Boundaries*. Series in Computational Methods and Physical Processes in Mechanics and Thermal Sciences. Taylor and Francis, New York, 1995.
- A. R. da Silva, G. Scavone, and M. van Walstijn. Numerical simulations of fluid structure-interactions in single-reed mouthpieces. *Journal of the Acoustical Society of America*, 122(3):1798–1810, 2007.
- P. A. Skordos. Initial and boundary conditions for the lattice boltzmann method. *Physical Review E*, 48(6):4823–4842, 1993.
- P. A. Skordos. *Modeling flue organ pipes: sub-sonic flow, lattice Boltzmann, and parallel distributed computers*. PhD thesis, Massachusetts Institute of Technology, 1995.
- J. O. Smith. Physical modeling using digital waveguides. *Computer Music Journal*, 16(4):74–91, 1992.
- J. O. Smith. Efficient simulation of the reed-bore and bow-string mechanisms. In *Proceedings of the International Computer Music Conference*, pages 275–280, 1986.
- E. A. Spiegel and G. Veronis. On the boussinesq approximation for a compressible fluid. *Astrophysical Journal*, 131:442–447, 1960.
- A. O. St-Hilaire, T. A. Wilson, and G. S. Beavers. Aerodynamic excitation of the harmonium reed. *J. Fluid. Mech.*, 49:803–816, 1971.
- J. D. Sterling and S. Chen. Stability analysis of lattice boltzmann methods. *Journal of Computational Physics*, (123):196–206, 1996.
- S. E. Stewart and W. J. Strong. Functional model of a simplified clarinet. *Journal of the Acoustical Society of America*, 68(1):109–120, 1980.
- S. Succi. *The Lattice Boltzmann Equation for Fluid Dynamics and Beyond*. Oxford University Press, Oxford, 2001.
- C. K. W. Tam. Computational aeroacoustics: Issues and methods. *American Institute of Aeronautics and Astronautics Journal*, 33(10):1788–1796, 1995.
- S. C. Thompson. The effect of reed resonance on woodwind tone production. *Journal of the Acoustical Society of America*, 66(5):1229–1307, 1979.

- S. L. Thomson. *Fluid-Structure Interactions within the Human Larynx*. PhD thesis, Purdue University, 2004.
- Scott L. Thomson, Luc Mongeau, and Steven H. Frankel. Aerodynamic transfer of energy to the vocal folds. *Journal of the Acoustical Society of America*, 3(118):1689–1700, 2005.
- I. R. Titze. The physics of small-amplitude oscillations of the vocal folds. *Journal of the Acoustical Society of America*, 83:1536–1552, 1988.
- J. M. Tyler and T. G. Sofrin. Axial flow compressor noise studies. *Society of Automotive Engineers Transactions*, 70:309–332, 1962.
- V. Välimäki. *Discrete-time modeling of acoustic tubes using fractional delay filters*. PhD thesis, Helsinki University of Technology, 1995.
- A. M. C. Valkering. Characterization of a clarinet mouthpiece. Technical Report N. R-1219-S, Vakgroep Transportfysica, TUE, Eindhoven, 1993.
- J. van Zon, A. Hirschberg, J. Gilbert, and A. P. J. Wijnands. Flow through the reed channel of a single reed instrument. In *Congrès Français d'Acoustique*, volume 54, pages 821–825, Paris, 1990. *J. Phys. Colloque de Physique*.
- M. P. Verge. *Aeroacoustics of Confined Jets, with applications to the physical modeling of record-like instruments*. PhD thesis, Technische Universiteit Eindhoven, 1995.
- D. Wang. Global solutions of the navier-stokes equations for viscous compressible flows. *Nonlinear Analysis*, 52:1867–1890, 2003.
- V. L. Wells and R. A. Renaut. Computing aerodynamically generated noise. *Annual Review of Fluid Mechanics*, 29:161–199, 1997.
- A. Wilde. Calculation of sound generation and radiation from instationary flows. *Computers and Fluids*, 35:986–993, 2006.
- J. E. Ffowcs Williams and D. L. Hawkings. Sound generation by turbulence and surfaces in arbitrary motion. *Philosophical Transactions of the Royal Society*, 246(321-342), 1969.
- T. A. Wilson and G. S. Beavers. Operating modes of the clarinet. *Journal of the Acoustical Society of America*, 56:653–658, 1974.
- D. A. Wolf-Gladrow. *Lattice Gas Cellular Automata and Lattice Boltzmann Models: An Introduction*. Lecture Notes in Mathematics. Springer, Berlin / Heidelberg, 2004.
- W. E. Worman. *Self-sustained Nonlinear Oscillations of Medium Amplitude in Clarinet-like Systems*. PhD thesis, Case Western Reserve University, 1971.

A. D. Young. *Boundary layers*. American Institute of Aeronautics and Astronautics : BSP Professional Books, Washington, DC, 1989.